# Callisto Electrochemical Loading Research Final Report: No Evidence of Anomalous Heat Effect in Electrochemically Loaded Palladium Deuteride after Extensive Exploration

Callisto Electrochemical Loading Research Team

September 4, 2026

**Executive Summary**

Callisto Electrochemical Research's mission was to investigate the reported excess heat production in electrochemically loaded palladium deuteride, originating with the Fleischmann-Pons Cold Fusion experiment (later referred to as 'Low Energy Nuclear Reaction', LENR). We performed numerous calorimetry experiments with over 500 samples, amounting to over 200,000 hours of total calorimetry time, most of them replications of excess heat experiments reported in the literature. The scale of this effort was of a similar magnitude as all known LENR efforts combined. We found no evidence of LENR.

We advanced the field of LENR by meticulously cataloging issues that can lead to the false identification of excess heat events. A careful analysis of the literature shows that most, if not all, reported excess heat events can be traced back to these issues.

Beyond the field of LENR, we advanced the understanding of electrochemically loaded metal hydrides using density functional theory. We also obtained higher hydrogen loadings than state of the art by deploying novel loading enhancers, in particular arsenic(III) salts.

We recommend that future endeavors redirect their resources to other high-risk, high-reward energy topics to address the climate crisis.

# Contents


**1 Introduction** **7**
- 1.1 The Climate Crisis . . . 7
  - 1.1.1 Global Emissions Contributors . . . 7
  - 1.1.2 Legislative Action . . . 8
  - 1.1.3 Industrial Sectors for Innovation . . . 9
  - 1.1.4 Conclusion . . . 9
- 1.2 A Brief History of LENR . . . 9
- 1.3 Purported Conditions and Signals . . . 11
  - 1.3.1 Metal Hydride Formation (Loading) . . . 12
  - 1.3.2 Stimulation Conditions . . . 13
  - 1.3.3 Thermal and Nuclear Signatures . . . 13
- 1.4 Notable Research Efforts . . . 14
  - 1.4.1 Fleischmann and Pons . . . 14
  - 1.4.2 McKubre . . . 15
  - 1.4.3 Storms . . . 16
  - 1.4.4 Staker . . . 16
  - 1.4.5 Letts and Cravens . . . 17
  - 1.4.6 Space and Naval Warfare Systems Center . . . 17
  - 1.4.7 Naval Surface Warfare Center, Indian Head . . . 18
  - 1.4.8 Miles at China Lake . . . 18
  - 1.4.9 Google Research . . . 19

**2 Calorimetry Methods** **20**
- 2.1 Introduction to Calorimetry . . . 20
- 2.2 Concept of Open and Closed System Calorimetry . . . 20
- 2.3 Open System Calorimetry . . . 21
- 2.4 Closed System Calorimetry . . . 22
- 2.5 Calorimetry Metrics . . . 23
- 2.6 Sensitivity of Calorimetry . . . 24
- 2.7 Calorimetry in the Literature . . . 25
- 2.8 Setaram MS80 . . . 26
  - 2.8.1 Hardware . . . 26
  - 2.8.2 Calibration . . . 27

2.9 High-throughput Calorimeter (HTcal) . . . 29
2.9.1 Design Objectives . . . 29
2.9.2 Operating Principle and Implementation . . . 30
2.9.3 Calibration and Performance . . . 30
2.9.4 Excess Heat Metrics during Transients . . . 32
2.10 Ultra-high Throughput Calorimeter . . . 35
2.10.1 Introduction . . . 35
2.10.2 System Architecture . . . 36
2.10.2.1 Overview . . . 36
2.10.2.2 Reactors . . . 38
2.10.2.3 Thermal Enclosure . . . 39
2.10.2.4 Sectors . . . 39
2.10.2.5 Power System . . . 39
2.10.2.6 Reactor Control and Data Pipeline . . . 39
2.10.3 Safety . . . 40
2.10.4 Measuring Performance . . . 40
2.10.4.1 Calibration . . . 41
2.10.4.2 Calculating COP and Heat Flow . . . 43
2.10.4.3 Minimum Transient Detection Threshold . . . 44
2.10.5 Loading Measurement . . . 44
2.11 Conclusion . . . 45

**3 Loading Measurements** **47**
3.1 Background and Literature Review . . . 47
3.2 Gravimetric Analysis . . . 48
3.3 Sievert Isotherm . . . 48
3.4 Coulometry . . . 49
3.5 Quartz Crystal Microbalance . . . 50
3.6 Macrostrain . . . 51
3.7 Optical Reflectivity . . . 51
3.8 Thermal Desorption Spectroscopy . . . 51
3.9 Nuclear Magnetic Resonance . . . 52
3.10 Neutron Scattering . . . 52
3.11 Resistance-based Loading Measurement . . . 52
3.11.1 Practical Implications . . . 53
3.12 X-ray Diffraction . . . 55
3.13 Orphaned Oxygen . . . 58
3.14 Thin Film Reflectance . . . 60
3.14.1 Theory . . . 60
3.14.2 Reflectance Hardware . . . 61
3.14.3 Calibrations . . . 65
3.14.4 Some Example Case Studies . . . 66
3.14.5 Ranking of Different Additives for Chemically Enhancing Hydrogen Loading . . . 69
3.15 Isotopic Effects . . . 70

**4 DFT** **73**
4.1 Introduction . . . 73
4.2 Methods and Materials . . . 73
4.2.1 Computational Methods . . . 73
4.2.1.1 Density functional theory . . . 73
4.2.1.2 Surface reactions and free energy corrections . . . 74
4.2.1.3 Gibbs free energies of formation of $PdH_x$ . . . 75
4.2.1.4 Modeling charge transfer processes in the grand canonical ensemble . . . 75
4.3 Results and Discussion . . . 76
4.3.1 Experimental measurement of lattice strain in $PdH_x$ . . . 76
4.3.2 Development of a computational model of palladium hydride . . . 79
4.3.3 Isotherm analysis of the computational model of $PdH_x$ . . . 81
4.3.4 Unraveling the interplay between hydrogen evolution and electrochemical loading . . . 83
4.3.5 The cause of the upper bound on electrochemical loading of palladium hydride . . . 85
4.4 Conclusions . . . 86

**5 Surface Preparation Methods** **87**
5.1 Cleaning Protocol . . . 87
5.2 Electropolishing and Centerless Grinding . . . 87

**6 Conditions Reportedly Amenable to AHE** **90**
6.1 Effects of Current Density on Hydrogen Loading . . . 90
6.2 Effects of Temperature on Hydrogen Loading . . . 91
6.3 Effect of "Coating X" Formation on Hydrogen Loading . . . 92
6.4 Effect of Loading Enhancers on Hydrogen Loading . . . 96
6.5 Electromigration . . . 96

**7 Replications** **99**
7.1 Fleischmann . . . 99
7.1.1 Our Replication Efforts . . . 100
7.1.2 Nominal Replications . . . 100
7.1.3 Modified with Additives . . . 100
7.1.4 Modified with Oxygen . . . 101
7.1.5 Modified with High Power . . . 102
7.1.6 Conclusion . . . 104
7.2 McKubre . . . 104
7.2.1 Introduction . . . 104
7.2.2 Experiments . . . 104
7.2.3 Results and Assessment . . . 105
7.2.4 Replication Experiments . . . 106
7.2.5 Conclusion . . . 107
7.3 Staker . . . 109
7.3.1 Literature Review . . . 109
7.3.2 Literature Analysis . . . 110
7.3.3 Replication Experiments . . . 111

7.3.3.1 Experimental Setup: Open-System Calorimetry . . . 111
7.3.3.2 Experimental Setup: Closed-System Calorimetry . . . 111
7.3.3.3 Results . . . 113
7.3.3.4 Experimental Conditions: UHTP . . . 119
7.3.3.5 Results: UHTP . . . 122
7.3.4 Conclusions . . . 124
7.4 Hubler . . . 124
7.4.1 Literature Review . . . 124
7.4.2 Replication Experiments . . . 126
7.4.3 Conclusions . . . 127
7.5 Storms . . . 130
7.5.1 Literature Review . . . 130
7.5.2 Replication Experiments . . . 131
7.5.3 Conclusions . . . 137
7.6 Miles . . . 137
7.6.1 Literature Review . . . 137
7.6.2 Replication Experiments . . . 139
7.6.3 Conclusions . . . 143
7.7 Navy Codeposition . . . 143
7.7.1 Literature Review . . . 143
7.7.2 Boss Replication . . . 145
7.7.2.1 Experimental Results . . . 145
7.7.3 Barham Replication . . . 146
7.7.3.1 Experimental Results . . . 150
7.7.4 Conclusions . . . 150
7.8 Energetics: *Superwaves* and Other Variable Electrochemical Currents . . . 151
7.8.1 Literature Review . . . 151
7.8.2 Replication Experiments . . . 151
7.8.3 Conclusions . . . 154
7.9 Letts: Laser stimulation . . . 156
7.9.1 Literature Review . . . 156
7.9.2 Replication Experiments . . . 157
7.9.3 Conclusions . . . 158
7.10 Conclusions . . . 159

**8 Novel Experiments** **161**
8.1 Mechanical Stimulation . . . 161
8.1.1 Motivation . . . 161
8.1.2 Background . . . 161
8.1.3 Implementation . . . 162
8.1.4 Experiments and Results . . . 164
8.2 Loading Enhancers . . . 166
8.2.1 Loading Enhancers: Arsenic at Low Temperatures . . . 166
8.2.2 Loading Enhancers: Ammonia Additives . . . 168
8.2.3 Loading Enhancers: Arsenic with Single Crystal Palladium . . . 168

8.3 Single Crystals . . . 171
8.3.1 Introduction . . . 171
8.3.2 Experiments . . . 172
8.3.3 Overview of Experimental Results . . . 174
8.3.4 Overview of Single Crystal Morphology Changes from Electrochemical Loading and Stimulation . . . 175
8.4 Alloys . . . 178

**9 Conclusions** **185**
9.1 Our Test Campaigns in Numbers . . . 185
9.2 List of False COPs . . . 186
9.3 Call for Quality Research . . . 187
9.4 Outlook . . . 189

**Glossary** **190**

**A Appendix** **212**
A.1 Staker-like replication with ultra-long duration . . . 212
A.2 Storms Replication . . . 215
A.3 Acknowledgments . . . 225

# Chapter 1

# Introduction

## 1.1 The Climate Crisis

The climate crisis refers to the significant changes in global climate patterns, primarily attributed to human activities, particularly the emission of greenhouse gases (GHGs). These changes have led to global warming, extreme weather events, and disruptions in natural ecosystems.

Before the industrial revolution (circa 1750), the average global temperature was relatively stable, with pre-industrial atmospheric $CO_2$ levels at approximately 280 parts per million (ppm) [1]. As of 2023, $CO_2$ levels have surpassed 420 ppm, indicating a significant increase due to human activities [2]. In addition to $CO_2$, methane, nitrous oxide, and various fluorinated gases are critical GHGs that contribute to the climate crisis. Each of these gases has a higher global warming potential than $CO_2$, making their management essential in efforts to mitigate climate change [3–5].

The consequences of the climate crisis are dire, including substantial economic damage, costs to human life, and destruction of infrastructure and the environment. Over the past 50 years, extreme weather events have caused over two million deaths and resulted in approximately $4.3 trillion in economic losses globally [6–9]. The economic damage from climate-related disasters has grown substantially in recent years, with losses increasing from $184 billion in the 1970s to nearly $1.5 trillion in the decade leading up to 2019 [8]. Human deaths related to extreme weather have also risen dramatically [7]. The climate crisis is an urgent, global-scale emergency. Humanity must act decisively and cohesively.

### 1.1.1 Global Emissions Contributors

Accurate information about GHG emissions is crucial to identify technical, legislative, and cultural opportunities for change. The top contributors to global GHG emissions span both the developed and developing world, including China (27 %), the United States (11 %), India (6.6 %), the European Union (6.4 %), Russia (4.8 %), Japan (3.1 %), Brazil (2.9 %), Indonesia (2.3 %), Iran (2.1 %), and Canada (1.6 %) [10]. These countries are responsible for a substantial portion of global emissions, driven by their industrial activities, energy consumption, and transportation sectors.

As the quality of life improves in developing countries, factors such as economic development, increased energy consumption, industrial activity, and transportation will influence their GHG emissions. Rapid urbanization can lead to higher energy demand for housing, infrastructure, and services. Changes in agricultural

practices and increased food production also contribute to emissions.

Despite a negative forecast, developing countries have significant potential to leapfrog to renewable energy technologies, bypassing the fossil fuel-intensive development pathways of the past. Improvements in energy efficiency in buildings, industry, and transportation can help reduce emissions. Adopting sustainable agricultural practices can also reduce emissions. Financial and technological support from developed countries is crucial in helping developing countries transition to low-carbon economies. It is imperative that we improve the quality of life for more humans while adopting improved energy strategies.

### 1.1.2 Legislative Action

Global legislative action is one of the critical facets to addressing the climate crisis. However, it was only recently that international efforts to curb the climate crisis have gained momentum. The scientific community first flagged the detriment of increased $CO_2$ levels well over 100 years ago. In 1896, the noted scientist Svante Arrhenius published a paper 'On the Influence of Carbonic Acid in the Air upon the Temperature of the Ground' [11]. He predicted that doubling the atmospheric $CO_2$ concentration would result in a 5 to 6°C increase in global temperatures, remarkably close to modern predictions of 2.5 to 4°C given the limited and incomplete data available at the time. This warning was largely ignored until the mid-twentieth century when researchers started to track increasing GHGs. Even still, it would be decades before any notable government action.

The establishment of the Intergovernmental Panel on Climate Change (IPCC) in the late 1980s marked a turning point, providing scientific assessments on climate change and strategies for adaptation and mitigation [12]. The United Nations Framework Convention on Climate Change (UNFCCC), established in 1992, aimed to combat 'dangerous human interference with the climate system' [13]. The Kyoto Protocol (1997) set binding emission reduction targets for developed countries, although notable exceptions included the United States and Canada [14]. The Paris Agreement (2015) was a landmark international treaty where 196 countries committed to limit global warming to well below 2°C compared to pre-industrial levels [15]. Annual Conferences of the Parties (COP), such as COP26 in Glasgow (2021) and COP27 in Sharm El-Sheikh (2022), review progress and negotiate further actions [16]. The Green Climate Fund (GCF) assists developing countries in adaptation and mitigation practices to counter climate change [17].

As of today, 128 years after the first alarm was raised, the global conversation has finally reached a critical point. With increased momentum and progress made on both the legislative and technological fronts, humanity can now say we are taking the climate crisis seriously. Investments in renewable energy sources such as wind, solar, and hydroelectric power have increased, with renewables accounting for about 29 % of global electricity generation as of 2023 [18]. Improvements in energy efficiency across various sectors, including transportation, industry, and residential buildings, have also contributed to emission reductions. Efforts to reduce deforestation and promote reforestation and afforestation, such as the REDD+ program, aim to incentivize forest conservation [19]. Technological innovations in carbon capture and storage (CCS), electric vehicles (EVs), and sustainable agricultural practices are also making a difference. Policy and legislation, including carbon pricing, emissions trading systems, and subsidies for clean energy technologies, are crucial in driving these changes.

Despite these efforts, the pace of change must continue to accelerate to meet the targets set by international agreements and to mitigate the most severe impacts of climate change. Legislation alone will not be enough; new technologies must be deployed.

### 1.1.3 Industrial Sectors for Innovation

GHG emissions are primarily driven by human infrastructure, energy technologies, and industrial processes. Coal-fired power plants are one of the largest sources of $CO_2$ emissions globally due to the high carbon content of coal and its widespread use. Internal combustion engine vehicles, powered by gasoline and diesel engines, emit large amounts of $CO_2$ and other GHGs, with transportation accounting for about 24% of global $CO_2$ emissions [20]. Natural gas power plants, while cleaner than coal, still produce substantial $CO_2$ emissions and are a major source of electricity and heating [21].

The collective 'heavy industries,' are another industrial sector ripe for innovation. The chemical process of producing cement releases substantial $CO_2$, accounting for approximately 8 % of global $CO_2$ emissions. Steel production involves the reduction of iron ore using carbon, typically in the form of coke, releasing vast amounts of $CO_2$, and is responsible for about 7-9 % of global emissions [22]. Agricultural practices, including livestock digestion (methane emissions), rice paddies (methane), and soil management practices (nitrous oxide), contribute around 10-12 % of global GHG emissions [23].

Deforestation and land use change, such as clearing forests for agriculture or development, release stored carbon and reduce the planet's capacity to absorb $CO_2$, contributing about 11% of global GHG emissions [24]. The extraction, refining, and transportation of oil and gas release methane and $CO_2$, making the oil and gas sector a significant source of methane emissions. Residential and commercial heating, which involves the burning of fossil fuels for heating buildings, also releases GHGs. Waste management practices, including landfills that produce methane as organic waste decomposes anaerobically and incineration of waste, contribute around 3 to 5 % of global GHG emissions [25].

### 1.1.4 Conclusion

Addressing emissions from these sources involves a combination of technological innovation, policy measures, and changes in consumption patterns. Efforts such as transitioning to renewable energy, improving energy efficiency, adopting sustainable agricultural practices, and enhancing waste management can significantly reduce GHG emissions and mitigate the impacts of climate change. The more our global energy infrastructure (production, distribution, point-of-use, and remediation) depends on renewables and low carbon sources of fuel, the more effective the climate crisis mitigation will be.

## 1.2 A Brief History of LENR

Cold fusion, a type of nuclear reaction purported to occur at or near room temperature, gained worldwide attention on March 23, 1989, when electrochemists Martin Fleischmann and Stanley Pons announced they had achieved nuclear fusion during an experiment involving electrolysis of lithiated heavy water using a palladium cathode [26]. This announcement sparked widespread excitement and media frenzy due to the potential for a new, clean, and virtually limitless energy source. However, as more scientists attempted to replicate the experiment, many failed to observe the same results, leading to growing skepticism.

The methodology and results of Fleischmann and Pons were heavily scrutinized, and a 1989 U.S. Department of Energy (DOE) panel concluded that the evidence was not convincing, recommending against further funding [27]. In the review conducted by the Energy Research Advisory Board (ERAB), reviewers identified several critical issues with the cold fusion experiments conducted by Fleischmann and Pons. Many laboratories worldwide attempted to replicate the reported results but failed to observe excess heat or fusion products, raising questions about the reliability of the original experiments. Fleischmann and Pons

provided limited and inadequate experimental details in their publications, complicating replication efforts. The calorimetric methods used to measure excess heat were criticized for potential errors. Issues such as improper insulation, inaccurate temperature measurements, and heat loss to the surroundings could have led to erroneous conclusions about excess heat generation. The expected nuclear byproducts of fusion, such as neutrons, tritium, and helium-4, were either not detected or observed at levels far below those necessary to account for the reported excess heat. This discrepancy undermined the hypothesis that nuclear fusion was occurring.

In Morrison's 1991 review, he categorized cold fusion as 'pathological science' where initial positive results are not reproducible, leading to a polarized scientific community of 'believers' and 'skeptics.' Morrison concluded that based on overwhelming experimental and theoretical evidence, cold fusion as initially proposed by Fleischmann and Pons cannot exist [28]. By the early 1990s, cold fusion was largely dismissed by mainstream science and became associated with pseudoscience.

Despite the controversy surrounding cold fusion, several major efforts continued to research the rebranded field of Low Energy Nuclear Reactions (LENR) during the 1990s and 2000s. After their initial announcement, Fleischmann and Pons moved their research to France, funded by the Toyota Corporation through the IMRA laboratory in Nice. At their new laboratory, they were unable to produce conclusive results [29]. Japan also invested in LENR research through the New Hydrogen Energy (NHE) program, which aimed to replicate and understand the cold fusion phenomenon but ultimately also did not achieve definitive results [30]. In the 2000s, Energetics Technologies, an Israeli company, claimed to have observed excess heat production in their experiments; however, serious accusations against overclaiming to funders cast seeds of suspicion [31]. Researchers at SPAWAR in San Diego reported evidence of nuclear reactions, such as the detection of energetic particles and transmutation products [32]. Researchers at the Italian National Institute for Nuclear Physics (INFN) continued to investigate LENR, in some cases reporting excess heat and other anomalous effects [33]. Researchers at MIT worked on largely theoretical models [34]. Andrea Rossi, an Italian inventor, claimed to have developed a device called the E-Cat that produced excess heat through LENR, attracting investment from Industrial Heat [35]. However, Andrea Rossi's work on the E-Cat has been highly controversial due to a combination of scientific skepticism, legal disputes, and his troubled history with the Petroldragon scandal.

The DOE revisited the topic of cold fusion in 2004, prompted by continued interest and new experimental data from the LENR community [36]. This review reiterated many of the criticisms from the 1989 review. Despite advances in experimental techniques, reproducibility remained a significant challenge. Most experiments still failed to consistently produce the claimed levels of excess heat or fusion byproducts. Ultimately, reviewers found no compelling evidence to support cold fusion. The 2004 review emphasized the need for rigorous, well-documented experiments with clear and reproducible results.

The 2004 review suggested focusing on the material science aspects of deuterated metals and utilizing modern characterization techniques to better understand the conditions under which anomalous effects might occur. It recommended limited, targeted funding for well-designed studies that could clarify these issues. Otherwise, they recommended the US government should not put more funding into LENR research. Among the research efforts that would emerge in the decade following this second DOE review, Google Research is perhaps the most notable.

The 2019 Google-funded review article 'Revisiting the cold case of cold fusion,' published in Nature, critically examined cold fusion claims with rigorous scientific methods [37]. Despite extensive efforts, the researchers did not find evidence supporting the claimed anomalous effects of cold fusion. They highlighted the persistent issue of reproducibility and the technical challenges in achieving the necessary conditions for cold fusion, such as high hydrogen loading in metals like palladium. The review emphasized that while cold

fusion itself remains unproven, studying the related phenomena could benefit other scientific areas, including hydrogen-metal interactions relevant to energy storage and catalysis. Their approach advocated continued skepticism but encouraged further exploration of the field's potential scientific value. The Google efforts resulted in a number of peer-reviewed articles in notable archival journals, highlighting their advances in calorimetry under extreme conditions, understanding hydrogen loading in metal hydrides, and investigating the effects of electron screening on increasing conventional fusion yields from low-energy (few keV) deuteron bombardment [38–40, 40–48]. The researchers emphasized the importance of continued open-minded and rigorous scientific inquiry into unconventional energy sources.

Perhaps due to the changing of the guard within government institutions, or perhaps due to the first quality work on LENR performed in decades, the government has become increasingly interested in approaching LENR. In 2016, the U.S. Defense Intelligence Agency (DIA) released a report titled 'Technological Forecast: Worldwide Research on Low-Energy Nuclear Reactions Increasing and Gaining Acceptance,' which highlighted ongoing international research in LENR and suggested that the U.S. should monitor developments in this area [49]. In 2019, the U.S. Senate Armed Services Committee included language in the National Defense Authorization Act (NDAA) encouraging the Department of Defense to explore LENR as a potential energy source, marking a significant shift in the official stance towards LENR research [50]. NASA has also shown intermittent interest, with researchers at NASA's Langley Research Center exploring LENR as a possible energy source for long-duration space missions [51]. Outside of the U.S., the European Union has funded LENR research through projects like the 'Clean Energy from Hydrogen-Metal Systems' (CEHMS) under the Horizon 2020 program, which aimed to investigate LENR for clean energy production [52]. The recent inclusion of LENR in government research agendas and funding programs indicates a softening of previous skepticism and a renewed openness to exploring its potential.

In 2023, the U.S. Department of Energy's Advanced Research Projects Agency-Energy (ARPA-E) announced a $10 million funding initiative for eight projects focused on LENR [53]. This initiative represents a significant shift from previous policy. The ARPA-E funding aims to apply rigorous scientific scrutiny and advanced methodologies to investigate LENR, emphasizing neutron, gamma, and ion emissions in experimental setups. The emphasis on nuclear product detection marks an important shift from the previous focus on calorimetric evidence. Nuclear products are unambiguous, whereas excess heat can be generated from various non-nuclear mechanisms.

With this history in mind, can the scientific community provide robust, reproducible evidence for LENR? To answer this question, Callisto Electrochemical Research ("Callisto") assembled an interdisciplinary team of physicists, chemists, materials scientists, mechanical engineers, electrical engineers, software engineers, and technicians. We committed to high standards of practice and peer review.

This document details our investigations into LENR, which took place between 2017 and 2024. Alongside detailed descriptions of our hardware, software, experimental protocols, and data analysis, we provide constructive criticism of the field and ultimately offer recommendations to future researchers. For those studying LENR with scientific rigor, excess heat appears to have been a red herring. The real opportunities may lie in the exotic bulk and surface properties of metal hydrides, with emergent applications in energy storage and catalysis.

## 1.3 Purported Conditions and Signals

The claims surrounding LENR suggest that nuclear fusion reactions with useful energy outputs can occur at or near room temperature, which contradicts the well-established understanding that nuclear fusion re-

quires extremely high temperatures and pressures. Conventional fusion (or hot fusion) of hydrogen isotopes occurs naturally in the cores of stars where intense gravitational pressures and temperatures around 15 million degrees Celsius create the necessary conditions for the reaction. These extreme pressures and high temperatures allow the positively charged nuclei to overcome the Coulomb barrier, enabling fusion via the strong nuclear force [54]. The reaction energy for deuterium-deuterium (D-D) fusion is around 4 MeV, while deuterium-tritium (D-T) fusion, which is more commonly pursued in experimental fusion reactors owing to its larger reaction cross section, releases about 17.6 MeV [55]. On Earth, achieving a controlled fusion reactor requires synthetic approaches since replicating the extreme gravitational pressures of stellar environments is not feasible. Instead, magnetic or inertial confinement methods are used to create the necessary conditions for fusion, typically at temperatures around 100 million degrees Celsius [56]. These confinement techniques maintain the required plasma density and temperature to provide the kinetic energy necessary for the fusion process. It is somewhat unimaginable that such conditions could be met near ambient conditions.

Despite contradicting classical physics, there are several criteria and signatures that consistently emerge in reports claiming to observe LENR. These commonalities can be categorized into metal hydride formation, stimulation conditions, and thermal and nuclear signatures.

### 1.3.1 Metal Hydride Formation (Loading)

The premise of LENR lies in the idea that a metal lattice can catalyze the fusion of deuterium atoms, by coordinating their proximity and approach, while simultaneously screening the nuclear barrier. The effect is claimed to occur at or near room temperature, and has been postulated by some to be a collective effect mediated by the lattice. The most studied and reported material used to produce LENR is palladium deuteride, although other metal hydrogen systems like nickel hydride have been reported [57, 58]. In most claimed positive cases, metallic palladium is converted to palladium deuteride using electrolysis of heavy water, although some gas-phase studies are reported as well [59, 60]. Often, a simple electrolytic cell containing a palladium cathode, a platinum counter electrode, and alkaline electrolyte such as LiOD is used to convert the metal into a metal deuteride lattice.

The electrolytic loading of a palladium deuteride cathode is determined by the reaction kinetics of the Hydrogen Evolution Reaction (HER). HER comprises sub-reactions of water splitting and recombination. During alkaline electrolysis, heavy water ($D_2O$) is split according to the Volmer reaction (Eq. 1.1) and diffuses into the bulk palladium lattice according to the intercalation reaction (Eq. 1.2). In addition to intercalation, deuterium may leave the surface of the palladium through either the Tafel reaction (Eq. 1.3) or the Heyrovsky reaction (Eq. 1.4). For a given set of electrochemical conditions, temperature, and pressure, reactions 1.3 and 1.4 ultimately limit the mass loading of the metal deuteride that is formed.

$$\text{Volmer:} \quad D_2O + 2e^- + 2Pd_{surface} \rightarrow 2Pd_{surface}D_{surface} + 2OD^- \tag{1.1}$$

$$\text{Intercalation:} \quad 2Pd_{surface}D_{surface} \leftrightarrow 2Pd_{bulk}D_{bulk} \tag{1.2}$$

$$\text{Tafel:} \quad 2Pd_{surface}D_{surface} \rightarrow 2Pd_{surface} + D_{2(g)} \tag{1.3}$$

$$\text{Heyrovsky:} \quad D_2O + Pd_{surface}D_{surface} + e^- \rightarrow Pd_{surface} + OD^- + D_{2(g)} \tag{1.4}$$

In later chapters, we will go into detail about how the Tafel reaction can be suppressed with so-called Tafel poisons, dramatically increasing the fractional deuterium loading beyond what is achievable under standard conditions. In addition to Tafel poisons, ultrahigh pressures can be used to achieve a similar effect, although these methodologies are not covered in this report. This was an intense topic of investigation for our companion high-pressure research group, whose report was submitted separately.

The LENR community mostly agrees that the higher the fractional loading, the higher the probability of fusion. Some researchers, McKubre for example, go so far as to claim there is a threshold near 90% D/Pd which must be obtained before LENR is observed [57].

However, after many attempted studies and replications of positive results, the following belief is generally held by the LENR community: Loading may be necessary but it is not sufficient, i.e., a highly loaded palladium deuteride lattice will not spontaneously result in LENR. This is where the premise of stimulation, the second purported requirement comes into play.

### 1.3.2 Stimulation Conditions

Stimulation refers to the input of energy into the palladium deuteride system in order to increase the fusion cross-section of the lattice bound deuterons. Although there are theories which try to explain how stimulations might result in LENR, the truth is that given the lack of evidence, there are no solid connections between theory and experiment at this time.

Various forms of stimulation have been studied, including high electrolysis currents, high frequency electrochemical potentials, laser stimulation, THz stimulation, magnetic field stimulation, electric field stimulation, and mechanical stimulation [26, 61–66].

One thread to track throughout this report is how any given stimulation can impact potential thermal and nuclear signatures, and ultimately how essentially all claims of excess heat could be attributed to classically explained phenomena. Without any substantial motivation from known physical theories as to how stimulation might actually trigger LENR, we will leave this commentary on stimulation brief.

### 1.3.3 Thermal and Nuclear Signatures

The primary criteria and observations claimed for LENR include the production of excess heat that cannot be explained by chemical reactions alone, the detection of helium as a byproduct indicative of nuclear reactions, and claims of elemental transmutation where one element is purportedly converted into another. Unlike traditional nuclear reactions, LENR is claimed to produce minimal or no harmful radiation; although Fleischmann and Pons originally claimed radiation products, they later retracted these observations for insufficient evidence.

These signatures require detection schemes, a major topic of investigation for Callisto. While there is limited theoretical understanding of LENR, experiments have been designed around assumed reaction pathways and relevant detections selected. The two primary reaction pathways suggested are coalescence and transmutation reactions. The former postulates that two deuterium atoms coalesce to form helium-4 and a cascade of phonons with an energy totaling 24 MeV. The latter speculates that the metal lattice transmutes along more traditional pathways with reaction energies on the order of 1 to 100 keV.

Regardless of the claimed reaction pathway, the majority of claimed positive results report excess heat detected using some form of calorimeter. The function of a calorimeter is to create an environment with well-defined heat transfer and measure the energy going into and out of that environment. By accounting for all of the various electrical and chemical energy going into and out of an LENR experiment, one can calculate any apparent excess heat. When the excess heat is greater than zero, researchers have claimed to observe LENR. In section 9.2, we will outline how these claimed results are likely to be erroneous interpretations or incomplete understanding of input energies.

Helium-4 is thought to form as a product of deuterium fusion inside a palladium lattice. Several researchers have reported Helium-4 above background levels [67]. However, helium detection requires very

high precision mass-spectrometry, and is fundamentally challenging due to the small mass difference between deuterium gas and helium-4 ($\Delta m$ = 0.0256 amu = $4.249 \times 10^{-29}$ kg). While modern equipment is capable of resolving near-equimolar concentrations of deuterium gas and helium-4 (verified by Callisto), without filtration and reaction product concentration techniques, measuring ppb to ppm concentrations of helium-4 in deuterium gas is incredibly challenging.

Finally, some have speculated that LENR results in the transmutation of the metal lattice itself, which can be measured using isotopic analysis. There are several methods for measuring the atomic composition of the metal lattice (energy dispersive spectroscopy, X-ray photoelectron spectroscopy, secondary ion mass spectrometry), however, very few methods offer low detection limits on the order of ppm. One concern over measuring changes to the chemical makeup of a metal cathode is how dirty electrochemical environments can be. Callisto found it incredibly challenging to maintain a highly pure electrochemical environment, even when ultrahigh purity materials were used. Degradation of the electrolyte, corrosion of cell components, dissolution of the counter electrode, among other reactions, can result in contamination build-up on the palladium cathode. The inherent dirtying of the cathode due to electrolysis obfuscates the ability to cleanly track chemical changes to the cathode. Isotopic changes are more easily tracked in gas-phase experiments, although those are not considered in this report.

In summary, high fractional deuterium loadings alongside some form of stimulation are generally claimed to be required to realize LENR. Due to the lack of fundamental understanding of the reaction itself, different detection schemes are required in order to verify a non-classical phenomenon.

## 1.4 Notable Research Efforts

It should be emphasized that despite the claims among LENR researchers, there has never been incontrovertible proof that LENR is a real, reproducible physical phenomenon. Modern scientific and peer-review standards for a positive result have never been met, in our view. Ultimately, over-claiming, misinterpretation, and in some cases subterfuge, are directly responsible for the stigma and taboo around LENR.

Emphasizing the aforementioned disclaimer, there are exemplary experiments and vocal researchers in the literature which we will highlight. The point in highlighting these experiments will be to illustrate the experimental concepts, datasets, and interpretations that are commonplace. We have limited the extent of our criticism in this section, rather striving to objectively report what the authors have claimed.

In a later chapter, we will highlight the manners in which researchers can produce a false positive. It is Callisto's current belief, based on years of our own research and attempts at replications, that every example of a claimed positive result was most likely due to either incomplete understanding of an experimental apparatus, incorrect data interpretation, cherry-picking of data, or in the worst case, deception. The experiments overviewed will be limited in scope to experiments using electrolysis to form palladium deuteride. Gas-phase experiments are excluded from this overview, although our review of the literature suggests that those experiments were similarly susceptible to false positive results, and the various claims of positive excess heat appear highly suspect.

### 1.4.1 Fleischmann and Pons

In their controversial 1989 paper titled 'Electrochemically Induced Nuclear Fusion of Deuterium', Martin Fleischmann and Stanley Pons investigated the behavior of palladium electrodes during electrolysis of heavy water [68]. Using palladium electrodes (cathodes) of various shapes and sizes, they intercalated deuterium

into the metal lattice from a concentrated LiOD solution. The electrodes were placed in Dewar cells to maintain a controlled temperature environment. Large platinum counter-electrodes surrounded the palladium electrodes, and temperatures were monitored with Beckmann thermometers and calibrated thermistors. They reported significant excess enthalpy generation at high current densities, with the observed excess heat reaching up to $10\,\mathrm{W/cm^3}$. Additionally, neutron and gamma-ray emissions were claimed, with neutron flux measured at approximately $4{\cdot}10^4$ neutrons per second and gamma-ray spectra suggesting the presence of 2.45 MeV neutrons, which they interpreted as indicative of nuclear fusion reactions. These radiation products were later retracted for lack of compelling evidence.

Following their preliminary findings in 1989, Fleischmann and Pons improved their calorimetric techniques and conducted more detailed experiments. In their 1990 publication, "Calorimetry of the Palladium Deuterium Heavy Water System" they described experiments using Dewar-type calorimeter cells [69]. These calorimeters were designed for uniform heat distribution and effective mixing. Both low and high current density experiments were conducted, with resistance heaters used to calibrate the heat transfer coefficients of the calorimeters. The authors claimed significant excess heat generation, particularly during 'burst' events, defined as short periods where the rate of excess enthalpy generation increased dramatically and unpredictably, often exceeding the energy input by factors up to 40. The magnitude of the observed excess heat led them to hypothesize that non-chemical processes were at play, as the total specific energy output during bursts could reach 50 $\mathrm{MJ/cm^3}$, which is far above what can be attributed to chemical reactions.

In their 1993 study 'Calorimetry of the Pd $D_2O$ System: From Simplicity via Complications to Simplicity' Fleischmann and Pons examined high rates of excess enthalpy generation [70]. They employed a method involving the measurement of time required to boil the cells to dryness, monitored through time-lapse video recordings. The experiments used single-compartment vacuum Dewar open calorimeter cells with a silvered top portion to control heat transfer by radiation. They observed increased generation of excess enthalpy over time, especially near the boiling point of the electrolyte solution. They noted a feedback mechanism where increased temperature led to higher rates of excess enthalpy generation, with some experiments achieving specific rates of enthalpy generation above 1 $\mathrm{kW/cm^3}$.

After the 1993 study, Martin Fleischmann and Stanley Pons continued their research on LENR, albeit with varying degrees of public and scientific support. Fleischmann moved to France with Pons to continue their work at the IMRA laboratory, a part of the Technova Corporation (a subsidiary of Toyota). However, their efforts did not lead to conclusive results, and the laboratory closed in 1998 after significant investment without achieving the desired breakthroughs.

### 1.4.2 McKubre

Michael C. H. McKubre, a principal scientist at SRI International in Menlo Park, California, extensively researched LENR. McKubre's primary goals were achieving reproducibility, attaining high deuterium loadings in palladium, performing high-quality calorimetry, and exploring various stimulation methods. Colloquially, he established the 'McKubre Threshold', a widely held belief that achieving a high atomic ratio of deuterium to palladium (D/Pd) above 0.85 was crucial for observing the excess heat [71]. He utilized calorimetric techniques to measure excess heat, aiming to attribute heat production to nuclear reactions rather than experimental artifacts. McKubre also explored methods such as electrochemical and gas loading, laser stimulation, and varying current densities and fluxes [72, 73].

Beyond calorimetry, McKubre was known for collaborating with others in the LENR community, evaluating other detection methods to identify and quantify nuclear reaction products. These included mass spectrometry for detecting helium isotopes ($^3$He and $^4$He), tritium, and other nuclear products; nuclear track

detectors (CR-39) for energetic charged particles; neutron and gamma-ray detectors for potential emissions; and isotopic analysis for detecting transmutation products. Notably, McKubre claimed that excess heat production correlated strongly with helium production, similar to the observations of Melvin Miles.

McKubre claimed that excess heat production in Pd/D systems, often correlated with high deuterium loading and specific conditions, could not be explained by chemical reactions or known physical processes. However, consistent reproducibility remained a challenge, influenced by material purity, experimental setup, and loading conditions. Over time, SRI funding being directed towards LENR declined and eventually petered out in the 2010s [74].

Callisto has replicated many of the McKubre protocols, which will be described in full detail in section 7.2.

### 1.4.3 Storms

Edmund Storms is another vocal LENR researcher, primarily known for his experimental, theoretical, and analytical methods [73, 75–79]. One significant aspect of his work is the use of a Seebeck calorimeter, which converts a temperature difference into an electrical voltage through the Seebeck effect. This calorimeter features a thermal envelope that surrounds the heat source and thermoelectric (Seebeck) modules that generate voltage proportional to the heat flow. It is calibrated using known heat sources and is highly sensitive, capable of detecting excess power down to the milliwatt range. The calorimeter design ensures uniform heat flow capture and minimizes errors due to heat distribution and temperature fluctuations.

Storms claims that his experiments have produced significant amounts of excess energy that cannot be explained by conventional chemical reactions. In his reports, Storms discusses the challenges of achieving reproducible results and the importance of the nuclear-active environment for initiating LENR. His work emphasizes the role of material treatment, temperature, and hydrogen loading in influencing LENR rates and proposed that unique local conditions within the materials are crucial for the observed nuclear reactions. Storms claims that LENR has Arrhenius behavior and advocates for experimenting at higher temperatures to achieve a higher reaction yield. However, similar to his peers, Storms has never provided inarguable evidence for the effect.

Callisto has replicated the protocols described by Storms, which will be described in full detail in section 7.5.

### 1.4.4 Staker

Michael R. Staker, a materials scientist, has focused on the preparation of the palladium-deuterium cathode used in experiments. He used coupled calorimetry and resistivity measurements to investigate the behavior of deuterium loading in palladium, attempting to elucidate the role of super-abundant vacancy (SAV) phases [80]. It is well established in the metallurgical literature that metal vacancies are stabilized by the presence of hydrogen in most face-centered cubic lattices [81, 82]. In the case of palladium, it is thermodynamically favorable to form six-fold coordinated metal-vacancy hydrogen clusters. Fukai postulated that under certain conditions, the diffusion and accumulation of these lattice defects can coalesce into a new extended phase, which he called the super-abundant vacancy phase [83,84]. Staker, Fukai, and others claim these vacancies can accumulate into ordered structures, creating channels that facilitate rapid transport conditions for deuterons, and which are hypothesized to play a crucial role in LENR. It should be noted that no experimental evidence for the SAV-phase has been provided at room temperature, despite Staker's strong claims of its existence.

Staker monitored the resistivity of palladium-deuterium specimens, hypothesizing the electronic behavior would provide insight into phase transitions. He claimed the SAV phase, or the $\delta$ phase as he refers to it, is associated with excess heat production. However, no robust data is provided to support the existence of these phases. Staker does not provide crystallographic evidence, nor do the trends in his resistance data support the existence of the SAV phase.

Using an isoperibolic calorimeter, Staker claimed excess power ranging from 0.10 W to 0.32 W, representing 4.7% to 9.6% of the input power. Additionally, he reported a substantial thermal runaway producing up to 2.4 W of excess power with an input of 1.2 W, among the largest in LENR literature. This claim was later modified by Staker in his published corrigendum to 1.78 W of excess heat on an input power of 2.66 W.

Callisto has investigated Staker's claims and will provide additional details in section 7.3.

### 1.4.5 Letts and Cravens

Dennis Letts and Dennis Cravens performed experimental work focused on the stimulation of deuterated palladium using laser irradiation [85–87]. Their research is motivated by theoretical considerations suggesting that lattice vibrations, or phonon modes, at certain frequencies might couple with energy states within the palladium-deuterium system, facilitating LENR processes. Letts and Cravens developed methods to fabricate palladium cathodes, involving processes of cold working, polishing, etching, and annealing to prepare the material for electrochemical loading with deuterium. Their experiments often involve dual laser setups producing terahertz beat frequencies rather than true terahertz radiation. Letts and Cravens claimed the application of external magnetic fields and gold co-deposition on cathodes influence the thermal response and reliability of excess power production. However, similar to other researchers, reproducibility and a lack of compelling evidence relegates their work to be considered mediocre at best. We will highlight a meta-analysis later in the document which suggests their data is heavily cherry-picked.

Callisto has extensively replicated the protocols described by Letts and Cravens, which will be described in full detail in section 7.9.

### 1.4.6 Space and Naval Warfare Systems Center

The Space and Naval Warfare Systems Center (SPAWAR), a division of the U.S. Navy, embarked on Low Energy Nuclear Reactions (LENR) research in the early 2000s. Researchers Dr. Pamela Mosier-Boss, Dr. Stan Szpak, and Dr. Frank Gordon developed what they called a *codeposition* method [88, 89]. During codeposition, palladium (Pd) ions from a palladium chloride ($PdCl_2$) solution are reduced and deposited onto a cathode surface in the presence of heavy water. This protocol aimed to achieve a high deuterium loading within the freshly deposited palladium layer, although no compelling evidence for higher fractional loadings were reported.

Another major feature of SPAWAR experiments was the use of detection techniques to monitor nuclear events and measure excess heat. CR-39 plastic detectors were used to capture high-energy particles emitted during potential nuclear reactions, revealing tracks that were analyzed to determine their nature. Additionally, SPAWAR used isoperibolic calorimeters to measure any excess heat generated during the electrolysis process. Analysis for nuclear byproducts, such as tritium and helium-4, was also conducted.

In various experiments, SPAWAR reported excess heat generation in the range of several hundred mW above the input power. CR-39 detectors consistently recorded tracks suggesting the emission of high-energy

particles, pointing to nuclear events at the palladium-deuterium interface. In future sections, we will highlight significant concerns regarding these low-cost nuclear detectors and the plethora of false signals that can arise.

### 1.4.7 Naval Surface Warfare Center, Indian Head

Building on SPAWAR's research, the Naval Surface Warfare Center (NSWC), Indian Head Division, continued exploring LENR. This program involved researchers from SPAWAR as well as new players, including Carl Gotzmer, Louis F. DeChiaro, Marc Litz, and Oliver Barham. They investigated protocols for more control over loading deuterium into the palladium cathode. A notable accomplishment, the Indian Head team published a peer-reviewed article in Applied Physics Letters Energy, claiming excess heat and nuclear ash under high electrochemical potentials [90]. Despite some concerns over the claims made in the paper which we will fully explore in a later section, the APL-E paper represents a departure from other research endeavors. Fairly complete descriptions of the hardware and protocol are included, positioning other researchers to replicate their results.

Improved CR-39 detectors were used to capture and analyze particle emissions, providing detailed information on the energy and type of particles produced. One notable feature of their nuclear detection was their use of a third party to analyze the detector tracks, mitigating bias from the researchers. A Seebeck calorimeter was used to measure heat output with higher precision than previously.

Similar to SPAWAR, Barham et. al. reported instances of excess heat generation that exceeded the energy input and expectations from chemical reactions. For instance, one experiment claimed an excess power of 5 W, on an input power of 15 W. Additionally, they detected radio frequency (RF) emissions up to 6 dB above the noise floor, which the authors claim are not attributable to background noise or known chemical reactions. Another interesting claim by the authors is that electrodeposited material structure included an unusual $Li_2PdD_4$ phase, normally synthesized under high-pressure, high-temperature conditions.

Callisto has extensively replicated the protocols described by both SPAWAR and NSWC, which will be described in full detail in section 7.7.

### 1.4.8 Miles at China Lake

With a background in chemistry and electrochemistry, Melvin Miles conducted electrolysis experiments, focusing on cathode preparation and nuclear byproduct measurements. Miles' primary goal was to achieve reproducible results that demonstrated excess heat production. Notably, Miles provided critical feedback on calorimetry early in the field [91]. Through calorimetric studies, Miles consistently reported excess heat generation. Notably, he was one of the first to correlate this excess heat with the production of helium-4, a potential nuclear byproduct [92]. This correlation provided seemingly compelling, albeit controversial, evidence supporting the nuclear nature of the reactions occurring in LENR systems.

In addition to his work with palladium-deuterium systems, Miles investigated the use of palladium-boron (Pd-B) cathodes. These cathodes, prepared at the US Naval Research Laboratory, demonstrated excess power effects in multiple experiments. Miles identified that the addition of boron improved the mechanical strength of the cathodes, reduced volumetric expansion during deuterium loading, and slowed deuterium escape, factors which potentially contributed to the observed excess heat. This work with Pd-B cathodes further supported the idea that material properties are crucial in achieving reproducible LENR results.

Callisto has replicated the materials and protocols described by Miles, which will be described in full detail in section 7.6.

### 1.4.9 Google Research

Google's initiative to revisit LENR represents a significant endeavor in scientific research, demonstrating a high standard of scientific rigor and yielding advancements across multiple fields [93]. The effort began in 2015. Google's program aimed to re-evaluate LENR with modern scientific techniques and a stringent peer-review process, involving around dozens of researchers from various prestigious institutions including the University of British Columbia, Massachusetts Institute of Technology, University of Maryland, and Lawrence Berkeley National Laboratory.

Despite thorough investigations, the team did not find any evidence to support the existence of cold fusion. However, the research provided valuable insights into hydrogen-loaded metals and extreme environment calorimetry. One of the significant achievements was the development of a high-temperature, high-pressure calorimeter designed for studying gram-scale heterogeneous reactions, capable of operating up to 1000°C and 100 bar. This calorimeter was validated using standard reactions and provided precise measurements, highlighting its utility in studying LENR and other high-energy chemical reactions [94, 95].

The project also focused on the accurate quantification of hydrogen absorption in palladium (Pd) nanoparticles and thin films using coulometric techniques. This method allowed for precise measurements of the H/Pd ratio, revealing that the hydrogen absorption varied with the size and surface structure of the Pd nanoparticles [96]. Another significant advancement was the development of an apparatus for *operando* X-ray diffraction (XRD) measurements on fuel electrodes of high-temperature solid oxide electrochemical cells. This apparatus, capable of operating at temperatures up to 745°C, enabled the study of structural changes in Pd electrodes under real operating conditions, providing insights into degradation mechanisms and enhancing the understanding of highly hydrided metals [97]. Although no evidence of cold fusion was found, the program advanced the understanding of metal hydrides, calorimetry under extreme conditions, and measurement techniques. This endeavor exemplifies the importance of revisiting controversial scientific claims with modern tools and methodologies.

While Callisto did not explicitly replicate the Google experiments, in evaluating similar hydrogen loading measurements, Callisto has levied a critique of their loading calculations by both coulometry and X-ray diffraction, which may have overestimated the fractional loading by as much as 10 %.

# Chapter 2

# Calorimetry Methods

## 2.1 Introduction to Calorimetry

Calorimetry is the science of the measurement of heat (from latin, *calor* - 'heat' and *metria* - 'measurement'), typically from chemical reactions, physical changes or phase transitions. Calorimetry is at the heart of most publications that have reported experimental measurements of LENR. In the absence of a cohesive theoretical underpinning of LENR it makes sense to measure the quantity that we care the most about from a practical perspective: heat. This measurement should answer the question whether the heat output exceeds the energy input, as reported in many LENR papers. While calorimetry is agnostic to the mechanism that produces the heat (chemical, nuclear or otherwise), its limitation is that a fairly large number of nuclear events are required in order to be above the sensitivity threshold of a conventional calorimeter, even if each single event releases more energy than a chemical reaction (e.g., > 1000 kJ/mol).

## 2.2 Concept of Open and Closed System Calorimetry

To perform calorimetry on an electrochemically loaded palladium hydride sample in situ, a typical electrolytic cell, consisting of a palladium cathode and a platinum anode residing in electrolyte, is operated inside the calorimeter. Application of a continuous electrochemical bias is critical to maintain high loading of the palladium hydride. Operating this electrolytic cell above the water splitting voltage will create hydrogen gas and oxygen gas (oxyhydrogen). Depending on the design of the calorimeter, the gas is a) allowed to escape or b) contained within the calorimeter and reverted back into water using a recombiner. Scenario a) is referred to as *(thermodynamically) open calorimetry* and scenario b) is referred to as *(thermodynamically) closed calorimetry*.

In open calorimetry, the chemical energy of the escaping oxyhydrogen gas must be accounted for in the heat balance, while in closed calorimetry, a recombiner must be deployed that reliably and constantly converts oxyhydrogen to water.

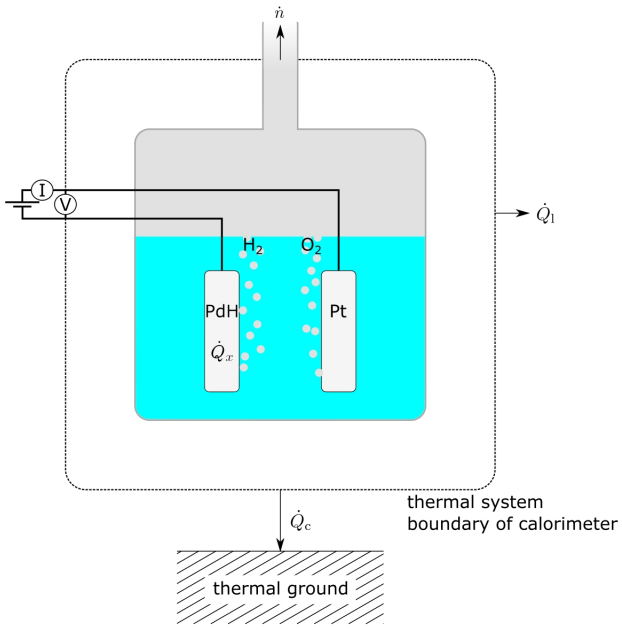



Fig. 2.1: Schematic illustration of an open system calorimeter. $\dot{Q}_x$, heat sources or sinks to be identified, often referred to as *excess heat* in the literature; $\dot{Q}_c$, heat measured by the calorimeter; $\dot{Q}_l$, heat losses escaping measurement by the calorimeter; $\dot{n}$, oxyhydrogen gas stream leaving the system

## 2.3 Open System Calorimetry

Open system calorimetry is widely used in the LENR research community due to its simplicity and safety (Fig. 2.1). Owing to the open nature of the system, electrochemical experiments are carried out at ambient pressure. There is little risk of potentially dangerous buildup of oxyhydrogen. As a downside, the energy balance is complicated by the fact that the chemical energy of the species leaving the system has to be accounted for. Furthermore, the system is never in steady state, as the electrolyte level changes over time. For the sake of measurement accuracy, if a system is not in steady state, its dynamic behavior, such as the ability of its thermal mass (heat capacity) to absorb or discharge heat, has to be accounted for in the heat balance. A simplified power balance for the open electrochemical system is:

$$|EI| - \dot{Q}_x = \dot{Q}_c + \dot{Q}_l - \dot{n}\Delta H_f \tag{2.1}$$

with

- $E$, the voltage applied to the electrochemical system measured at the thermal system boundary [V]
- $I$, the electrolysis current [A]
- $\dot{Q}_x$, the heat sources or sinks to be identified, often referred to as *excess heat* in the literature [W]
- $\dot{Q}_c$, the heat measured by the calorimeter [W]

- $\dot{Q}_\mathrm{l}$, heat losses escaping measurement by the calorimeter[W]
- $\dot{n}$, the oxyhydrogen gas stream leaving the system [mol/s]
- $\Delta H_\mathrm{f}$, the formation enthalpy of liquid water, -286 kJ/mol.

The gas flow $\dot{n}$ leaving the system can be measured using a flowmeter, or it can be computed:

$$\dot{n} = \frac{\eta_\mathrm{F} I}{2F} \tag{2.2}$$

with $\eta_\mathrm{F}$ being the Faradaic efficiency and $F$ being the Faraday constant ($9.65 \cdot 10^4$ C/mol). Alternatively, to account for the chemical energy of the oxyhydrogen leaving the system, one can subtract the thermoneutral potential from the applied voltage, assuming that $\eta_\mathrm{F} = 1$. The Faradaic efficiency, $\eta_\mathrm{F}$, is typically close to 1 for current densities > 150 mA/cm$^2$ [98, 99].

Due to these and other assumptions built into open system calorimetry, we found them to be particularly susceptible to producing erroneous indications of excess heat.

## 2.4 Closed System Calorimetry

In a closed system, a recombiner is needed to revert the oxyhydrogen back to water (Fig. 2.2). Thus, there are no mass flows across the thermal system boundary and the power balance simplifies to:

$$EI + \dot{Q}_x = \dot{Q}_\mathrm{c} + \dot{Q}_\mathrm{l}. \tag{2.3}$$

Typically, a platinum catalyst with a large surface area is used as recombiner, e. g., platinum black [100]. We used platinum coated carbon cloth with a platinum loading of 4 mg/cm$^2$ and a high specific surface area (fuelcellstore.com, item 72500514). If the recombiner works perfectly, and neglecting the pressure buildup due to the generation of 'orphaned' oxygen when the sample is initially loaded with hydrogen, the pressure in the system will remain at ambient. If the sample mass is not negligible, the orphaned oxygen pressure $p$ will go up slightly, depending on the headspace volume $V_\mathrm{h}$ compared to the sample mass $m_\mathrm{Pd}$ and the loading $x_\mathrm{H}$:

$$\Delta p = \frac{x_\mathrm{H} m_\mathrm{Pd} RT}{2 M_\mathrm{Pd} V_\mathrm{h}}, \tag{2.4}$$

with $M_\mathrm{Pd}$ being the molar mass of palladium. In practice, the recombiner might need a certain overpressure to work. We found this to be the case in particular when the recombiner surface is contaminated, e. g., with an electrolyte layer or with salt deposits from the electrolyte. In that case, the vessel pressure goes up and chemical energy $Q_\mathrm{p}$ is stored in the headspace as well as pressure-volume work $Q_\mathrm{pV}$ :

$$Q_\mathrm{p} = \frac{2 \Delta p V_\mathrm{h} \Delta H_\mathrm{f}}{3RT} \tag{2.5}$$

$$Q_\mathrm{pV} = \Delta p V_\mathrm{h} \tag{2.6}$$

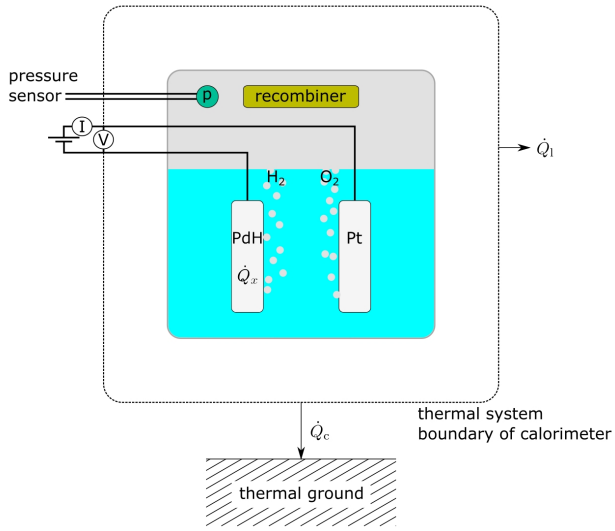



Fig. 2.2: Schematic illustration of a closed system calorimeter. $\dot{Q}_x$, heat sources or sinks to be identified, often referred to as *excess heat* in the literature; $\dot{Q}_c$, heat measured by the calorimeter; $\dot{Q}_l$, heat losses escaping measurement by the calorimeter; $p$, pressure sensor measuring pressure inside the vessel

## 2.5 Calorimetry Metrics

There are two metrics widely used in the LENR field:

1. Excess heat, $\dot{Q}_x$. In quasi-steady state (keeping input power constant), the excess heat is the difference between the output thermal power, $P_{\text{out}}$, and the input power, $P_{\text{in}}$:

$$\dot{Q}_x = P_{\text{out}} - P_{\text{in}} \tag{2.7}$$

2. Coefficient of performance, COP. In quasi-steady state, the COP is the output power normalized with the input power:

$$\text{COP} = \frac{P_{\text{out}}}{P_{\text{in}}} = 1 + \frac{\dot{Q}_x}{P_{\text{in}}} \tag{2.8}$$

A derived metric of the COP is the $\text{COP}_e$ (with $e$ for energy, as opposed to power). It is defined as the integrals of output power over input power:

$$\text{COP}_e(t) = \frac{\int_0^t P_{\text{out}} d\tau}{\int_0^t P_{\text{in}} d\tau}. \tag{2.9}$$

Due to limitations in experimental accuracies and varying sizes and input powers of electrochemical systems in the literature, COP has become a popular metric to normalize the excess heat with respect to the input power, even though it is not fundamentally clear why any processes generating excess power should scale with input power.

## 2.6 Sensitivity of Calorimetry

There are various mechanisms at play that limit the accuracy of a calorimeter:

- Accuracy of input power measurement: Ideally, all voltages and currents (electrochemistry, stimulation, heater etc.) must be measured at the thermal system boundary. In practice, this boundary might be poorly defined or it might be impractical to apply voltage sensors in that location.
- Faradaic efficiency variation: In open system calorimetry, the Faradaic efficiency might be less than unity, or generally change over time or with electrochemical current. In the absence of a flowmeter, this leads to inaccuracies in the accounting of chemical energy leaving the system. Even with flowmeters installed, it might be difficult to determine the chemical energy, given that the composition of the gas stream is unknown (e. g., some of the oxyhydrogen might recombine on exposed platinum).
- Recombiner inefficiency: There might be fluctuations in the reaction rates on the recombiner, depending on recombiner temperature, contamination with salt or liquid water. This leads to pressure buildup and a suppression of measured heat. Conversely, if oxyhydrogen has accumulated in the headspace and is being reacted by the recombiner, a transient increase in heat will be the result.
- Calorimeter efficiency: Even the best calorimeter will not capture all the heat put into the electrochemical system. Some of the heat will be transferred along poorly defined pathways, e. g., electric wires. These loss pathways might change over time, e. g., between calibration and experiment. Moreover, the thermal ground (environment) might change in temperature.
- Transient signals: In many experiments reported in the literature, the input power is varied over time. This leads to different steady state vessel temperatures depending on the input power (assuming a constant heat transfer resistance between the vessel and the thermal ground outside of the calorimeter). Depending on the thermal mass of the system and how the dynamics of the system are accounted for, this can lead to limited accuracy of the calorimeter for the duration of several thermal time constants after the input power change.
- Varying electrolyte level in open system calorimetry. Due to the nature of the open system and the ongoing electrolysis, the electrolyte level varies. This will likely change the heat transfer from the electrodes through the electrolyte into the vessel and the calorimeter.
- Calibration accuracy: Heat is not measured directly. Instead, typically a voltage is measured, representing a temperature (in an RTD) or a temperature difference (in a thermopile or thermocouple). Sometimes the conversion from temperature to heat is based on first principles (as in a thermal bar), but oftentimes it is based on calibration with a known input power (as in isoperibolic calorimeters). This input power might not be in the exact same location or have the same heat transfer resistance as the heat sources (electrodes, electrolyte, recombiner, lead wires etc.) during the experiment, leading to inaccuracies.

In addition to these fundamental limitations, which are present even in a well-behaved calorimeter, we have identified a variety of other potential causes for false signals; see section 9.2.

By performing calorimetry using various devices, we concluded that based on the fundamental limitations listed above, errors on the order of 1 to 10 mW in closed system calorimeters and several hundred mW in open system calorimeters are to be expected. The thermal time constant of common calorimeters is on the

order of tens of minutes, so any powers of interest exceeding those errors would have to be present for several minutes in order to be detectable. Postulating nuclear fusion events each with an energy of 24 MeV occurring over a period spanning the calorimeter time constant, a minimum of $10^{11}$ events (0.4 J) are required in closed calorimeters and $10^{14}$ events (0.4 kJ) are required in open calorimeters to be picked up by the calorimeter. For comparison, a Pd wire sample (25 mm length, 0.5 mm diameter) contains $3 \cdot 10^{20}$ atoms.

## 2.7 Calorimetry in the Literature

Various calorimeters have been described in the literature. Almost all LENR researchers built their own calorimeters, with the isoperibolic calorimeter being the most popular. It measures the temperature difference between a probe inside the vessel (in the electrolyte near the cathode) and a probe outside the vessel (which is held at constant temperature). Among others, McKubre [101], Energetics [102], Preparata [103], Letts [104] and Staker [105] used isoperibolic calorimeters. A major problem with this type of calorimeter is that the heat transfer resistance to the temperature probe in the electrolyte can change, e. g., due to bubbling depending on the electrolysis current or due to the presence or absence of a magnetic field [104, 106–109]. Moreover, submerging temperature probes into the highly alkaline, often warm, electrolyte for extended durations can result in their degradation, leading to faulty temperature readings. Most of the reported isoperibolic calorimeters were open. McKubre used a closed isoperibolic calorimeter as well mass flow calorimeters, where the heat is transfered to a liquid medium, the change in temperature of which is measured [110].

Groups involved with the Google effort created isoperibolic calorimeters that operate at elevated temperatures [93,111,112]. MacLeod et al. built a versatile calorimeter, not explicitly designed for electrochemistry, which can perform in-situ calorimetry on chemical reactions at up to 1232°C and 33 bar hydrogen pressure [111]. The sample is contained in a reaction tube, which is surrounded by a heater and an isothermal jacket. 14 thermocouples are placed in various locations and parameters of a heat flow model are fit to the thermocouple response during calibration. Young et al. built a miniature calorimeter around a solid state electrochemical cell with an RTD attached to the cell with an operating temperature of up to 1000°C [112]. Similarly to MacLeod, a model containing heat capacitances and resistors is fit to the readouts of the cell RTD as well as three other RTDs.

A more direct way to measure heat transfer across the thermal system boundary of the electrolysis vessel is to tile it with Seebeck sensors. These sensors are based on the thermoelectric effect, producing a voltage proportional to the temperature difference across the sensor. Examples of Seebeck calorimeters include those used by Storms [113] and Barham [106]. A related measurement method uses the Tian-Calvet principle, which covers the surface of the vessel of interest as well as the surface of a reference vessel with thermopiles [114]. Both vessels are contained in the same isothermal reservoir. (For a detailed description see section 2.8.1).

Most LENR studies neglect to account for the time-dependent response of the calorimeter when computing excess heat or COP. For example, when reducing the input power (e. g., stepwise), an apparent excess heat (as defined in eq. 2.7) is to be expected for a few thermal time constants of the calorimeter until it has sufficiently approached its new steady state. To address this problem, McKubre and Storms used compensation heaters to keep the total input power constant [110,113]. In the absence of such a heater, the electrolysis input power should be kept constant, or the metrics of excess heat and COP will result in erroneous readings as the system adjusts to its new steady state upon a change of input power. Notably, Chiang et al. characterized the instrument response function in order to model the dynamic system behavior and thus enable interpretation of excess heat and COP across input power changes [115]. (For further reading, see section 2.9.1.)

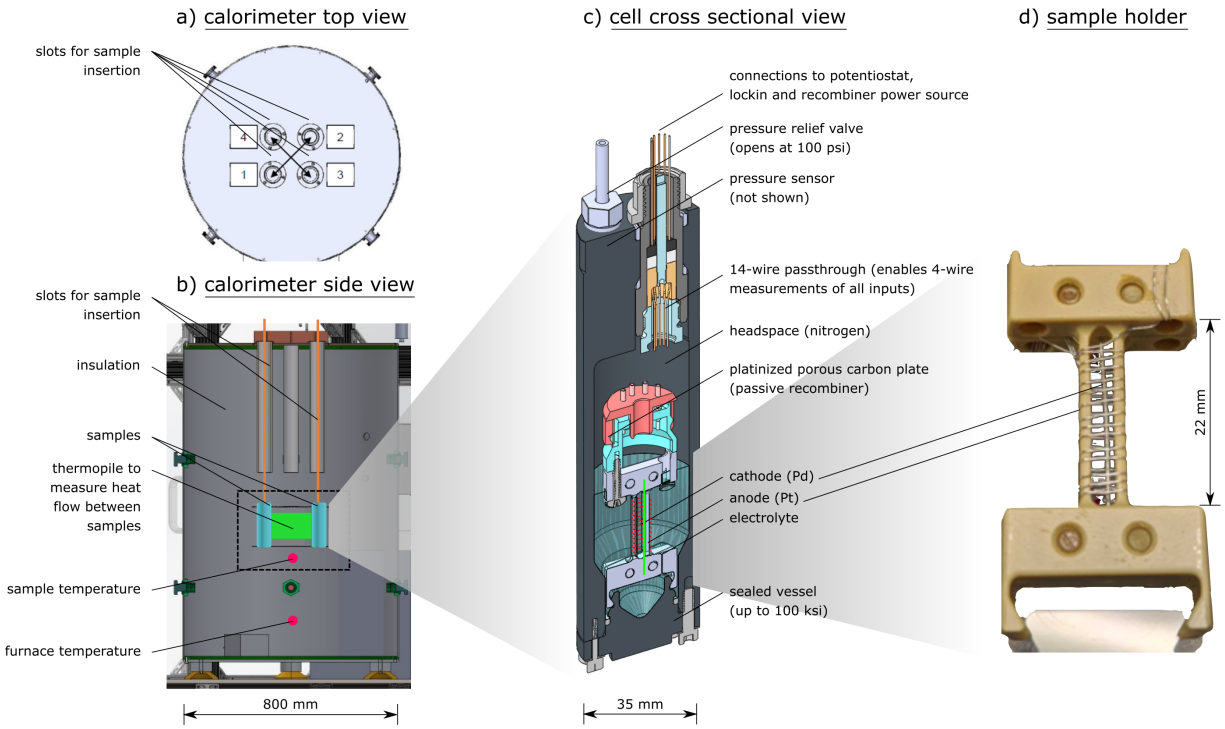



Fig. 2.3: Setaram MS80 calorimeter setup. a) Calorimeter top view, showing the relative heat measurements between cells 1 and 2, and cells 3 and 4. b) Calorimeter side view, showing the location of the in-situ cells within the calorimeter. c) Cell cross-sectional view, showing all major components of the electrolytic cells (custom made). d) Photograph of the sample holder made from PEEK polymer, showing the electrode arrangement.

## 2.8 Setaram MS80

### 2.8.1 Hardware

The Setaram MS80 is one of the most accurate commercially available calorimeters with a sample space large enough to accommodate a custom-made apparatus for in-situ calorimetry during electrochemical experiments (Fig. 2.3). It is based on the Tian-Calvet principle. It contains four bores for samples, each of which is surrounded by a thermopile measuring the heat flow between the bore and an isothermal block. The four thermopiles are configured as two pairs of sample and reference cells. For each pair, the differential heat flow between the sample bore and the reference bore is measured. Each bore has an inner diameter of 35 mm and a depth of 500 mm, of which the lower 100 mm is covered with thermopiles.

We designed and built vessels for closed system electrolysis experiments that fit into the MS80 bores (Fig. 2.3 c). Each vessel contains a palladium cathode (typically a 0.5 mm diameter, 25 mm length wire, though various sample geometries can be accommodated), a helically wrapped platinum anode (0.2 mm diameter) with an electrode spacing of ~ 3 mm, a recombiner (platinized carbon plate, fuelcellstore.com, SKU 72500511,

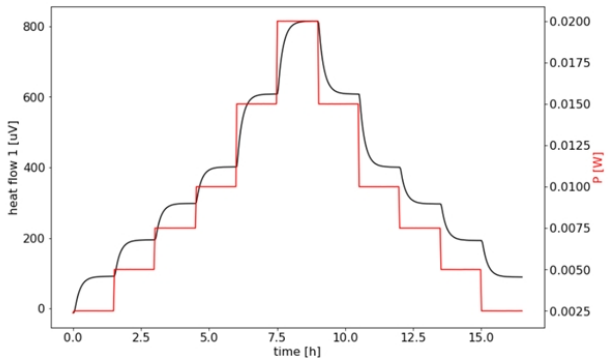



Fig. 2.4: Calibration of MS80, using a staircase of known input powers into the calibration resistor to obtain a conversion factor from reported thermopile voltage (called 'heat flow 1 [uV]' in the MS80 software) to heat flow. Calibration resistor input power is plotted on the right axis, shown as the red curve. The resulting thermopile voltage is plotted on the left axis, shown as the black curve.

65 mm x 8 mm), a calibration resistor (for resistive heating during calibration) and a pressure transducer. The vessel is filled with 17.7 ml electrolyte, leaving a headspace of ~ 23 ml. A pressure relief valve at the top of the vessel opens if the vessel pressure exceeds 7 bar. Because detonations could result in pressure transients faster than the reaction time of the relief valve, the vessel is designed to withstand pressures of up to 700 bar. The sample resistance is continuously measured using a four-wire measurement, with the lead wires (0.13 mm diameter Pt wire coated with PFA, A-M Systems) laser-welded onto the sample wire. The spacing between the current supply leads is ~18 mm and the spacing between the voltage sense leads is ~12 mm. The lead wires for the electrochemistry, the resistance measurements (to determine loading) as well as for optional axial electromigration currents along the cathode are routed through a custom-made feedthrough at the top of the vessel. The voltage sense locations for all electrical power inputs into the vessel are located just outside of the vessel. The currents for electrochemistry and axial currents are provided by computer-controlled current sources (BioLogic VSP 300, Keithley, NI-PXIe 4141, NI-PXIe 4144, NI-PXIe 4145, NI-PXIe 4154, depending on use case). The voltages are measured using either the four-wire probe provided by the current source instrument or are independently measured using a voltmeter (Keysight 34461A or NI PXI-4071, NI PXI-4081).

### 2.8.2 Calibration

The heat flow is measured using the software provided with the MS80. In order to convert the reported differential thermopile voltage to a heat flow, we perform a calibration, inputting a known power into a calibration resistor mounted within the electrolyte close to the electrodes (Fig. 2.4). A linear fit to the steady state relationship between input power and thermopile voltage yields a conversion factor to compute the heat flow based on the reported voltage. The reference (control) cell is typically a vessel with a comparable configuration and similar input powers, however either both electrodes are platinum or the electrolyte is light water, to act as a control. The input power is taken as the sum of all electric input powers (electrochemistry, axial current, resistance measurement, resistor calibration), with the voltage senses near the thermal system boundary of the calorimeter. Excess heat and COP were computed following equations 2.7 and 2.8. The

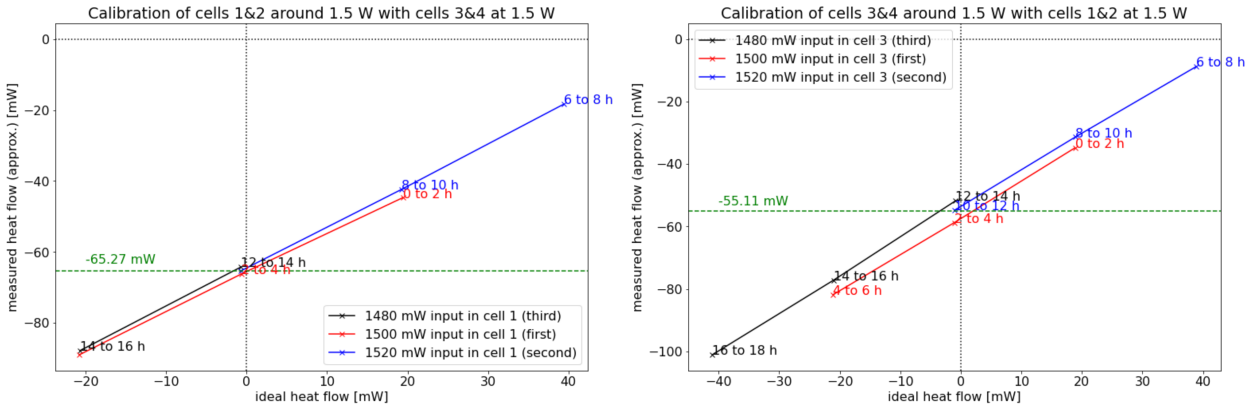



Fig. 2.5: Calibration of MS80 with 1.5 W input power in the reference cells (cells 2, 4) and 1.5 W ± 20 mW in the experiment cells (cells 1, 3), showing an offset of ~ 60 mW between the measured heat flow and the input power (~ 4 %).

MS80 accuracy specification covers differential and absolute heat flows up to 500 mW. However, we often operated at input powers of up to 3 W for both vessels in a pair, with differential heat flow up to 500 mW.

In order to ensure accurate measurements while operating outside of the specified range, we performed calibrations with known input powers in the experiment cells and the reference cells. For instance, Fig. 2.5 shows how there was an offset of ~60 mW between the measured heat flow and the input power (~ 4 %).

In addition, there is some sensitivity to the type and location of the heat source. As shown in Fig. 2.6, if both cells' input power is applied through electrochemistry, the indicated heat flow from cell 2 to cell 1 is 50 mW at 1.5 W input power (a 3 % false signal). If a calibration resistor (placed within the electrolyte near the electrodes) is used instead of the electrochemistry, a false heat flow signal of up to 150 mW (10 %) is measured. In the extreme case, when the heat originates from a resistor in the headspace in the reference cell (cell 2), a heat flow of 300 mW (at 1.5 W electrochemical input power in the experiment cell 1) is measured, corresponding to a false heat flow signal of up to 20 %. This is likely due to the different coupling of heat sources to the thermopile and to the loss pathways (wires leading to the vessel, top and bottom faces of the vessel).

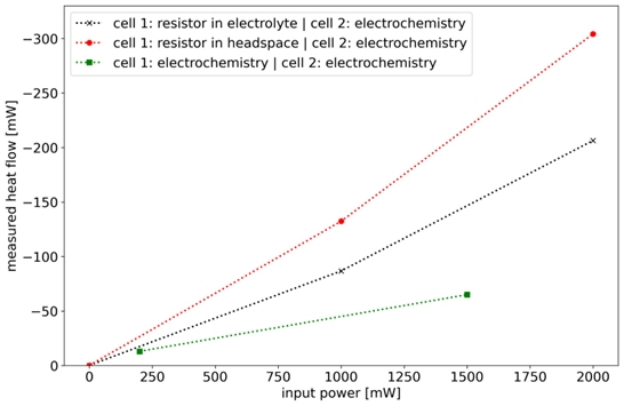



Fig. 2.6: Location dependence of power input in MS80 calorimeter leading to false differential heat signals despite equal power inputs. The sign convention is that positive heat flow is from cell 1 to cell 2.

## 2.9 High-throughput Calorimeter (HTcal)

As an alternative to the bulky and expensive Setaram MS80 with its industry-leading accuracy, we employed various homemade calorimeters, which were designed for ease of use, enabling a higher sample throughput to cover a large parameter space in a short amount of time. We noticed that the heat flow accuracy of the MS80 was limited by the fluctuation in recombiner efficiency rather than the calorimeter itself, so we could not take full advantage of the MS80's capabilities in any case.

### 2.9.1 Design Objectives

We dubbed this type of high throughput calorimeter the *HTcal*. Its distinguishing features are:

- Closed system calorimetry: To reduce the number of potential false signals, closed system calorimetry is essential. Pressure is monitored in order to diagnose recombination events (which represent the most frequent cause for false elevated COPs).
- Single-ended calorimetry: As opposed to the MS80, the HTcal measures heat flow against a thermal ground as opposed to against a reference cell. This design allows us to accommodate twice the number of experimental vessels in a given space and eliminates the time to set up reference cells.
- Direct measurement of heat flow: Using a thermal bar (Fig. 2.7a) of known geometry and known thermal conductivity, we convert the measured temperature gradient to heat flow (eq. 2.10). This design makes fewer assumptions than other designs relying heavily on calibration (e. g., isoperibolic calorimeters with a single temperature sensor). Linearity of the temperature along the thermal bar verifies accuracy. Five sensors ensure reliable measurements even if one or two sensors are faulty.
- Streamlined sample mount: The sample is clamped between platinum contacts. This is much easier than laser welding and proved to form a reliable electrical connection even after multiple load-deload cycles. Four contacts are provided to enable a four-wire resistance measurement to determine the loading.

- Streamlined vessel assembly: The vessel is operated at pressures up to 6 bar, with a burst pressure of 15 bar. The moderate burst pressure enables the usage of a PEEK lid, containing all passthroughs. Electrical passthroughs are made with commercially available connectors (LEMO) and gas connections for the vent line and the safety relief valve are made with push-to-connect fittings.
- Streamlined architecture: Almost all electrical devices, such as current sources (EC, EM, calibration) and measurement devices, e. g., multimeters (DMM) and temperature sensors (RTDs) for environmental monitoring and heat flow calculation, are unified into a NI PXI system (Fig. 2.7c).
- Streamlined data recording and analysis: All data streams are recorded using Python in Jupyter notebooks and saved into a database. Analysis is done in Python as well.

### 2.9.2 Operating Principle and Implementation

Fig. 2.7 b shows a photograph of the HTcal. It typically contains four electrolytic cells sharing a thermal baseplate. The centerpiece of each cell is a vessel (made from aluminum, lined with a 0.5 mm thin machined PEEK liner) which is connected through a thermal bar to a thermal ground (an isothermal aluminum base plate, the temperature of which is controlled through a Peltier element, TE Technology CP-031). About 90 % of the heat generated inside the vessel leaves through the thermal bar, while the rest escapes through less well-defined pathways (e. g., through the insulating closed-cell foam or along the electrical or gas lines).

The measurement principle is to measure the temperature gradient along the thermal bar. It is related to the heat flow $\dot{Q}$ as follows:

$$\dot{Q} = kA\frac{dT}{dx} \tag{2.10}$$

with $k$ being the thermal conductivity of the thermal bar, $A$ being the cross sectional area of the thermal bar and $\frac{dT}{dx}$ being the temperature gradient along the thermal bar. For a robust determination of the gradient, we measure the temperature in five locations along the thermal bar. The spacing between locations is 10 mm. This determines the length of the thermal bar (65 mm). The diameter of 17 mm is determined by the optimum balance between maximizing the sensitivity (smaller diameter results in larger temperature gradient at a given heat flow) and minimizing the thermal time constant (larger diameter results in shorter thermal time constant) to resolve transient signals. The Peltier element keeps the base plate at a constant temperature (typically 30°C) with a standard deviation < 10 mK. The enclosure temperature is kept constant with a standard deviation of 30 mK by using two stages (preconditioning chamber, calorimetry chamber) of heater fans conditioning the air from the lab. The fans run continuously, while the heaters (Stego 03114.9-00 HVL031 DIN Rail Enclosure Fan Heater 300 W 120 VAC) are controlled by a PID thermostat with a continuous output (made in house). The temperature uniformity within the thermal enclosure is ensured by a large mixing fan.

### 2.9.3 Calibration and Performance

Figure 2.8 characterizes the performance of the HTcal. A typical calibration procedure for a four-cell unit is shown in Fig. 2.8a, with resistor input powers up to 2 W. A selection of resulting temperature profiles along the thermal bars is shown in Fig. 2.8b. *Corrected temperature* refers to the correction to compensate for RTD offsets, as Pt100 RTDs typically yield readings with sensor-to-sensor variations of ~0.2 K when all the sensors are attached to the same thermal ground. The temperature gradient is obtained through a linear fit to the temperature profiles, resulting in the measured heat flow (using eq. 2.10, Fig. 2.8c). The measured

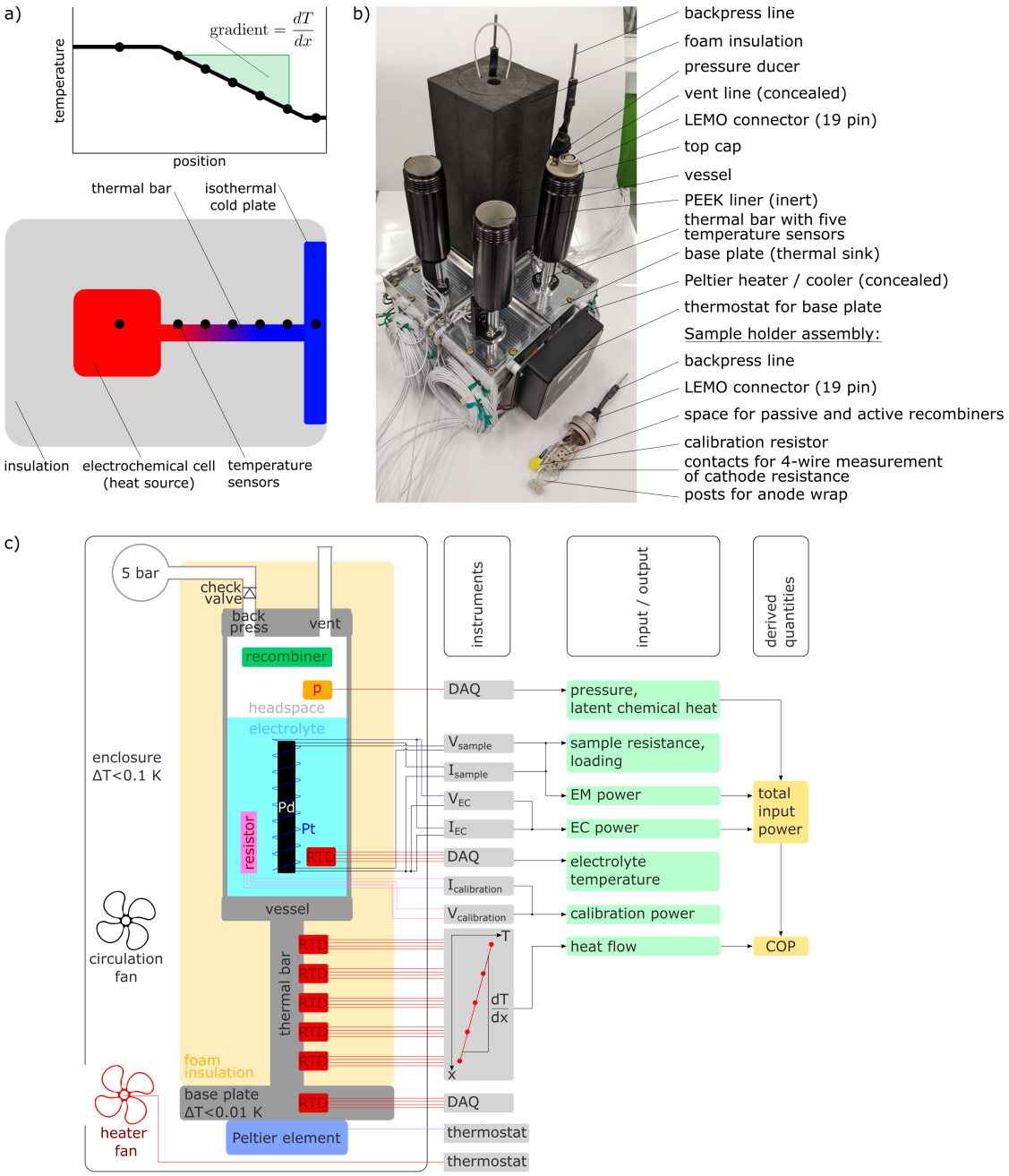



Fig. 2.7: High-throughput calorimeter (HTcal). a) Heat flow measurement principle of thermal bar (see eq. 2.10). b) Photograph of an HTcal unit with four cells. c) Electrical diagram of HTcal. Note that the vent port is closed during experiments.

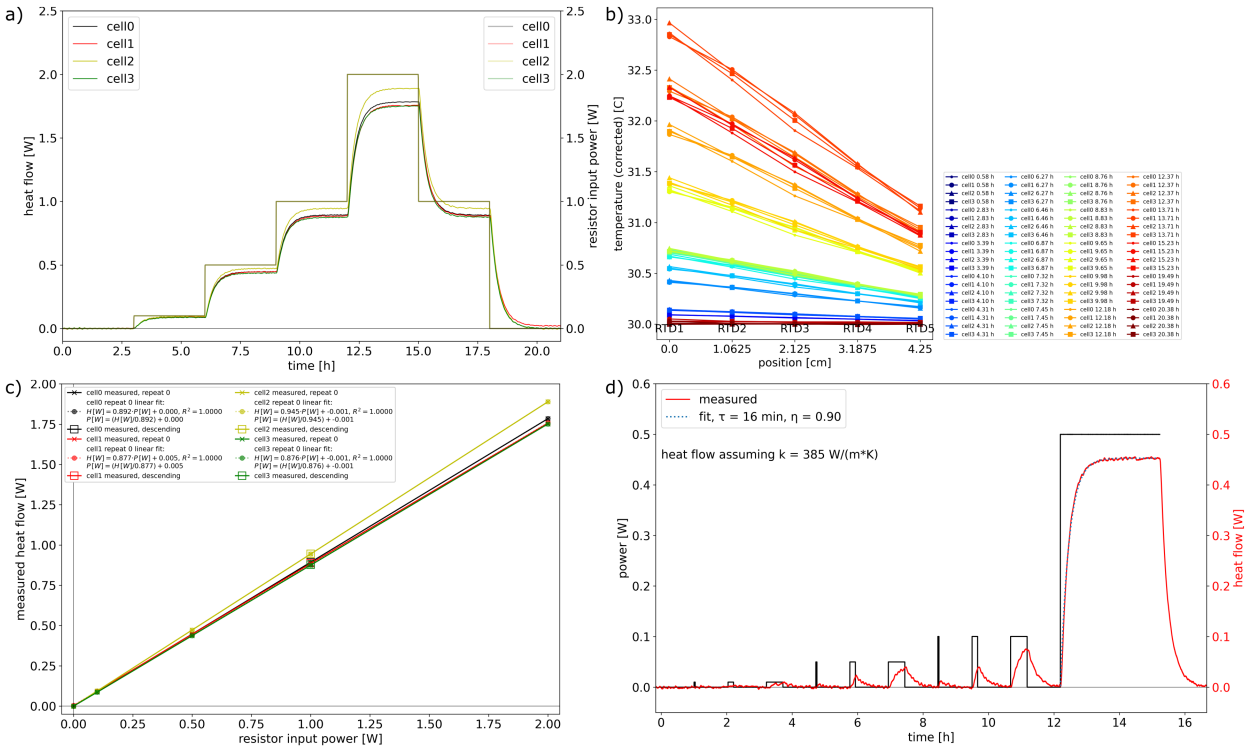



Fig. 2.8: HTcal calibration. a) Staircase calibration procedure to investigate linearity of measured heat flow vs. calibration resistor input power. b) Temperature profiles along thermal bar during application of staircase calibration. c) Measured heat flow from temperature profiles vs. calibration resistor input power, along with linear fits. The open symbols refer to the descending step, showing that there is no significant drift or hysteresis. d) Application of calibration resistor input power pulses of [2, 10, 30] minutes length and [10, 50, 100] mW power with a final 3-hour, 500 mW step, along with simple exponential fit of $\tau = 16$ min and an efficiency of $\eta = 0.90$.

heat flow varies linearly ($R^2 = 1.0000$) with the calibration resistor input power, with a constant of 0.89±0.05 (the calorimeter efficiency, $\eta$). In other words, about 90 % of heat put into the vessel leaves through the thermal bar. As mentioned previously, the efficiency is a trade-off between sensitivity and time resolution. Depending on the thermal bar geometry, the thermal time constant of the HTcal is around 15 to 25 minutes (Figs. 2.8d and 2.14a). This allows us to resolve a 30-minute 10-mW pulse or a 2-minute 50-mW pulse. $\eta$ is a function of the vessel and thermal bar and varies typically $< 0.5\%$ when repeating a calibration for a given assembly and $< 2\%$ when repeating a calibration before and after assembling a cell.

### 2.9.4 Excess Heat Metrics during Transients

Previously, we introduced excess heat $\dot{Q}_x$ and COP (eqs. 2.7 and 2.8). While these equations hold true in principle (and are a good approximation in steady state), the measured heat flow not only depends on

the power leaving the vessel, $P_{\text{out}}$, but it is also a function of the calorimeter, in particular its instrument response function $F$. As can be seen in Fig. 2.9a) and b), after application of a step function to the input power, the expected heat flow (assuming $\dot{Q}_x = 0\,W$) approaches steady state gradually, in theory following the convolution of the input power $P_{\text{in}}$ with the impulse response function $F$:

$$\dot{Q}_{\text{expected}} = P_{\text{in}} \circ F \tag{2.11}$$

In practice, we obtain the impulse response function $F$ as the derivative of the measured heat flow after an input power step (Fig. 2.9a). Often, the impulse response function is represented by an exponential fit, but we found that using an empirical response function gave better results. Using the quantity of *expected heat flow*, we can define the excess heat and COP, accounting for the calorimeter response:

$$\dot{Q}_{x,\text{convolved}} = \dot{Q}_{\text{measured}} - \dot{Q}_{\text{expected}} \tag{2.12}$$

$$\text{COP}_{\text{convolved}} = \frac{\dot{Q}_{\text{measured}}}{\dot{Q}_{\text{expected}}} \tag{2.13}$$

with $\dot{Q}_{x,\text{convolved}}$ being the excess heat (convolved) and $\text{COP}_{\text{convolved}}$ being the COP (convolved). Figs. 2.9c) and d) illustrate that generally $|\dot{Q}_{x,\text{convolved}}| << |\dot{Q}_x|$ and $|\text{COP}_{\text{convolved}} - 1| << |\text{COP} - 1|$, in particular after input power changes.

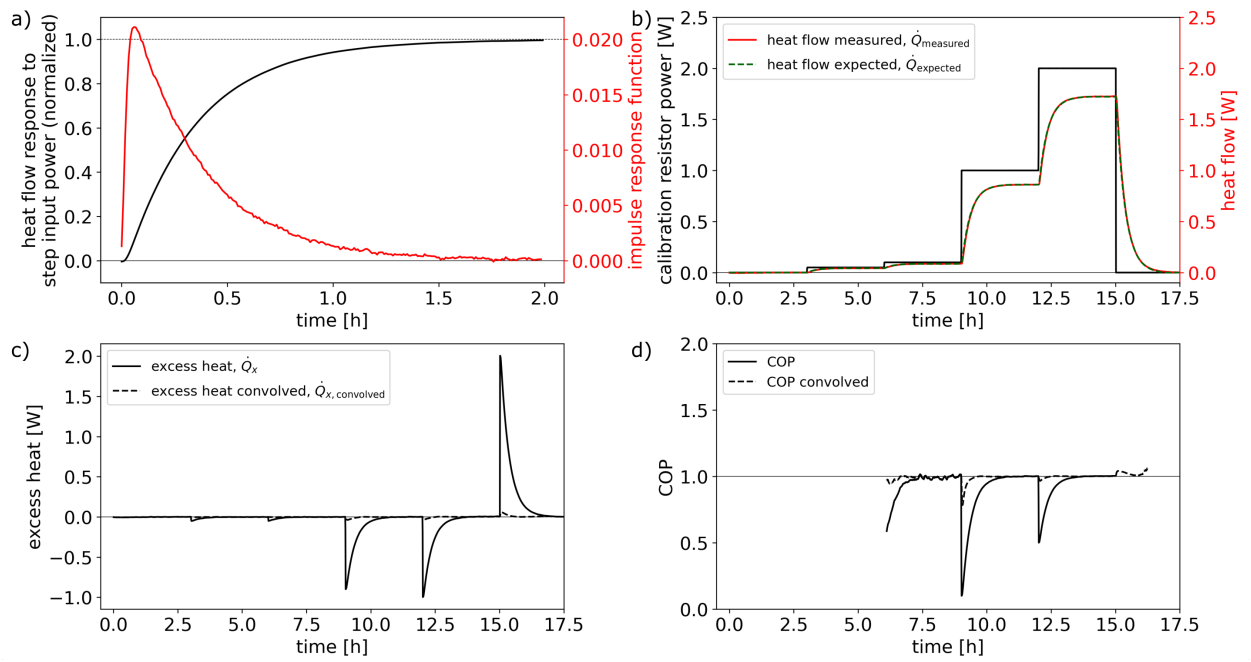



Fig. 2.9: Accounting for transient input powers in HTcal. a) Heat flow response to step input power (normalized, step at time = 0 h) along with impulse response function (derivative of heat flow response). b) to d) Application of impulse response function convolution to a calibration experiment. b) Calibration resistor input power follows a staircase. The expected heat flow, computed using eq. 2.11 closely fits the measured heat flow. c) The excess heat, $\dot{Q}_x$ shows major depressions following input power increases, owing to the thermal mass of the system. After accounting for it, the excess heat (convolved), $\dot{Q}_{x,\mathrm{convolved}}$ is much closer to 0 W after input power changes. d) COP (convolved) is much closer to unity than COP.

## 2.10 Ultra-high Throughput Calorimeter

### 2.10.1 Introduction

To date, electrochemical experiments run for the purpose of creating and detecting Anomalous Heat Events (AHE) have been primarily run in our High Throughput Calorimeters (HTcal). Hundreds of experiments have been run over the years, typically using clusters each consisting of four calorimeters (section 2.9.1) and running for days to weeks. Many lessons have been learned, but no definitive signs of AHE were found. A potential explanation could be that there is only a small statistical likelihood in which AHE will occur. To explore this space, more calorimeters running for longer durations would be required. Replicating the HTcal systems to increase experimental throughput is expensive from both budget and real estate points of view. To address these issues, an Ultrahigh Throughput Calorimeter (UHTP) system was developed. This system consists of 100 electrochemical cells with in-situ calorimetry running in parallel for an indefinite length of time (Fig. 2.10). The UHTP program increased our experimental throughput by nearly 5x, going from 26 to 126 calorimeters. The purpose is to screen vast parameter spaces and to detect excess heat signals of at least 100 mW (typically COP > 1.2). If we find signals of that magnitude, we can investigate those samples more closely in the MS80 or HTcal.

The UHTP system was designed with cost and scalability in mind. A custom PCB was developed to consolidate the required functions of the general-purpose National Instruments PXI chassis onto a single board (Fig. 2.11). Power and data was provided via Power over Ethernet (PoE), reducing system cable count. Experimental control, data transfer and storage are handled by Python running in a Jupyter notebook on a general purpose computer. Data is then replicated on our internal servers for analysis. The electrochemical vessel is borrowed in part from the HTcal design. It has been updated to be mass-produced by a contract manufacturer.

The UHTP PCB can supply up to 10 W (10 V at 1 A) of electrochemical power and drive up to 4 A of electromigration current into a milliohm load. The electromigration current is additionally used to measure the resistance of the sample with a resolution of 100 µΩ. Integrating power meters on both the electrochemical and electromigration power supplies can measure electrical input power to the cell with 1 mW accuracy. RTDs located in the electrolyte and on the base plate measure temperatures with 100 mK accuracy. A pressure transducer measures the pressure in the vessel with a resolution of 24 µpsi and a temperature accuracy of 100 mK.

### 2.10.2 System Architecture

#### 2.10.2.1 Overview

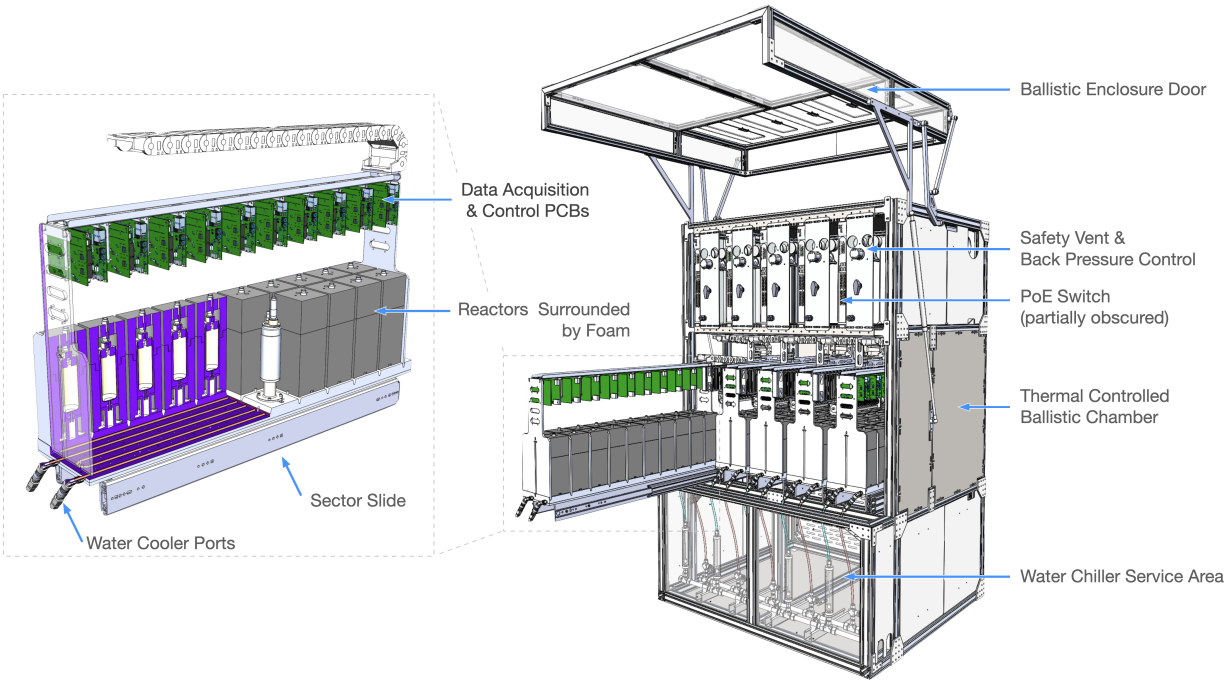



Fig. 2.10: UHTP enclosure with detailed sector breakout.

The UHTP system consists of the following main components (Fig. 2.10):

1. Super Structure: The Super Structure functions as both the primary structural framework and a protective safety barrier for the UHTP system. It contains Ethernet switches for communication, thermal enclosure and over pressure relief infrastructure for the calorimeters.
2. Reactors: 100 closed isoperibolic electrochemical calorimeters containing a variety of electrochemical cells.
3. Thermal Enclosure: Provides a constant temperature enclosure used to minimize parasitic reactor heat exchange with the environment.
4. Sectors: Each sector contains 20 calorimeters, their supporting PCBs, and a water cooled base plate.
5. Power System: To minimize cable count in the system, Power over Ethernet (PoE) is used for both power and data transfer.
6. Reactor Control and Data Pipeline: A system to send commands to and receive data from the reactors (Fig. 2.11).

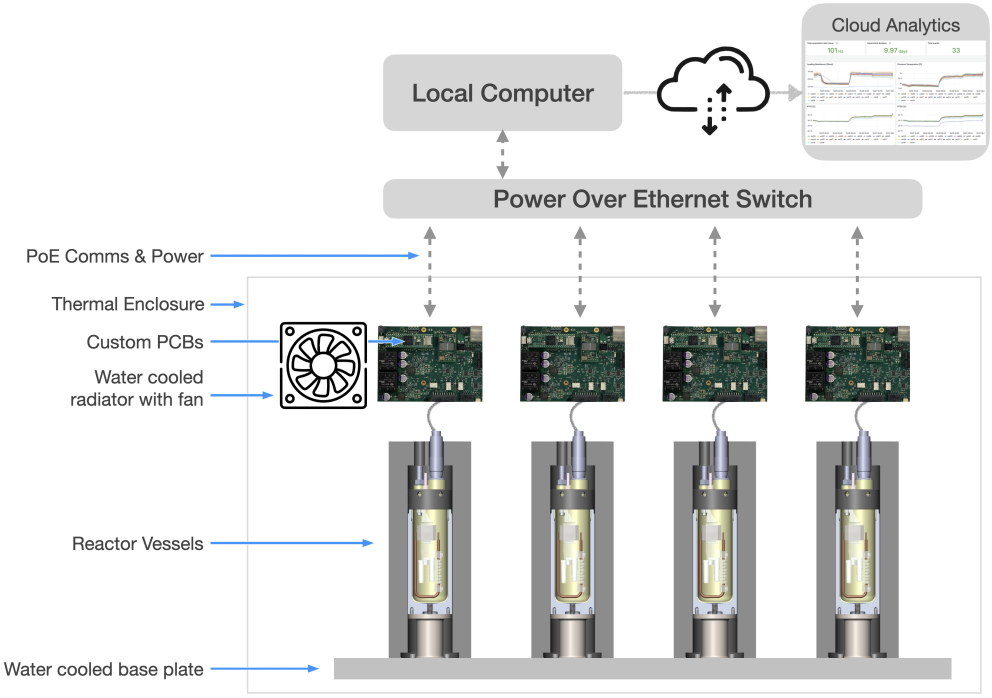



Fig. 2.11: System Diagram

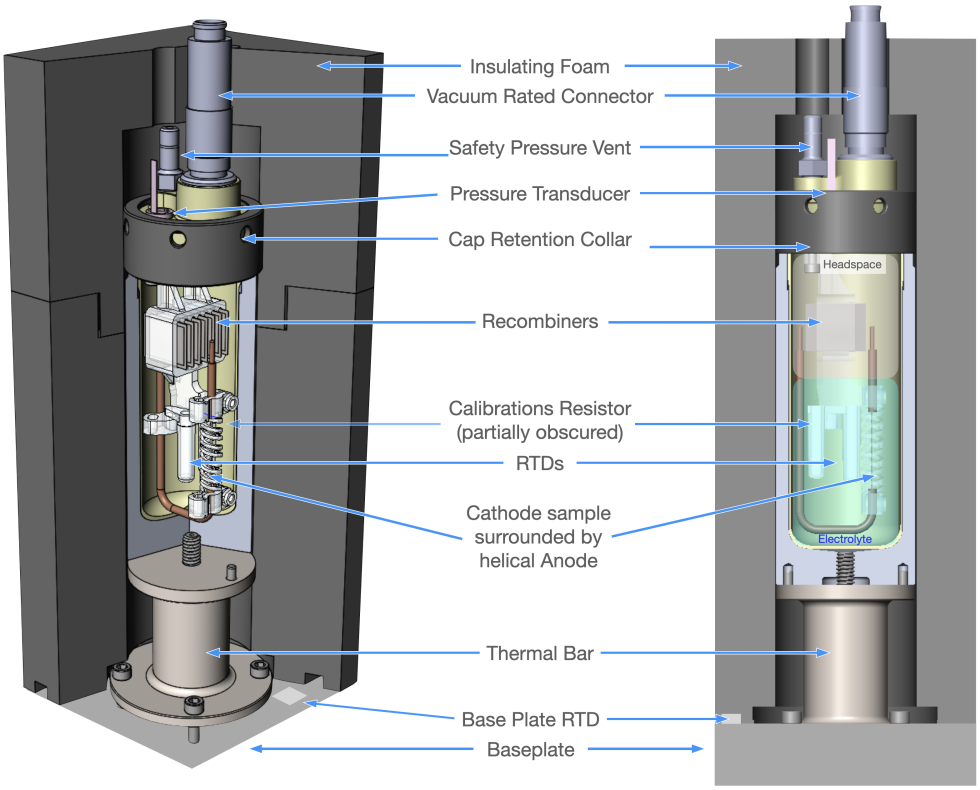



Fig. 2.12: Schematic cross-sectional views of a UHTP vessel.

#### 2.10.2.2 Reactors

The UHTP reactor is a closed isoperibolic calorimeter largely based on the HTcal design with a few modifications (Fig. 2.12). Heat flow is calculated from the temperature difference between the electrolyte temperature and the base plate temperature, based on calibrations with known input powers. Constant base plate temperature is achieved by using water cooled base plates to remove nearly all heat from the cells. Water cooled radiators and fans are used to remove heat generated by the PCBs and to ensure uniform air temperatures throughout the enclosure. This reduces the amount of heat added or removed from the cells by ambient air. RTDs are prone to failure over time due to the corrosiveness of the electrolyte. Unlike HTcal, which measures heat flow using an external thermal bar, UHTP relies solely on the temperature difference between the electrolyte and base plate. A second RTD was added to mitigate a single point of failure. Switching heat flow measurement methods from a thermal gradient to a $\Delta T$ reduced the sensitivity of the system. To compensate for this, the thermal bar was altered to increase its thermal impedance and therefore sensitivity to ensure small signals would not go undetected.

Each reactor contains a cathode (typically a 25 mm long by 0.5 mm diameter wire sample) of either palladium (active cells) or platinum (control cells). The cathode is surrounded by an anode consisting of

230 mm long 0.2 mm diameter platinum wire completing approximately 12 revolutions at a radius of 3 mm. The electrodes are submersed in 48 ml of either LiOD (active cells) or LiOH (control cells). In a typical experiment, each sector contains 17 active and three control cells totaling 85 active and 15 control cells for the UHTP system.

Each reactor is surrounded by thermal foam, designed to direct the majority of heat flow from the reactor through the thermal bar and into the base plate, thereby minimizing heat exchange with the surrounding environment.

#### 2.10.2.3 Thermal Enclosure

As mentioned in the reactor section, the primary heat transfer pathway in the system is from the reactor to the base plate. However, several additional routes exist for heat to enter and exit the reactor. To minimize heat exchanged with the environment, an insulated thermal enclosure is employed. The thermal enclosure uses water-cooled radiators and fans to assist the base plate in maintaining a constant temperature outside of the reactors.

An effort was made to keep all heat sources (PoE switches, circulation fan power supplies, water pumps, etc.) outside the thermal enclosure to minimize the exchange of parasitic heat with the reactors. Due to high electromigration current (3 A) an exception was made for the control and data acquisition PCBs. A comprehensive trade-off analysis led us to prioritize signal integrity between cells and PCBs, as well as ease of assembly and servicing, over optimal thermal performance. Although placing components outside the enclosure would enhance thermal management, the chosen configuration offers a better balance of overall system efficiency and practicality.

#### 2.10.2.4 Sectors

Bringing 100 reactors online at once in a new system can be risky. Physically working with a large number of reactors is also challenging. To keep UHTP easy to work with and scalable, 100 reactors were designed to be built in sectors of 20 cells each as shown in Figure 2.10. The calorimeters are arranged in a two wide by 10 deep configuration. When the enclosure is fully populated, it contains a ten by ten array of 100 calorimeters. The sectors are built on slides allowing for easy access and quick installation of calorimeters. As designed, the UHTP enclosure can run with one to five sectors installed. Each sector has its own PoE switch and chiller attachment points. This allows the system to be built up, repaired, or upgraded in sections. This also enables parallel workflows as the system can be run while work takes place on sectors outside the enclosure.

#### 2.10.2.5 Power System

Power over Ethernet (PoE) is used to power the PCBs. The PCBs have isolated power supplies that convert 48 V PoE voltage to the 0-10 V required for electrochemistry and 100 mV at 4 A required for electromigration and sample resistance measurements. This system is designed to carry out long duration experiments (~ two months). In the event of a mains power failure, the entire system is backed up with an Uninterruptible Power Supply (UPS) that can maintain full system operation for 3-4 hours.

#### 2.10.2.6 Reactor Control and Data Pipeline

At the center of the UHTP Reactor Control and Data Pipeline is a general purpose computer. This computer sends control commands and receives data from the micro-controller on the PCBs via Ethernet using

JavaScript Object Notation (JSON). JSON was chosen because it is a lightweight and human readable protocol, easy to implement and debug. This computer stores the data in a local database as well as replicating it to the cloud based Science Hub database where it's further processed using Python with the Pandas package.

Each PCB has a unique IP address that is manually configured using rotary hexadecimal switches on the board. This method allows us to easily encode the reactor's physical location in the array into the last two octets of the IP address. Knowing the cell locations relative to each other is key in understanding potential thermal crosstalk between the cells. It also helps identify potential gradients in a uniform temperature enclosure. In this experiment, the reactors are arranged in a 10 x 10 array. For instance, IP address 192.168.1.2 refers to the reactor in the second column and in the third row (with counting starting at 0).

In addition to controlling the vessels, the custom PCBs monitor environmental conditions such as enclosure temperature, pressure release rail pressure, room temperature, and barometric pressure.

### 2.10.3 Safety

There are several factors that could potentially cause hazardous conditions and/or events. The UHTP enclosure was designed to mitigate three main hazards.

1. Pressure buildup: Electrolysis produces heat and oxyhydrogen which pressurizes the cell. If this is not addressed, the cell could potentially explode due to over pressure or rapid recombination. To mitigate this, recombiners are employed to recombine oxyhydrogen into water in a controlled manner. In addition to recombiners, there is a safety relief valve that will vent the cell if pressure exceeds 85 psi.

2. Runaway AHE: Should a larger than anticipated AHE event occur, it is possible this could cause the cell to explode. To mitigate this as well as events where the recombiners and safety vent fail, the cells are located in a ballistic enclosure designed to contain shrapnel in an explosive event.

3. Oxyhydrogen builds up in the enclosure: If the safety vent system or the cells leak, oxyhydrogen may enter the enclosure itself. This gas can accumulate and create a hazardous condition. To mitigate this, a fan cycles room air through the enclosure and exhausts it into the laboratory exhaust vent. This is done at a rate such that the enclosure volume is replaced every 36 hours.

Reactors are controlled en masse from one to several notebooks. Should a safety event occur that affects one or more reactors, a command can be issued to shut down or restart reactors individually without affecting other reactors in the same controlling notebook.

### 2.10.4 Measuring Performance

The goal of this effort is to produce more energy than is consumed. There are two metrics used to measure performance: Coefficient of Performance (COP) and excess heat flow (see section 2.5).

Accounting for measurement system error, the excess heat calculation is a reliable metric for determining if a cell is producing more power than it is consuming. What this metric does not tell is the efficiency of the system. It is important to know if it took 1 W or 1 kW to produce 100 mW of excess heat, which is captured in the COP.

At a minimum, both COP and excess heat should be used to determine if the system is in fact producing excess heat.

#### 2.10.4.1 Calibration

To calculate COP and excess heat we must know input and output power. Input power is easily and accurately measured and in the form $P_{\text{in}} = VI$, with $I$ being the current and $V$ being the voltage (for each electric circuit entering the calorimeter). The voltage is measured close to the thermal system boundary.

Measuring output power is not as straight forward. Unlike HTcal, where output power is measured via a temperature gradient across a thermal bar, heat flow in UHTP must be inferred by measuring the electrolyte to base plate temperature difference, $\Delta T$, and knowing the thermal impedance of the system, $Z_{\text{th}}$.

$$P_{\text{out}} = \frac{\Delta T}{Z_{\text{th}}}$$

$Z_{th}$ is found empirically by calibration. There are several sources of heat in the UHTP system. Heat due to ohmic heating of the electrolyte (from electrochemical current), heat due to (electro-)chemical reactions (at the electrodes and at the recombiners), heat due to the electromigration current passing through the cathode and the lead wires, and hopefully excess heat from low energy nuclear reactions. Each source of heat takes a slightly different path from source to the base plate. The $Z_{\text{EC}}$ path, resulting from application of electrochemical voltage to the electrodes, is dominated by electrolyte. Given that the electrolyte resistance is much greater than that of the wires, relatively little heat is lost in the wires. As such, heat due to electrochemistry is tightly coupled from the electrolyte to the vessel wall to the thermal bar.

Unlike the electrochemistry electrical circuit, the electromigration electrical circuit is essentially a loop of wire with two thirds of this loop residing outside of the immediate electrolytic cell. The voltage sense lines of the electromigration power meter were attached immediately outside the reactor. This is to ensure heat dissipated into the reactor is accounted for while the parasitic heat from the wire harness is not. Also, unlike the electrochemistry thermal path, which is from the electrodes to the electrolyte and to the vessel walls, only about half of the electromigration power is coupled into the electrolyte. The rest is coupled to the vessel via the head space and wires leading to the PCB. This is the reasoning for using separate thermal impedances for electrochemistry and electromigration.

Determining the thermal impedance of unknown heat sources, $Z_x$, is a challenge as we would need to know the location of the unknown heat source and how it couples to the temperature sensors in the electrolyte. For now we can assume $Z_x$ is bounded by $Z_{\text{EC}}$ and $Z_{\text{EM}}$. For the purposes of this paper and the UHTP experiments, a $Z_x$ value of 5.5 K/W is assumed. If $Z_x$ is in fact bounded by $Z_{\text{EC}}$ (5.8 K/W max) and $Z_{\text{EM}}$ (4.1 K/W min), this would yield a maximum error of 22 %.

Determining $Z_{\text{EC}}$ is done by applying a constant power to the power resistor that resides in the electrolyte. While any amount of power can be used for calibrating the reactor, once the relationship between power input and change in electrolyte temperature was demonstrated to be linear, 2.5 W was chosen for calibration, as it is the average of the power levels intended to be used in the system. The resistor is used as a proxy in lieu of an electrochemical heat source. We verified that the calibration with resistors closely matches the calibration with inert electrodes.

$Z_{\text{EM}}$ is found by applying 3 A DC to the cathode. This results in ~600 mW being sourced into the system with ~300 mW of heat being dissipated in the electrolyte.

Calibration begins after the enclosure has dwelled for 24 hours to ensure it has equilibrated. EC calibration begins by applying 2.5 W to the power resistor and letting the electrolyte temperature reach equilibrium after five time constants of 43 minutes each. Power is removed and the calorimeters are allowed to dwell for five time constants to return to equilibrium. A current of 3 A is then applied to the cathode for five time constants. Power is then removed, and the enclosure is allowed equilibrate for five time constants before the

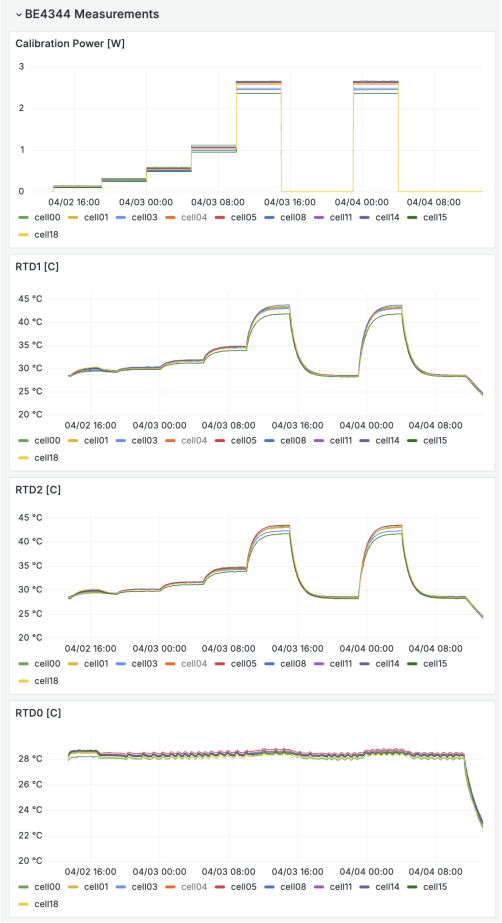
experiment begins. It should be noted that power into the cell, electrolyte, and base plate temperature are recorded at a 1 Hz rate during calibration.

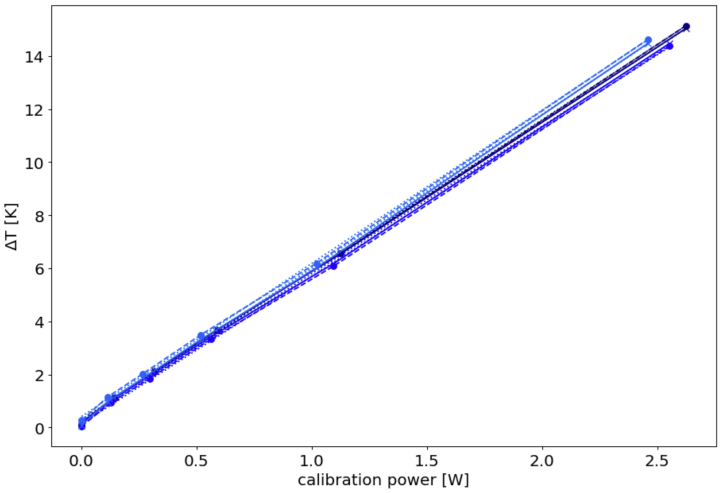
To investigate the linearity of the calorimeter, a staircase calibration was performed at 150 mW, 250 mW, 500 mW, 1 W, and 2.5 W resistor powers (held for several thermal time constants, Fig. 2.13). After validating that the thermal impedance is independent of the resistor input power, calibrations were performed at a single power level.

Along with the steady state thermal resistance, the instrument response functions, $S_{\mathrm{EC}}$ and $S_{\mathrm{EM}}$ are obtained during calibrations. This enables us to calculate the expected electrolyte temperature during the transients in EC power and EM power. The expected temperature difference (between electrolyte and base plate) is calculated as follows:

$$\Delta T_{\mathrm{expected}} = (P_{\mathrm{EC}} Z_{\mathrm{EC}}) \circ S_{\mathrm{EC}} + (P_{\mathrm{EM}} Z_{\mathrm{EM}}) \circ S_{\mathrm{EM}}, \tag{2.14}$$

where $\circ$ is the convolution operator. The parameters $Z_{\mathrm{EC}}$, $Z_{\mathrm{EM}}$, $S_{\mathrm{EC}}$ and $S_{\mathrm{EM}}$ are calibrated and tabulated individually for each cell. Additional details on calibration can be found in section 2.8.2.




| cell | RTD1 offset [K] | RTD1 linear [K/W] | RTD1 R2 | RTD2 offset [K] | RTD2 linear [K/W] | RTD2 R2 |
|---|---|---|---|---|---|---|
| 00 | 0.293430 | 5.617317 | 0.999827 | 0.243105 | 5.676249 | 0.999821 |
| 01 | 0.233890 | 5.561895 | 0.999693 | 0.138313 | 5.562052 | 0.999680 |
| 03 | 0.227363 | 5.787277 | 0.999591 | 0.409358 | 5.775344 | 0.999609 |
| 04 | 0.477407 | 5.492763 | 0.999578 | 0.464404 | 5.472777 | 0.999721 |
| 05 | 0.107149 | 5.568385 | 0.999772 | 0.160515 | 5.602619 | 0.999727 |
| 08 | 0.306723 | 5.943332 | 0.999237 | 0.199163 | 5.597781 | 0.999462 |
| 11 | 0.148925 | 5.579426 | 0.999749 | 0.171404 | 5.549331 | 0.999727 |
| 14 | 0.296407 | 5.603953 | 0.999303 | 0.081532 | 5.486755 | 0.999467 |
| 15 | 0.236423 | 5.574253 | 0.999149 | 0.125986 | 5.573934 | 0.998999 |
| 18 | 0.386301 | 5.632505 | 0.999132 | 0.342747 | 5.604380 | 0.999423 |

Fig. 2.13: Results from multi-step calibration. Left panel, from top to bottom, shows calibration input power steps, followed by the temperature response of the two RTDs in the electrolyte, followed by the temperature of the base plate. The top right panel shows that reactor sensitivity is linear with input power. The bottom right panel shows the raw gain (K/W) and offset (K) from calibration.

#### 2.10.4.2 Calculating COP and Heat Flow

It should be noted that, in its current configuration, UHTP is functioning as a screening test. It is performing 100 concurrent experiments searching for potential AHE. The methods for the screening tests are outlined below. Experiments with positive signals would be replicated in the HTcal to confirm reproducibility, and would also be replicated in the MS80 calorimeter in order to more accurately quantify the amount of excess heat observed.

In the presence of excess heat, the electrolyte temperature will be greater than the expected temperature for a given input power. At this point, we can make our first COP computation. This calculation is based

on expected temperature rather than expected heat as is used in HTcal. We denote the difference by adding a subscript 'T' to the COP.

$$\mathrm{COP_T} = \frac{\Delta T_{\mathrm{measured}}}{\Delta T_{\mathrm{expected}}} \tag{2.15}$$

A $\mathrm{COP_T}$ significantly greater than 1 tells us that excess heat is present (and AHE might be occurring), but does not tell us how much excess power is being produced. The excess heat can be computed based on certain assumptions. Given a measured excess temperature, it can be converted to excess heat using the thermal impedance. We don't know the exact thermal impedance $Z_x$ for an excess heat event, because we don't know its location. It might be occurring near the cathode, in which case $Z_{\mathrm{EC}}$ is a good approximation for $Z_x$. In general, for most scenarios, $Z_{\mathrm{EM}} \leq Z_x \leq Z_{\mathrm{EC}}$. This typically bounds the excess heat by ±10 %.

Assuming $Z_x$ is the weighted average of $Z_{\mathrm{EC}}$ and $Z_{\mathrm{EM}}$ (weighted with the respective input powers), the excess heat, $P_{\mathrm{excess}}$, follows as:

$$P_{\mathrm{excess}} = P_{\mathrm{in}}(\mathrm{COP_T} - 1). \tag{2.16}$$

More generally,

$$P_{\mathrm{excess}} = \frac{\Delta T_{\mathrm{measured}} - \Delta T_{\mathrm{expected}}}{Z_x} = \frac{\Delta T_{\mathrm{excess}}}{Z_x}. \tag{2.17}$$

#### 2.10.4.3 Minimum Transient Detection Threshold

To determine the sensitivity of the calorimeters, a series of constant power pulses were applied to the calibration resistor (Fig. 2.14b). Pulses ranged in duration and magnitude from 1 mW for 1 min to 50 mW for 45 min. This test demonstrated that a 5 mW pulse for 5 min (1.5 J) could be detected. However, this test was done under ideal conditions, starting from equilibrium with no electrochemical or electromigration input power. 5 mW for 5 min would be below the noise floor (driven by diurnal swings and recombiner variations) of a typical experiment which operates between 650 mW and 5.6 W.

### 2.10.5 Loading Measurement

The change in resistance of a palladium wire can be correlated to the change in the amount of hydrogen loading. This resistance change is in the milliohm range on a milliohm sample, necessitating a sensitive four-wire measurement. Given space and power constraints of the UHTP system, it was designed to leverage the electromigration current to measure sample resistance. When electromigration current is not required, the electromigration power supply sends a four-second two-level current (600 mA and 300 mA) pulse every 60 seconds. These values are the minimum pulse size and duration to get an accurate resistance measurement while introducing the least amount of parasitic heat into the calorimeter.

When electromigration is required, UHTP uses 3.2 A / 2.8 A level changes around a 3 A electromigration current. This two-level measurement is made at the same 4 seconds per 60 seconds cadence. The two-level measurement is accounted for in the input power balance, but at ~1 mW, has little impact on the system.

It should be noted that a trade-off was made between accurately measuring sample resistance and accurately measuring the electromigration input power in the choice of the placement of the voltage sense wires. For accurate resistance measurements, voltage senses should be placed on the sample, whereas for accurate heat measurements, voltage senses should be placed at the thermal system boundary. Because accurate calorimetry is a priority and qualitative loading measurements are sufficient, voltage senses were placed at the thermal system boundary.

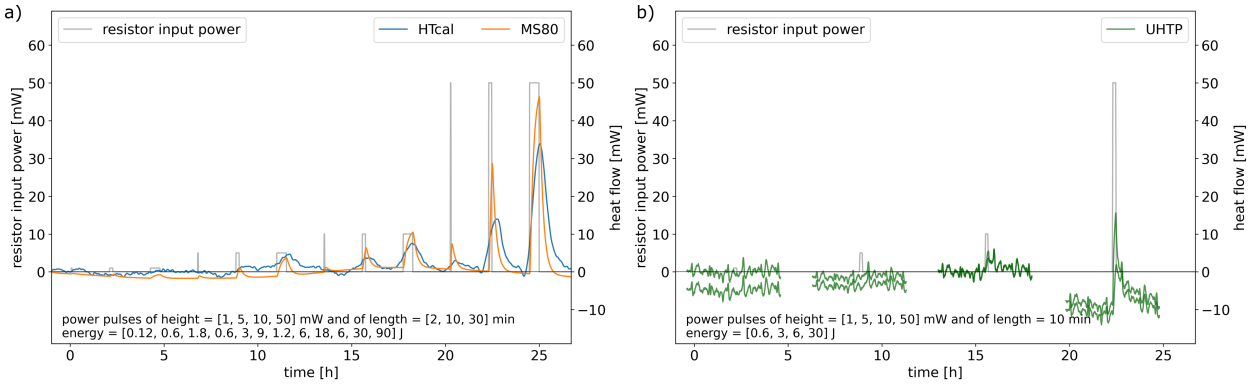



Fig. 2.14: Comparison of calorimeter heat flow responses to pulsed inputs in various calorimeters (MS80 and HTcal (a) and UHTP (b)). Note that all the pulses were applied consecutively in the MS80 and HTcal (a), but were assembled from different times in the UHTP (b). The two green lines in (b) represent the two temperature sensors in a given cell. Heat flows are shown for a single random cell per calorimeter, representing all cells.

## 2.11 Conclusion

The Setaram MS80 as well as the HTcal and the UHTP calorimeters should be more than sufficient to detect excess heat signals reported in the literature (Fig. 2.15). In contrast, we found that open system calorimetry is amenable to errors of similar magnitude as many reported excess heat measurements.

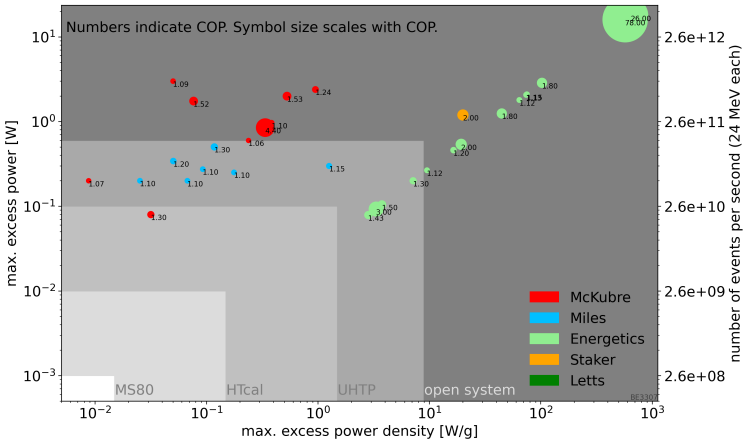



Fig. 2.15: Illustration of detection thresholds with our calorimeters (MS80, HTcal, UHTP, open system) calorimeters compared to excess heat reports in the literature. Note that the white space in the lower left is 'uncharted territory', not easily resolvable with our calorimeters.

# Chapter 3

# Loading Measurements

## 3.1 Background and Literature Review

Given the fantasy and biasing that exists around studying LENR, Callisto sought to ground their research program in principles of physics and chemistry. Within this framework, one of our primary thrusts was to understand, control, and maximize deuterium loading in palladium and other relevant metals. Regardless of observing any excess heat, we could certainly develop methods for enhancing the fractional loading of hydrogen isotopes. Success depended on accurately measuring the hydrogen loading, exploring methods for increasing this loading, and ultimately optimizing these methods to yield the highest possible fractional loadings near ambient conditions.

The focus of this section is on measurement techniques that can be used to estimate the fractional loading of hydrogen in a metal hydride. The majority of our work was performed on palladium protide (PdH) and palladium deuteride (PdD), although Callisto did investigate a few other metal systems including palladium alloys, nickel, and several rare-earth metals. Not only is palladium considered a model system, but it is also widely believed to be the most relevant material for LENR. Herein, we will emphasize methods and literature that work well for palladium hydride, although these methods can be extended to other metal hydride systems.

We can classify loading measurements as either direct or indirect. In a direct loading measurement, the moles or mass of hydrogen is tracked directly. Typically, direct measurements offer higher measurement accuracy, given there is less error propagation. However, direct methods are typically more constrained, making it hard to apply an arbitrary form factor or in situ to an experiment. In contrast, indirect loading measurements offer more flexibility in experimental design, albeit at the cost of lower certainty.

In an indirect loading measurement, a proxy property is measured and is correlated with hydrogen loading, either using an empirical calibration or a first principles model. Any indirect loading measurement must be motivated by a first principles understanding of the hydrogenation process. Hydrogen atoms occupy octahedral interstitial sites in the face-centered cubic lattice of palladium, leading to its lattice expansion. The absorption of hydrogen into interstitial sites leads to significant alterations in the electronic structure, primarily through interactions between hydrogen atoms' electrons and palladium atoms' electronic states. The interstitial hydrogen atoms contribute their 1s electrons, which interact with the palladium d-band electrons, leading to hybridization and modification of the electronic structure. Additionally, palladium's s and p orbitals (5s and 5p) participate in hybridization, resulting in bonding and anti-bonding states that

affect the density of states at the Fermi level.

Due to the combined effects of electronic band structure changes and mechanical effects of interstitial occupation and atomic displacement, many electrical, mechanical, and optical properties change along a continuum as the fractional loading of hydrogen increases.

The following sections cover various methods used in the literature to measure hydrogen loading in palladium hydride.

## 3.2 Gravimetric Analysis

Mass loading, or gravimetric analysis, involves measuring the change in mass of the metal before and after hydrogen absorption. By accurately determining the mass difference, the amount of hydrogen absorbed can be quantified as follows:

$$x \text{ in } \mathrm{PdH}_x : x = \frac{n_\mathrm{H}}{n_\mathrm{Pd}} = \frac{\Delta m}{m_\mathrm{Pd}} \times \frac{M_\mathrm{Pd}}{M_\mathrm{H}} \tag{3.1}$$

Where $n_{\mathrm{H,Pd}}$ are moles, $m_\mathrm{Pd}$ is the mass of palladium, $\Delta m$ is the mass difference before and after hydrogen absorption, and $M_{\mathrm{H,Pd}}$ are the molar masses.

This technique is straightforward but requires a precise balance and isolation from environmental variables. A modern scale has a typical precision of 100 µg, meaning that for a loading precision of 0.1 %, a minimum mass of palladium of 100 mg is required. Given these requirements, common form factors like wires and thin films may be limited in their use for gravimetric loading measurements due to their relatively small mass. For example, a 500-micron diameter palladium wire that is 30 mm long has a mass of approximately 70 mg, which is below the 100 mg threshold for the desired precision. Similarly, a thin palladium film with a thickness of 100 nm and an area of 1 $\mathrm{cm}^2$ has a mass of about 120 µg, which is significantly less than the required mass for high-precision measurements.

Gravimetric methods are widely applicable to measuring hydrogen uptake in different materials and have been used for decades to characterize hydrogen loading in both elemental and composite systems [116–118]. Besides constraints around form factor, in-situ gravimetric analysis during electrolysis is prohibitive due to impurity depositions and moisture retention [119]. These issues necessitate the use of alternative measurement techniques, such as in-situ resistance or optical measurements to measure fractional hydrogen loading under electrochemical conditions.

## 3.3 Sievert Isotherm

Another common direct loading measurement is the Sievert method, which relies on measuring the pressure change in a closed system as hydrogen gas is absorbed by the metal [120]. Assuming first-order kinetics, the amount of hydrogen absorbed can be calculated using the ideal gas law and the known volume of the system:

$$x \text{ in } \mathrm{PdH}_x : x = \frac{n_\mathrm{H}}{n_\mathrm{Pd}} = \frac{n_\mathrm{absorbed}}{n_\mathrm{Pd}} = \frac{1}{n_\mathrm{Pd}} \frac{V \Delta p}{RT} \tag{3.2}$$

Where $n_\mathrm{absorbed}$ is the moles of hydrogen absorbed by the metal, $n_\mathrm{Pd}$ is the moles of metal, $V$ is the system volume, $R$ is the gas constant, $T$ is the system temperature, and $\Delta p$ is the pressure change after hydrogen absorption.

However, researchers have shown that the palladium hydride system deviates from this first-order behavior, primarily due to the dissociation of hydrogen being a rate-limiting step and the effects of concentration polarization, where the rate of hydrogen transport through a palladium membrane exceeds its supply from the bulk gas [121, 122]. As a result, a more complex model is required to accurately calculate hydrogen loading based on Sievert isotherms when using a membrane configuration. If bulk palladium is encapsulated in a closed system, the first order behavior captures the mass loading well-enough.

The Sievert method is also useful for characterizing the differences in hydrogen storage capacity between bulk and nanomaterials. For example, it was observed that palladium nanoparticles exhibit modified thermodynamics and kinetics for hydrogen storage compared to bulk palladium, including reduced hysteresis, lower desorption temperatures, and different enthalpy and entropy values [123].

Despite its advantages, the Sievert method has limitations. Sample form factor and reactor design can limit precision. For instance, to achieve 0.1% precision for a 70 mg wire, a pressure gauge with ~ 10 µbar precision and a range of 10 mbar is required. Such experimental setups are neither accessible nor inexpensive. Similar to the gravimetric method, the Sievert method also improves with increased sample mass. Additionally, the Sievert method is specific to gas-loaded metal hydrides and is not readily translatable to electrolytically loaded metal hydrides due to gas evolution simultaneous with loading and dissolution of gas into the electrolyte.

## 3.4 Coulometry

Coulometry is an effective electrochemical technique for quantifying hydrogen or deuterium loading in palladium and palladium alloys [124, 125]. This method involves measuring the total charge passed during the oxidative discharge of hydrogen from the palladium, which can then be related to the amount of absorbed hydrogen. The coulometric analysis is based on Faraday's laws of electrolysis, which states that the amount of a substance altered at an electrode during electrolysis is proportional to the total electric charge passed through the substance. In the context of hydrogen loading, the fractional loading is given by:

$$x \text{ in } \mathrm{PdH}_x : x = \frac{Q}{F n_{\mathrm{Pd}}} \tag{3.3}$$

where $Q$ is the total charge passed during the electrolysis, $F$ is Faraday's constant (approximately 96,485 C/mol), and $n_{\mathrm{Pd}}$ is the number of moles of palladium atoms.

Despite its facile implementation, coulometry does have its limitations. Ideally, a flow cell geometry is used, which mitigates the hydrogen oxidation reaction which convolutes the electron flow and can lead to overestimates in loading [126]. In multi-modal studies that use complementary loading measurements, it was found that the method is most accurate for low fractional loadings [127]. Additionally, the use of additives in the electrolyte can introduce inaccuracies due to the presence of other Faradaic processes. For instance, arsenic salts (extremely relevant to subsequent discussion) can significantly affect the measured loading levels due to concurrent oxidation reactions during discharge [128]. For this reason, early in Callisto's investigations, it was concluded that coulometry was incompatible with additive-based loading enhancement strategies. As such, the focus shifted to methodologies that did not require a complete understanding of the Faradaic reactions present in an experiment.

## 3.5 Quartz Crystal Microbalance

Quartz crystal microbalances (QCMs) are another valuable tool for studying hydrogen storage materials, capable of detecting minute mass changes on the order of nanograms, allowing for precise and quantifiable measurements of hydrogen uptake in thin films [129–131]. Not only can QCMs be used to quantify loading in thin film metal hydrides, but they are also versatile and can be adapted for use in different environments including electrochemical cells and gas-loading cells [126, 132]. QCMs provide real-time, sensitive measurements of mass changes associated with hydrogen absorption and desorption in palladium and its alloys, offering insights into the loading processes and material behaviors [133].

QCMs operate by measuring the frequency shift of a quartz crystal resonator as a thin film of palladium absorbs or desorbs hydrogen. The mass change associated with hydrogen uptake or release induces a corresponding shift in the resonant frequency, which can be quantitatively related to the amount of hydrogen absorbed, given by the Sauerbrey equation:

$$\Delta m = -\frac{\Delta f A}{2 f_0^2} \sqrt{\frac{\mu_q}{\rho_q}} \tag{3.4}$$

Where $\Delta f$ is the change in resonant frequency, $f_0$ is the fundamental frequency of the quartz crystal, $A$ is the area of the crystal, $\rho_q$ is the density of quartz, $\mu_q$ is the shear modulus of quartz, and $\Delta m$ is the mass change.

However, the frequency shift measured by QCMs is not solely due to mass changes but also includes contributions from stress within the palladium film as it expands or contracts during hydrogen absorption and desorption. This complicates the interpretation of data and requires careful analysis to separate mass and stress. Additionally, rough or irregular surfaces may introduce additional frequency shifts unrelated to mass changes, leading to errors in loading estimates. External factors such as temperature fluctuations, pressure variations, and the presence of contaminants can impact QCM measurements as well. These need to be carefully controlled and accounted for during experiments to ensure reliable loading estimates. Given these corrections, one can use the modified Sauerbrey equation to calculate mass change in hydrogen-loaded thin films:

$$\Delta m = -\frac{A}{2 f_0^2} \cdot \sqrt{\frac{\mu_q}{\rho_q}} \cdot (\Delta f - C_\sigma \Delta\sigma - C_r \Delta r) \tag{3.5}$$

Where additional terms: $C_\sigma$ is a system-dependent stress coefficient, $\Delta\sigma$ is the change in stress due to hydrogenation, $C_r$ is a system-dependent roughness coefficient, and $\Delta r$ is the change in roughness due to hydrogenation.

In addition to providing quantitative loading for thin film metal hydrides, QCMs are particularly useful for investigating isotopic effects, such as differentiating between protium (H) and deuterium (D) absorption in palladium. The mass difference between these isotopes leads to distinct frequency shifts, and deuterium loading resulting in a larger frequency change compared to protium due to its higher atomic mass.

In Callisto's efforts to use QCM measurements to quantify loading in thin film systems, several challenges arose when using chemical enhancement to increase the deuterium loading, including stress corrections, motional resistance corrections, and catastrophic blistering of the film, which led to large errors in the QCM signal. As a result, we did not find QCMs a useful method for measuring loadings over 80 % in thin films.

## 3.6 Macrostrain

The use of strain measurements to quantify hydrogen loading in palladium dates back to the 1800s. This method can be performed using optical strain measurements, strain gauges, or X-ray diffraction techniques [134, 135]. For palladium hydride, the strain induced by hydrogen loading increases linearly with fractional hydrogen loading. Fig. 3.2 a) illustrates various loading-strain relationships reported in the literature, with a broad range in slopes. For this discussion, we will use the following relationship:

$$x \text{ in } PdH_x : x = 17\epsilon = 17\frac{L - L_0}{L_0}, \tag{3.6}$$

where $\epsilon$ is the strain, $L$ is the length and $L_0$ is the initial length.

As mentioned previously, the strain can be measured with either strain gauges monitoring the macrostrain, or with X-ray diffraction monitoring the lattice expansion.

## 3.7 Optical Reflectivity

For palladium hydride and other metal hydride systems, the optical properties of the material change continuously with hydrogen uptake [136–139]. This continuum can be leveraged to estimate the fractional hydrogen loading. The most fundamental optical constants that can be calculated are the permittivity coefficients for a material, $\epsilon_1$ and $\epsilon_2$. However, these require detailed modeling to arrive at accurate numbers [140] . Another complicating factor is that surface roughness on the order of the studied wavelength can influence the optical parameters that are measured. For instance, it has been observed that the substrate material and the evolution of surface roughness of palladium significantly affected its optical response to hydrogen [141]. Due to this, it is challenging to use reflectance-based approaches on bulk metal hydrides.

However, the substrate constraint in a thin film structure allows for more precise control and measurement of the optical response. By monitoring backside reflectance in a thin film device, one can effectively estimate fractional hydrogen loading. Despite roughening at the frontside palladium-electrolyte interface, the backside palladium-substrate interface remains smooth during hydrogen cycling. This methodology, as it applies to thin film metal hydrides, will be discussed in more detail in a section 3.14, as it was critical for Callisto's investigation into loading enhancers.

## 3.8 Thermal Desorption Spectroscopy

Thermal desorption spectroscopy (TDS) provides insights into hydrogen content and binding energy by heating the metal hydride and measuring the desorbed hydrogen as a function of temperature. TDS's ability to produce detailed desorption profiles enables differentiation between various hydrogen trapping sites and the analysis of a variety of metal hydrides [142–146]. Specifically, it can examine differences in binding energies and the amount of surface versus bulk-absorbed hydrogen. Despite its high sensitivity, capable of detecting hydrogen at ~1 wt. ppm, phase transitions, and complex desorption processes may require data modeling for accurate interpretation of results. Additionally, water absorption can significantly affect measurements, necessitating careful handling in an inert atmosphere. Given these experimental constraints, TDS is unsuitable for measuring hydrogen loading in electrolytically loaded metal hydrides.

## 3.9 Nuclear Magnetic Resonance

Nuclear magnetic resonance (NMR) works by exploiting the magnetic properties of atomic nuclei. When placed in a strong magnetic field, nuclei with a magnetic moment (such as hydrogen) can absorb and re-emit electromagnetic radiation at a characteristic frequency. This frequency is influenced by the local environment of the nuclei, including electronic structure and interactions with neighboring atoms. By analyzing the resulting NMR spectra, information about the hydrogen atom's local environment, such as the number of hydrogen atoms and their local environment can be obtained. This makes NMR a powerful tool for directly probing the proton population inside the metal lattice [147–152]. However, its use is limited to the expensive nature of the measurement equipment.

## 3.10 Neutron Scattering

Neutron scattering (NS) and small-angle neutron scattering (SANS) are analogous techniques to X-ray scattering methods, used to measure the scattering patterns of neutrons to determine the distribution and quantity of hydrogen within a metal lattice. Despite neutrons' direct interaction with lattice-bound protons, neutron scattering is considered an indirect measurement due to the need for a complex physical model to determine fractional hydrogen loading.

NS measurements in palladium protide and palladium deuteride confirmed that hydrogen atoms occupy octahedral positions in the face-centered cubic (fcc) palladium lattice [153]. Other early NS studies on the thermal motion in palladium hydride showed that hydrogen atoms have isotropic thermal motion within the palladium lattice [154]. Additionally, NS methods are valuable for characterizing the electron and phonon band structures of palladium and palladium hydride, important for understanding the material's thermal response and hypothesizing effective stimulation schemes [155].

While NS and SANS are powerful techniques for characterizing hydrogen loading in palladium hydride, providing deep insight into structural and thermochemical behavior, they are fairly inaccessible as large-scale scientific facilities are required to perform these measurements.

## 3.11 Resistance-based Loading Measurement

Electrical resistivity is probably the most widely used indirect method to estimate fractional hydrogen loading in palladium hydrides [156–165]. The primary reason for this is the continuous change in electrical resistivity with hydrogen absorption, which allows for facile, in-situ monitoring of hydrogen content. As hydrogen atoms are absorbed into the palladium lattice, they initially act as scattering centers for conduction electrons, leading to an increase in electrical resistivity. This increase continues until about 75% hydrogen loading at room temperature. However, as hydrogen loading continues to increase towards stoichiometric unity (PdH), the resistivity starts to decrease. This decrease at high fractional loading can be attributed to the donation of electrons to the conduction band, where the scattering from hydrogen atoms becomes less effective.

One of the advantages of using electrical resistivity is its capability for in-situ monitoring. This is particularly useful in dynamic systems where hydrogen cycling is critical. Additionally, the method is relatively straightforward to implement in both electrolytic and gas-loading schemes. It involves simple electrical measurements, which can be easily integrated into various experimental setups. Finally, electrical resistance measurements are non-destructive, allowing for continuous monitoring without affecting the sample.

However, the method is not without its challenges. The relationship between hydrogen loading and electrical resistivity is not linear. The resistivity increases with hydrogen uptake until about 75% loading, after which it decreases, leading to a non-linear relationship with two possible loading values for any particular resistance. This double-valued property can complicate the interpretation of the data, particularly near the maximum in the resistivity versus loading curve. There are also discrepancies in the literature regarding the exact mapping between hydrogen loading and resistivity changes. These discrepancies can arise from various factors, including differences in the palladium samples' form factor, the resistance measurement implementation, and experimental conditions such as temperature and reactor cleanliness. Additionally, as hydrogen is absorbed into the palladium lattice, it can induce stress and create defects, which further impact the electrical resistivity. These additional factors need to be considered when interpreting resistance measurements.

To address some of these challenges, Zhang et al. derived an empirical formula based on literature that provides a reasonable mapping between fractional loading and resistivity changes for $PdH_x$ and $PdD_x$ [166]. This formula provides an accurate representation of the relationship. According to Zhang et al., the fractional loading can be described by the following equations:

$$\frac{R_{\mathrm{PdH}_x}}{R_{\mathrm{Pd}}} = 1 + 1.69731x - 5.34162x^2 + 13.4472x^3 - 9.87644x^4, \tag{3.7}$$

$$\frac{R_{\mathrm{PdD}_x}}{R_{\mathrm{Pd}}} = 1 + 1.88402x - 6.94933x^2 + 17.2941x^3 - 12.0073x^4, \tag{3.8}$$

where $R_{\mathrm{Pd}}$ is the initial palladium resistance and $R_{\mathrm{PdH}_x}$, $R_{\mathrm{PdD}_x}$ are the resistances of palladium protide and palladium deuteride, respectively.

### 3.11.1 Practical Implications

The resistivity of palladium is $1.05 \cdot 10^{-7}\,\Omega\cdot\mathrm{m}$. A typical sample, e. g., a 25 mm long, 0.5 mm diameter wire has a resistance of 13.4 mΩ. Samples with larger ratios of cross-sectional area to length, e. g., thicker wires, foils, rods, often have even lower resistances in the mΩ or µΩ range.

In order to measure these low resistances, a four-wire measurement is necessary. The measurement current is introduced into the sample through two leads connected to the ends of the sample, while the voltage difference is measured between the sense leads, which are attached to the sample between the current leads. This way, contact resistances are minimized and resistances within the current leads are excluded from the circuit. Maximum test currents for resistance measurements are often 1 mA (e. g., NI PXIe-4071 digital multimeter), resulting in voltages of a few µV. In order to increase the voltage signal, higher probe currents can be applied using a source measure unit (SMU) instead of a digital multimeter (DMM). Source and sense leads are attached to the sample either through laser welding or through clamping (Fig. 3.1). We found that repeated loading and deloading can affect the robustness of laser welds, but clamping the lead wires (instead of laser welding) is a reliable contacting method in this case.

If resistance measurements are performed in situ, co-conductance through the electrolyte must be considered, but it is significant only for very thin wire samples. For a 25 mm long, 0.5 mm diameter wire sample in 0.5 M LiOH, the electrolyte resistance is ~1000 x the sample resistance.

If the resistance is measured in situ in the presence of an electrochemical bias, crosstalk between these two signals can occur. As the electrochemical current flows through the cathode to different extents before it flows through the electrolyte to the anode, it creates a superimposed voltage gradient within the cathode,

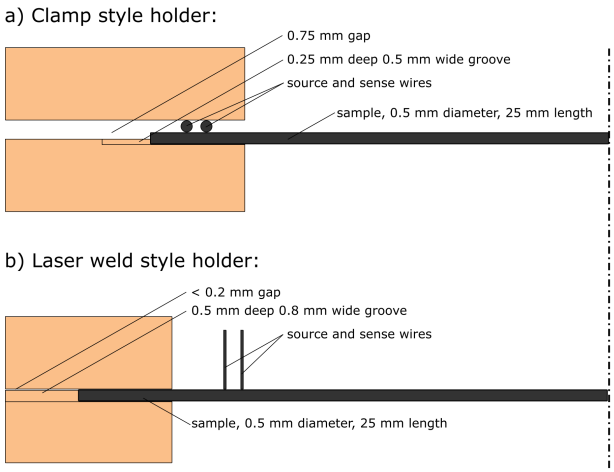



Fig. 3.1: Methods to connect leads (for resistance measurement or electrochemical current) to wire samples: a) clamp style or b) laser weld. In the clamp style holder, the clamps are pressed together using PEEK screws. The source and sense wires are 0.5 mm diameter platinum wires, which are in turn laser-welded to insulated copper leads. In the laser weld style holder, source and sense leads are typically 0.13mm diameter platinum wire coated with PFA (A-M Systems) laser welded directly to the palladium sample. Drawing is not to scale.

depending on the electrochemical current, the electrolyte resistance and the cathode resistance. The variation in electrolyte resistance due to bubbling can cause fluctuations in that superimposed voltage difference, complicating the measurement of the cathode resistance. To disentangle the two potentials, we can apply the resistance measurement probe current using a lock-in amplifier (Zurich Instruments MFLI). It overlays a harmonic reference current on top of the electrochemical current and can demodulate the measured signal to extract the in-phase component, from which the sample resistance can be calculated. For the HTcal (section 2.9.1), we emulated the lock-in principle digitally, taking advantage of the microsecond time resolution of the NI PXIe-4139 source measure unit. To cancel out the potential contribution from the electrochemical current, the resistance probe current follows a square wave with an amplitude of 100 mA centered around 0 mA, i.e. it covers both polarities. Four square waves (each with 10 sampling points) with a period of 1 ms are applied for each resistance measurement (typically 1 Hz).

One thing to note is that strictly speaking only the resistivity $\rho$ is a material property, while the resistance $R$ is the quantity being measured. They are related by

$$R = \rho \frac{L}{A}, \tag{3.9}$$

where $L$ is the length and $A$ is the cross-sectional area. It is frequently observed that the sample changes its geometry upon cycling (loading and deloading). Straight wires can end up curved. More importantly, they tend to become shorter and thicker with the number of loading cycles, decreasing the resistance [167]. This is likely due to the loading gradient (caused by diffusion kinetics) during the initial phase of the loading. With the core experiencing less volumetric strain than the shell, the shell will expand radially more than axially. This should be reversible upon deloading, but in practice we have seen wires remaining bent after deloading

and becoming shorter over several loading cycles, depending on the sample retention and sample geometry. Additionally, repeated loading and deloading can introduce defects into the palladium lattice, increasing the resistance. Both effects mean that after a load-deload cycle the resistance ratio (sample resistance normalized with the initial resistance of the deloaded sample) rarely falls exactly on 1 and is typically suppressed by a few percent. In order to measure the loading for the subsequent cycle, we re-normalize the resistance ratio. We expect slight deviations from the established loading-resistance relationships depending on the microstructure (grain size, defect density caused by cycling or annealing), however these effects have not been quantified.

While often a single loading value is taken to represent the entire sample, in practice we have frequently observed non-uniform loading within a sample. In samples with large cross-sectional area, the diffusion of hydrogen through the palladium lattice considerably slows down the loading and deloading kinetics. Depending on the current, in a >1 mm thick wire it can take more than an hour to achieve uniform loading throughout the cross-section. We have shown that thinner wires load faster than thicker wires. During the loading transient, surface-sensitive and bulk-sensitive methods are expected to yield different loading values.

Similarly, loading gradients along the length of the sample have been identified. This is most pronounced when the ends of the sample are occluded from electrolyte exposure, e. g., due to being mounted into a sample holder. The occluded surface means that this area is not available for Volmer reactions and hydrogen insertion. Hence, the underlying palladium can only load through diffusion from non-occluded parts of the sample. Accordingly, we have measured higher loadings in the center section of a sample compared to the entire sample, which included the occluded areas due to sample clamps. For this experiment, we have attached multiple sense leads (0.13 mm diameter Pt wire coated with PFA, A-M Systems) to various segments of the wire sample by laser welding.

## 3.12 X-ray Diffraction

X-ray diffraction (XRD) has been extensively used to study hydrogen absorption dynamics and structural changes in palladium [40, 168–172]. The advantages of using XRD-based strain measurements include high precision and the ability to provide detailed information about the crystallographic structure and internal stresses of thin films and low-mass samples. XRD is non-destructive and can be used in-situ to monitor real-time changes during hydrogen cycling. However, there are disadvantages as well. The methodology requires highly controlled conditions and sophisticated equipment, which can limit its accessibility. Despite these limitations, the benefits of XRD in providing detailed, accurate strain measurements make it very useful for estimating hydrogen loading of palladium hydride.

To estimate strain from X-ray diffraction, we must invoke Bragg's law:

$$n\lambda = 2d_{hkl}\sin\theta \tag{3.10}$$

where $n$ is the order of the reflection, $\lambda$ is the wavelength of the incident X-ray, $d$ is the spacing between crystal planes with Miller indices $hkl$, and $\theta$ is the angle of incidence. By measuring the shift in the diffraction peak positions ($\Delta\theta$) one can calculate the change in d-spacing ($\Delta d$), which directly relates to the strain in the material.

Palladium is typically a polycrystalline material, and so is palladium hydride. With the insertion of hydrogen on the interstitial octahedral sites during loading (gas or electrochemical), the palladium host lattice expands. Due to the inverse relationship between the reciprocal space, represented by the X-ray diffraction pattern, and the real space, the diffraction peaks shift to smaller diffraction angles as the lattice

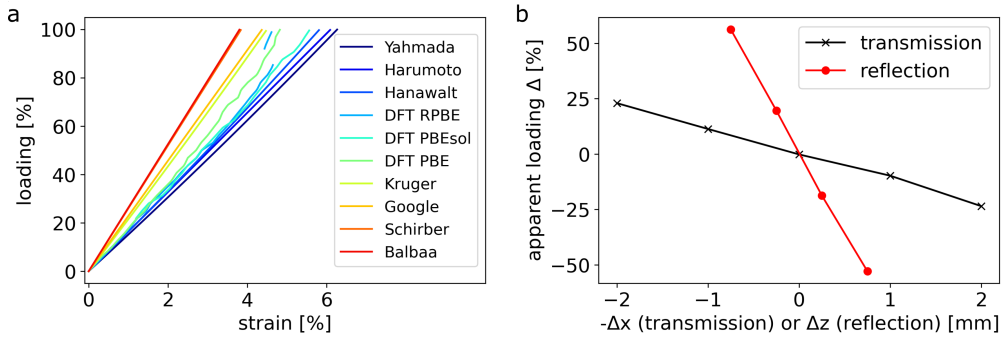



Fig. 3.2: a) Strain-loading relationships reported in the literature by Yahmada [173,174], Harumoto [175,176], Hanawalt [173,177], Kruger [178], Google [179], Schirber [173,180], Balbaa [181] and computed using DFT [182]. b) Effect of sample misalignment due to buckling (in transmission of reflection geometry) on change in apparent loading, resulting from apparent strain from XRD peak shift.

expands during hydrogen loading. Thus, from the shifts in X-ray diffraction peaks (e.g., (111) or (200) peaks), the lattice strain can be computed and hence the degree of loading can be derived qualitatively. The precise relationship between the lattice strain and hydrogen loading however is not known a priori. Various relationships can be found in the literature, sometimes with rather poor agreement (Fig. 3.2 a). This makes XRD an indirect loading measurement method. On the other hand, while the precise relationship between lattice strain and loading is not known, theory and experiments suggest that the relationship is monotonous, i. e., the higher the strain, the higher the loading. Hence, XRD is a useful method to rank the loadings of various palladium hydride samples, e. g. as a function of electrochemical current, loading enhancer or sample preparation.

In order to avoid outgasing of the sample during handling, we designed and built an in-situ XRD apparatus, acquiring diffractograms of palladium hydride while the sample was in electrolyte and electrochemical bias was applied. While these types of in-situ experiments are typically performed at synchrotron X-ray sources, we resorted to a rotating anode laboratory source with molybdenum as anode material. Compared to the more commonly used copper anode, the shorter wavelength of the Mo K $\alpha$ spectral line (0.71 Åvs. 1.54 Å) results in a much longer attenuation length in water (1 cm vs. 1 mm). For the X-ray to interact with the sample, two geometries are common: reflection and transmission (Fig. 3.3). In the reflection geometry, the X-ray hits the sample at an incident angle, which is typically chosen to be the same as the diffraction angle in order to maximize signal (and minimize absorption by electrolyte). This geometry probes the top tens of µm of the sample. The advantage is that wires, foils as well as films can be probed. The downside is that the thickness of the electrolyte layer on top of the sample must be kept to a minimum in order to avoid excessive X-ray attenuation due to the long path length at the incident angle (~9° for (111) peak). Too thin of an electrolyte layer makes it difficult to obtain a uniform electric field around the working electrode and hydrogen bubbles on top of the electrode extending through the electrolyte layer might present an unfavorable deload pathway. In practice, the main difficulty with reflection geometry was that buckling of the sample (palladium foil or wire) during loading led to major diffraction peak shifts, despite keeping the sample under slight tension with a spring mechanism. A theoretical comparison of the effect of sample misalignment (due to buckling) on XRD peak position is shown in Fig. 3.2 b). We considered accounting for the peak shift using crystalline reference materials on the surface of the palladium sample, but determined

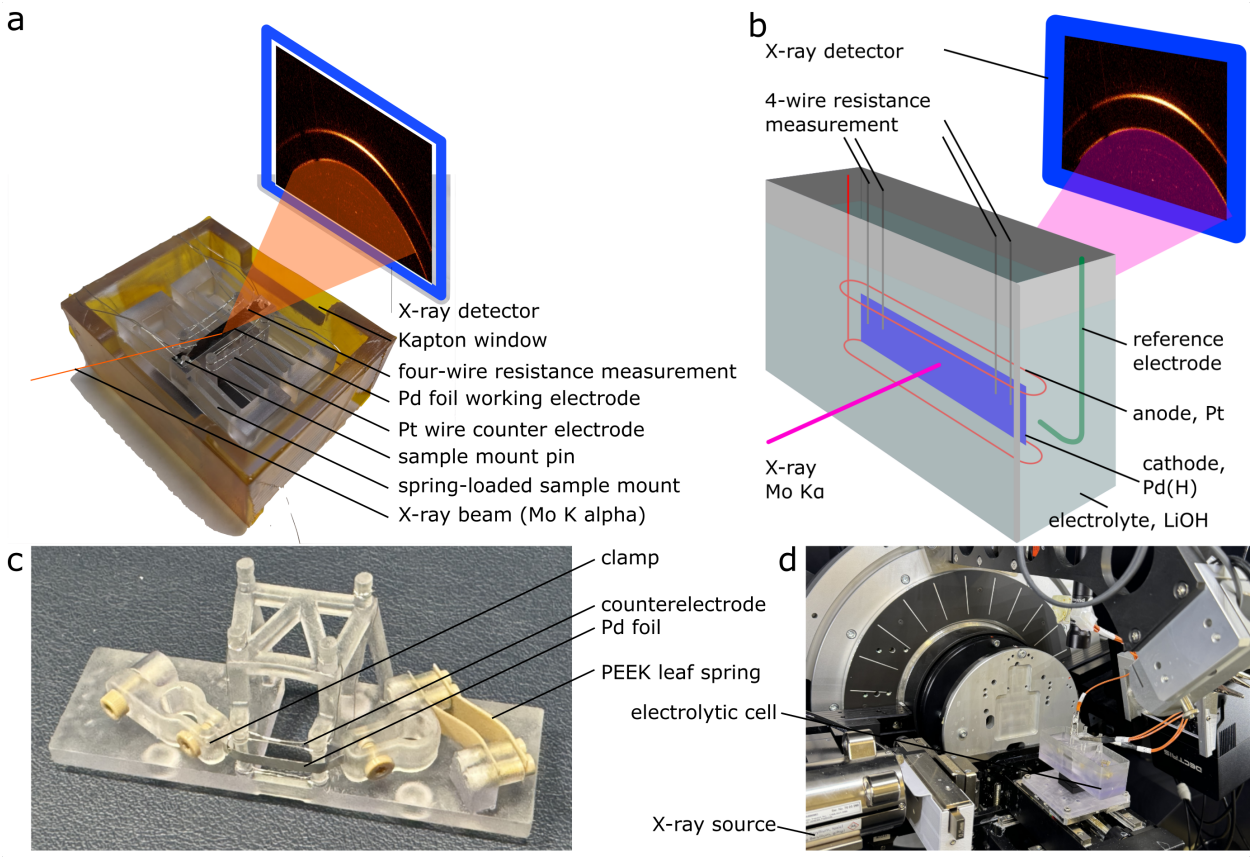



Fig. 3.3: Devices for in-situ XRD during electrochemical loading: a) Schematic of reflection geometry setup; b) Schematic of transmission geometry setup; c) Photograph of transmission geometry setup without vessel; d) Photograph of transmission geometry setup in X-ray diffractometer

that this would alter the loading.

For that reason, we abandoned the reflection geometry and implemented an in-situ vessel with transmission geometry. This geometry limits the choice of samples to foils, typically 50 µm thin, 30 mm long and 3 mm wide. The sample is held under slight tension by PEEK leaf springs, keeping buckling to a minimum (Fig. 3.3). A sophisticated mechanism avoids overconstraining the foil, thus elimating out-of-plane displacement, keeping the sample-to-detector distance constant. During the in-situ XRD experiment, electrochemical voltage (using a NI PXIe-4138) is applied between the palladium foil and a platinum counterelectrode, made from 0.5 mm wire, at an electrode spacing of 4 mm, submerged in 0.5 M LiOH aqueous electrolyte. The resistance of the palladium foil is measured using a four-wire measurement in the same manner as in the HTcal (i. e., employing a square wave on a precision source measure unit (NI PXIe-4141), see section 2.9.1). The experiments were performed on a Bruker D8 Discover. XRD exposure times were typically 200 s, with about 30 s of dead time between exposures. Data analysis was performed in the Bruker Diffrac.Eva software and Python. An example XRD experiment is illustrated in Fig. 3.4. It shows the transition from the $\alpha$

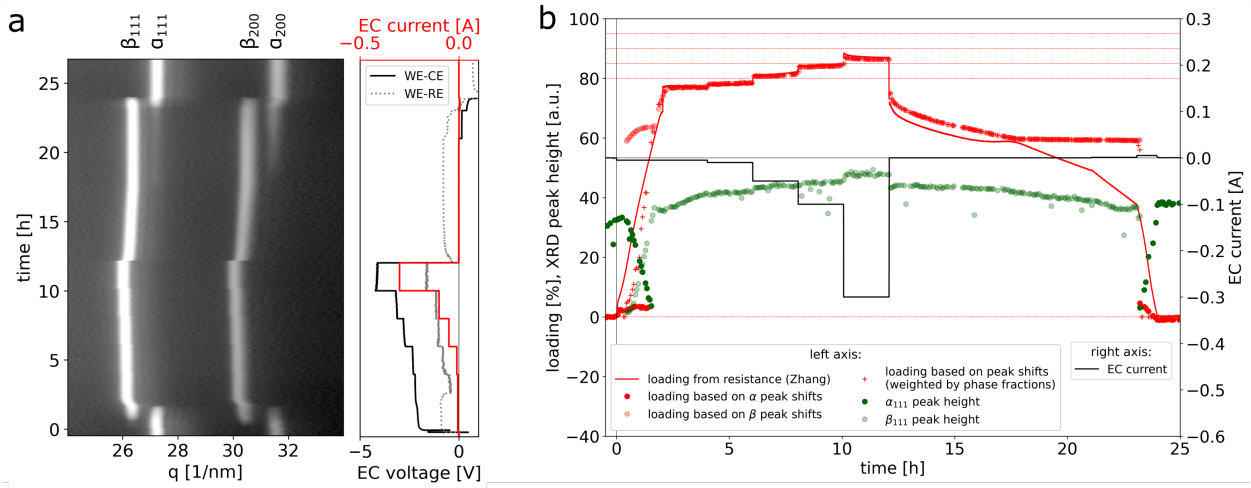



Fig. 3.4: Example of XRD results: a) Waterfall plot (time vs. scattering vector magnitude q) from an in-situ load-deload experiment, assembled from 2D diffractograms. The brightness represents the scattering intensity. The right panel shows the loading conditions (current and voltage). b) Derived quantities (lattice strain, loading from peak shift using DFTsol conversion, loading from resistance ratio using Zhang conversion) from the same experiment.

phase (which barely loads) to the $\beta$ phase, which starts highly loaded and increases in loading as well as in phase fraction as the loading progresses. Upon cessation of electrochemical bias (~12 h), the lattice contracts and, as the bias is reversed, transitions back to the $\alpha$ phase, with some transient co-existence of $\alpha$ and $\beta$ phases.

## 3.13 Orphaned Oxygen

Among other methods, the partial loading of deuterium (D) and hydrogen (H) into the palladium (Pd) lattice was calculated by measuring the orphaned oxygen in the headspace of the thermodynamically closed calorimeter. The intercalation of hydrogen into the palladium lattice leads to a non-stoichiometric mixture of oxyhydrogen gas and assuming perfect recombination, the pressure increase upon application of electrolytic current can be used to estimate the hydrogen locked into the Pd lattice. If the headspace volume and the Pd mass are well defined, the moles of orphaned oxygen can be related to the H and D loading using the equation below. This oxygen remains "orphaned" until the sample is deloaded and the hydrogen is made available to recombine with the oxygen.

$$n_{\mathrm{O}_2} = \frac{V_{\mathrm{Pd}} \rho_{\mathrm{Pd}} x}{4 M_{\mathrm{Pd}}} \tag{3.11}$$

Eq. 3.11 describes how orphaned oxygen can be calculated based on the volume, density, and loading fraction $x$ of the Pd cathode where $n_{O_2}$ are moles of orphaned oxygen, $V_{\mathrm{Pd}}$ is the volume of the Pd cathode, $\rho_{\mathrm{Pd}}$ is the density of Pd, $M_{\mathrm{Pd}}$ is the molar mass of Pd. Once the expected moles of orphaned oxygen are calculated the pressure exerted by the newly produced gas in the head space can be calculated . For example, a 70 mg

Pd wire, in a 60 ml headspace, at 90% H loading, and 30°C yields about 0.289 mmol of $n_{O_2}$. Using the ideal gas law, the pressure exerted by these moles of oxygen in our 60 ml headspace can be calculated to be 0.120 atm (1.76 psi) of oxygen gas in the headspace.

Of course, this process can be reversed to estimate loading percentages of the Pd cathode, in addition to or in the absence of resistance measurements. In our experiments, this lack of reliable resistance measurement usually occurs in Pd and Pd alloy samples with low aspect ratio as it is challenging to measure resistances less than a milliohm accurately. Pressure increases from orphaned oxygen can be converted to moles of $n_{O_2}$ and plugged into a rearranged version of Equation 3.11 to solve for $x$. While this is a viable method to approximate loadings in the absence of resistance measurements, the accuracy of the loadings determined by orphaned oxygen calculations can vary between 10 to 20 % from actual loadings when compared to control experiments using four-point resistance measurements. Ultimately, we found that not all observed pressure increases were due to orphaned oxygen. Many times, when the loading could be considered stable, the pressure would fluctuate due to variations in recombination reaction rates. In a few cases, we observed pressure buildup due to inactive recombiners, which sometimes was relieved by abrupt recombination (detonation of oxyhydrogen), resulting in a heat flow spike.

While we've discussed the value of using orphaned oxygen to calculate loading in the absence of electrical resistance data, assumptions regarding our system's Faradaic and recombiner efficiency are made. Firstly, we assume near 100% faradaic efficiency in our system, meaning that all our applied current goes to electrolysis, and we use that assumption to calculate our expected gas production. Of course, this assumption does not always hold true in an aqueous electrochemical environment with metal components despite our best efforts to mitigate side reactions. Secondly, we assume our activated carbon-Pt recombiner packets operate at a constant 100% efficiency, preventing the build up of gases from electrolysis in the headspace. Recombiner efficiency is not always 100% as we have observed large pressure increases after loading equilibrates suggesting that gases produced outside of loading are not being recombined. Given these conditions, without a dedicated mass spectrometer (MS) it is difficult to reliably deconvolute the two gas streams produced from electrolysis and orphaned oxygen from loading.

Another consideration when using orphaned oxygen to calculate H loading is the need for a well-defined system boundary with reliable pressure sensors. Without a sealed vessel, orphaned oxygen would leak from the vessel and there would be no way to accurately measure the production of gas. Simultaneously, it is also necessary to create a fail-safe against over pressurization of the vessel which can lead to dangerous failure of the hardware. In our systems we use back-pressure lines connected to a valve that acts as a pressure relief valve to prevent over pressurization. While in closed systems unintentional leaks must be avoided for accurate measurement, measuring gaseous products in a semi-open system using mass flow meters is a viable and well-established strategy in the field of HER and $CO_2$ reduction ($CO_2$ R) [183]. Whether in a fully sealed system using pressure sensors or in a semi-open system with mass flow meters, sensitive and robust hardware are necessary to measure deviations from expected gas production from electrolysis.

As a final note, non-faradaic and unintended faradaic reactions must be considered when using orphaned oxygen as a proxy for loading. Non-faradaic processes leading to other gases being produced could also lead to erroneous measurements in the amount of orphaned oxygen in the head space as other gaseous products can be produced. An example of this would be using additives such as ammonia to enhance loadings, where unintended faradaic electrochemical processes (i.e. electrolysis of ammonia at the cathode) produce nitrogen, hydrogen, and some gaseous ammonia which can severely skew the orphaned oxygen pressure contributions. To avoid this, careful attention to experimental design, specifically the system's composition and reactions pathways, is essential. One way to avoid this is doing proper control experiments and measuring electrolyte change and measuring headspace composition of the gaseous product with gas chromatography.

## 3.14 Thin Film Reflectance

### 3.14.1 Theory

The intercalation of hydrogen into palladium and other metals significantly alters their optical properties due to changes in their electronic structure. When hydrogen atoms are absorbed into a metal lattice, they introduce additional electrons, modifying the electronic density of states near the Fermi level. This process leads to a narrowing of the d-band and an increase in s-p hybridization, impacting both interband and intraband transitions. Interband transitions occur when electrons are excited from the valence band to the conduction band, contributing significantly to the absorption spectrum. Intraband transitions, on the other hand, involve the excitation of lower energy electrons within the conduction band to higher energy states in the same band, affecting the material's reflectivity.

The electronic structure of a metal can be described by the density of states (DOS), $g(E)$, which represents the number of electronic states at each energy level that are available to be occupied by electrons. When hydrogen atoms intercalate into the palladium lattice, they introduce additional states and alter the existing ones. This can be modeled as:

$$g(E) = \sum_k \delta(E - E_k) \tag{3.12}$$

where $g(E)$ is the DOS at energy $E$, $E$ is the energy at which the DOS is being calculated, $E_k$ are the discrete energy levels of the electrons in the system with the index $k$ representing different quantum states, and $\delta$ is the Dirac delta function. This function is zero everywhere except at $E = E_k$, where it is infinite, and its integral over all space is equal to one. Essentially, it "picks out" the energy levels $E_k$ and contributes to $g(E)$ only at those specific energies. Therefore, equation (1) represents the sum of Dirac delta functions centered at each energy level $E_k$, ensuring that the DOS is non-zero only at the discrete energy levels $E_k$. In other words, it counts the number of states at each energy level.

The DOS plays a crucial role in determining the optical properties of a material, as it influences how electrons interact with photons. The connection between DOS and optical properties can be established through the material's dielectric function or permittivity $\epsilon(\omega)$, which governs the material's response to an external electromagnetic field. The dielectric function $\epsilon(\omega)$ is related to the electronic structure and the transitions between energy states in a material. The real part of the dielectric function $\epsilon_1(\omega)$ and the imaginary part $\epsilon_2(\omega)$ can be derived from the electronic band structure and the DOS. $\epsilon_1(\omega)$ represents the dispersive response of the material, indicating how the phase velocity of light is affected as it propagates through the material, while $\epsilon_2(\omega)$ represents the absorptive response, indicating how much energy from the light is absorbed by the material. The Kramers-Kronig relations express the fact that the real and imaginary parts of a complex function (like the dielectric function) are not independent but are related through integral transforms. These relations are derived from the principle of causality, which states that the response of a system to an external perturbation cannot precede the perturbation itself. This interdependence is characterized as [184]:

$$\epsilon_1(\omega) = 1 + \frac{1}{\pi} P \int_{-\infty}^{\infty} \frac{\epsilon_2(\omega')}{\omega - \omega'} \, d\omega' \tag{3.13}$$

$$\epsilon_2(\omega) = -\frac{1}{\pi} P \int_{-\infty}^{\infty} \frac{\epsilon_1(\omega') - 1}{\omega - \omega'} \, d\omega' \tag{3.14}$$

$$\epsilon(\omega) = \epsilon_1(\omega) - i\epsilon_2(\omega) \tag{3.15}$$

In palladium hydride, as the hydrogen content increases, the real part of the dielectric function $\epsilon_1(\omega)$ increases in the near-infrared range, while the imaginary part $\epsilon_2(\omega)$ decreases. This makes the material less metallic and more transparent. As a result, one can correlate the change in reflectivity to the fractional loading of hydrogen in the metal lattice. The reflectivity, $R$, of a material can be related to its permittivity function by:

$$R = \left| \frac{\sqrt{\epsilon(\omega)} - 1}{\sqrt{\epsilon(\omega)} + 1} \right|^2 \tag{3.16}$$

Metals other than palladium may undergo more or less dramatic changes to their optical properties. For example, magnesium, titanium, and certain rare earth metals undergo a more dramatic transformation from a highly lossy metal to an insulator upon full hydrogenation. On the other hand, zirconium shows relatively minor changes in its optical properties with hydrogen intercalation, with only the imaginary part of the dielectric function increasing, indicating a slight increase in absorption.

Given this first principles understanding of the optical response to hydrogen intercalation, Callisto set out to design a measurement apparatus that could be used to quantify the fractional loading of hydrogen in palladium, with the ultimate goal of using this apparatus to rapidly identify and optimize additive-based loading enhancers. Despite this fundamental understanding, to make this measurement work in practice, we needed to calibrate the method against another vetted loading measurement. In subsequent sections, we will highlight how we used both quartz crystal microbalances and x-ray diffraction to arrive at a quantitative mapping between reflectance and fractional hydrogen loading. For the remainder of this section, we will highlight the hardware, the results of the calibrations (not the methods), and several case studies that were investigated using this calibrated reflectance method.

### 3.14.2 Reflectance Hardware

Callisto leveraged its engineering resources to design and implement custom reflectance-based loading measurements. Over the course of our investigations, we deployed several generations of reflectance hardware. The first generation of hardware used a supercontinuum laser with a wide range of wavelengths. The setup, shown in Fig. 3.5, involved splitting light from the laser with a beam splitter, directing one path to a spectrograph for analysis and the other to reflect off the sample. A detector measured the reflected light, allowing us to probe how reflectivity across the visible and near-IR spectrum changes with loading. An example of the hardware setup used for these measurements is shown in Fig. 3.6, and includes fiber controls and electronics, an active stabilization system with a 6-axis stage, and a MEMS mirror for fine adjustments. The fiber optics system ensures precise delivery and collection of light, while the active MEMS stabilization maintains alignment and minimizes vibrations, crucial for accurate measurements with minimal drift.

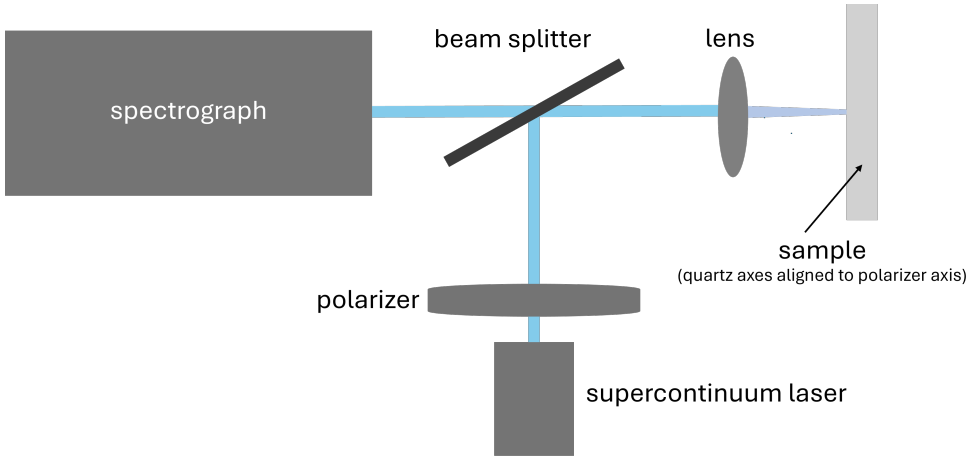



Fig. 3.5: Schematic of first generation reflectance hardware setup using supercontinuum laser.

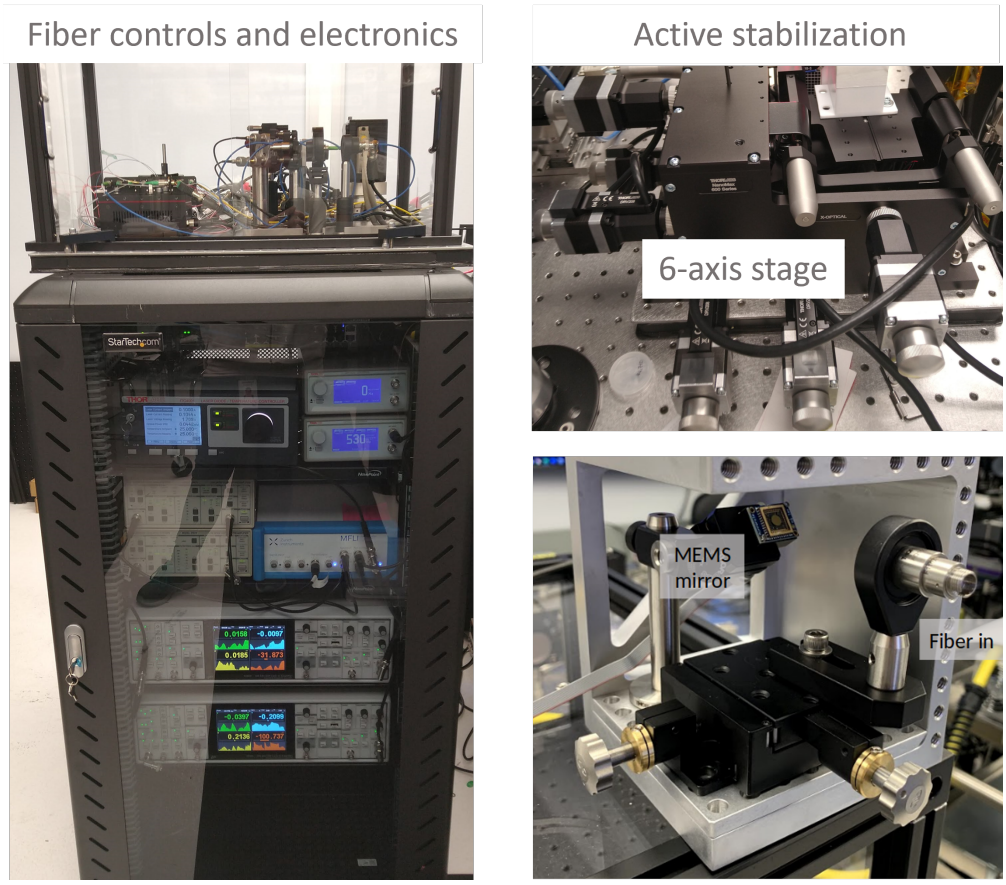



Fig. 3.6: Reflectance hardware.

We used this first-generation apparatus to probe how reflectivity across the visible and near-IR would change with loading, the latter measured by quartz crystal microbalances. An illustrative example of how reflectivity in palladium hydride changes with increasing frequency shift in the QCM is shown in Fig. 3.7 a). Here, we observed the reflectivity decreases roughly monotonically with increasing frequency shift. Additionally, the use of different loading enhancers resulted in further decreases in reflectivity, shown in Figure 3.7 b). These results not only proved our ability to use reflectance to measure loading but also demonstrated that we could use optical methods to rank the performance of different loading enhancers.

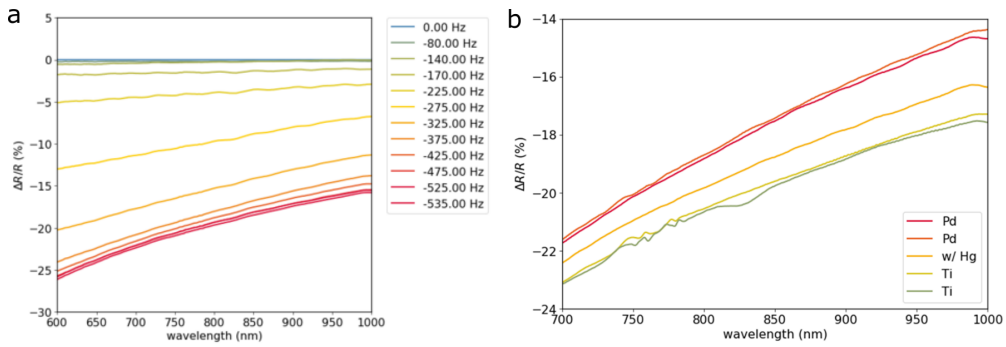



Fig. 3.7: a) Change in reflectance for palladium film as a function of frequency shift in QCM. b) Reflectivity measurements using the first-generation apparatus

With this proof-of-concept in hand, we simplified the measurement design by restricting the laser to a single wavelength. This change allowed us to miniaturize and decrease the cost of the apparatus, so that we could more readily replicate it into multiple setups. We also deployed several 785 nm and 1550 nm reflectance setups, the former showing strong monotonic and linear response to increases in fractional loading while the latter showed non-linear changes to reflectance as the fractional loading approached stoichiometry.

In another iteration of reflectance hardware shown in Figure 3.8, we developed a spatially resolved reflectance setup that allowed us to monitor changes to loading across an entire sample, as opposed to in a single point as in the first generations. This setup included a camera for capturing spatially resolved data, enabling us to observe any non-uniformity in loading that might occur from cell geometry, bubbling, or application of an electric field.

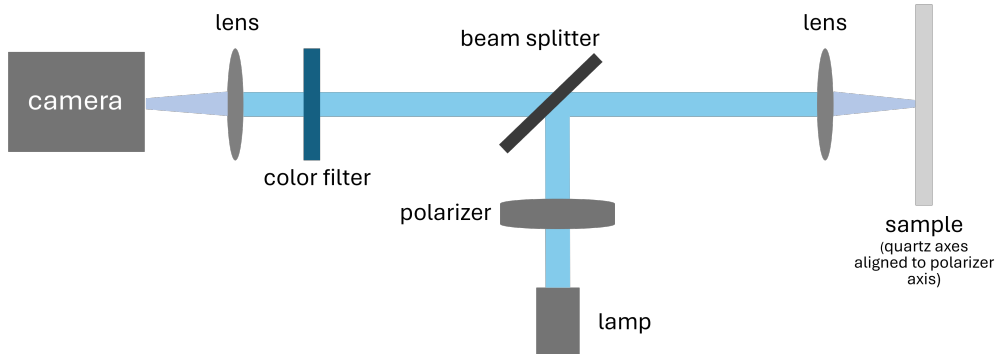



Fig. 3.8: Spatially resolved reflectance hardware setup.

Each of these generations was calibrated against x-ray diffraction measurements to obtain a quantitative mapping between reflectance and fractional hydrogen loading. It should be noted that Callisto's reflectance-based measurements probed the substrate-film interface as opposed to the film-electrolyte interface. Due to the complicating effects of evolving surface roughness with hydrogen cycling, the frontside interface resulted in inconsistent data. The backside interface, however, remained smooth throughout hydrogen cycling and therefore resulted in consistent data, with minimal sample-to-sample variation.

### 3.14.3 Calibrations

In order to perform calibrations, we implemented simultaneous backside reflectance and x-ray diffraction measurements. A cross-section of the electrolysis cell and its implementation in a diffractometer are shown in Figure 3.9. The cell was designed to retain 1 inch diameter thin film devices which comprised a sapphire substrate, a 5 nm titanium adhesion layer, and palladium thin films with thicknesses between 20 nm and 4000 nm. Two frontside contacts connect the device to a potentiostat, allowing us to pass current between the palladium film and a platinum counter electrode. A 0.5 M LiOH or LiOD solution was used as the electrolyte, and arsenic salt, typically AsCl3, was used to achieve nearly stoichiometric loadings.

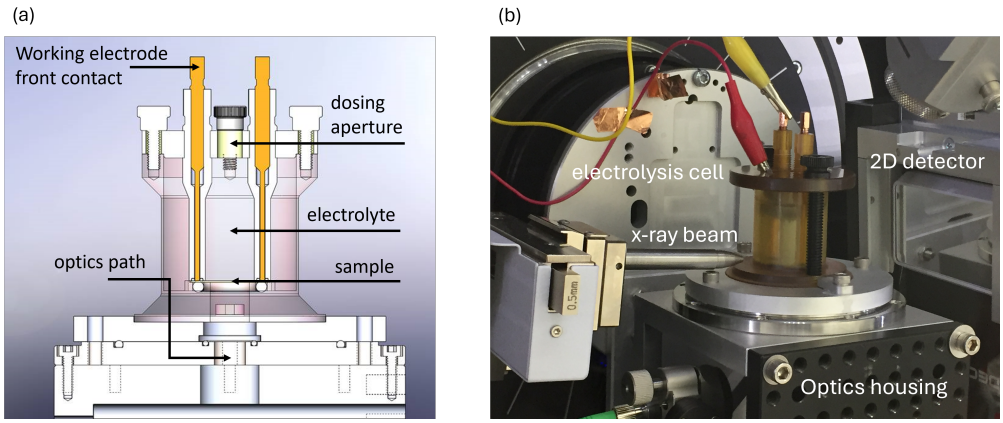



Fig. 3.9: a) Cross-section of the electrolysis cell; b) Implementation in a diffractometer

The x-ray diffraction setup is briefly described here. We used a Bragg-Brentano geometry with Mo K-alpha radiation, which has an energy near 17 keV. A collimated beam with an aperture of 0.5 mm was directed at the sample at an incident angle of 9.1° $2\theta$. A Dectris 500K two-dimensional detector was placed at 9.1° $2\theta$, opposite the beam. We calculated the total volumetric expansion of the thin film from hydrogen intercalating by analyzing both in-plane and out-of-plane diffraction peaks. The film expansion is constrained in-plane by bonding to the substrate, resulting in asymmetric expansion with lower-than-expected in-plane and greater-than-expected out-of-plane expansion. Ignoring this effect could lead to overestimating fractional loading by as much as 10%.

The results of these calibrations are shown in Figure 3.10, which depicts the mapping at both 785 nm and 1550 nm. The calibration for 785 nm demonstrates good linearity from 0 to nearly 100% PdH loading, regardless of isotope. In contrast, we observed a slight discrepancy between PdH and PdD for 1550 nm, although it was within the measurement scatter. We focused on calibrating loadings between 70% and 100% because of its relevance to our LENR research and the challenges in achieving low loadings with electrolytic methods. Using these calibrations, we were able to quickly and robustly probe the loading parameter space.

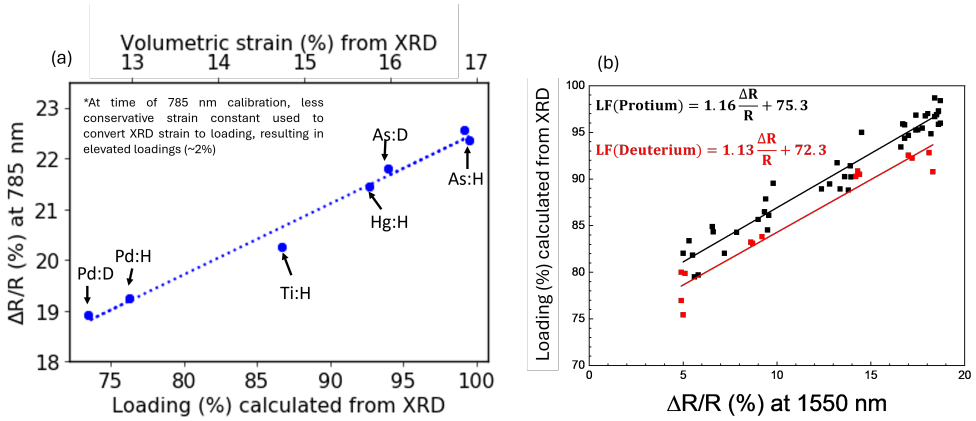



Fig. 3.10: Calibration results at 785 nm (a) and 1550 nm (b)

### 3.14.4 Some Example Case Studies

In this first case study, we looked at the effect of current density on chemically enhanced ($AsCl_3$ additive) loadings, with the results shown in Figure 3.11. In this example, we see that there are diminishing returns for applying current densities greater than 20 $mA/cm^2$. Conversely, decreasing the current density below 20 $mA/cm^2$ resulted in a dramatic decrease in loadings. Interestingly, the ideal current density for thin films is not the same as for bulk cathodes, which we found to be around 120 $mA/cm^2$. Although there is no strong fundamental reason for this discrepancy between nanoscale and bulk current densities, it is nonetheless important to characterize. If we were to speculate, it may be related to the combined effect of high surface-to-volume ratio and high grain boundary density in thin film cathodes compared to bulk. Essentially, diffusion of protium from the surface into the lattice is much more efficient in the thin film system, requiring a much smaller driving force to intercalate a similar amount of hydrogen.

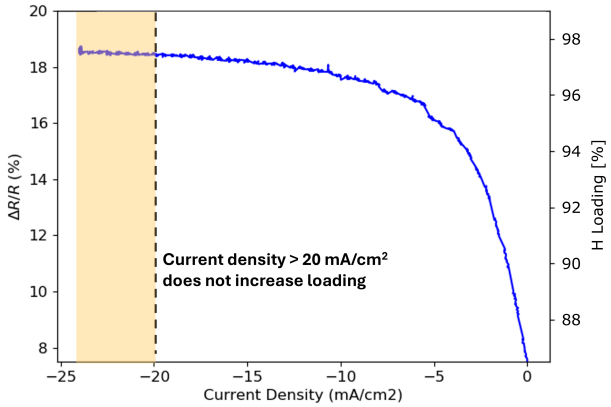



Fig. 3.11: Effect of current density on chemically enhanced (0.5 mM $AsCl_3$ additive) loadings.

In a second case study, we looked at how different parameters might impact the longevity of chemically

enhanced (0.5 mM $AsCl_3$ additive) loadings. In Figure 3.12, we examine the effects of current density, film thickness, and electrode spacing. We observed that higher current densities were better for longevity, while performance was largely unimpacted by film thickness and electrode spacing. Because of the facile setup of the measurement and implementation of the loading protocol, we were able to rapidly move through this parameter space.

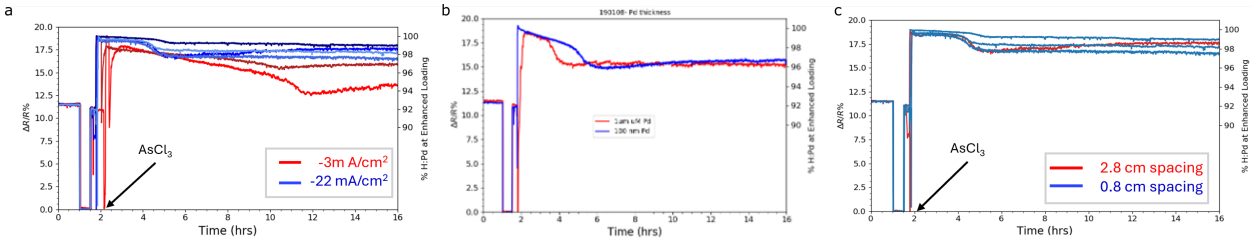



Fig. 3.12: Effects of current density (a), film thickness (b), and electrode spacing (c) on loading longevity.

In a third example, we used the spatially resolved reflectance apparatus to look at the effect of bubbling on thin film cathodes. In Figure 3.13, we observe lower loadings in areas where bubble attachment was prevalent. While it may be intuitive to expect that bubbling is detrimental to loading, we were able to provide direct evidence. When a bubble forms, there is no longer an electrochemical driving force to split water, resulting in the Tafel reaction dominating the reaction landscape. The loss of loading through gaseous recombination lowers the loading both locally and globally. One avenue explored by our companion high-pressure research team was to increase the system pressure, one of the effects being the suppression of bubbles and therefore the suppression of gaseous recombination. A separately submitted report covers this in more detail.

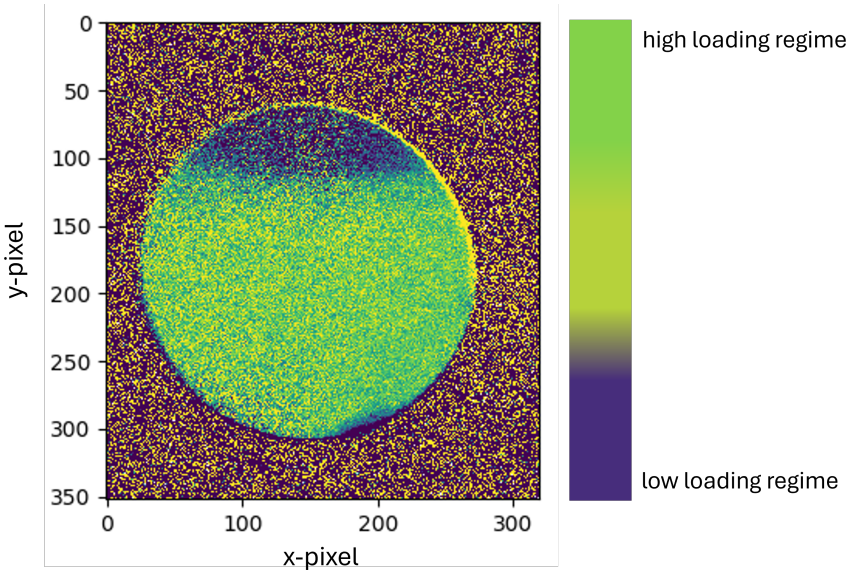



Fig. 3.13: Effect of bubbling on thin film cathodes. The circular thin film Pd cathode was oriented vertically, resulting in bubble accumulation at the top portion of the circle.

In a final case study presented in this report, we used our reflectance-based loading measurement to replicate chemical enhancement observed by another research organization, Coolescence [185]. This study is highlighted in Figure 3.14. In their study, Coolescence used both bismuth and combinations of bismuth and platinum to enhance the hydrogen loading in palladium cathodes. They estimated loadings using coulometry, which has its limitations at high loadings. In our replications, we applied their protocol for chemical enhancement while monitoring the loading via reflectance. One advantage of our methodology is the time-resolved nature of the data stream, whereas coulometry is best used for steady-state estimates. In addition to replicating Coolescence's loadings, we were able to show similar surface compositions following the experiment using energy-dispersive spectroscopy, overviewed in Fig. 3.15. Note that our replication study looked at using their chemistries in palladium deuteride thin films, as opposed to palladium hydride thin films which was the topic of the original study. As such and as expected from isotopic differences, we achieved slightly lower fractional loadings. Despite the admirable performance of their chemistries, our own chemical enhancement strategies proved to be more effective.

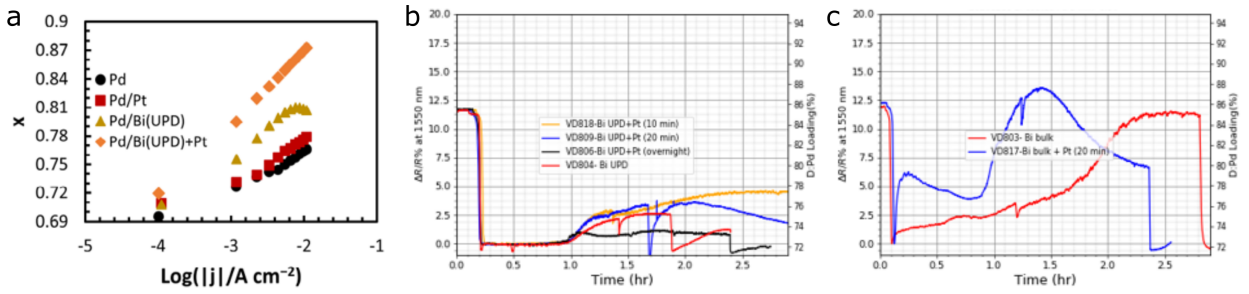



Fig. 3.14: a) $x$ vs. $\log(|j|)$ reproduced from Coolescence [186]; b) Change in reflectance for replicated underpotential deposition; c) Replication of chemical enhancement observed by Coolescence

| | Atomic % | | | | | |
|---|---|---|---|---|---|---|
| | **Pre/Post Loading** | **Pd** | **Pt** | **Bi** | **Pt/Bi** | **Peak Loading** |
| **VD806** | Pre | 98.6 | 0.4 | 1.0 | 0.4 | 74% |
| | Post | 98.5 | 0.5 | 1.0 | 0.5 | |
| **VD809** | Pre | 99.2 | 0.1 | 0.7 | 0.14 | 77% |
| | Post | 98.7 | 0.2 | 1.1 | 0.18 | |
| **VD818** | Pre | 98.8 | 0.3 | 0.9 | 0.33 | 78% |
| | Post | 98.8 | 0.2 | 1.0 | 0.2 | |
| **Coolescence** | | | | | **Pt/Bi** | **Peak Loading** |
| **Pd\|Bi(UPD)** | | | | 1.8 | | 80% |
| **Pd\|Bi(UPD)+Pt** | | | | | 0.13 | 87% |

Fig. 3.15: Surface compositions following Coolescence protocol for chemical enhancement. Coolescence data is from [186]. VD806: Underpotential deposition (UPD) of Bi and Pt (overnight); VD809: UPD of Bi and Pt (20 min); VD818: UPD of Bi and Pt (10 min)

### 3.14.5 Ranking of Different Additives for Chemically Enhancing Hydrogen Loading

The primary objective for developing the reflectance-based loading measurement was to deploy a high throughput measurement system for ranking different chemical additives and their impact on deuterium loadings in thin film palladium. The idea was that thin films loaded much more rapidly than bulk cathodes, allowing us to proceed through the parameter space much more quickly than using bulk cathodes, which

would take hours to reach steady-state.

In Figure 3.16, we present the most interesting additives that were investigated using our reflectance-based methods. The figure shows the deuterium loading percentage in palladium thin films when different promoters were used. The data points are represented by different symbols to indicate the electrolyte used: blue squares for $^{6}$LiOD, blue circles for $^{7}$LiOD, and red diamonds for $D_2SO_4$. The x-axis lists the various promoters, while the y-axis shows the D/Pd loading percentage.

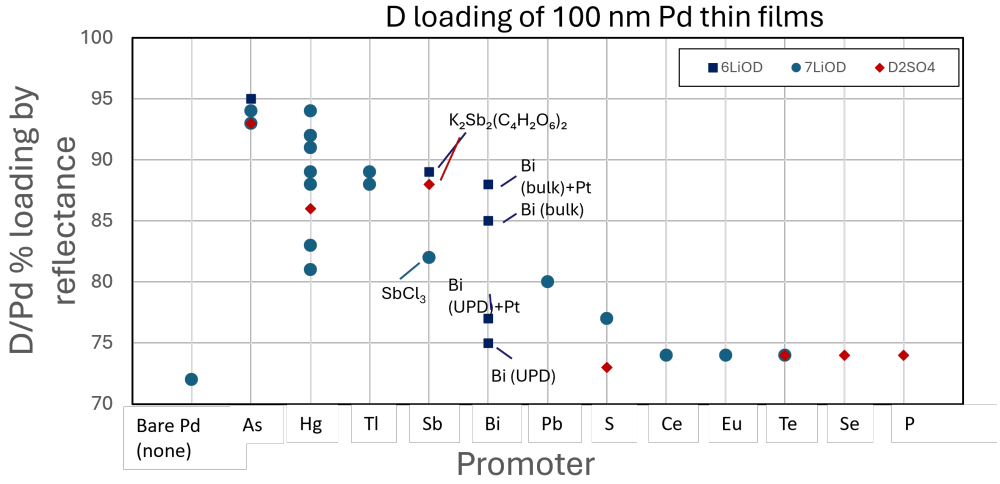



Fig. 3.16: Ranking of different additives for chemically enhancing deuterium loading in palladium thin films.

From the figure, we can observe that arsenic salts yielded the best performance, followed by mercury, thallium, antimony, and bismuth. Of note, the best results with mercury were comparable to arsenic, however, the spread in performance was much more significant. Some additives, such as sulfur, cerium, europium, tellurium, selenium, and phosphorus, did not significantly enhance loading. This comprehensive study allowed us to identify the most effective chemical additives for enhancing deuterium loading in palladium thin films.

Based on these findings, Callisto decided to focus on optimizing arsenic chemistries for both thin film and bulk cathodes to maximize deuterium loadings in our LENR experiments. Many of these additives' performances were corroborated by XRD measurements and QCM measurements, discussed in other sections, providing a robust validation of our reflectance-based ranking system.

## 3.15 Isotopic Effects

Given the nature of Callisto's research, we were concerned with characterizing the fractional hydrogen loading of both protonated and deuterated palladium lattices. From a first principles perspective, there are fundamental reasons why the driving forces for protium and deuterium uptake are different under identical conditions. The thermodynamic and kinetic requirements for the catalytic dissociation of deuterium gas or electrocatalytic heavy water splitting are greater than for hydrogen gas and light water. As a result, there are higher proton loadings for the same driving forces, as well as selective uptake of protium over deuterium in a mixed environment. Despite a fundamental understanding that palladium protide and palladium deuteride

should have different fractional loadings when everything else is controlled, the exact differences must still be determined empirically.

Regarding direct loading measurements, the isotopic effect is self-evident. For gravimetric analysis, while the molar mass of the isotopes is different, the analysis remains largely the same. The Sievert method's analysis is generally unaffected by isotope, except under ultrahigh pressures (> 1 kbar) where gas behavior deviates from ideality; this condition, however, is beyond the scope of this discussion.

For certain indirect loading measurements, the isotope impact is more pronounced. For example, Zhang et al. provided an empirical mapping between electrical resistance and fractional loading for palladium deuteride, which varied substantially from palladium hydride. This variation is attributed to differences in electron scattering mechanisms, where deuterium causes approximately twice the electron scattering effect compared to hydrogen, significantly affecting electrical resistivity. During our exploration of optical measurements, we determined that there were pronounced isotopic differences in the near-IR spectrum, but less so in the visible spectrum. These findings align with other studies, indicating that the isotopic mass affects the optical phonon excitations differently, leading to variations in the elastic constants and other material properties of PdH, PdD, and PdT [63].

Another critical observation is that protium is preferentially absorbed over deuterium in mixed light and heavy water electrolytes (Fig. 3.17). When adding increasing concentrations of light water to heavy water electrolyte in subsequent load-deload cycles, the loading $x$ as measured by QCM goes down. In isotopically pure LiOD in $D_2O$, $x = 73\,\%$. In isotopically pure LiOH in $H_2O$, $x = 78\,\%$. Assuming the total loading varies linearly between 73 % and 78 % with isotopic composition of the electrolyte, the isotopic composition of the hydrogen loaded into the palladium can be computed from the relative mass increase per palladium atom as measured by QCM, $\frac{m_H+m_D}{n_{Pd}}$:

$$\frac{a}{a+b} = 2 - \frac{1}{0.73 + 0.05 f_H} \frac{m_H + m_D}{n_{Pd}}, \tag{3.17}$$

where $\frac{a}{a+b}$ is the fraction of protium in mixed isotope palladium hydride ($PdH_aD_b$) and $f_H = \frac{V_{H_2O}}{V_{H_2O}+V_{D_2O}}$ is the protium fraction in the mixed isotope electrolyte. The analysis shows that at 3 % protium content in the electrolyte, almost 40 % of the occupied sites are loaded with protium (Fig. 3.17b). Given that the loading is determined by the kinetic balance of various reactions (see chapter 4) and given that protium reaction kinetics are typically faster than deuterium reaction kinetics [187], the observation of a preferential uptake of protium is not surprising.

One notable consequence of this observation of isotopic poisoning is the need to start with and maintain high isotopic purity in any electrolyte used for LENR experiments. Atmospheric light water can readily contaminate an open-cell experiment, poisoning the heavy water electrolyte at rates up to 1 % a day initially. LENR in electrolytic cells was believed by Fleischmann and Pons to be exclusive to PdD, so the presence of PdH may prevent the reaction from initiating (although we admit this is speculation).

These observations underscore the importance of one of Callisto's major efforts: to robustly characterize the difference in isotopic loading behavior under different conditions.

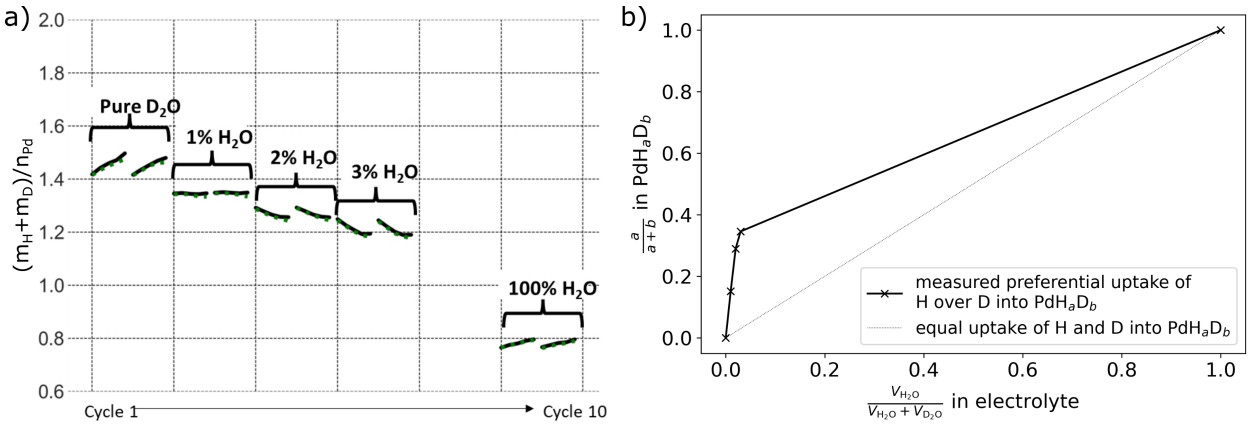



Fig. 3.17: Preferential loading of protium from mixed isotope electrolyte (LiOH in $H_2O$ / LiOD in $D_2O$). a) QCM measurements showing the decrease in relative mass $\frac{m_H+m_D}{n_{Pd}}$ as light water is added before every other load-deload cycle. b) Fraction of protium in mixed isotope palladium hydride ($\frac{a}{a+b}$ in $PdH_aD_b$) as function of the protium fraction in the mixed isotope electrolyte, $\frac{V_{H_2O}}{V_{H_2O}+V_{D_2O}}$, acc. to Eq. 3.17.

# Chapter 4

# DFT

## 4.1 Introduction

As discussed in section 1.4, the majority of reports in the LENR field agree that high hydrogen loadings are either required or at least beneficial to observe excess heat. Several researchers reported superstoichiometric palladium hydrides ($PdH_x$ with $x > 1$) [188, 189], however the experimental evidence of these is weak. While the mechanism of gas loading is rather simple and the major parameter to increase loading is increased pressure, the situation is more complicated with electrochemical loading. Several surface and bulk reactions must come together to result in hydrogen loading. To get a more quantitative understanding of these reactions and to inform our search for loading enhancers, we carried out DFT calculations.

## 4.2 Methods and Materials

In this section, we outline the methods used to probe electrochemical hydrogen loading in palladium and its compounds, in addition to synthesis and characterization protocols. Further details related to computational methods, particularly related to modeling of electrochemical processes in DFT, can be found in the Supporting Information (SI). The computational methods are briefly summarized in Scheme 4.1, where circles represent outcomes that are compared to experiment where possible.

### 4.2.1 Computational Methods

#### 4.2.1.1 Density functional theory

Simulations utilized density functional theory (DFT) at the generalized gradient approximation (GGA) to probe energetics of relevant (electro)chemical reactions and bulk crystal optimizations. Surface reaction energetics (e.g., HER sub-reactions) were probed using the revised Perdew-Burke-Ernzerhof (RPBE) [190] exchange-correlation functional by Hammer and Nørskov. Bulk crystal energetics and dynamics were investigated using the PBEsol functional [191] which has been demonstrated here and in reported literature [192] to perform well in capturing bulk behavior. Given the significant difference in predicted lattice constant between RPBE and PBEsol, appropriate $PdH_x$ bulk crystals were re-optimized with RPBE to minimize surface strain when probing surface processes. The Vienna Ab initio Simulation Package (VASP) [193–195]

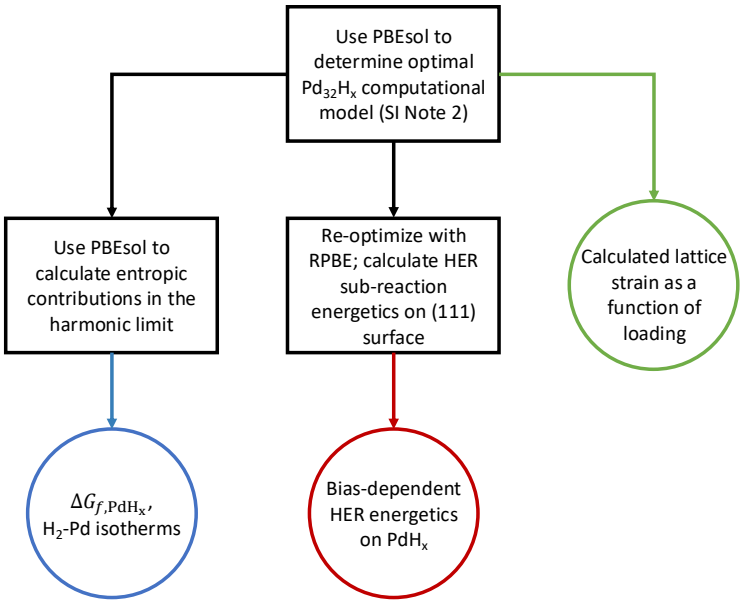



Fig. 4.1: Flowchart briefly illustrating computational methods described in more detail below and in greater detail in the SI. Here, circles represent outcomes that are compared to experiment where possible.

interfaced with the atomic simulation environment (ASE) [196] was used to perform all DFT calculations. For each atom in our simulations, core electrons were described using projector augmented wave (PAW) pseudopotentials, [197] while valence electrons were expanded as plane waves up to a kinetic energy cutoff of 500 eV. The Brillouin zone was sampled using a Monkhorst-Pack [198] k-point mesh, with the density depending on the system size. In general, the number of k-points multiplied by the magnitude of the unit cell vector in that dimension is approximately 30. For a 3×3×1 $PdH_x$(111) supercell, this corresponds to a 4×4×1 k-point mesh.

#### 4.2.1.2 Surface reactions and free energy corrections

Gibbs free energies were calculated for gas phase molecules (e.g., $H_2$, $H_2O$) by making an ideal gas approximation. For reactions involving surface-bound species, e.g. *H, atoms were treated as having only vibrational degrees of freedom, and with those vibrational degrees of freedom treated harmonically. As such, the Gibbs free energy of reaction was calculated as,

$$\Delta G = \Delta E_{\text{rxn}} + \Delta ZPE - T\Delta S \quad . \tag{4.1}$$

Here $\Delta E_{\text{rxn}}$ refers to the reaction energy determined by DFT total energies, $\Delta ZPE$ is the change in total zero point energy from initial to final state, and $T\Delta S$ is the entropic contribution to the Gibbs free energy. We neglect several possible entropic contributions, such as rotational and translational degrees of freedom, and anharmonic vibrational contributions. [199, 200] These approximations have been shown to be valid in the limit of small molecules on fairly strong binding surfaces. [201]

#### 4.2.1.3 Gibbs free energies of formation of $PdH_x$

Similar to the calculation of surface reactions and their free energy corrections, we calculated the Gibbs free energy of formation of $PdH_x$ ($\Delta G_{f,PdH_x}$) by determining the free energy of reaction of

$$\mathrm{Pd}(s) + \frac{x}{2}\mathrm{H_2}(g) \rightarrow \mathrm{PdH}_x(s) \quad . \tag{4.2}$$

Here, the entropic contributions of gas phase species (i. e., hydrogen gas) were determined in the ideal gas limit, taking into account translational, rotational, and vibrational degrees of freedom. Solid species (i. e., Pd and $PdH_x$) were determined in the harmonic limit using the CrystalThermo class implemented in the Atomic Simulation Environment. [196] Finite cell size effects were tested for smaller unit cells, with more details found in SI Note 5. For the $Pd_{32}$ supercell, finite-cell size effects in the phonon spectra calculation were found to be negligible, and so a supercell size of (1,1,1) was used. In addition to entropic contributions arising from vibrational degrees of freedom in the crystal, we also included configurational entropy contributions associated with degenerate (or nearly degenerate) configurations of H via the equation,

$$S_{\mathrm{conf}} = k_{\mathrm{B}} \ln\left(\frac{N!}{n!(N-n)!}\right) \quad . \tag{4.3}$$

Here, $k_{\mathrm{B}}$ is the Boltzmann constant, $N$ is the total number of available lattice positions (i. e., 32 for the $Pd_{32}$ supercell), and $n$ the number of H atoms in the supercell. We wish to highlight two caveats with this expression for the configurational entropy. First, this expression is a special case of Boltzmann's entropy formula, $S = k_{\mathrm{B}} \ln W$, for the case where the energy of each lattice position is identical. As we discuss below, generally this is not the case; H atoms seem to prefer maximal spatial homogeneity, disfavoring lattice positions close to another H atom except when no other sites are available. However, as we discuss further in the SI, the magnitude of the energetic penalty is relatively small, suggesting that this expression may be a reasonable approximation. Second, Equation 4.3 is valid only in the limiting case of large $N$. As a result, we compute $S_{\mathrm{conf}}$ using $N$=512, and $n = 16 * m$, where $m$ is the number of hydrogen atoms in the $Pd_{32}$ supercell. This correction is minor for the case of $Pd_{32}$, but the correction is significant for smaller supercells, e.g., Pd4 which has been previously reported. More details can be found in SI Note 6.

#### 4.2.1.4 Modeling charge transfer processes in the grand canonical ensemble

For reactions involving charge transfer (e.g., the Volmer reaction), electrons were treated grand canonically as we have described in previous works. [202–205] Briefly, electrons are modeled as following proton transfer adiabatically in a coupled proton-electron transfer (CPET) reaction. Fractional electrons from an external reservoir compensate for transferred charge across the reaction coordinate, with countercharge being placed by solving the linearized Poisson-Boltzmann equation as implemented in VASPsol. [206–208] In addition to continuum solvation with a bulk dielectric constant set to 78.4, charged states (i. e., hydronium) were solvated with two explicit water molecules. We calculate the grand canonical free energy $\Omega$ as

$$\Omega = E - q\Phi \quad , \tag{4.4}$$

where $E$ is the total energy from DFT, $q$ the net system charge, and $\Phi$ the work function of the electrode. We refer the reader to previous works where we describe corrections required to account for the nonzero bulk electrolyte, [204] which can cause significant finite cell-height effects if uncorrected.

The overall thermodynamics of CPET reactions were modeled using the computational hydrogen electrode (CHE), [209] while activation barriers were estimated using our previously described [205, 210] one dimensional constrained bond length scan. In this approach, the O-H bond length for the transferring proton was systematically stretched, and the geometry optimized at constant potential subject to the fixed bond length constraint. The end result is an excellent estimate of the (grand canonical) energy surface, with the peak along the path taken to be the energy of the transition state. Given ongoing challenges with modeling hydroxide via semi-local DFT, [202,211] we considered hydronium ($H_3O^+$) as the proton donor for any CPET reaction. Activation barriers for non-CPET reactions (e.g., Tafel) were modeled using a machine-learning accelerated nudged elastic band routine which trains a Gaussian Process Regression model on-the-fly. [212] For additional details, we refer the interested reader to SI Note 1.

## 4.3 Results and Discussion

### 4.3.1 Experimental measurement of lattice strain in $PdH_x$

The XRD setup is illustrated in Fig. 4.2A). Details are provided in section 3.12. Panels B and C of Figure 4.2 show the transition from the $\alpha$ phase (which experiences minimal lattice strain) to the $\beta$ phase, which starts highly loaded and increases in loading as well as in phase fraction as the loading progresses. Upon cessation of electrochemical bias (at 12 h), the lattice contracts and, as the bias is reversed, transitions back to the $\alpha$ phase, with some transient co-existence of $\alpha$ and $\beta$ phases. The strain is calculated from the peak shift relative to the peak position of the initial pristine palladium sample. Various relationships between strain and loading have been reported (Figure 4.3A), some of them with greatly varying slopes. If the PBEsol strain-loading relationship is chosen, the relationship between resistance ratio (resistance normalized with initial resistance of pristine palladium) is in agreement with the relationship reported by Zhang [167] (Figure 4.3B).

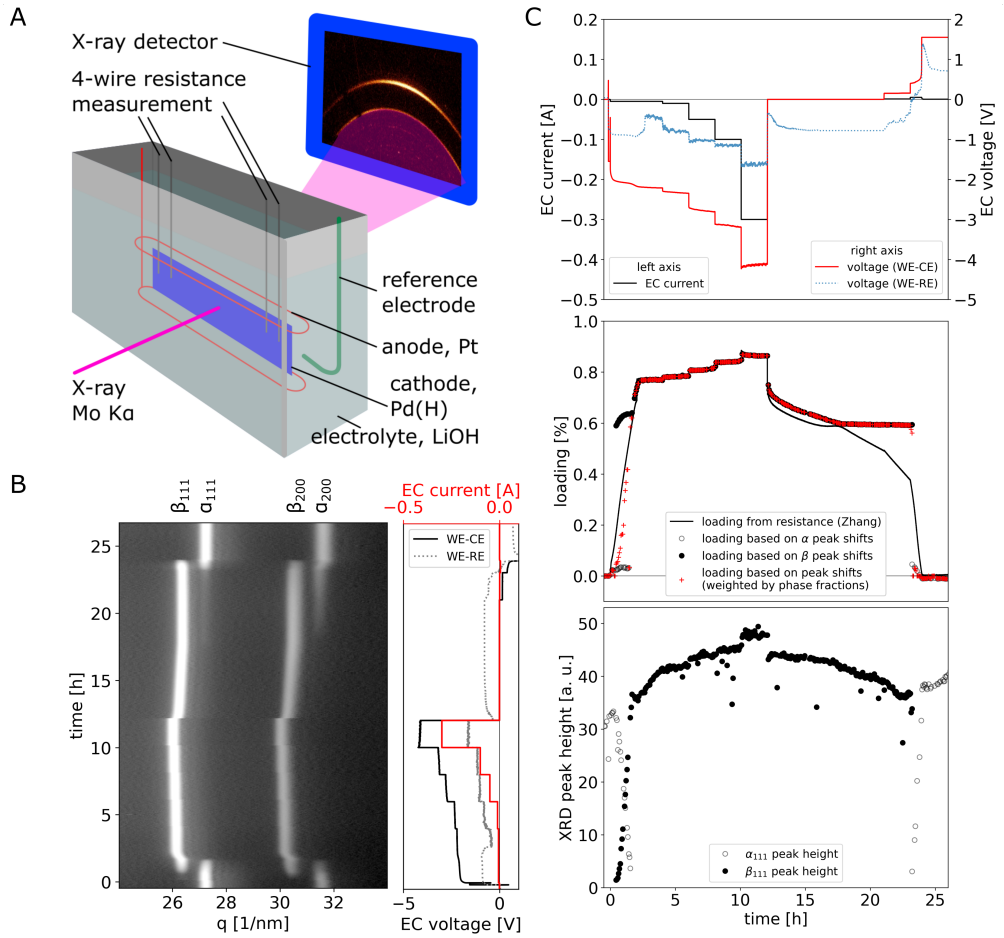



Fig. 4.2: XRD experiments to determine strain induced by hydrogen loading. (A) Schematic of the in-situ XRD electrochemical loading setup. (B) Waterfall plot obtained by stacking integrated XRD diffraction patterns of an in-situ loading experiment. Electrochemical current and voltage (between working electrode WE and counterelectrode CE as well as between working electrode WE and reference electrode RE) is plotted to the right. (C) EC current and voltage; loading obtained from the measured resistance ratio using the Zhang relationship (resistance ratio vs. loading), loading based on XRD strain using the PBEsol relationship (strain vs. loading); peak height of the $\alpha$ and $\beta$ 111 peaks.

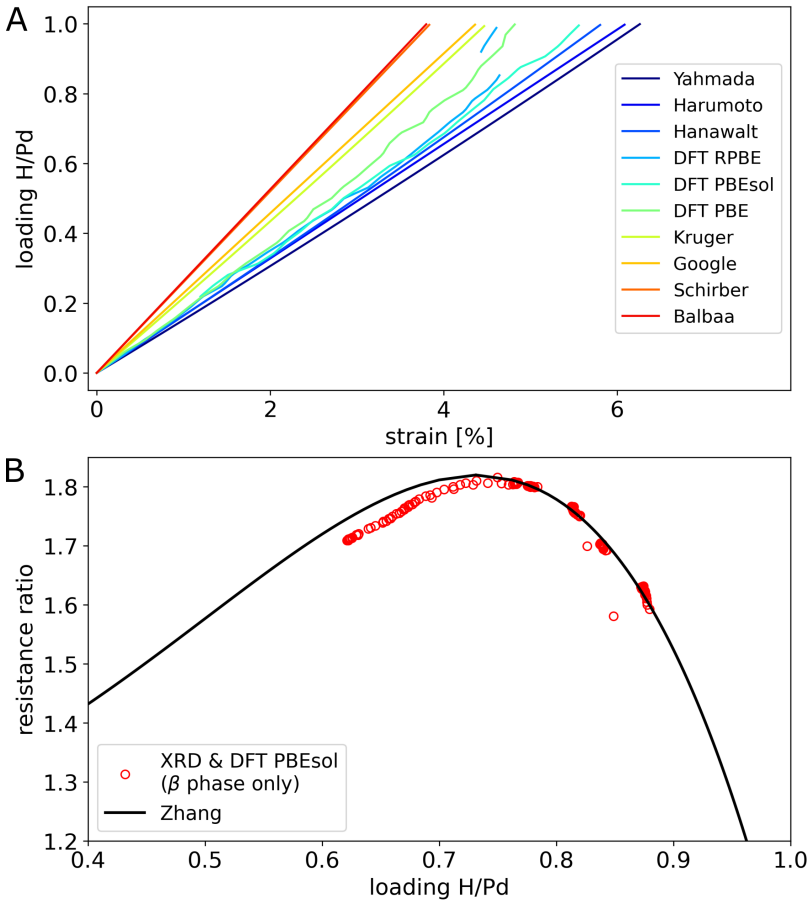



Fig. 4.3: (A) Strain-loading relationships reported in the literature by Yahmada [173, 174], Harumoto [175, 176], Hanawalt [173, 177], Kruger [178], Google [179], Schirber [173, 180], Balbaa [181]. (B) Resistance ratio vs. loading relationships. The black solid line is the curve reported by Zhang [167] and the red circles are from Figure 4.2C.

### 4.3.2 Development of a computational model of palladium hydride

To create a platform with which to probe hydrogen evolution reaction and intercalation energetics, we first generated a sequence of models for $PdH_x$, with $x$ varying between zero and one in 33 increments. Briefly, we began with a 32 Pd atom supercell of $Pd_{32}H_{32}$, i. e. palladium hydride at stoichiometric loading, and systematically determine the most energetically favorable configuration with one hydrogen removed. By symmetry, all configurations of $Pd_{32}H_{31}$ are degenerate. To determine the optimal geometry for $Pd_{32}H_{30}$, we take the optimized geometry for $Pd_{32}H_{31}$ and generate all possible structures for $Pd_{32}H_{30}$; for this stoichiometry, there are 30 possible configurations. Each structure is then optimized using three separate semi-local DFT functionals: RPBE, [190] PBE, [213] and PBEsol. [191] Taking the lowest energy configuration, the process is repeated until $Pd_{32}H_0$ is recovered. Further details related to the protocol for generating these structures, and a more complete illustration of the Pd-Pd distance distributions can be found in SI Note 2. The result of these calculations was a library of structures for $PdH_x$ as a function of loading $x$. An analysis of the library generated using PBEsol, with comparison to experimental measurements reported above, is given in Figure 4.4.

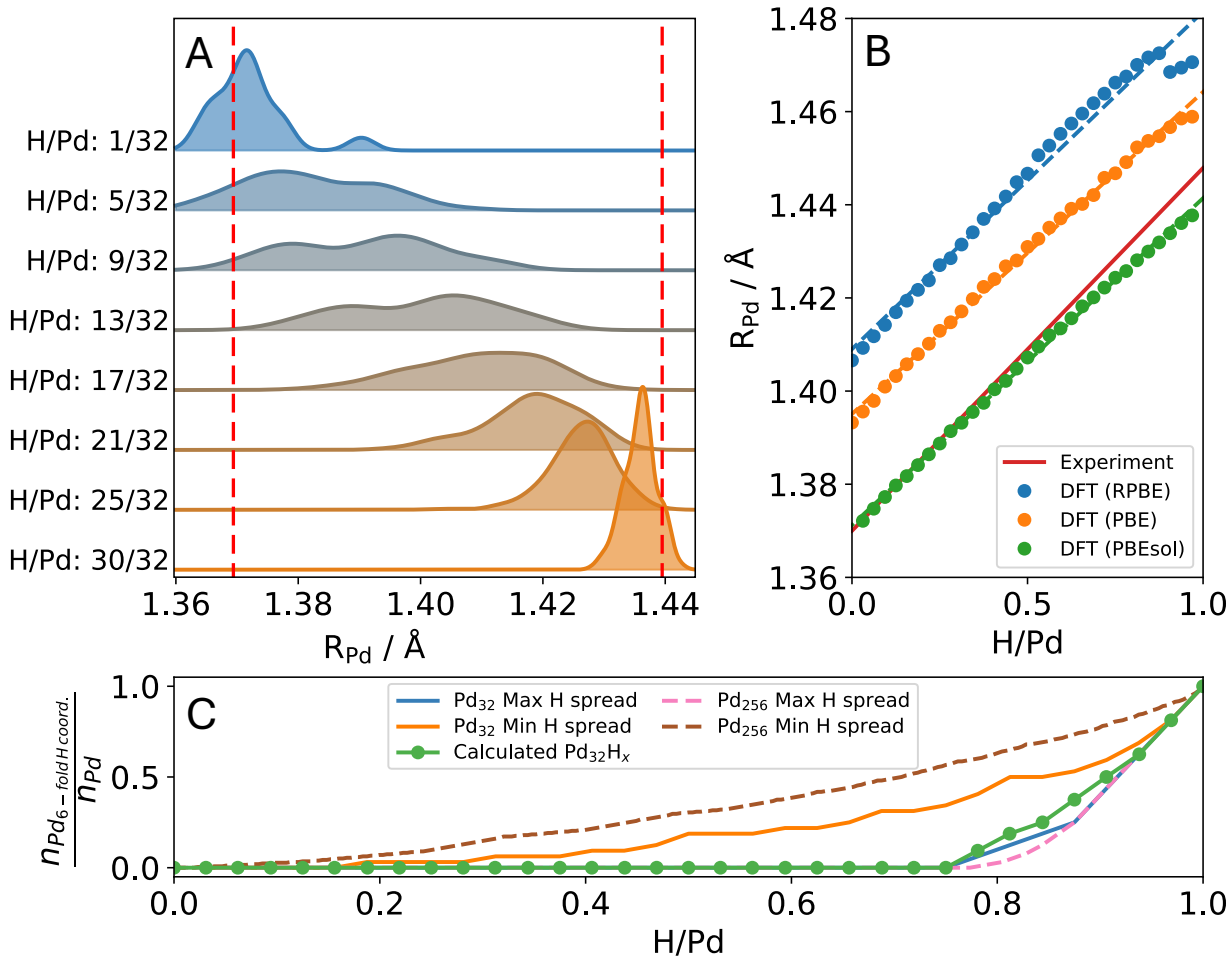



Fig. 4.4: (A) Distributions of Pd-Pd distances observed in the simulated $Pd_{32}H_x$ systems calculated using PBEsol, a semi-local density functional. Dashed vertical lines denote $PdH_0$ and $PdH_1$ lattice spacings. (B) Mean of the distributions for three different density functionals as a function of the hydride loading, with comparison to experimental measurements taken at near-stoichiometric loading. (C) Fraction of Pd atoms in $Pd_{32}$ supercell that are 6-fold coordinated to hydrogen as a function of loading, with bounding cases for maximal and minimal hydrogen homogeneity.

In Figure 4.4A, we observe the characteristic two-phase coexistence of $\alpha$- and $\beta$-$PdH_x$, as shown in the splitting of the Gaussian kernel density estimate [214] distributions at moderate hydride loading. Here, the two vertical dashed lines denote the average lattice spacing for $PdH_0$ (i. e., pure Pd) and $PdH_1$ calculated with PBEsol. We observe formation of two distinct peaks in the lattice spacing distribution as soon as a stoichiometry of 1/32, with the relative locations of each peak shifting as the loading is increased. At high loadings, approximately 25/32, the two peaks coalesce, consistent with $\beta$-PdH.

An analysis of the three semi-local density functionals considered in this work is shown in Figure 4.4B. Here, we report average lattice Pd-Pd ($R_{Pd}$) spacings as a function of hydride loading. As has been illustrated in previous literature, [215,216] the choice of functional has a significant impact on the predicted equilibrium lattice spacing. Although all functionals qualitatively capture the experimental trend of increasing lattice strain with higher loading (c.f. Figure 4.3), RPBE notably predicts an unphysical contraction of the Pd-Pd spacing at high loading, and is quantitatively the least accurate in predicting the correct lattice strain compared to modern experimental results. PBEsol in contrast is remarkably close to the experimental measurement, with moderate underprediction of the lattice spacing in the high-loading regime. Here we wish to highlight the substantial experimental uncertainty illustrated in Figure 4.3, and as such it is difficult to resolve whether the discrepancy between PBEsol and experiment in the high loading regime is due to the DFT, the experiment, or both. We further note that although our Pd-Pd spacing distributions reflect the two-phase coexistence of $\alpha$- and $\beta$-$PdH_x$, this fine detail is lost in the averaging reported in Figure 4.4B. Since the peak locations shift to larger Pd-Pd spacings at higher loading, the net average Pd-Pd spacing (as would be determined from, e.g., XRD) is a smooth, monotonic increase.

Beginning with pure Pd, as the hydriding process occurs, the spatial distribution of hydrogen atoms is difficult to resolve experimentally. Neutron diffraction experiments suggest that H randomly occupies octahedral sites in the $\beta$-$PdH_x$ phase, [217] but confirming with X-ray techniques may not be feasible. Hydrogen atoms may distribute homogeneously, preferring to spread apart, or may distribute heterogeneously, preferring to form hydrogen 'islands' within the bulk Pd. An analysis of this tendency for our $PdH_x$ system is shown in Figure 4.4C. Here, we calculated the fraction of Pd atoms in our $Pd_{32}H_x$ supercell that have six hydrogen atoms as their nearest neighbor – corresponding to a fully occupied nearest neighbor octahedral sites. The blue line represents maximum hydrogen spatial homogeneity, a lower bound corresponding to hydrogen atoms preferring to coordinate to Pd atoms with minimal pre-existing H coordination. In orange is the opposite limit, representing minimal hydrogen spatial homogeneity, corresponding to the case where hydrogen atoms prefer to be coordinated to Pd atoms that are already highly coordinated. We find that, generally, hydrogen atoms prefer to be homogeneously distributed, with our calculated $PdH_x$ system much more closely representing the lower limiting case. Dashed lines represent the same limiting cases as before, but for a $Pd_{256}$ supercell rather than $Pd_{32}$. Here we can directly see the extent of a finite cell-size effect for our system. In the limit of maximum H spatial homogeneity, we observe a non-negligible finite cell-size effect, particularly in the region of H/Pd=0.8. A more detailed breakdown of H-coordination is shown in SI Note 3.

### 4.3.3 Isotherm analysis of the computational model of $PdH_x$

Given our computational model of $PdH_x$ for $0 \leq x \leq 1$, we calculated the Gibbs free energies of formation as a function of both temperature and hydrogen pressure, illustrated in Figure 4.5(A) and (B) below.

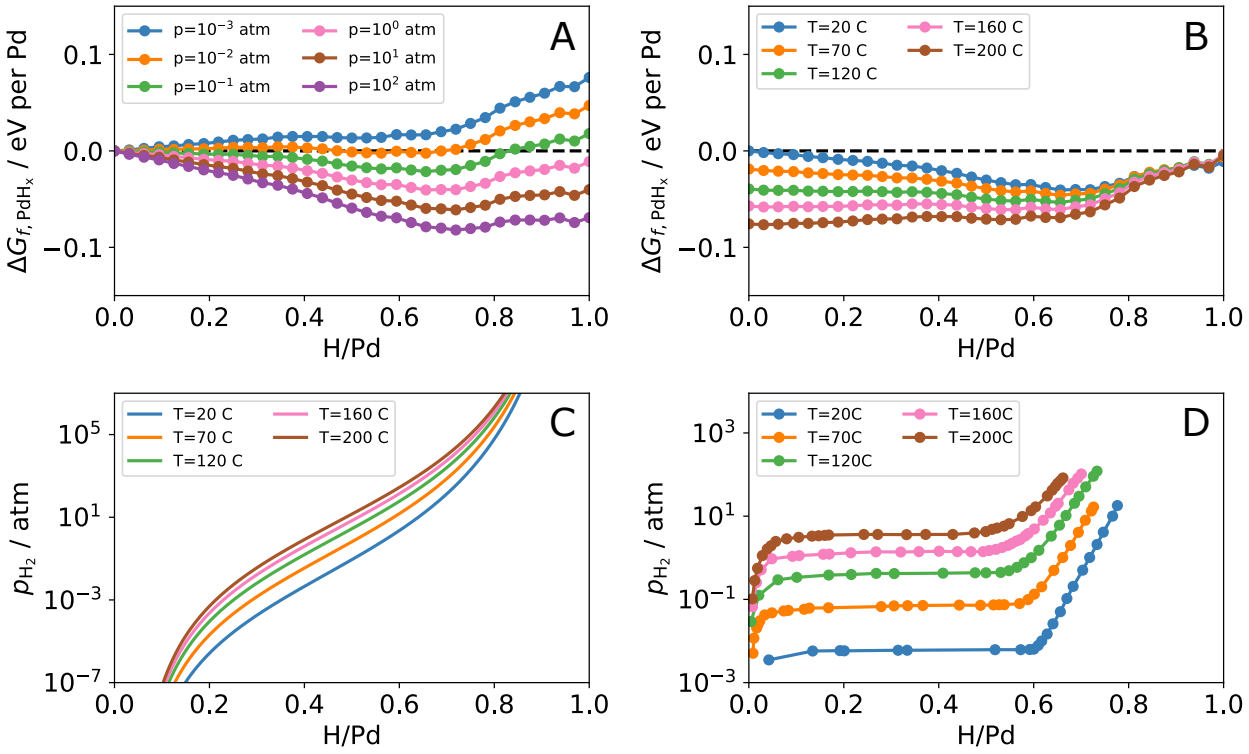



Fig. 4.5: Calculated Gibbs free energies of formation for $PdH_x$ as a function of (A) $H_2$ pressure at T = 298 K, and (B) temperature at $p_{H_2}$ = 1 bar. Additionally, (C) illustrates predicted temperature and pressure dependent isotherms, while (D) illustrates the experimentally measured isotherms. Panel (D) was adapted from Ref. [218].

Here $\Delta G_{f,\mathrm{PdH_x}}$ was determined with pure Pd metal and $H_2$ gas as the reference, with entropic corrections for the solid being determined in the harmonic limit (in addition to inclusion of configurational entropy), and with entropic corrections for the gas being determined in the ideal gas limit; more details can be found in the methods section. Reliable experimental references for $\Delta G_{f,\mathrm{PdH_x}}$ were not found for this system. However, reported enthalpies of formation ($\Delta H_{f,\mathrm{PdH_x}}$) show qualitatively similar behavior as a function of loading near standard temperature and pressure - convex with a minimum at H/Pd=0.5. [219] Given the configurational entropy contribution peaks at H/Pd=0.5, we hypothesize that the experimental $\Delta G_{f,\mathrm{PdH_x}}$ would show a minimum of H/Pd=0.7 as suggested by our calculations.

From the Gibbs free energies of formation and their temperature and hydrogen pressure dependence, we determined simulated isotherms for the $PdH_x$ system, shown in Figure 3(C), with a digitized and re-plotted experimental reference [218] shown in Figure 3(D). For a given temperature and pressure, equilibrated loadings (i. e., H/Pd) were determined as a Boltzmann weighted average of the Gibbs free energies of formation, i. e.,

$$x = \mathrm{H/Pd} = \frac{\sum_i x_i \exp\left[-\frac{\Delta G_{f,\mathrm{PdH_x}}}{k_\mathrm{B}T}\right]}{\sum_i \exp\left[-\frac{\Delta G_{f,\mathrm{PdH_x}}}{k_\mathrm{B}T}\right]} \quad . \tag{4.5}$$

Here, $x$ represents the equilibrated H/Pd ratio, and $x_i$ are the incremental H/Pd ratios at which we determined $\Delta G_{f,\mathrm{PdH_x}}$, i. e., ranging from 0 to 1 in 33 total increments for the Pd32 supercell. Although our simulated isotherm agrees reasonably well, qualitatively, with the experimental reference (higher equilibrium loading at lower temperature and higher pressure, three apparent regimes at low, medium, and high loading), our isotherm does not capture the two-phase coexistence of the $\alpha$- and $\beta$-$\mathrm{PdH}_x$ denoted by the flat regions in the isotherm at moderate loading. We hypothesize that this may be due to finite cell-size effects, as suggested by nanoscopic $\mathrm{PdH}_x$ synthesis and characterization experiments from the groups of Schmid-Ott and Zoric, [220, 221] who similarly report no two-phase coexistence regime between the $\alpha$- and $\beta$-PdH systems. The former study, which reported synthesis of nanoscopic rings of varying thickness and associated isotherms, suggests that length scales on the order of 100 nm would be necessary to capture the two-phase coexistence regime, which is computationally intractable at the GGA-DFT level of theory.

### 4.3.4 Unraveling the interplay between hydrogen evolution and electrochemical loading

Unlike gas-phase loading of Pd, electrochemical loading is driven by the applied bias, producing adsorbed hydrogen atoms on the surface which then intercalate given sufficient driving force and facile kinetics. Considering the equilibrium between the bulk hydride phase and the electrolyte, at first glance this seems to be a very attractive route to achieving higher bulk loadings. A simple analysis of the thermodynamics in the bulk-to-bulk equilibrium formalism would suggest that linearly changing the applied bias is equivalent to logarithmically changing the hydrogen pressure. In other words, considering just the bulk phases, utilizing an easily achievable applied bias would lead to loading driving forces that are equivalent to gas-loading pressures that are not realistic with current capabilities. [222] However, in reality, equilibrium between these two bulk phases is never achieved, as a third phase must be considered – the surface – which ultimately prevents equilibration, since surface-bound hydrogen reacts to form molecular hydrogen via the hydrogen evolution reaction (HER) faster than intercalation.

Towards unraveling this complex co-dependency, we calculated the dependence of the three HER sub-reactions on the surface hydrogen coverage $\theta_H$, applied bias $U$, and hydrogen loading $x$. Specifically, the three HER sub-reactions considered are,

$$\text{Volmer}: \quad (\mathrm{H}^+ + e^-) + * \rightarrow *\mathrm{H} \tag{4.6}$$

$$\text{Tafel}: \quad 2 * \mathrm{H} \rightarrow 2 * + \mathrm{H}_2(g) \tag{4.7}$$

$$\text{Heyrovsky}: \quad (\mathrm{H}^+ + e^-) + *\mathrm{H} \rightarrow * + \mathrm{H}_2(g) \tag{4.8}$$

Energetics for all three sub-reactions were calculated, but primary focus was on the Volmer and Tafel reactions, as experimental Tafel slope analysis suggests that $\mathrm{PdH}_x$ operates in a Volmer-Tafel limiting regime. [223] Briefly, multi-feature linear regression models were fit for the Volmer and Tafel reaction to capture the (inter-)dependence of the sub-reaction energetics on $\theta_H$, $U$, and $x$. Contour plots illustrating the fit models are shown in Figure 4.6. Further details related to the calculated energetics, computational geometries, thermodynamic references utilized, and parameters for the multi-feature linear regression model are given in SI Note 4. Additionally, all DFT input and output files used in producing these figures can be found

in a separate electronic supporting information zip archive. Note that the Tafel energetics reported here correspond approximately to enthalpies, rather than Gibbs free energies. We expect the entropic contribution would be an approximately constant shift over the investigated energetic landscape, and the choice of pressure for the gas-phase $H_2$ product would introduce substantial uncertainty into the magnitude of this shift, and as such we choose to report the enthalpy.

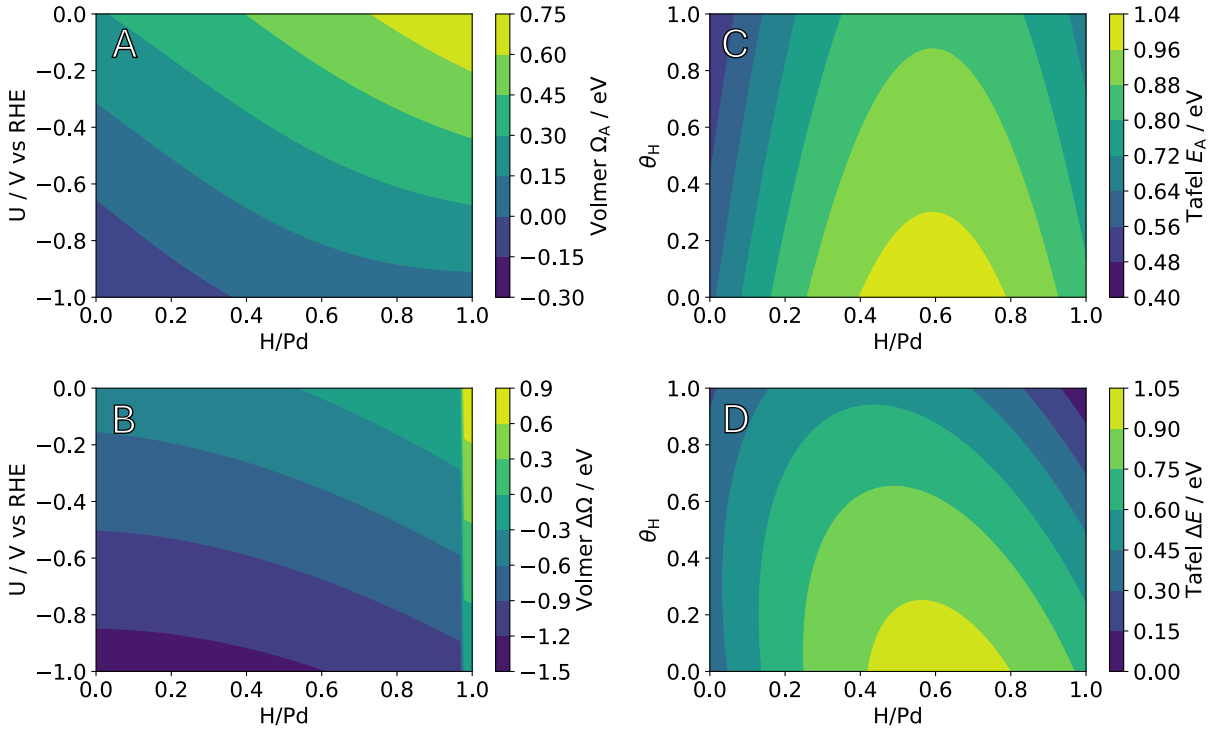



Fig. 4.6: Computed hydrogen evolution reaction (HER) sub-reaction energetics. (A) and (B) illustrate proton reduction (i. e., the Volmer reaction) activation barriers and reaction energies, respectively, as a function of loading and applied bias. Energetics here were calculated treating electrons grand canonically, as described in the methods section. Panels (C) and (D) illustrate molecular hydrogen production activation barriers and reaction energies, respectively, driven by the Tafel reaction.

As the H loading increases at a fixed applied bias, we find a significant increase in the bias-dependent Volmer activation barriers reported in Figure 4.6A. Higher barriers suggest reduced overall activity towards the HER at high loading, and is consistent with weaker H-binding found at high loadings. We note that the reported negative activation barriers are caused by utilizing bulk protons as the energetic reference (i. e., via the CHE) for the transition state energy; a small, exergonic energy change is associated with bringing a proton from the bulk electrolyte to the reaction plane under reducing conditions. Similarly, we find generally increasing (i. e., less favorable) Volmer reaction energetics as the H loading increases at a fixed bias, as shown in Figure 4.6C. The energetics become particularly less favorable as the loading approaches 100 % (H/Pd =

1.0). For loadings > 97 %, the favorable 3-fold binding sites that H prefers are no longer available, forcing H into a less favorable binding configuration (see SI Note 7), explaining the step increase in Volmer $\Delta\Omega$ visible in Figure 4.6C.

We wish to highlight the very strong dependence of the Tafel reaction on surface H coverage $\theta_H$. Indeed, for coverages > 1 (i. e., all 3-fold hollow sites occupied , consistent with the step increase in Volmer reaction energetics, see SI Note 7), the Tafel reaction is barrierless and has a strong exergonic driving force. From our calculations it is difficult to determine a steady-state $\theta_H$ without implementation of a microkinetic model. Given the clear dependence of the critical reaction energetics on local structure, a mean-field approach is likely insufficient. Determination of the steady-state $\theta_H$ would therefore likely require, e.g., a kinetic Monte Carlo approach, which is beyond the scope of this study but would be an interesting area of future work. However, given facile (de)intercalation as evidenced by observation of hydride formation at potentials > 0 $V_{\mathrm{SHE}}$ and spontaneous deintercalation of bulk H at low $\theta_H$ or high H/Pd, we anticipate that at steady-state, $\theta_H$ should be at least of a similar magnitude to the loading H/Pd, i. e., $0 \ll \theta_H < 1$.

### 4.3.5 The cause of the upper bound on electrochemical loading of palladium hydride

Experimentally (see Figure 4.2C), the loading is observed to have an upper bound of approximately 0.7-0.85, far lower than the equilibrated loadings predicted theoretically. [222, 224] Based on the results of our computational model of $PdH_x$ and calculated HER sub-reaction energetics we hypothesize the cause for this sub-unity upper bound on electrochemical hydrogen loading to be a confluence of several factors. First, and perhaps most importantly, at high surface H coverages $\theta_H \to 1$, the Tafel activation barrier peaks at around 80 % loading, before quickly decreasing. For $\theta_H > 1$, corresponding to > 1 H per surface Pd (with Hs occupying the 3-fold hollow site), the Tafel reaction is calculated to be barrierless – meaning that the Tafel reaction rate is determined entirely by the attempt frequency in the pre-factor of an Eyring-like expression. In other words, the surface coverage will likely never exceed 1 H per surface Pd on timescales relevant for H intercalation, imposing an upper bound on the possible electrochemical driving force for H loading, far below the driving force one obtains when neglecting the surface.

In addition to the dynamic changes in HER catalysis with increasing loading, we found the differential Gibbs free energy of formation of $PdH_x$ to become positive (i. e., endergonic) for loadings above 70 %, depending on the pressure (Figure 4.5). The change in sign for the differential Gibbs free energy of formation is likely driven by the requirement of filling the 6th octahedral site of Pd above about 70 % loading, as discussed in SI Note 3. Filling this last octahedral site is energetically unfavorable, requiring an increased driving force to exceed 70-80 % loading.

Given the above factors imposing a fundamental limit on electrochemical H loading, strategies to go beyond this limit must focus on either inhibiting the Tafel reaction (i.e., Tafel poisons), ideally without simultaneously hindering H intercalation and without accelerating the Heyrovsky reaction or impeding the Volmer reaction. Alternatively, identification of materials with more favorable hydride formation energetics may be able to undergo electrochemical loading with lower $\theta_H$, which would inhibit both the Tafel and Heyrovsky reactions.

## 4.4 Conclusions

To summarize, in this work we developed a novel computational model of palladium hydride at incremental hydrogen loadings, with the resulting lattice spacings validated by operando experimental XRD measurements. From this computational model, we calculated Gibbs free energies of formation which were used to simulate gas-loading isotherms of $PdH_x$. From these simulated isotherms, we found that the well-known two-phase coexistence of $\alpha$- and $\beta$-$PdH_x$ is a macroscopic phenomenon, in support of experimental measurements of gas-loading isotherms on nanoscopic samples of Pd. By cutting a (111) surface of $PdH_x$ at incremental loadings and calculating HER sub-reaction energetics at different potentials, loadings, and surface coverages, we determined that dynamic changes in the energetics of these crucial sub-reactions impose an upper bound on the feasible electrochemical loading of Pd. In contrast to a simple thermodynamic analysis of the equilibrium between bulk $PdH_x$ and protons/electrons, which would suggest that superhydride formation is feasible at reasonable conditions, our analysis incorporating HER catalysis supports experimental measurements of a maximum 70-80 % hydride loading by electrochemical means in Pd. Our results suggest that incorporation of the surface phase is critical when examining new materials for electrochemical hydrogen storage. By suppressing the Tafel reaction, electrochemical loading may be enhanced, but equilibration between the bulk $PdH_x$ and electrolyte phases is unlikely. An interesting area of future work will be to incorporate the energetics and active loading dynamics into a kinetic Monte Carlo calculation, which may reveal finer-grain details relating the interplay between HER energetics and electrochemical H storage in different metal hydrides.

# Chapter 5

# Surface Preparation Methods

## 5.1 Cleaning Protocol

During our investigations, we discovered the impact that sample surface character has on loading and the consequent need for rigorous sample preparation. We developed a multi-step cleaning process for ridding the samples and hardware of contaminants. Samples were cleaned by a 10-minute sonication bath in laboratory detergent water, DI water, acetone, IPA, and a final Radio Corporation of America (RCA) clean. While all these solvents are widely used in literature, the final RCA clean, which removes surface organic contaminants, has shown a strong correlation to a decreased spread in loadings. We posit that this increased consistency in loadings is due to the lack of residual surface organic compounds which could block active sites for H adsorption and intercalation. The exact mechanism of this organic-electrolyte reaction is currently unknown.

## 5.2 Electropolishing and Centerless Grinding

Another surface characteristic that we found to significantly impact sample loading is the surface roughness. A common method used to refine material surfaces is electropolishing. Electropolishing is an electrochemical process in which the surface roughness of a metal sample of interest is decreased or "polished" by applying a positive bias and dissolving a thin layer of surface metal ions into solution. The sample acts as the positive anode, the counter electrode is generally stainless steel, and the electrolyte is usually comprised of sulfuric and phosphoric acid mixture, which both conducts electrical current and dissolves the metal ions released from the surface. By electropolishing our samples in acidic media, the Pd surface was removed of any debris, cracks, and trenches. Additionally, we observed the exposure of grain boundaries of the sample after an optimal time of electropolishing (~30 min.). These features can influence the conformal coating formed during electrolysis and its robustness, specifically, how long Pd cathodes maintain enhanced loading. Figure 5.1 depicts the change in surface character as a function of electropolishing time using SEM. The figure also shows electrochemical loading data for first cycle loading percentage (red) and normalized resistance (grey) in 0.5M LiOD as a function of time for unpolished and polished Pd wires, respectively. We can observe from the figure that as the polishing time for samples increased, the rough surface features decreased until we reach a point where local anisotropy led to pit formation as observed in the 45-minute polish. It is important to note that a 25mM $NaAsO_2$ loading enhancer was introduced to all samples after 2.5 hours of

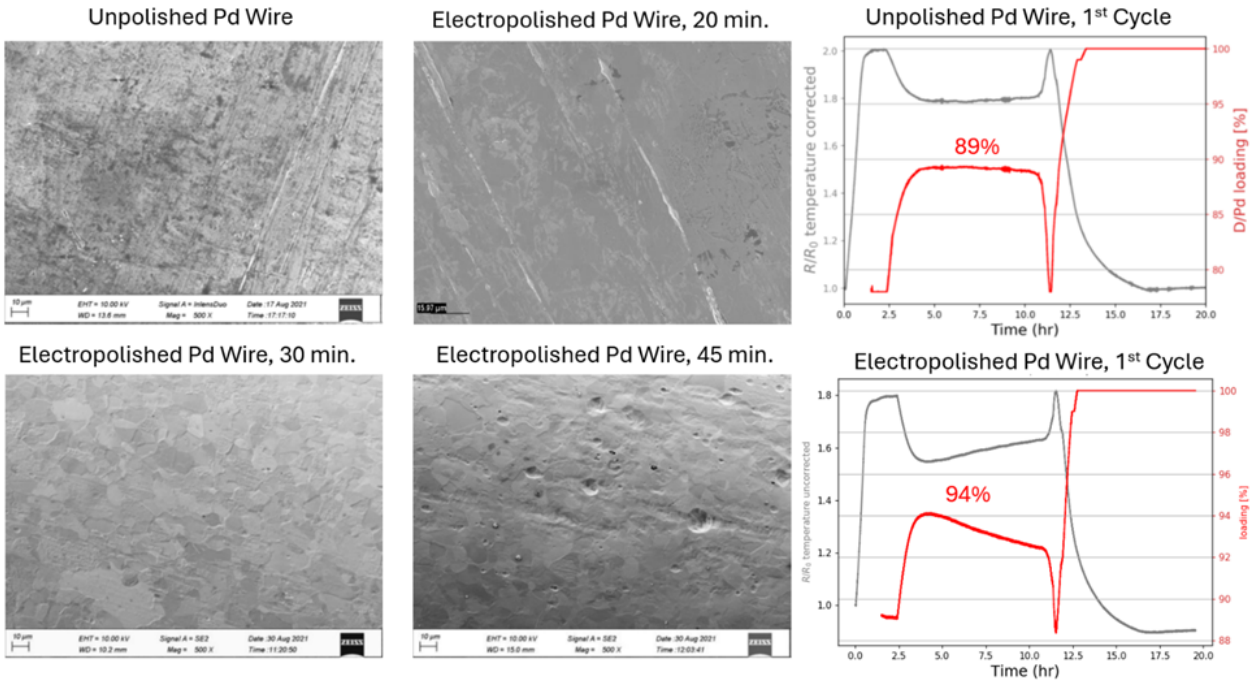



Fig. 5.1: Scanning electron microscopy (SEM) images comparing unpolished Pd wires to electropolished wires exposed to various electropolishing times (20, 30, and 45 minutes). Right panels show electrochemical loading data in 0.5 M LiOD electrolyte for unpolished Pd wires (top) and 45 min. electropolished Pd wires (bottom) after being dosed with 25mM NaAsO2 enhancer. (Data came from slide 196 in cumulative summary deck in 08/2021)

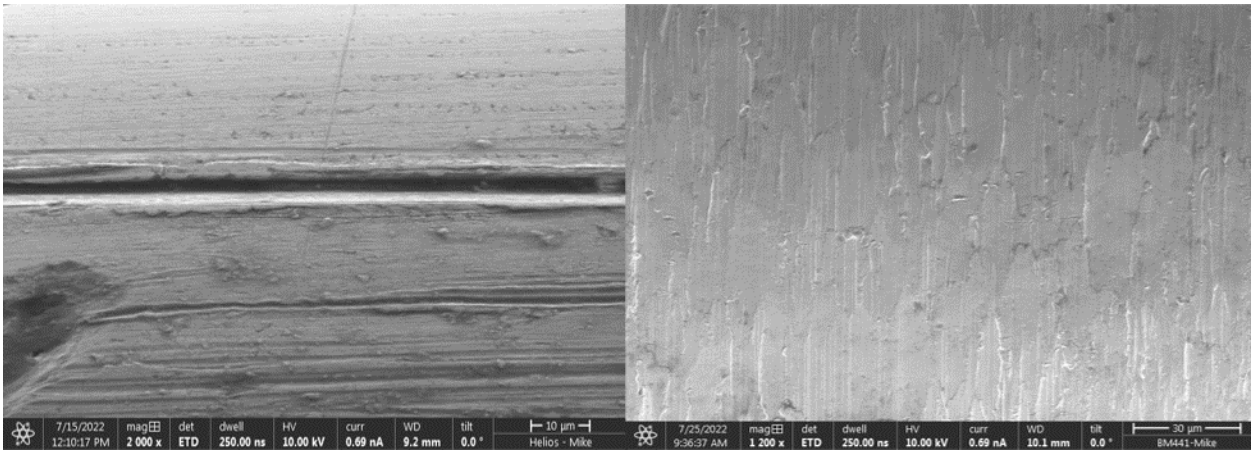


Fig. 5.2: SEM images comparing untreated Pd wire with longitudinal crack surface defect (left) to a Pd wire after centerless grinding treatment. (Data came from slide 1897 in cumulative slide deck)

unenhanced loading. This loading enhancement strategy is discussed at length in the following section. The grain boundaries can be clearly seen after the 30min polishing. The panels to the right show representative effects on loading of the total surface preparation procedure on unpolished and polished wires respectively. There is a clear increase in peak loading, 89% unpolished compared to 94% polished, upon Arsenic (As) enhancement when samples receive the exact same treatment outside of electropolishing. This study shows the large impact that surface pretreatment can have on an electrochemical study where deuterium loading is thought to be a vital parameter.

Despite positive outcomes of the electropolishing, the inability to efficiently produce these high-quality samples in large batches onsite became gating. SEM pre-imaging uncovered that the major source of the variability in loading performance and longevity was the presence of longitudinal cracks along many of the Pd wire samples. This longitudinal crack was found to be a weak point in the interfacial coating formed on the electrode surface that normally acts as a Tafel inhibitor and ultimately leads to longer loading longevities. We determined that the ideal Pd sample for obtaining high loadings would be devoid of these longitudinal cracks but also be mass produced unlike with electropolishing. It was determined that the best course of action was to outsource samples for centerless grinding and then post-treat samples onsite. Centerless grinding is a process in which the removal of the outer layer of a material is achieved by rotation against a coarse grinding wheel. Figure 5.2 illustrates this finding as well as before and after SEM images showing the removal of the longitudinal surface crack. Ultimately, we found that centerless grinding was effective in removing surface defects that lead to loading failure; although, it was not as efficient in exposing grain boundaries as electropolishing. Regardless, centerless grinding allowed for more consistent loadings across our samples and large-batch sample preparation facilitating higher experimental output.

# Chapter 6

# Conditions Reportedly Amenable to AHE

As previously discussed, there are many commonalities across studies done in the LENR field that build a framework for the conditions purportedly beneficial to observing an AHE event. Chiefly among these conditions is the purported need to have a highly loaded Pd sample. While the exact threshold of "highly-loaded" is not explicitly established, it is commonly accepted that $\geq 90\%$ deuterium loading is necessary to foster an environment conducive to AHE. Parameters that purportedly have influence on deuterium loading include current density, temperature, formation of a coating from the unintentional deposition of trace elements from the electrolyte onto the sample (dubbed in our work as "Coating X"), and additives that lead to loading enhancement. In the following sections we will discuss our experimental findings on each of these conditions' effect on loading and relevant conclusions that can be drawn.

## 6.1 Effects of Current Density on Hydrogen Loading

Many notable works in the field from authors like Fleischmann and Pons, McKubre, the U.S. Navy, Google [26, 93, 106, 110], and the like have all applied a negative bias to the Pd cathode in a heavy-water electrolyte to load it with deuterium. This intercalation occurs via the surface adsorbed hydrogen atom proceeding through the well-established Volmer-Heyrovsky-Tafel mechanism for hydrogen evolution reaction (HER) in alkaline media. As previously described in the introduction, these three steps can be described by the following:

$$\text{Volmer} : H_2O + Pd_{surface} + e^- \rightarrow Pd_{surface}H_{adsorbed} + OH^- \tag{6.1}$$

$$\text{Heyrovsky} : H_2O + Pd_{surface}H_{adsorbed} + e^- \rightarrow Pd_{surface} + OH^- + H_2 \tag{6.2}$$

$$\text{Tafel} : 2Pd_{surface}H_{adsorbed} \rightarrow 2Pd_{surface} + H_{2(g)} \tag{6.3}$$

$$\text{Intercalation} : 2Pd_{surface}H_{adsorbed} \leftrightarrow 2PdH_{bulk} \tag{6.4}$$

The first three descriptors can be combined to describe two reaction pathways. We also pose a third pathway of "intercalation". 1) Volmer-Heyrovsky (V-H) proceeds via an initial surface adsorbed hydrogen ($H_{adsorbed}$) produced at the Volmer step followed by an interaction of the adsorbed H with a water molecule

causing disassociation from the surface and formation of $H_2$ gas and a hydroxide ion, 2) Volmer-Tafel (V-T) proceeds after two surface adsorbed H produced in the Volmer step come into close proximity and recombine, leaving the surface as $H_2$ gas, and 3) Intercalation proceeds as surface adsorbed H produced in the Volmer step enters the bulk of the Pd crystal lattice. While all of these pathways play a role in the intercalation of D into Pd, literature as well our independent studies confirm that HER on Pd proceeds predominately via the V-T pathway. We also found that the Volmer step is the kinetically limiting step in the range of 1 to $50\,mA/cm^2$ using our own Tafel analysis measurement.

In alkaline media, the short surface residence time of $H_{adsorbed}$ is also an issue at low current densities because adsorbed species experience competing reaction pathways: V-T, V-H (though not relevant here), and intercalation. This causes the V-T pathway to be a parasitic reaction in loading procedures as it directly impacts the ability of $H_{adsorbed}$ to be incorporated into the Pd lattice. We will discuss in later sections strategies used to inhibit the V-T pathway leading to higher H loadings in our Pd samples. As we increase the current density we also increase the rate of the HER reaction, leading to more surface coverage with $H_{adsorbed}$ atoms. This increase in $H_{adsorbed}$ surface coverage and current density allows for higher rates of intercalation. However, higher current density also leads to high rates of bubbling as $O_2$ and $H_2$ gas leave the surface of the Pd cathode. If these bubbles stay on the surface, particularly $H_2$ gas from V-T, then catalytically active sites can be blocked inhibiting further HER and ultimately limiting available $H_{adsorbed}$ for intercalation. If current densities are too high they can also have negative effects on the sample integrity (e.g. crack formation) as well as unwanted reactions on the electrical contacts.

Another consideration when running high currents to load Pd in aqueous environment is the inevitable presence of unwanted ions in solution from electrolyte impurities, counter electrode and hardware degradation, etc. Over the course of long duration experiments at high currents, ions such as Cu, Fe, and Zn can leach from hardware and other sources. This ion leaching is especially true for the Pt counter electrode which is oppositely biased in our experiments. Based on Pourbaix diagrams, the negative potentials at which most experiments are carried out overlap with plating potentials for these leached ions in solution, causing them to co-plate as metallic deposits on the Pd surface during intercalation. While this plating can lead to blocked active sites given high ionic concentrations, the formation of an over-layer of metal constituents can be controlled and lead to a beneficial coating, coined "Coating-X", that acts as a V-T inhibitor and increases residence time of $H_{adsorbed}$ and by extension, H loading. We will discuss in later sections how we strategically selected for "Coating X" and leveraged it as a V-T inhibitor.

In addition to the the current density, the duration of current application is also vital to achieve highly loaded samples. Pd samples must load for some optimal time in order to achieve an optimal H/Pd ratio. This optimum ratio is indicated by a stabilization in the resistance measurements of the sample upon current application and introduction of loading enhancements. The time to reach this fully loaded state varies from sample to sample based on form factor, size, and current density. For example, larger bulk palladium samples at low current density would take far longer to reach high loadings compared to a thin Pd foil at high current densities.

## 6.2 Effects of Temperature on Hydrogen Loading

Temperature is an important parameter regarding AHE because it plays such a vital role in aqueous electrochemical systems in general. The main limiting factor in carrying out electrolysis reactions in aqueous environments is staying within the stability window (i.e., freezing and boiling point) of the electrolyte. In most cases that window will be between 0° C and 100° C, as water will make up the majority of the solution.

Temperature increase can affect the rate of electrolysis by increasing the thermal energy and conductivity of the solution helping ions to reach the Pd surface more readily [225]. While increased temperature can be beneficial, it is important to consider that once power is input into the system for electrolysis the electrolyte temperature can increase tens of degrees Celsius over the duration of the loading period. This is a vital consideration when designing an AHE experiment above room temperature as the electrolyte could readily reach boiling point and depletion long before an AHE event could be observed. Despite operating near boiling point resulting in the loss of electrolyte, there are some studies that purposefully investigated AHE reactions in this temperature regime.

We performed several studies below room temperature that showed increased peak and longevities of loadings when compared to room temperature experiments under the same conditions. We will discuss these low temperature experiments in detail in the loading enhancement section as we investigated the synergistic effects of loading enhancements and low temperatures. Regardless, operating near and below 0 °C necessitates careful experimental design and additives to prevent freezing and avoid lowering electrolyte conductivity to an unacceptably low value. To address this, we added antifreeze agents such as methanol, ethylene glycol, and ammonia to the electrolyte when carrying out studies below 0 °C. These antifreeze agents did present a challenge for closed cell calorimetry, as they can electrochemically split into $H_2$, $N_2$, $NH_3$ and $CO_2$. All of these gases can accumulate in the headspace and increase the pressure, and in most cases are not recombinable. Consequently, our studies below 0 °C were carried out in open cells and our closed cell experiments were carried out slightly above 0° C, where antifreeze additives were not required. Ultimately, we found that in conjunction with loading enhancers, temperatures near 0 °C had a direct positive effect on the maximum and longevity of loadings which allows the conditions purportedly amenable to AHE to persist longer and increase the likelihood of an event.

## 6.3 Effect of "Coating X" Formation on Hydrogen Loading

Many studies in the field have observed the reduction of metallic ionic impurities from the electrolyte, either intentional or not, onto the surface of the Pd cathode after experimentation. While this surface deposition being vital to AHE is not explicitly called out by any one researcher, we were interested in its commonality across multiple works in the field. Letts and Cravens' work claimed excess heat after intentionally electrodepositing gold on the Pd cathode surface in the presence of a 700 gauss magnetic field and laser stimulation [226]. As described earlier, when applying negative currents to load samples in aqueous environments there is often a co-deposition on the cathode surface based on the ions plating potential on their Pourbaix diagrams. This electrodeposited coating's thickness varies based on the amount of current applied, the duration of the current application, and the concentration of ions (and their ionic activity) in solution. Each of these factors increases the amount of deposition, with increasing current affecting the rate of deposition. As observed in many electrochemical systems, this over-layer essentially becomes the new catalytically active surface interfacing with our electrolyte once it reaches a certain surface coverage and thickness. An example is in Pd-hydride systems used in HER where the formation of surface $PdH_x$ changes the surface energetics of the pure Pd and weakens the H adsorption on the surface leading to increased reaction rates for HER [227]. In our own studies we began to consistently observe the recurring presence of certain elements on the surfaces of highly loaded samples.

We have coined this interfacial layer formed in our experiments "Coating X", as its composition varies slightly (similar to the variable "x") but the constituents remain largely unchanged. Electron dispersive X-ray spectroscopy (EDS) determined the common constituents of this surface overlayer to be Cu, Fe, Zn,

| | $Log(J_{0,Volmer})$ | | $Log(J_{0,Tafel})$ | |
|---|---|---|---|---|
| | Log(A/cm²) | | | |
| | Bare Pd | As-Enhanced | Bare Pd | As-Enhanced |
| Tidepool | -4.7 | -5.1 | **-3.3** | **-6.9** |
| Coolescence | -5.1 | N/A | -3.0 | N/A |

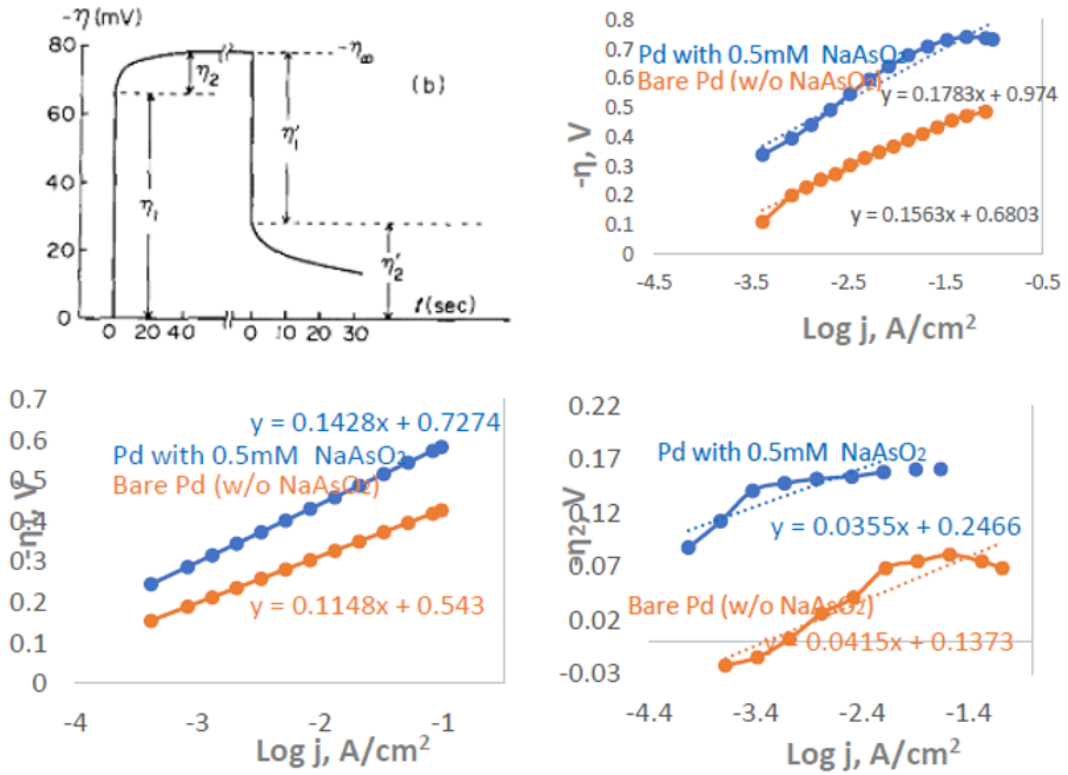



Fig. 6.1: Summary data comparing the effect of arsenic (As) additive on the Volmer and Tafel reaction rates with bare Pd and published data from Coolescence as references. The Tafel plots for the data are also included comparing the results of bare Pd to Pd with a 0.5 mM $NaAsO_2$ additive.

and Pt from the counter electrode. Sources of the Cu, Fe, and Zn have been determined to stem from electrolyte salt impurities and at times, a degradation of cell hardware in solution over time. These ions are usually found in relatively low concentrations in the electrolyte – less than a few ppm – and deposit onto the cathode over long time frames with high loading currents. The presence of Pt ions in solution is a much more complex problem to deal with as they stem from the Pt counter electrode in solution and their ionic concentration is much higher since they are exposed to an oxidizing potential. We found that over the course of long duration experiments Pt ions tend to electrodeposit on the Pd cathode surface, blocking active sites for intercalation and ultimately negatively impacting loading. This is especially the case for experiments that are cycled multiple times as the Pt ion concentration is allowed to continuously build up. We investigated how much this unwanted deposition impacted loading and how we could mitigate its formation by implementing a membrane compartment comprised of semi-permeable membranes housing the Pd cathode. This compartment allowed electrolyte to flow through the membranes to reach the Pd surface but prevented the Pt ions from reaching the cathode. Results showed a noticeable decrease in Pt deposition on the Pd surface and higher peak loadings by 2 - 4%. Unfortunately, these high loading results were not consistent and the experimental setup was tedious compared to the benefit.

These observations of "Coating X"'s natural occurrence during the formation of $PdH_x$ and its recurrence across multiple works in the field, inspired us to create our own tailored overlayer. The hypothesis was that this overlayer acted similarly to $PdH_x$ formation on pure Pd in changing the surface energetics as previously described. However, unlike in published HER studies where the goal was to increase the rate of V-T or V-H to facilitate increased $H_2$ production, our goal was to inhibit or "poison" these pathways to increase surface residence time of the $H_{adsorbed}$ atoms to increase loading of the Pd lattice. As previously established, our main loss of the $H_{adsorbed}$ atom produced in the Volmer step (1) was via the V-T reaction pathway. To this end, we began to screen additives that could suppress the the V-T pathway by monitoring changes in resistance in order to achieve the highest increase in peak D loadings. The results of this investigation are shown in Figure 6.2 and will be discussed in the following sections on loading enhancers.

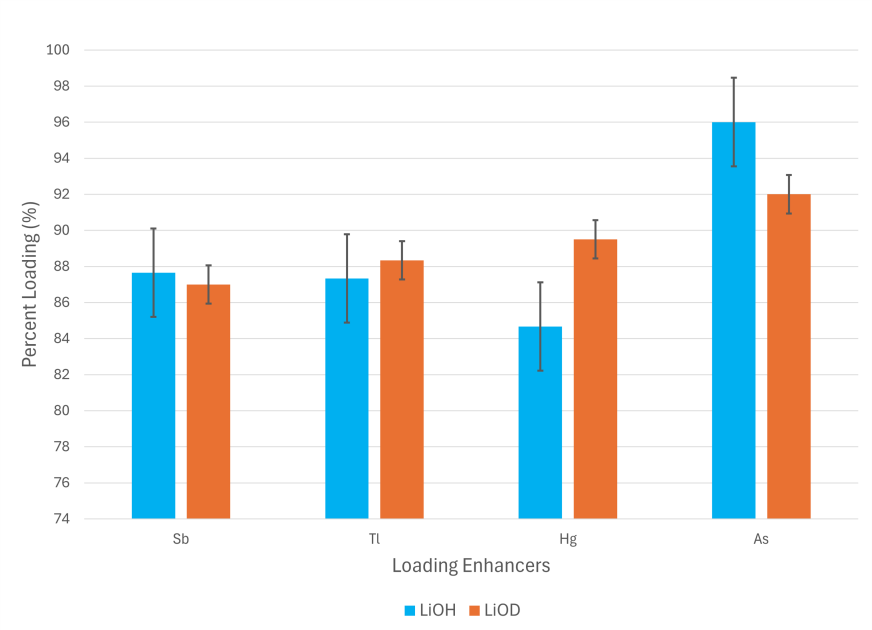



Fig. 6.2: Peak loadings of of various additives achieved in 0.5 M LiOH (blue) and 0.5 M LiOD (orange), respectively. Additives were delivered in 2 mL doses of 25 mM concentrations of the Sb, Tl, Hg, and As in LiOH or LiOD after loading plateau was reached, usually after 20 minutes of loading. Samples were 0.5 mm diameter and 30 mm long Pd wires. Current was a constant 50 mA.

## 6.4 Effect of Loading Enhancers on Hydrogen Loading

As mentioned above, we carried out various studies probing the best additives to increase the hydrogen (and in particular deuterium) loading in palladium cathodes. In a first screening, we vapor-deposited 100 nm layers of Hg, Ti, Ni or Pb onto Pd thin films. Neither resulted in a consistent loading enhancement effect. We thus dosed the additive to the electrolyte instead. Figure 6.2 shows the elemental salts (Sb, Tl, Hg, and As) that we added to the electrolyte at 25 mM concentration in 2 ml doses (yielding a final concentration of 0.83 mM in solution) and their corresponding peak loadings achieved. Arsenic (As) was determined to yield the best and most consistent results regarding loading enhancement, consistently achieving 92 to 98 % H/Pd loadings. These values are based on the resistance data and calculated using the Zhang formula. We observed that these higher loadings usually occurred on the second loading cycle (i. e., loading and deloading before loading again) which is likely due to some nano-structure preconditioning of the Pd surface. Figure 6.1 shows arsenic's effect on the suppression of V-T compared to bare Pd and its relatively small effect on the rate of the Volmer reaction. During these studies we discovered that As dosing had an optimal time frame during loading – within the first 20 minutes of loading for 0.5 mm Pd wires – to observe its loading enhancing benefit. This is likely because too much Coating X would be allowed to form if too much time elapsed during loading before introducing As into the system.

While As showed promise as the best "Tafel poison", the longevity of this inhibition only lasted for two to three hours on average. This lack of longevity led to a search for strategies to increase the duration of the V-T inhibition and by extension, the longevity of D loading in our Pd samples to trigger an AHE event. As seen in 6.2, other additives' effects on loading were investigated and some showed promise; however, they were plagued by other issues that excluded them from use in our experiments. For example, Mercury (Hg) enhancers showed largely varying range of enhancement as well as displaying an aggressive coating formation that often coated the Pt contacts to our Pd sample leading to errors in current application and improper loadings.

One trend that we did observe across nearly all of our studies is that the protium-loaded samples tended to load higher than their deuterium counterparts. This held true for nearly all studied enhancers except Hg which had the inverse relationship but also inconsistently exhibited the high loading behavior. It is well documented that the rate of the Volmer and Tafel reactions are higher in HER than in DER due to electrolytic H/D separation factors [228, 229]. This explains why H samples load quicker than D and evidences the apparently isotopically unique peak loading difference, as D is more easily disassociated from the catalytic surface compared to H. This could also be compounded by steric hindrance due to the difference in the size of H and D atoms. In a later section we discuss As enhancement experiments and the optimization of its loading enhancement in detail.

## 6.5 Electromigration

Several researchers, most notably McKubre [101] and Staker [105, 230], have claimed that the application of a current along the length of the palladium hydride cathode wire is beneficial or critical to observing AHE. This current is often referred to as *electromigration current* or *axial current*.

The underlying assumption is typically that the current causes an electric field along the wire, which in turn affects the distribution of hydrogen ions within the wire. Staker proposed a theory according to which the axial current causes a gradient in deuterium ion concentration along the wire, with one end of the wire having a concentration as high as 5 x compared to the other end of the wire (0.5 mm diameter, 25 mm

length wire, 3 A electromigration current) [105]. Upon closer inspection, the proposed model is based on assumptions that do not hold. Most critically, the highly loaded palladium hydride cannot be considered a dilute regime (in terms of interstitial site occupancy) and thus the equations presented by Staker are not applicable [231]. In a recent paper published in an Elsevier journal, Staker reiterates the claim that electromigration enhances loading, even above stoichiometry, but does not provide any data to back up the claim [230].

Apart from the electric field exerted due to the axial voltage, ions also interact with the electrons through momentum transfer. This process is referred to as *electromigration*, and the force of the electrons is likened to an *electron wind*. It can lead to a net transport of metal ions in an electric conductor, particularly at defects, e. g., grain boundaries, where charge symmetry is broken. Typically, these processes are slow and occur over weeks to months. Unlike material transport due to electromigration in thin-film integrated circuits, palladium hydride has the added complexity of other transport processes occurring in parallel. Hydrogen diffusion in the bulk as well as loading and deloading processes at the surface must be accounted for. Both of these processes typically occur at much higher rates than hydrogen transport through electromigration, thus likely swamping any potential effect from electromigration.

McKubre applied an axial current (up to 7 A) in some of his experiments. He noted that "During times when axial current is passing both loading information and calorimetry were seriously inaccurate: Calorimetry was poor because the axial input power was not measured at the calorimeter boundary. Loading measurements were inaccurate because the actual temperature of the cathode could not be determined. [...] During the axial current experiment the scatter in the excess power measurement increased to ±150 mW, but averaged to 0 W." [101]. The relationship between axial current and excess power remains unclear. However, McKubre's comments illustrate that the added complexity from additional power sources (for applying axial current in addition to electrochemical current) can introduce calorimetry errors. In particular, the high axial currents (compared to typical EC currents) can cause parasitic resistive losses if the wires are not dimensioned properly, generating ohmic heating. Parasitic losses scale with the square of the current for a given wire resistance. This additional ohmic heating can cause calorimetry errors if the voltage sense points are not positioned properly or if the calorimeter has different sensitivities depending on the location of the heat sources within the calorimeter.

To our knowledge, there is no experimental data in the literature showing any effect of axial current on loading in an electrochemically loaded palladium wire. For that reason, we performed our own experiments. We measured the local resistance in an electrolytically loaded Pd cathode wire near the ends of the wire with and without application of an axial current, as well as with different polarities of axial current. We found no significant difference in local resistance (hence in loading) as a function of axial current (Fig. 6.3). However, we did notice a temperature effect, with 3 A axial current typically elevating the wire temperature between 5 K and 10 K (for a 25 mm long, 0.5 mm diameter wire), depending on loading.

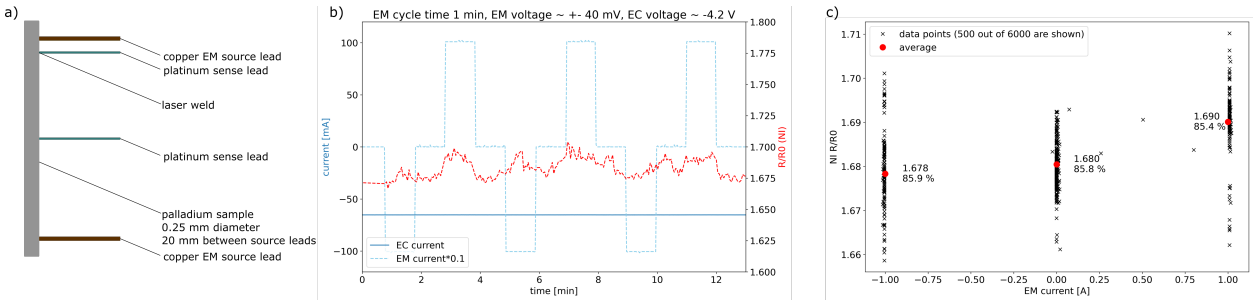



Fig. 6.3: Local loading measurement (by resistance) under axial current. a) Device setup to measure resistance in a palladium wire sample between the platinum sense leads. Depending on the polarity of the axial current, the segment of sample under test will be closer to the positive or negative polarity of the axial current. b) Example dataset showing the measured resistance ratio (compared to the resistance of the deloaded sample) while the axial current is varied between [1, 0, -1] A. c) Statistics of 6000 resistance ratio data points, showing no significant effect of axial current magnitude or polarity on resistance ratio.

# Chapter 7

# Replications

## 7.1 Fleischmann

In 1989, Martin Fleischmann and Stanley Pons reported experimental evidence suggesting that nuclear fusion could occur at room temperature, which they referred to as 'cold fusion' [232]. Their work, conducted via electrolysis of heavy water ($D_2O$) on palladium electrodes, reported what they described as anomalous energy production, later referred to as 'excess heat', beyond what conventional chemical reactions could explain. Fleischmann and Pons employed calorimetric methods to measure energy output, observing bursts of energy under specific conditions of prolonged electrochemical polarization. Notably, some of their experiments claimed heat outputs several times larger than the energy input, which they hypothesized as evidence of a nuclear reaction pathway distinct from traditional fusion processes involving neutron emission and tritium production.

Although the initial announcement generated significant excitement, subsequent replication efforts by other laboratories often failed, leading to skepticism about the validity of their findings [233]. Fleischmann and Pons argued that subtle experimental variables – such as electrode preparation, electrolyte purity, and precise control over electrolysis parameters – were critical to producing excess heat. They noted that only after prolonged polarization periods and substantial deuterium loading into the palladium lattice did excess heat manifest, suggesting that high deuterium-to-palladium loading ratios, often exceeding 0.85, were essential [234, 235]. However, their limited reporting on critical preparation steps, such as heat treatments and cleaning of palladium electrodes, further complicated replication efforts.

The original experiments used relatively large palladium samples and high current densities, often exceeding $500\,\mathrm{mA/cm^2}$, which presented several challenges for calorimetry. Their system consisted of a Pd cathode in sheet, rod, or cube form factor in 0.1 M LiOD in 99.5% $D_2O$ + 0.5% $H_2O$ solutions with a Pd-D reference electrode loaded to the $\alpha$-$\beta$-phase equilibrium. A Pd sheet cathode (2 mm x 8 cm x 8 cm) surrounded by a large Pt sheet counter electrode, or alternatively a Pd rod (1, 2 and 4 mm diameter x 10 cm long) surrounded by a Pt wire anode wound on a cage of glass rods, was used in the low (1.6 $\mathrm{mA/cm^2}$) and high (8 to 512 $\mathrm{mA/cm^2}$) current density experiments, respectively. Fleischmann and Pons employed thermodynamically open Dewar-type calorimeters, which allowed for the electrolyte to evaporate during electrolysis. However, this evaporation altered the thermal environment, complicating heat measurements. In isoperibolic calorimetry, where temperature changes are referenced to a stable environment, any shifts in the electrolyte level could disrupt heat accounting. To mitigate these issues, they sealed the experimental

setups with Parafilm and periodically replenished the electrolyte, but these efforts highlighted the difficulty of maintaining precise thermal conditions under open-system operation.

Other concerns levied against these inaugural LENR experiments include over-interpretation of their data. Critics argued that the bursts of excess heat reported could be explained by classical chemical processes. Specifically, as the electrolyte level dropped and exposed the electrodes, recombination of oxygen and deuterium gas could result in increased temperatures which would be interpreted as excess heat.

### 7.1.1 Our Replication Efforts

While the scientific community largely moved away from cold fusion research due to challenges in reproducibility, the work of Fleischmann and Pons continues to influence the field of LENR. Any serious effort to determine the physical reality of LENR must revisit the Fleischmann and Pons experiments and evaluate the critical parameters identified in their work. Over the course of our replication attempts, we explored multiple strategies to maintain stable thermal environments and tested several modifications to the original setup. In addition to designing stable thermal enclosures, we implemented two different types of electrolyte refill mechanisms including a gravity-fed water leveler and syringe pump dosing. In total, we performed more than 40 formal and modified replications of the Fleischmann and Pons experiments. Despite better control over electrolyte levels and calorimeter thermal stability, no excess heat was observed. These experiments fall into the following groupings:

### 7.1.2 Nominal Replications

For these experiments, we applied high currents (>500 mA) to large palladium samples (>10 g) for various durations. These tests were done in open beakers with 35 ml of 1 M LiOD electrolyte, with the heat being measured in an isoperibolic calorimeter with an RTD temperature sensor placed in the electrolyte near the cathode. Additional RTDs were placed in the water bath surrounding the electrolytic cell and in the thermal enclosure. Control experiments were performed with light water. Some experiments lasted less than an hour, while others ran for over 100 hours with the aid of electrolyte replenishment systems. Despite consistent application of current, we never observed any thermal signatures or temperature responses indicative of excess heat. Calibration and control experiments that were performed had temperature profiles similar to the 'active' samples. We did, however, note an increase in input power over time at constant current. We hypothesize this effect was likely due to the reaction of atmospheric carbon dioxide with lithium hydroxide in the electrolyte, forming lithium carbonate, a non-conductive, insoluble salt, a reaction which is well documented in literature [236]. As the salt precipitated, the electrolyte's conductivity decreased, causing the cell voltage to rise when operating at constant current. An example of a long-duration test is shown in figure 7.1. From the figure, we observed an initial input power of 2 W, which increased to 3 W over ~125 hours. Periodic fluctuations in temperature correlated with the syringe pump delivery of heavy water to maintain the electrolyte volume.

### 7.1.3 Modified with Additives

We hypothesized that the samples may have been prepared in a manner which influenced the replication. Given the large sample sizes, we speculated that they may have been machined, and poorly cleaned prior to use. We identified cutting fluids that were used in the late 1980s and early 1990s. We both soaked the samples and dosed the electrolytes with Rapid Tap cutting fluid. However, no excess heat was ever observed.

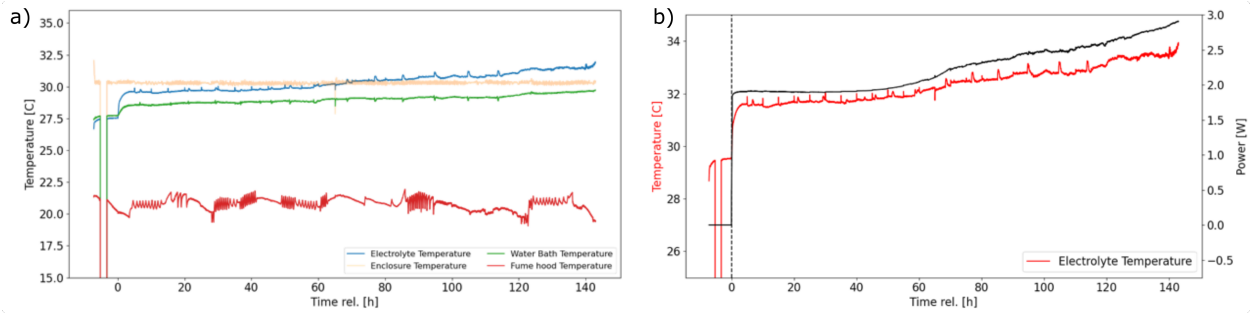



Fig. 7.1: Example of temperature (a) and input power (b, right axis) versus time for a long-duration test.

While nothing noteworthy came from these experiments, an example of the temperature and power profile versus time is shown in figure 7.2.

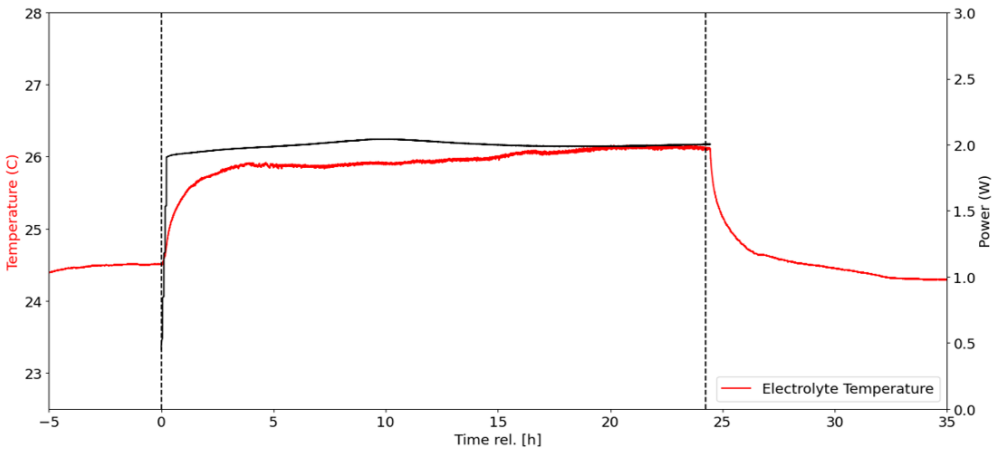



Fig. 7.2: Temperature and power profile for tests with cutting fluid additive.

### 7.1.4 Modified with Oxygen

We explored the possibility that orphaned oxygen produced during deuterium loading could have contributed to the reported anomalies. To test this, we bubbled gaseous oxygen directly beneath the cathode during electrolysis. While the introduction of oxygen initially caused an increase in current noise and a small temperature rise (several hundred millikelvin), these effects quickly subsided. We attributed this behavior to increased convective heat transfer, which facilitated more efficient heat transfer from the electrodes to the RTDs (this convection effect is commonly observed where bubbling is present in electrochemical cells), rather than any nuclear phenomenon. An example of this temperature rise is shown in figure 7.3.

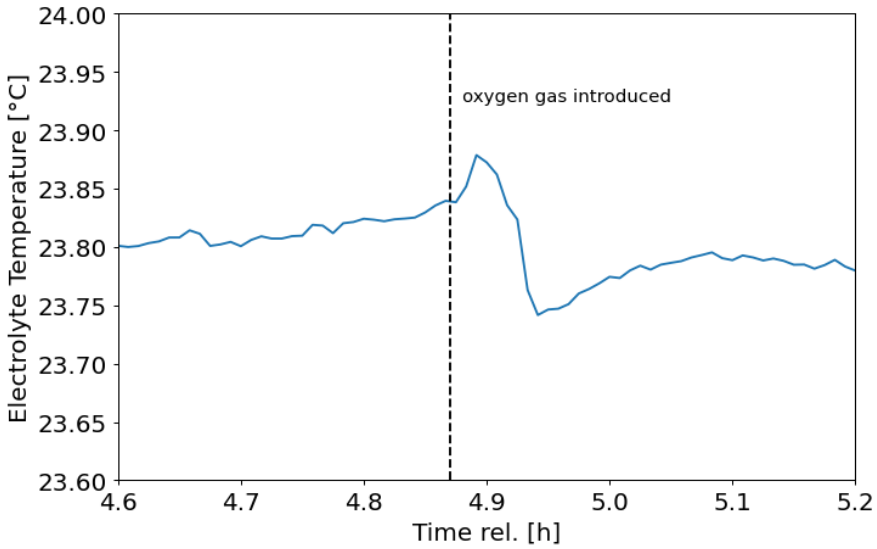



Fig. 7.3: Temperature transient observed during tests with oxygen bubbling beneath cathode.

### 7.1.5 Modified with High Power

In a separate set of experiments, we deviated from the original design by applying high input power between 100 W and several kilowatts (up to 15 A, 300 V) for short durations. This caused rapid heating of the electrolyte to boiling. At boiling, we observed a striking effect: the electrode emitted light and sparked sporadically. In some cases, when the electrolyte level dropped, the electrode glowed red hot. However, we concluded that this effect was classical in nature for two reasons:

a. The phenomenon occurred in light water with protonated salts, which are thought incompatible with LENR, or in any event would not be expected to behave similarly to the deuterated systems if nuclear processes were responsible for the effect.

b. The effect was replicated with stainless steel, nickel, and titanium cathodes, which are not generally associated with LENR.

Once convinced that the effect was non-nuclear, we further explored the underlying mechanism. We hypothesized that the observed light emission resulted from a liquid plasma discharge. As gas bubbles formed during boiling, they created conditions conducive to ionization. Using a photospectrometer, we identified sharp emission lines corresponding to excited Pd, Li, and OH species. All four cathodes show sharp Li emission near 670 nm, metal specific emission between 325 and 550 nm, and UV emission between 250 and 350 nm. These findings aligned with classical physics, confirming that the phenomenon was unrelated to LENR. A photograph of the effect and optical emission spectra are shown in figure 7.4. When the electrode becomes exposed such as in figure 7.4 c), the cathode began to glow red hot, likely due to insufficient cooling from the surrounding fluid.

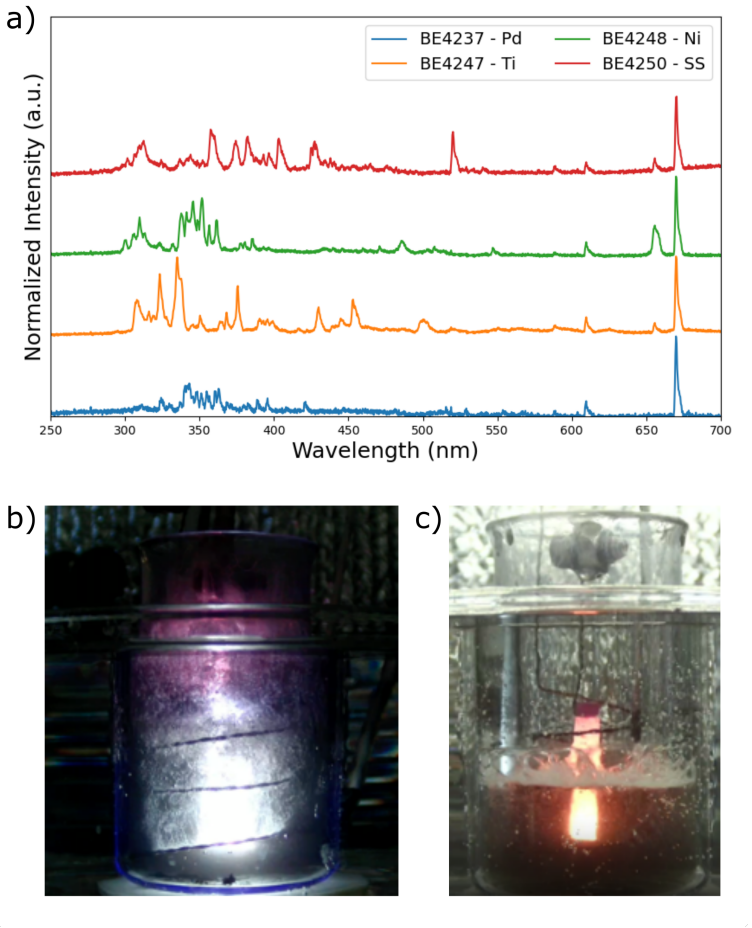



Fig. 7.4: High power experiments: a) Optical emission spectra. b) Plasma discharge glow when electrode is submerged. c) Sustained glow when electrode is exposed.

### 7.1.6 Conclusion

At no point during our replication efforts of the original Fleischmann and Pons experiments did we find compelling evidence for LENR. Whether this is due to insufficient details provided in the original studies or because the effect itself is not grounded in physical reality remains technically inconclusive. With the very limited data provided in Fleischmann's paper [26] – notably absent of any electrochemical or calorimetry figures – it is impossible to uncover the root cause of the discrepancies between their experimental outcome and our experimental outcomes. Although scientific rigor allows only for proof of a phenomenon's existence, not disproof, our extensive testing – including hundreds of LENR experiments and more than 20 sample-years – strongly suggests that no LENR effect can be reliably observed under any reasonable and experimentally obtainable conditions. These Fleischmann and Pons replications make up a small portion of the conditions we tested; the majority of our experimental efforts are documented in subsequent sections.

## 7.2 McKubre

### 7.2.1 Introduction

Michael McKubre studied cold fusion in palladium hydrides from 1989 to the early 2000s [74]. He was a researcher at SRI International (Menlo Park, CA), with a major portion of his research funding coming from EPRI (Electric Power Research Institute, Palo Alto, CA). Contrary to most other researchers in the LENR field, his work was funded by mainstream funding sources and carried out at mainstream institutions, enabling him to perform scientific work to higher standards than most contemporaries. Overall, his work is well documented. Most details are provided in two EPRI Technical Reports from 1994 and 1998, each of them measuring several hundred pages [101, 110]. Contrary to other researchers in the LENR field, he took a systematic approach, studying loading enhancers to maximize electrochemical loading, designed various open and closed calorimeters, characterized his calorimeters, and also employed various techniques to characterize materials and processes, as is common in the mainstream materials research community (e. g., mass spectroscopy).

McKubre reported excess heat was repeatedly observed if the palladium hydride was highly loaded ($>0.9$), the electrochemical loading current was sufficient ($>100\,\mathrm{mA/cm^2}$) and an incubation time of one week had passed [101].

### 7.2.2 Experiments

Cathode: In most experiments, McKubre used 3 mm diameter palladium rods, 30 to 50 mm long. Palladium (99.9 %) was supplied by Engelhard and machined to 3 mm diameter. After cleaning, they were annealed in vacuum for 2 hours at 850 °C [110, p. 3-27] or 3 hours at 800 °C [110, p. 3-8]. They note that other suppliers' palladium also worked well [101, p. 27].

Electrolytic Cell: In most experiments, a 0.5 mm diameter platinum wire (Engelhard) was helically wound around a cage made of silica rods and PTFE discs, surrounding the cathode (Fig. 7.5 a).

Electrolyte: 1 M LiOH or LiOD was used, obtained by dissolution of lithium (Aesar) in light water or heavy water [110].

Additives: McKubre added aluminum, silicon, boron or copper in concentrations of 200 ppm to many of his experiments, either in elemental or in oxide form [101, pp. vi, 2-2, 2-13]. He reported that silicon increases the loading and aluminum increases the longevity of loading [110, p. 3-48].

Electrochemical Conditions: Typical electrochemical current densities were 300 to 600 $mA/cm^2$, but occasionally up to 6.4 $A/cm^2$ [110, p. 1-3]. Current densities below 200 $mA/cm^2$ were found to yield the highest loadings [101, p. 2-2]. Sometimes, lower currents (10 $mA/cm^2$) were used [110, p. 3-8] and various types of current ramps were applied [110, pp. 2-15, 3A-5, 3A-8]. Typical durations were a few hundred hours, as excess heat was reported to occur no earlier than a week into the experiment [110]. Some experiments lasted thousands of hours.

Electromigration Conditions: The early studies did not contain electromigration / axial currents. In the later studies, axial currents of up to 7 A were applied [101, p. 3-13].

Loading: McKubre reported that electrolytic deuterium loadings up to 0.9 and protium loadings up to 0.95 were achieved [110, p. 2-5]. 61 % of their cells reached loadings > 90 % [101, p. 2-1]. He performed loading optimization studies in open system electrolytic cells, with up to ten cells running in parallel [101, p. v] and a total of over 100 loading experiments [110, p. 2-18]. Loading was inferred from measuring the resistance ratio, using a four-terminal AC measurement [110, p. 3-9]. It is not clear if the resistance was renormalized when several load-deload cycles were applied. Additives studied as potential loading enhancers included $As_2O_3$, sulfides, iodides, aluminum, zinc, bismuth, mercury and silica [110, p. 2-18]. As noted above, silicates were found to enhance loading [101, p. 2-12]. This could explain the observed higher loadings in quartz vessels compared to PTFE [101, p. 2-12]. Furthermore, pre-annealing of palladium at 850 °C for 3 h was found to increase loading [101, p. 2-2]. Contrary to Callisto's loading studies, McKubre found that arsenic(III) yielded very slow loading rates and no elevated loading [110, p. 2-24]. In agreement with other researchers [105], McKubre noted that slow loading can minimize crack formation and elevate loading [110, p. 2-16]. He also postulated that platinum may serve as loading inhibitor [110, p. 2-16] and that uniform electric fields increase the loading [101, p. 2-11].

Calorimetry: At the center of McKubre's studies were closed system mass flow calorimeters [110, p. iii]. The electrochemical cell was surrounded by heat transfer fluid (silicone oil), which was pumped at a constant rate and whose inlet as well as outlet temperatures were measured (Fig. 7.5 b) [110, p. 3-14]. The accuracy was specified as the greater of 50 mW or 0.5 % and the precision was the greater of 10 mW or 0.1 % [110, p. 1-3]. They also used other calorimeters in addition to mass flow calorimeters [101, p. 1-2], e. g., a Seebeck calorimeter [101, p. 3-3]. They used a compensation heater to correct for changes in electrochemical power so that the sum of the heater and electrochemical power input to the calorimeter was held constant, so the system remains isothermal regardless of EC power [110, p. 1-4]. COPs were typically reported with respect to the electrochemical input power only, so skepticism of the quoted COPs is warranted, as the total input power was up to 45 W regardless of EC power [110, pp. 1-3, 3-55], and a small percentage error in calorimetry could nullify the claimed excess heat.

### 7.2.3 Results and Assessment

In his 1994 report, the reported excess heat was up to 1.1 MJ and COPs were up to 3.5 [110]. Fig. 7.5c) shows a plot of excess powers compiled from Table 3-1 [110, p. 3-3]. The table shows that the COP of 340 % (in P19) corresponded to an excess power of 850 mW on top of an EC input power of 250 mW. The total input power (including the heater) was presumably 12 W. However, there were several hardware failures, some close to the reported excess heat events [110, p. 3A-63]. The axial current was 2 A. While no problems with the axial current in this experiment were reported, McKubre notes in a later experiment "During times when axial current is passing both loading information and calorimetry were seriously inaccurate: Calorimetry was poor because the axial input power was not measured at the calorimeter boundary." [101, p. 3-11] In our own research we have encountered inaccurate calorimetry when high axial currents were applied due to the

relatively large voltage loss (and thus power dissipation) in the lead wires compared to the sample. Even when the voltage is measured at the thermal system boundary, the location of heat dissipation is different from the location of electrochemical input power dissipation and can thus affect calorimetry. Calibration of these effects is further complicated by the fact that the sample resistance and thus the relative contribution of heat dissipation change as a function of loading.

While the claimed COP amounts to 350 % (3.5) compared to the EC input power, it is much less compared to the overall input power, when including the heater. McKubre specifies that the calorimeter has an accuracy of 0.5 % [110, p. 1-3], but the noise in the heat flow measurement is already 0.4 % [110, p. 3A-6]. This leaves very little error to input power measurement errors, heat source location dependent errors (heater vs. EC power vs. EM power) and errors due to pressure variations / recombination fluctuations in the headspace. We posit that a conservative estimate would raise the uncertainty of the excess power substantially. The fact that the noise in the heat flow is much larger than the uncertainty, exemplifies that the uncertainty was underestimated by McKubre [110, p. 3-24].

Other excess heat events reported by McKubre were well below 10 %, and could be due to the errors listed above. However, in contrast to P19, very limited data is available for those experiments.

The 1998 report fails to support or extend the claims made in the 1994 report [101, 110]. 30 isoperibolic calorimetry experiments and 24 mass flow calorimetry experiments were conducted, but only two of them showed excess heat. In experiment M1, the maximum excess power observed was 100±40 mW or 0.6 % of the total input power. The integrated energy was 27±12 kJ. This is close to the noise of the calorimeter. In experiment M4, two periods of excess heat, each about a day long, were observed. The maximum excess power was ~400 mW at 12 W input power, which is corresponds to 3.3 %. While this is low, it should be above the noise of the calorimeter. However, during the same period, the sample resistance exhibits a much higher noise than usual. This could be due to a bad contact, resulting in imperfect input power measurements or increased input power from the resistance measurement. Notably, when the resistance measurement noise subsides, the excess heat subsides.

The absence of strong evidence of excess heat after several years of research and numerous experiments with various calorimeters leads McKubre to the conclusion "With hindsight, we may now conclude that the presumption of repeatable excess heat production was premature, and that this has limited the progress achieved in this study." [101, p. 4-3]. Curiously, despite this, McKubre is regarded as a major scientific figure in the LENR field and as a proponent of the anomalous heat effect. Moreover, the frequently cited "conditions [...] characteristic of all cells yielding episodes of excess heat" [101, p. vi] (incubation time, loading >90 %, current density > 0.1 $A/cm^2$) were based only on those two above mentioned experiments.

### 7.2.4 Replication Experiments

McKubre's main achievement was to pose a list of conditions that are allegedly required, though not sufficient, to generate excess heat. These conditions include high loading (> 0.9), sufficient EC current (> 100 $mA/cm^2$) and long incubation times (>1 week). He obtained the high loadings using additives. For that reason, we decided to focus our replication attempts on fulfilling these conditions and employing the additives he used. We did not attempt to replicate the flow calorimeters, as we had our own well-characterized closed system calorimeters available (section 2). Performing the replications inside the HTcal calorimeters necessitated scaling the sample down to a 0.5 mm diameter, 28 mm long wire and adapting the currents in order to obtain comparable current densities. We added boron, silicon, aluminum, copper and silica at a concentration of 200 ppm (by mass) to the electrolyte (one additive per experiment). However, we did not find a noticeable increase in loading with any of these additives (Fig. 7.6). Each additive was used in three repeat cells

0060 fig3-11a, fig 3-7, BE4500

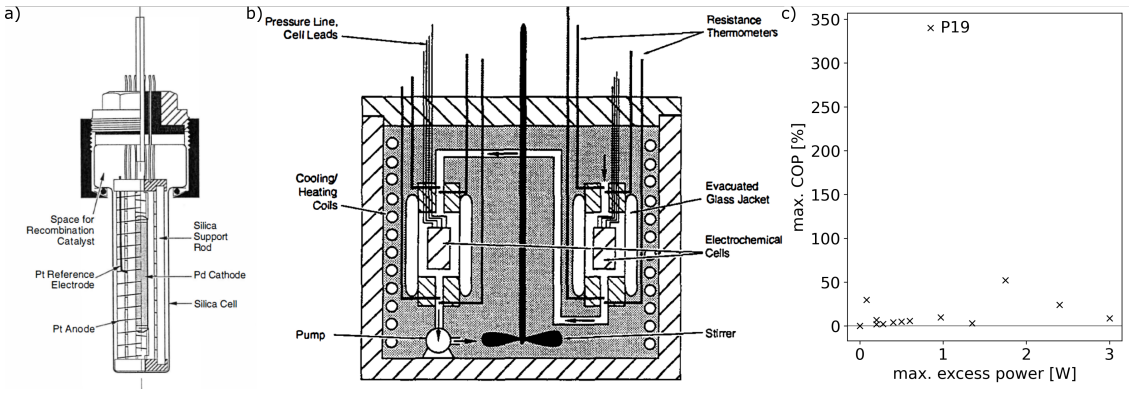



Fig. 7.5: a) Electrochemical cell for Pd resistance measurements [110, p. 3-25]. b) Schematic diagram of *differential calorimeter*. Note that McKubre used only one cell [110, p. 3-14]. c) Maximum COP (relative to EC power, disregarding heater power) and maximum excess power of 14 experiments. Plot generated by Callisto based on data listed in Table 3-1 [110, p. 3-3].

(except six for silica, two for silicon) and one reference cell (with a Pt cathode). EC was applied in power control mode at levels of [-0.2, -0.5, -1.0, -2.0] W for 10 h each with 10 h ramps to increase power (similar to McKubre). These power levels correspond to roughly [-0.1, -0.25, -0.5, -0.8] A/cm$^2$. No axial currents were applied (except for small currents to measure the loading). The total experiment durations were several hundred hours (similar to McKubre). Note that the spikes in COP are caused by the changes in input power and cancel each other out, as evidenced in the smooth $COP_e$ plot. (See section 2.5 for definition of $COP_e$.) The constant offset in some of the COPs can be attributed to drift in the calorimeter calibration. Some experiments stopped prematurely due to recombiner failure, causing pressure buildup and ultimately causing the system to open. We did not observe any measurable excess heat (Fig. 7.7).

### 7.2.5 Conclusion

We could not replicate the excess power reported by McKubre in his 1994 report [110]. First, we would like to note that even his 'most spectacular' excess heat was less than 10 % of the total input power (including the heater input power). In his later report [101], after four years of research, the largest reported excess heat was even lower, at 3 %. Luckily, McKubre provided a wealth of data in his reports. The datasets for both these experiments show hardware malfunction during or near the reported excess heat period. McKubre admits that during application of electromigration currents, the calorimetry was "seriously inaccurate". This applies to the first experiment with the 'most spectacular' excess heat. As noted above, during the second experiment (with 3 % excess heat), the loading measurement malfunctioned. We have observed various mechanisms which could cause false excess heat signals of similar magnitude (section 9.2). We therefore

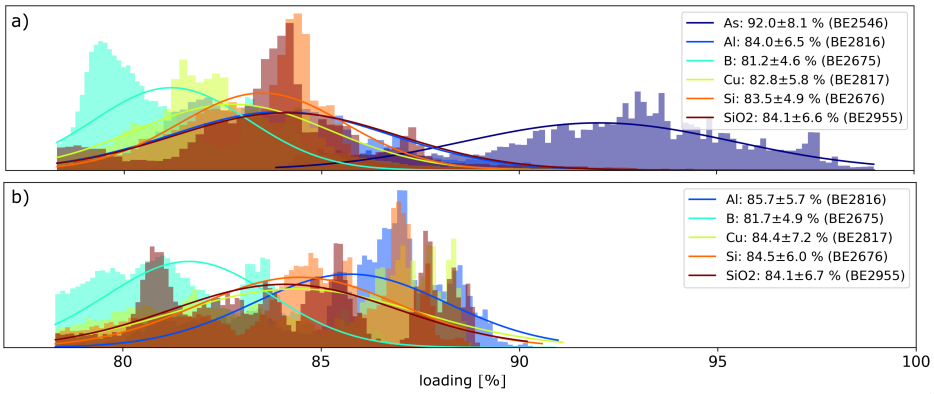



Fig. 7.6: Effect of additives on loading in heavy water. Arsenic was added in the form of 25 mM $NaAsO_2$ in 0.5 M LiOD electrolyte. All other additives were added at a concentration of 200 ppm by mass in 1 M LiOD electrolyte. a) EC current -100 $mA/cm^2$, b) EC current -300 $mA/cm^2$.

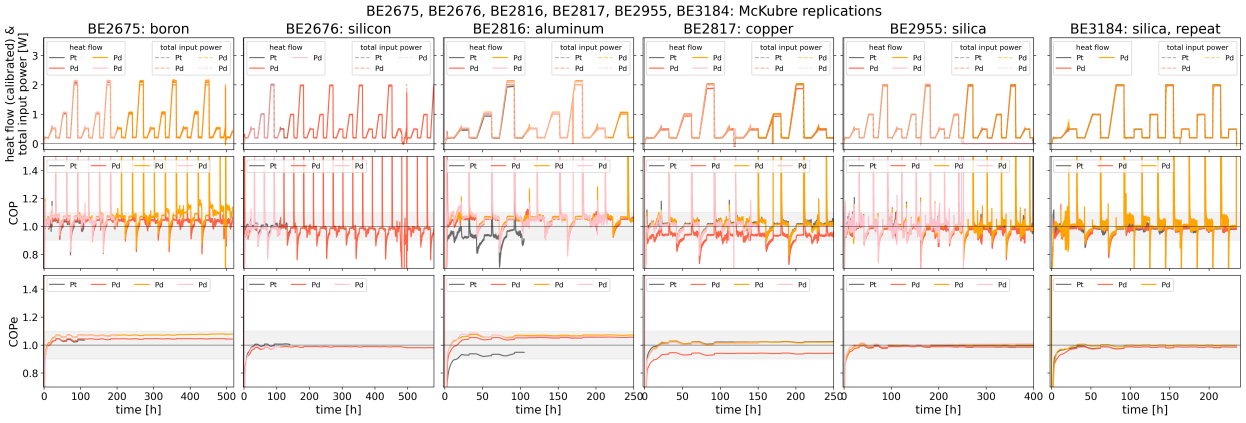



Fig. 7.7: Overview of McKubre replication attempts performed by Callisto, using various additives.

concur with McKubre that "With hindsight, we may now conclude that the presumption of repeatable excess heat production was premature" [101, p. 4-3].

## 7.3 Staker

### 7.3.1 Literature Review

Michael Staker published several works [237–239] claiming the successful observation of excess heat, similar to the original Fleischmann-Pons experiment that reported excess heat output compared to the expected heat from input power [240]. In his 2019 work 'Coupled Calorimetry and Resistivity Measurements, in Conjunction with an Emended and More Complete Phase Diagram of the Palladium-Isotopic Hydrogen System', Staker reports 100 % excess power (2.4 W of output with 1.2 W of input) after rapidly increasing the input current in two separate instances [237]. He also reports that aside from these two 'run away' events, that excess energy out of the system was 150 MJ/cm$^3$ of Pd for 46 days. The author cites the presence of three new, thermodynamically stable phases marked by super-abundant vacancies (SAV) as key factors leading to this excess heat event. Staker postulates that these SAV-phases ($\gamma$ ($Pd_7$ $VacD_{6-8}$), $\delta$ ($Pd_3VacD_4$– octahedral), $\delta$' ($Pd_3VacD_4$ – tetrahedral)) should be added to the Pd-H phase diagram to properly represent structural changes as a result of H (D) loading ≥70 % in the Pd structure. In this review we use 'H' to represent all of the isotopes of hydrogen and unless explicitly called out, all loadings refer to D. It was theorized that once enough of these SAV-phases were formed (specifically the $\delta$ and $\delta$' phases) they form a lattice arrangement of tubes that allowed ultra-high mobility of the intercalated $H^+$ ions. It is important to note that the author has presented no experimental evidence for these claims and are all based on his own theory.

Samples used in this experiment were unalloyed 0.5 mm diameter, 25.4 mm long Pd wires from Johnson-Matthey with Cu leads that were braze-bonded around the end of the Pd specimen and connected to a current-controlled DC power supply. The electrolyte was 18.0 ml of 0.5 mol LiOD in 99.8 % deuterium oxide from Cambridge Isotope Laboratory. The cells were constructed by nesting four slightly different size Pyrex test tubes, each separated by two O-rings and a thin air space. A Teflon top, sealed with an O-ring, excluded ambient atmosphere by allowing the positive pressure of $O_2$ and $D_2$ gas to exit through a capillary tube into a reservoir of vacuum pump oil. Electrolyte level in cells was maintained using a Harvard Apparatus Model 22 Digital Syringe Pump outfitted with two syringes, one with heavy water from Cambridge Isotope with 99.8 % D and one with double distilled light water. The input current for the experiments ranged from 442 to 535 mA. During these current applications, 10 to 18 °C temperature increases were observed when compared to the control cells [237].

Staker proposes that an anomalous heat event (AHE) occurs only after the formation of SAV-phases, Pd samples are highly loaded (H/Pd >1.14 according to his proposed phase diagram), and $H^+$ ions occupy the octahedral sites in the Pd-H lattice. Change in resistivity is used as a measure of H loading in Pd as well as phase changes. The combination of excess heat being accompanied by a decrease in resistance, instead of the expected increase due to their directly proportional relationship, is used as evidence that both the Pd-H $\delta$ – octahedral and $\delta$' – tetrahedral phases were formed (change in resistance and occupation by H ions) and $\delta$ – octahedral was occupied by H ions (yielding the production of excess heat).

In later works in 2023, Staker reports similar excess heat and power between 0.01 - 1.25 W but quenches the reaction in an ice bath [238, 241]. After equilibration, the reaction does not return to its previously elevated temperature and by extension does not exhibit any excess power or heat. The author uses this lack of continuation of the purported LENR event after returning to room temperature post-quench as evidence

supporting his theory of the intercalated $H^+$ ions occupying the Pd octahedral interstitial site ($\delta$) instead of the tetrahedral site ($\delta$') during AHE. He states that upon the quench, highly mobile $H^+$ ions hopped from the octahedral site to the $\delta$' – tetrahedral site which is reportedly more stable at lower temperatures. It is noteworthy that the author published a corrigendum to this work in 2024 stating that the value of the highest excess power density was 361 W/cm$^3$, not 240 W/cm$^3$, but the effective COP was significantly reduced from 2.0 (1.2 W input, 2.4 W output) to 1.67 (2.66 W input, 4.44 W output) [241].

In this work we assess the claims of AHE made by Staker through our own replication experiments. Additionally, we present a brief literature analysis of Stakers's published works addressing interesting points made, questions that arose, and discrepancies or missing data that hamper the work's scientific value.

### 7.3.2 Literature Analysis

Despite some interesting theories Staker presents in these works, there are many shortcomings in his studies that must be addressed for the good of the scientific community, specifically those in the LENR field interested in replicating these works. Chief among the areas of weakness in these publications is the lack of relevant, clear data supporting the claims of AHE. In the original 2019 publication [237], several key figures (i.e. calibrations and power plots) had hard to decipher data and unlabeled axes. All figures with time as the x-axis value were hard to decipher as the unit of time was 'data taken every 15 minutes'. Even after calculating several scenarios using the given time values, none of the time data aligned to total the reported 46 days of experiment duration. This leaves the reader and anyone trying to replicate the work to guess the incubation period before these 'runaway' events occur, as an incubation period has been theorized to be vital to AHE events [240]. A major shortcoming of the main figure is that the excess heat plots presented displayed very different heats for similar input powers. The author also uses a decrease in resistance as an indicator of both H/Pd loading and phase changes to the SAV-phases; however, there is no precedent for correlating a change in resistance to the formation of these phases. This is especially true considering that all references used validating the formation of SAV-phases were carried out under high-pressure and high temperature conditions (e. g. up to 6 GPa and 900 °C) [242–244].

In Staker's 2023 work 'The role of superabundant vacancy delta to delta prime transformation in stopping Fleischmann-Pons heat effect in palladium-deuterium' no new or relevant data was presented outside of a plot (figure 4 in [238]) illustrating deuteron oscillation in the Pd lattice [238]. Neither how these calculations were done nor the nature of the sample used are discussed in this work. This work also fails to present any resistance, temperature, XRD, or other relevant electrochemical and structural data to support the claims of AHE or crystal structure changes as a function of $H^+$ ion location in the Pd lattice. As an electrochemical paper claiming a phenomenon that releases excess power out compared to power in, the omission of any electrochemical data from the entire work is a cause for concern to any reader. The failure to produce these experimentally relevant pieces of data severely weaken the author's claims on the mechanism by which the purported excess heat event occurs and the effect lowering temperature has to stop it (i. e., $H^+$ transition from the octahedral site to the tetrahedral site at lower temperatures). Inclusion of a plot showing Pd resistance, H/Pd loading, and electrolyte and ambient temperature as a function of time would benefit this work immensely. Another weakness of this work is the author's continual self-citing of previous works [237,239] to support his claims in this work, especially as it relates to the existence of SAV-phases at room temperature and their role in AHE. Finally, considering that this work also had a significant corrigendum amending the original excess power claim (which was never presented in the original work), it calls the validity of the work as a whole into question.

### 7.3.3 Replication Experiments

In our studies we carried out multiple replications, both exact replications of Stakers original thermodynamically-open calorimeter (open-system) and also 'Staker-like' replications performed in thermodynamically-closed high throughput calorimeters (closed-system).

#### 7.3.3.1 Experimental Setup: Open-System Calorimetry

Our open-system was isoperibolic, whereas the closed-system had an independent heat flow measurement through a thermal bar (for details see section 2.9.1). Our open-system set-up is shown in Figure 7.8. This isoperibolic calorimeter has an RTD close to the electrodes for temperature monitoring. The cell consists of a test tube nested inside another test tube, similar to the original Staker experiment. Temperature is measured using RTDs connected to a NI cDAQ. Power was supplied using Keithley supplies and independent voltage measurement used Keysight 34661A DMMs. We used 30 mm length, 0.5 mm diameter Pd wire from various wire manufacturers (described in the list below) and Pt counter electrodes wrapped around the sample retention. Resistance was monitored using 2-wire and 4-wire NI square wave measurements for the open- and closed-cell testing, respectively. These samples were exposed to a gentle ($\leq$50 mA/cm$^2$) 3-cycle loading-deloading pre-treatment in either 18 or 44 mL of 0.5 M LiOH depending on open or closed cell testing. The temperature of the enclosure was maintained at ~30 °C. Temperatures inside the cell were measured using a NI cDAQ with Pt100 RTDs. A typical experiment's duration was one week and hundreds of days (300+) for open-system and closed-system tests respectively. Over the course of these studies we measured the heat of Pd and Pt cathodes exposed to electromigration (EM) current and control cells exposed to standard electrochemical (EC) current. We also carried out post-mortem spectroscopic analysis (i. e., scanning electron microscopy (SEM) and energy dispersive X-ray spectroscopy (EDS)) to observe macroscopic structural changes and surface chemical composition. We did not investigate Staker's claims of the existence of SAV-phases and their purported necessity in LENR reactions in this work.

In our open-system testing we used conditions matching the details reported by Staker as closely as possible in addition to many tests with variations for completeness. These conditions are described in the list below:

- Pd Vendor: Johnson Matthey, Goodfellow, Sigma Aldrich
- Pd Form Factor: 0.5 mm diameter wire, 0.5 mm thick foil
- Electromigration Field: 0 to 35 mV/cm (~15 to 35 mV/cm)
- Lithium Isotope: $^6$LiOD (95 % $^6$Li), $^7$LiOD (92.5 % $^7$Li)
- EC and EM Inputs: EC up to 100 µHz – 100 Hz, DC ¿95 % DC, and AC EM (up to 1 kHz)
- Pd Pre-treatment: Annealing, w/ and w/o load-deload cycling before 'active' cycle, aqua regia etch
- Vessel Material: Pyrex (borosilicate) glass, Perfluoroalkoxy alkane (PFA), Quartz

#### 7.3.3.2 Experimental Setup: Closed-System Calorimetry

The closed-cell experiments were carried out in similar conditions with small variations such as: 4-wire resistance measurements, 1.8 to 2.4 W active cycle, and EM constant power 0.01 W (pre-cycle) and 0.1 W (active cycle). Regular duration experiments were performed over 80 to 90 days and ultra-long duration

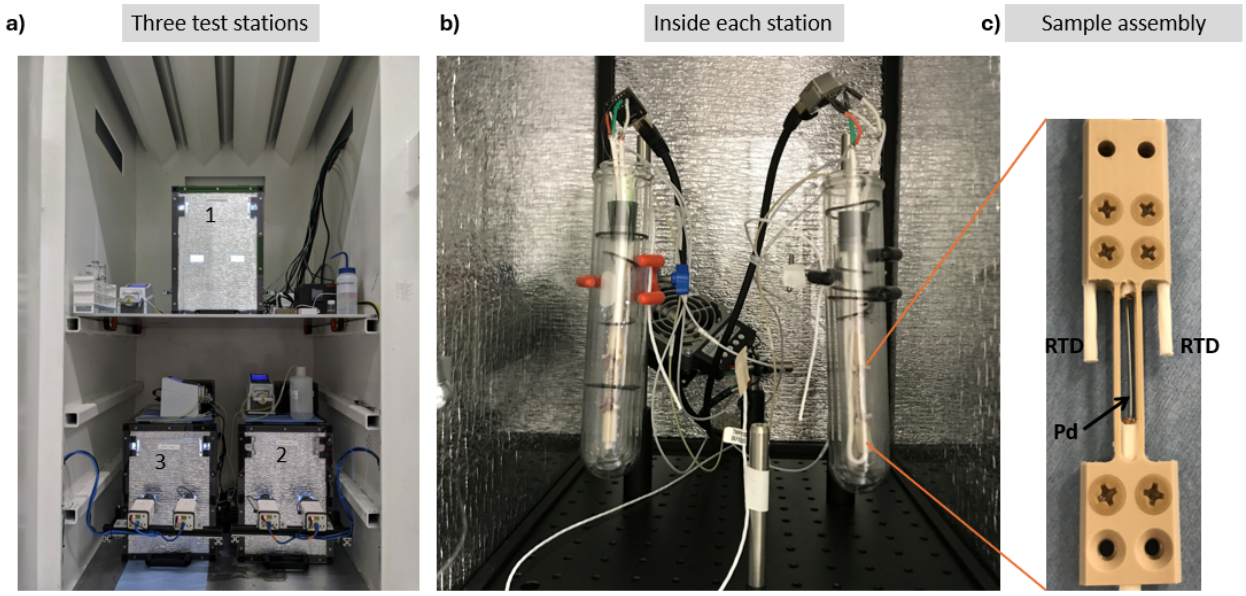



Fig. 7.8: Image of our Staker replication apparatus. The thermal enclosures with connections for the resistance temperature detectors (RTDs) and electrical sensors.(a) A visual depiction of our cells containing Pd cathode, Pt anode, 2 RTDs, electrochemical current controlled make-up water inlet, and 4-wire resistance ratio measurement on cathode. (b) A representative image of the sample assembly with the Pd cathode and RTDs visible. Pt counter electrode and 4-wire resistance sense leads not shown.(c)

experiments were carried out over 250 days. In one of the ultra-long duration experiments, the temperature (of the enclosure and the cold plate) was increased from 30 °C to 40 °C after ~5150 h in order to achieve an electrolyte temperature that is closer to the electrolyte temperatures recorded by Staker [93].

#### 7.3.3.3 Results

Figure 7.9 summarizes the COP (previously described) results for both long duration open-cell (Fig. 7.9a) and closed-cell calorimetry experiments (Fig. 7.9b). As shown in Fig. 7.9a) we include an upper bound of the COP's error resulting from foaming and gradual electrolyte level change. We corroborated this by including cameras in our open-cell systems which recorded the samples at all times. In our studies we found that foaming and electrolyte level change was almost always accompanied by a large heat flow effect that could be interpreted as excess heat. It is suspected that this combination of changes to the electrolyte eventually exposes ~30 to 40 % of the cathode to the headspace and foam, and is responsible for the spikes in COP. The several green traces depicting the long-duration tests exhibit this behavior, defining the upper error bounds near a COP of 1.6. Our direct replications of Staker's conditions (Figure 7.9a, blue trace) did not show any elevated heat that could not be explained by these effects. Our longest direct replication of Staker's work, surpassing 46 days (the duration of Staker's purportedly successful experiment showing large excess heat) is shown in red, and does not indicate any excess heat. From the onset of the experiment we actually observed a suppressed COP before returning to baseline briefly at 600 h and then being suppressed until equilibration at ~1000 h. We believe the reason for this suppression is likely changes in the electrolyte level.

Notwithstanding our attempts to replicate the original Staker experiments as closely as possible, it is clear that many improvements can be made by transitioning to closed-cell calorimetry testing. These improvements include: elimination of COP error due to electrolyte level changes, lower calorimetry errors due to foaming, PEEK vessel liners enabling longer duration experiments compared to borosilicate vessels, constant power EM in order to eliminate transient input power signals compared to Staker's current controlled EM, and the use of integrated recombiners such that the heat of recombination of $H_2$–$O_2$ remains in the thermal envelope of the vessel. We have observed the formation of an overlayer – coined 'Coating X'– on the Pd cathode surface typically comprised of Cu, Fe, Zn and other elements in varying concentrations depending on the electrochemical environment. We theorize that this overlayer acts a 'Tafel poison', preventing the deloading process via the Tafel pathway and leading to higher loadings. It is of note that Staker does not discuss any surface depositions on his samples.

Figure 7.9b shows a summary of our results from a three-month long closed-system Staker-like experiment without interruption, with Pd cathodes under various stimulation conditions and one Pt control. All cell COPs remain near unity for the majority of the testing period, outside of some suppressed heat in Cell 2 starting at ~83 days (which can occur when a closed cell becomes open following over-pressure activation of a protective check valve). The spikes in COP observed are transient effects of input power changes.

The results of the ultra-long duration experiments are shown in Fig. 7.10. The full dataset is available in the Appendix (section A.1). The EC power was cycled between [0.8, 2.4, 2.0] W (loading polarity) every 10 h, but some cells hit the compliance voltage of the SMU, thus limiting the current. The increased cell resistance was presumably due to buildup of coating on the electrode and due to loss of electrolyte conductivity as salt deposits formed in the headspace. The spike in excess heat at 6400 h is an artifact due to a server outage lasting a few hours. Due to faulty communication between the NI SMU and the gRPC server, no data was recorded (interpreted as 0 power), but the SMU kept on applying the most recent set current before the outage occurred. The electromigration current failed to be applied in the platinum control cell (cell0) after ~900 h, presumably due to a bad contact. Non-steady state recombination (possibly due to foaming or salt

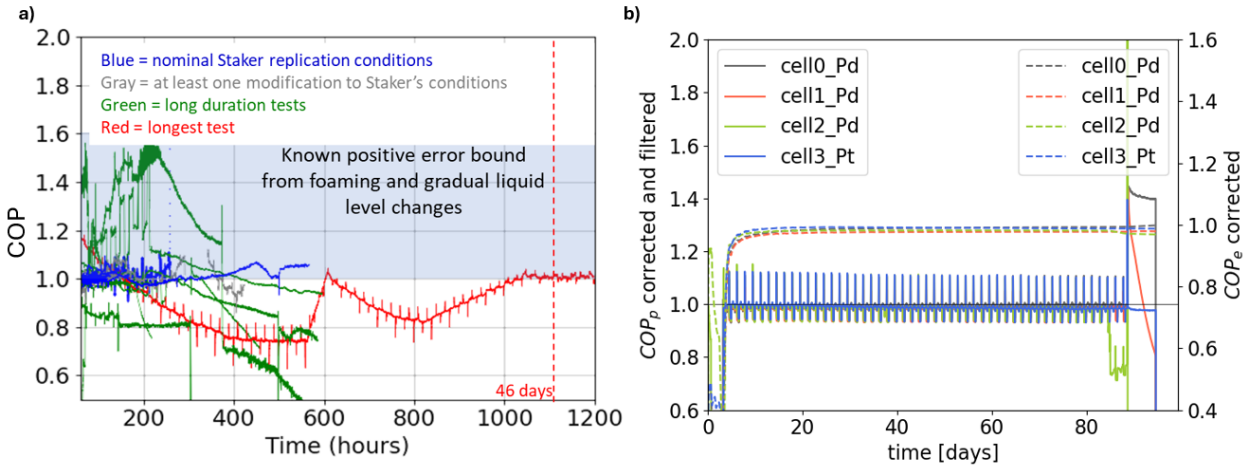



Fig. 7.9: Summary figures of thermodynamically-open calorimetry (a) and thermodynamically-closed calorimetry (b) Staker and Staker-like replications. Figures show the reported COP as a function of time for various experimental conditions described in the key of each figure. In the thermodynamically-closed calorimetry the conditions of the cells are as follows: Cells 0 and 1: nominal Staker replication conditions (i.e., Pd with EM), Cell 2: Pd without EM, and Cell 3: Pt with EM. $COP_p$ = COP power. $COP_e$ = COP energy (integral of power out over integral of power in). The spikes in panel b) are due to changes in input power.

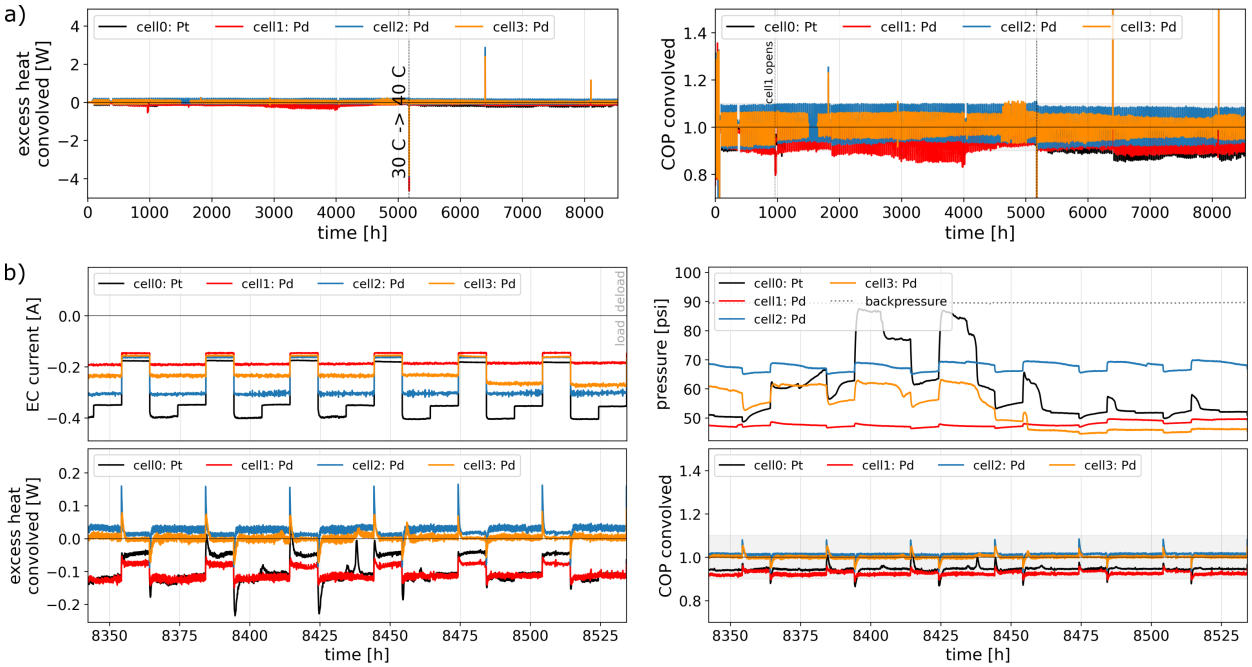


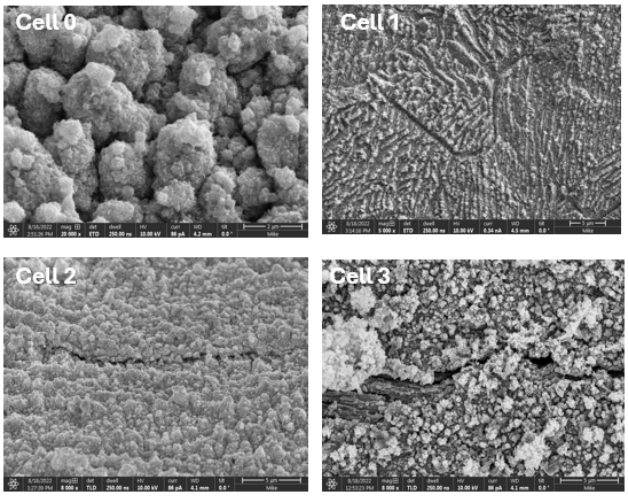

Fig. 7.10: Ultra-long duration Staker-like replication in an HTcal. a) Overview of excess heat and COP during the full experiment. b) Zoom into an arbitrary week towards the end of the ultra-long duration experiment.

buildup on the recombiner) led to build-up and release of pressure in the headspace, resulting in transient suppressions and peaks in heat flow due to the lack or excess of heat of recombination. This is particular prevalent in the platinum control cell (cell0). Cell3 likely experienced a drift in calorimeter efficiency since the last calibration at the beginning of this experiment, leading to a suppressed heat flow. No unexplained excess heat signals were observed over the entire duration of the 250 day experiment.

We observed in a closed-system Staker-like replication (experiment BE1476 shown in Figure 7.9b and Figure 7.11) cells (Cells 0 and 1) that when EC stopped, the heatflows did not decay in the same manner, possibly due to different deloading kinetics. In our control cell with Pd that received no EM current (Cell 2) behavior was standard when EC was stopped, i.e., heatflow fell to 0 as expected. Similarly in our Pt control (Cell 3) when EC stopped, heat flow falls to the expected amount for the applied EM power. While no instances of AHE were observed over the nearly 90 day period of testing, we did observe nearly 30 excursions that have all been proven to be consistent with temporary recombiner failure. These recombination events highlight the importance of accurate calorimetry and energy accounting to avoid mis-attributing energy released from chemical events to small, localized LENR events. Additionally, the results show the benefit of closed-cell calorimetry especially relating to the quality of data that can be achieved in the absence of excessive foaming, electrolyte level change, chemical energy of oxyhydrogen leaving the vessel, and the other challenges observed in open cells.

Figure 7.11 depicts post-mortem SEM and EDS sample analysis for the long-duration Staker-like replication in the thermodynamically-closed calorimeter. The SEM images show that all cells had surface depo-

a)




b)

| | Cell0-BD2315 | Cell1-BD2316 | Cell2-BD2317 | Cell3-BD2318 |
|---|---|---|---|---|
| C | 12.49 | 23.32 | 20.77 | 26.00 |
| O | 37.14 | 25.63 | 30.89 | 25.77 |
| Sn | 8.84 | <1% | 5.54 | 12.19 |
| Pt | 2.88 | 6.43 | 5.48 | 30.26 |
| Pb | 3.13 | 0.68 | 4.06 | 2.42 |
| Cu | 5.78 | 1.48 | 2.30 | 1.55 |
| Zn | 1.30 | 1.53 | <1% | 1.10 |
| Pd | 20.48 | 21.57 | 24.42 | <1% |
| Al | 1.86 | 0.77 | 1.11 | <1% |
| Fe | 9.90 | 19.27 | 6.28 | <1% |
| Cr | 4.06 | 1.49 | 6.40 | <1% |
| F | <1% | <1% | 2.26 | 10.26 |

* Values in the table are atomic %, averaging at least 3 spots per sample.

Fig. 7.11: Scanning electron microscopy (SEM) images of each cell after the long duration Staker-like replication in the thermodynamically-closed calorimeter (BE1476). Scale bar for Cell 0 is 2 $\mu$m and 5 $\mu$m for Cells 1-3.(a) Cells 0 and 1: nominal Staker replication conditions, Cell 2: Pd without EM, and Cell 3: Pt with EM. A table summarizing the average atomic percent (from three different sample locations) of elements found on the surface of each cell's cathode determined by energy dispersive X-ray spectroscopy (EDS).(b)

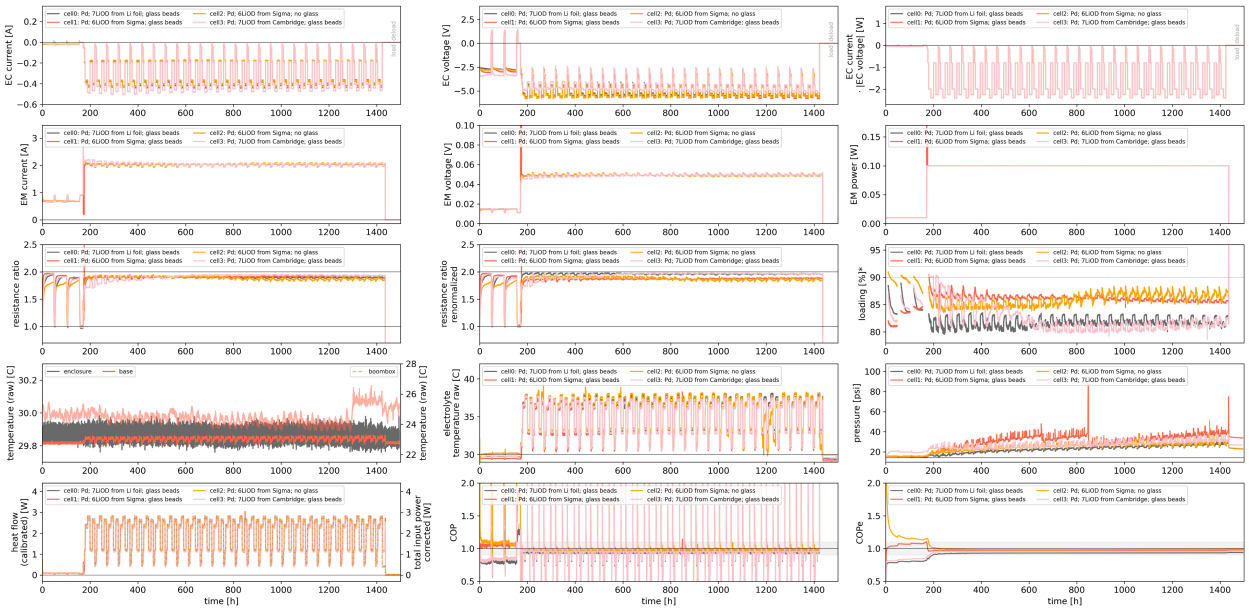



Fig. 7.12: Summary of all relevant experimental components of an approximately 60-day Staker-like experiment with glass bead additives. (From left to right) The first row shows the EC current, voltage, and power. The second row shows the EM current, voltage, and power. The third row shows the Pd resistance ratios, the resistance ratios renormalized to a baseline period with no input power, and the H loading percentage calculated from the Zhang formula. The fourth row shows temperature of system's enclosure, base plate, and external 'boombox', electrolyte temperature, and the pressure for each cell. The final row shows the calibrated heat flow, COP (power), and $\mathrm{COP}_e$.

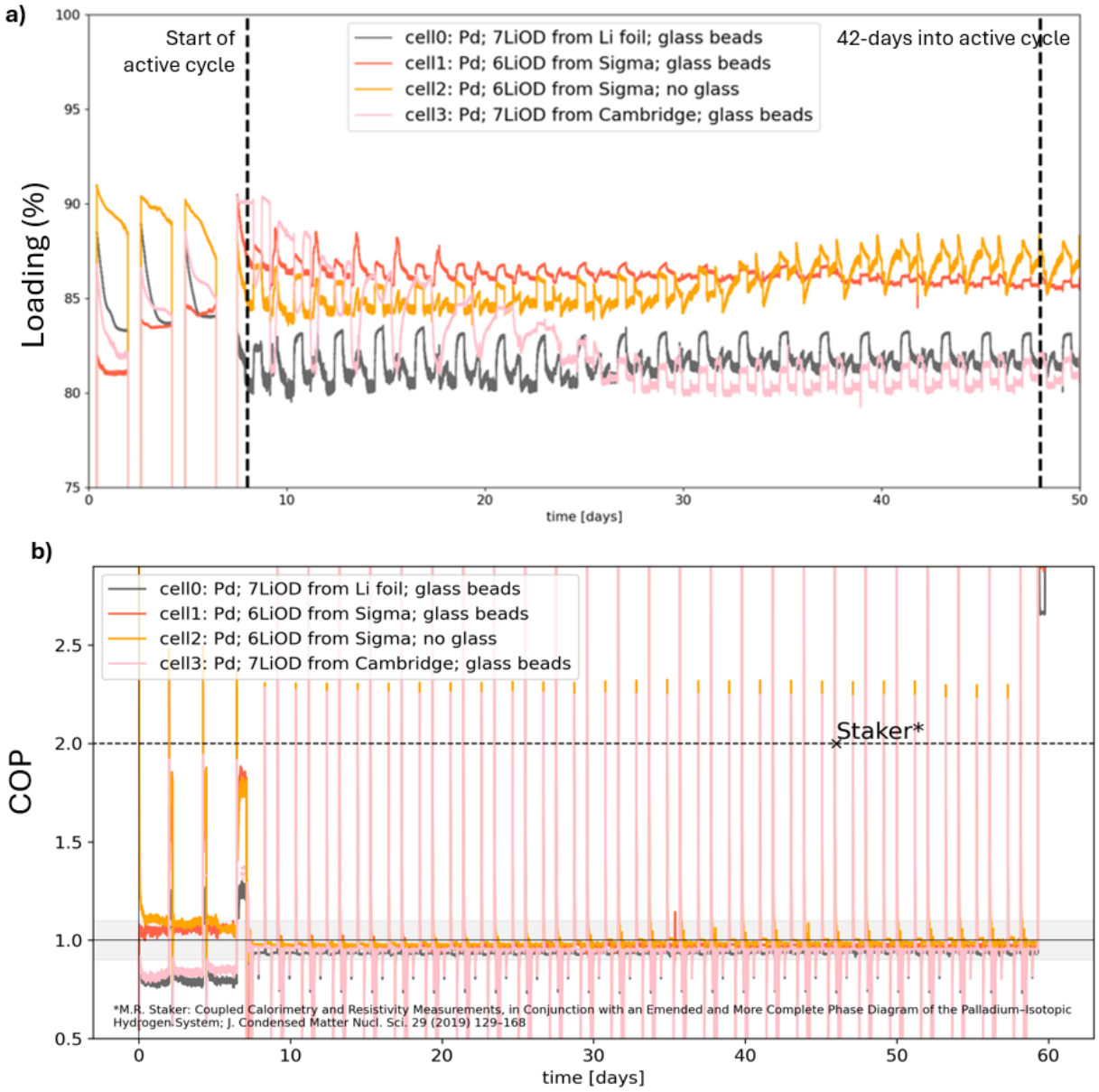



Fig. 7.13: Loading of all cells from 60-day long-duration Staker-like test with glass bead additive and various electrolytes. Loadings remained above 80 % for nearly all cells for the entire experiment. (a) COP for each cell with error band (grey).(b) All steady-state COPs were near unity for the duration of the experiment. All COP outliers (vertical lines) are due to heat flow transients when input power was changed as prescribed. A dashed horizontal indicator showing Staker's originally reported excess power COP is included for reference.

sitions regardless of their electrochemical treatment. The EDS summary table shows that direct replications (Cells 0 and 1) and controls (Cells 2 and 3) all had elements of 'Coating-X' (Cu, Fe, and Zn) present on their surfaces. While these elements are to be expected to be present after our experiments due to known electrolyte impurities, other elements such as Sn, Pb, and Cr are likely due to hardware degradation resulting from the foaming electrolyte contacting soldered leads. These soldered connections were shielded with PTFE shrink wrap and Miccrostop (Brand of Tolber) but over the course of long duration experiments electrolyte can work its way past these protective measures. These elements from the degradation of this solder are not observed in Cell 1, likely because there was no intermittent recombiner failure as occurred in other cells (Figure 7.11b).

Figure 7.12 is a summary figure of a 60 day Staker-like replication in closed-cell calorimeters with glass beads additives. These glass beads were introduced to mimic the electrochemical environment of the original experiment which Staker carried out in a quartz vessel. Considering the fact that alkaline electrolytes – especially at high temperatures – have been observed to attack quartz, [245, 246] in conjunction with many LENR reports being carried out in quartz vessels, it is feasible that some unintended Si additive could play a role in triggering AHE. Figure 7.13 shows the loading (7.13a) and COP (7.13b) of all cells in the the 60 day Staker-like replication experiment. The loading for each cell is shown to be above 80 % for duration of the experiment with vertical markers showing the start of EM stimulation after pre-cycling and 42 day mark, respectively. This 42 day mark is to mark a comparable time of experimentation to Staker's experiment. As previously discussed, maintaining high loadings is reportedly a prerequisite for an AHE event to be observed, though we concede our loadings did not remain as high as reported by Staker in his works (however owing to Staker's use of only a 2-point resistance measurement, rather than 4-point, the accuracy of his loading claims are subject to skepticism). In Figure 7.13b we show the COP for all cells over the duration of the experiment with COP error bars highlighted in grey and a horizontal marker depicting Staker's original claim of COP 2.0 (later retracted to 1.67) excess power for reference. The COP outliers (vertical lines) are due to heat flow transients when input power changes as prescribed. They cancel out with those outliers induced by the changes in input power in the opposite direction. During the duration of this experiment we did not observe any AHE events or unaccounted excess heat. Any excursions were readily explained by energy accounting and determined to be chemical in nature (i.e., recombination events) and not nuclear.

#### 7.3.3.4 Experimental Conditions: UHTP

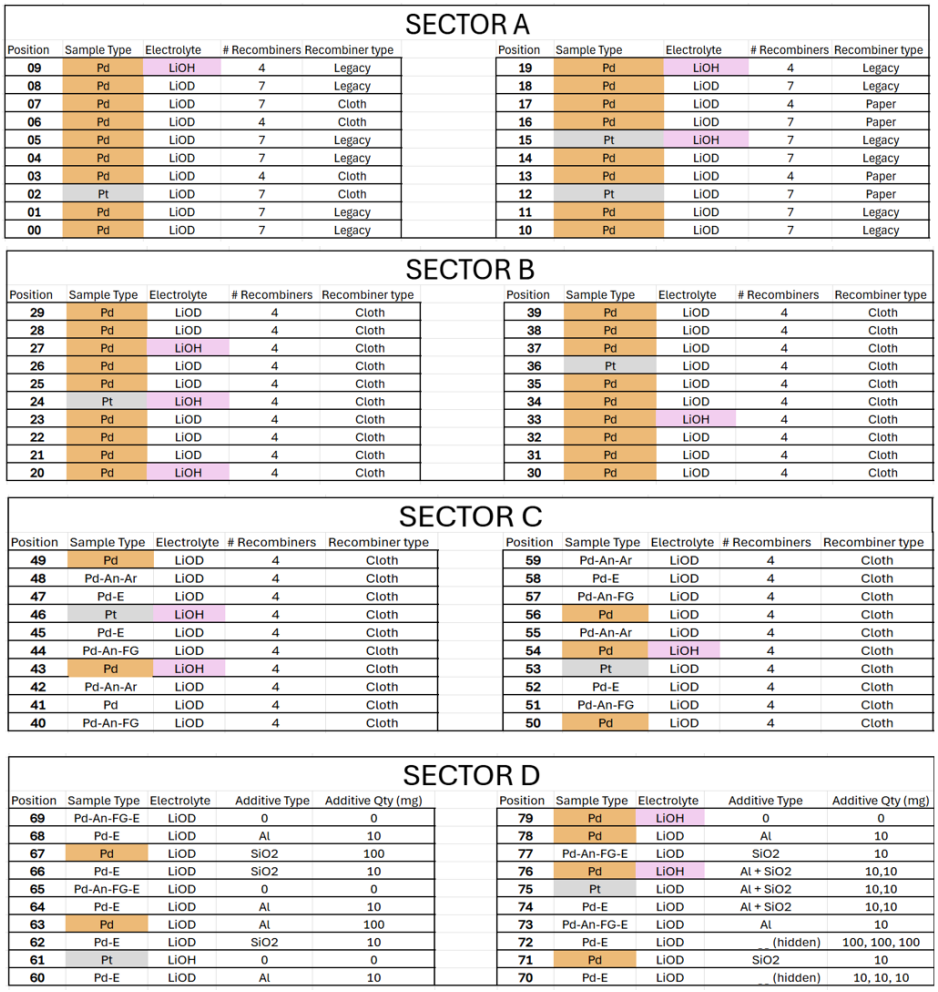
The UHTP calorimetry system was designed to replicate experiments inspired by Staker's report. Most critically, it has the option to apply an electromigration current along the wire sample. See section 2.10 for calorimeter details. The experimental campaign detailed in this section is our first long duration experiment (BE4445) with 80 experimental cells (sectors A - D) as the last 20 cells in sector E were still being brought online. In addition to Staker-like conditions, we also found inspiration in other reports of AHE, in particular in the selection of additives [101] and we designed the experiments accordingly.

Figure 7.14 shows a summary of the conditions for each of the experimental cells in the UHTP system. Each cell contained a 0.5 mm diameter and 30 mm long Pd (or Pt control) cathode. The Pd cathodes were either used as received, annealed in argon, annealed in forming gas, or etched in acid. Each cell had 48 ml of 0.5 M LiOD for active cells or 0.5 M LiOH for control cells. The EC treatment for each sector was roughly similar for every sector except Sector B, which did not receive electromigration (EM) current. The EC treatment started with a pre-cycle of the samples undergoing the following steps:

- EC was ramped to a cathodic 130 mW over 2 hours and held at that negative bias for 7 hours.

- EC was ramped to 0 mW over 1 hour and held at open circuit voltage for 2 hours.
- Samples were actively deloaded at 1.2 V and 1.4 V for 3 and 9 hours, respectively.
- Samples allowed to dwell for 5 hours.

This pre-cycling process was repeated three times. For the EC/EM loading cycles a 3 A EM current was applied to sectors A, C, and D for the duration of the experiment, with sector B receiving no EM current. While EM power was constantly being applied, the samples were ramped to 130 mW (negative bias) over a two hour period. The power was held constant at a cathodic 130 mW, 300 mW, and 1 W for 12 hours each. This is shown in the input power plot in Figure 7.15. This constant power application loop was repeated continually for 50 days. Considering we ran 80 samples in parallel, the cumulative time of calorimetry amounted to 11 years in this single experiment.



SECTOR A

| Position | Sample Type | Electrolyte | # Recombiners | Recombiner type |
|---|---|---|---|---|
| 09 | Pd | LiOH | 4 | Legacy |
| 08 | Pd | LiOD | 7 | Legacy |
| 07 | Pd | LiOD | 7 | Cloth |
| 06 | Pd | LiOD | 4 | Cloth |
| 05 | Pd | LiOD | 7 | Legacy |
| 04 | Pd | LiOD | 7 | Legacy |
| 03 | Pd | LiOD | 4 | Cloth |
| 02 | Pt | LiOD | 7 | Cloth |
| 01 | Pd | LiOD | 7 | Legacy |
| 00 | Pd | LiOD | 7 | Legacy |

| Position | Sample Type | Electrolyte | # Recombiners | Recombiner type |
|---|---|---|---|---|
| 19 | Pd | LiOH | 4 | Legacy |
| 18 | Pd | LiOD | 7 | Legacy |
| 17 | Pd | LiOD | 4 | Paper |
| 16 | Pd | LiOD | 7 | Paper |
| 15 | Pt | LiOH | 7 | Legacy |
| 14 | Pd | LiOD | 7 | Legacy |
| 13 | Pd | LiOD | 4 | Paper |
| 12 | Pt | LiOD | 7 | Paper |
| 11 | Pd | LiOD | 7 | Legacy |
| 10 | Pd | LiOD | 7 | Legacy |

SECTOR B

| Position | Sample Type | Electrolyte | # Recombiners | Recombiner type |
|---|---|---|---|---|
| 29 | Pd | LiOD | 4 | Cloth |
| 28 | Pd | LiOD | 4 | Cloth |
| 27 | Pd | LiOH | 4 | Cloth |
| 26 | Pd | LiOD | 4 | Cloth |
| 25 | Pd | LiOD | 4 | Cloth |
| 24 | Pt | LiOH | 4 | Cloth |
| 23 | Pd | LiOD | 4 | Cloth |
| 22 | Pd | LiOD | 4 | Cloth |
| 21 | Pd | LiOD | 4 | Cloth |
| 20 | Pd | LiOH | 4 | Cloth |

| Position | Sample Type | Electrolyte | # Recombiners | Recombiner type |
|---|---|---|---|---|
| 39 | Pd | LiOD | 4 | Cloth |
| 38 | Pd | LiOD | 4 | Cloth |
| 37 | Pd | LiOD | 4 | Cloth |
| 36 | Pt | LiOD | 4 | Cloth |
| 35 | Pd | LiOD | 4 | Cloth |
| 34 | Pd | LiOD | 4 | Cloth |
| 33 | Pd | LiOH | 4 | Cloth |
| 32 | Pd | LiOD | 4 | Cloth |
| 31 | Pd | LiOD | 4 | Cloth |
| 30 | Pd | LiOD | 4 | Cloth |

SECTOR C

| Position | Sample Type | Electrolyte | # Recombiners | Recombiner type |
|---|---|---|---|---|
| 49 | Pd | LiOD | 4 | Cloth |
| 48 | Pd-An-Ar | LiOD | 4 | Cloth |
| 47 | Pd-E | LiOD | 4 | Cloth |
| 46 | Pt | LiOH | 4 | Cloth |
| 45 | Pd-E | LiOD | 4 | Cloth |
| 44 | Pd-An-FG | LiOD | 4 | Cloth |
| 43 | Pd | LiOH | 4 | Cloth |
| 42 | Pd-An-Ar | LiOD | 4 | Cloth |
| 41 | Pd | LiOD | 4 | Cloth |
| 40 | Pd-An-FG | LiOD | 4 | Cloth |

| Position | Sample Type | Electrolyte | # Recombiners | Recombiner type |
|---|---|---|---|---|
| 59 | Pd-An-Ar | LiOD | 4 | Cloth |
| 58 | Pd-E | LiOD | 4 | Cloth |
| 57 | Pd-An-FG | LiOD | 4 | Cloth |
| 56 | Pd | LiOD | 4 | Cloth |
| 55 | Pd-An-Ar | LiOD | 4 | Cloth |
| 54 | Pd | LiOH | 4 | Cloth |
| 53 | Pt | LiOD | 4 | Cloth |
| 52 | Pd-E | LiOD | 4 | Cloth |
| 51 | Pd-An-FG | LiOD | 4 | Cloth |
| 50 | Pd | LiOD | 4 | Cloth |

SECTOR D

| Position | Sample Type | Electrolyte | Additive Type | Additive Qty (mg) |
|---|---|---|---|---|
| 69 | Pd-An-FG-E | LiOD | 0 | 0 |
| 68 | Pd-E | LiOD | Al | 10 |
| 67 | Pd | LiOD | SiO2 | 100 |
| 66 | Pd-E | LiOD | SiO2 | 10 |
| 65 | Pd-An-FG-E | LiOD | 0 | 0 |
| 64 | Pd-E | LiOD | Al | 10 |
| 63 | Pd | LiOD | Al | 100 |
| 62 | Pd-E | LiOD | SiO2 | 10 |
| 61 | Pt | LiOH | 0 | 0 |
| 60 | Pd-E | LiOD | Al | 10 |

| Position | Sample Type | Electrolyte | Additive Type | Additive Qty (mg) |
|---|---|---|---|---|
| 79 | Pd | LiOH | 0 | 0 |
| 78 | Pd | LiOD | Al | 10 |
| 77 | Pd-An-FG-E | LiOD | SiO2 | 10 |
| 76 | Pd | LiOH | Al + SiO2 | 10,10 |
| 75 | Pt | LiOD | Al + SiO2 | 10,10 |
| 74 | Pd-E | LiOD | Al + SiO2 | 10,10 |
| 73 | Pd-An-FG-E | LiOD | Al | 10 |
| 72 | Pd-E | LiOD | _ (hidden) | 100, 100, 100 |
| 71 | Pd | LiOD | SiO2 | 10 |
| 70 | Pd-E | LiOD | _ (hidden) | 10, 10, 10 |

Fig. 7.14: Summary plots of each of the 80 experimental cells composition including cell number, sample type, electrolyte, number of recombiners and their type, and additive type and quantity. All electrolyte concentrations are 0.5 M. The key for the Pd samples is as follows: Pd (Palladium), Pt (Platinum), Pd-Ar (Palladium - As received), Pd-An-Ar (Palladium annealed in argon), Pd-An-FG (Palladium annealed in forming gas), and Pd-E (Palladium etched).

#### 7.3.3.5 Results: UHTP

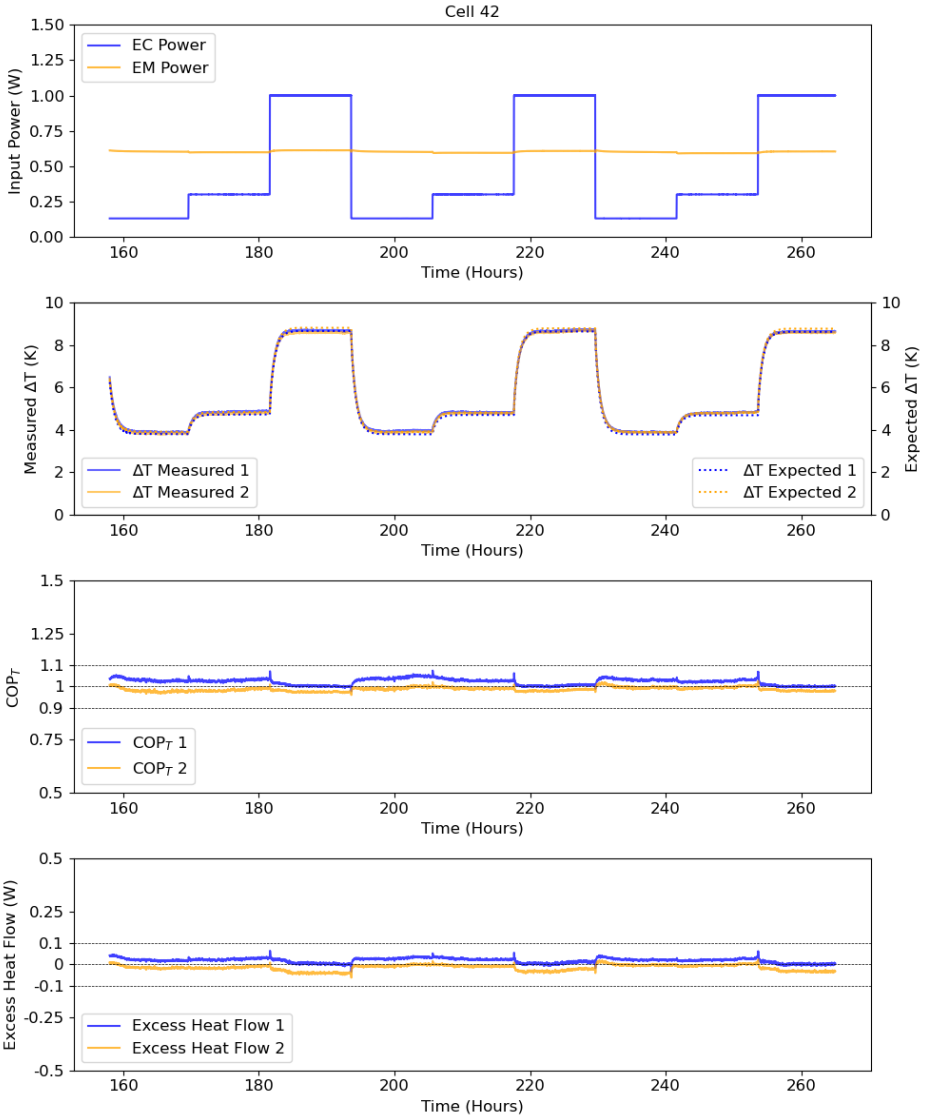



Fig. 7.15: A representative example of an experimental cell (Cell 42, Pd in LiOD) and the standard data streams monitored in the UHTP system for an 100 hour window during the experiment. Data include (from top to bottom) input power (both EC and EM Power), measured $\Delta$ T, COP$_T$, and excess heat flow.

Figure 7.15 is a representative example of an experimental cell and the data streams we typically monitor in the UHTP system. These include input power (W), measured $\Delta$T (K), COP$_T$, and excess heat flow (W).

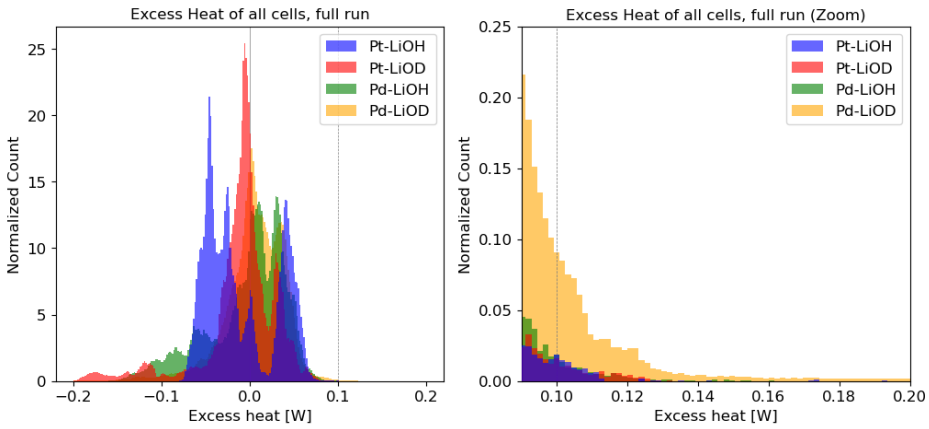



Fig. 7.16: Histogram comparing excess heat for all 80 experimental cells. The left panel shows excess heat of control cells (Pt in LiOH) in blue, Pt in LiOD in red, Pd in LiOH in green, and Pd in LiOD in yellow. The right panel of the figure is a zoom in on any excess heat above 0.1 W. Counts are normalized to cause the total area under the histogram to equal to one. This allows comparison between different sized data sets (i. e., 18 control cells compared to 62 active cells).

Measured $\Delta$T is calculated by subtracting the expected temperature from the measured temperature. In this example cell the electrochemical stimulation scheme is shown in the input power plot (7.15) where input power is held constant for ~10 hours before increasing to the next power step. The effect of these power increases can clearly be seen in the $\Delta$ T plot. Small changes in the $\mathrm{COP_T}$ and excess heat flow plots can be seen when changes in input power occur. These changes are well within the error bands shown and thus can not be ruled out as an excess heat event, but are likely caused by transients due to the change in input power change. These data streams combined give us reliable readings across all cells in the system and allow us to view relevant conditions in the event of any AHE. They also allow us to rule out any false positives due to various failure modes we have observed in previous experiments (i. e., hardware failure, electrode contact error, and spontaneous oxyhydrogen recombination after a failing recombiner recovered).

The results of our first UHTP experimental campaign are shown in Figures 7.15 ($\mathrm{COP}_T$ and excess heat) and 7.16. While we did not observe a significant excess heat, we were able to reliably track heat flow of 80 individual cells and generate meaningful statistics, a testament to both the highly parallel and sensitive nature of the UHTP system. Figure 7.16 shows a comparison of excess heat with control cells (Pt in LiOH) in blue, Pt in LiOD in red, Pd in LiOH in green, and Pd in LiOD in yellow. The right panel of both figures shows a zoomed in plot of the excess heat flows greater that 100 mW, a minimum threshold we would expect for any real anomalous heat event. It appears that we have excess heat above 100 mW in the right panel of Figure 7.16, but upon closer inspection we found that a faulty RTD in one of the cells contained 64 % of all samples $\geq$ 100 mW. This error finding is a prime example of how the UHTP's data visualization would clearly allow us to see an excess heat event in comparison to the control cells and investigate which cells were responsible.

While no excess heat was found, this first long duration test in the UHTP system proved its utility as a highly parallel system that vastly improves experimental throughput while boasting a reasonable sensitivity to detect AHE events. After proving out the first long duration UHTP test, we were ready to implement

multiple different conditions we hypothesized could lead to AHE whether from previous works or our own research. These tests are ongoing.

### 7.3.4 Conclusions

Callisto put tremendous effort into the replication of Staker's experiment producing excess heat. After more than 200 experiments, we have not found definite excess heat. However, we encountered various circumstances which produced false excess heat signals with an apparent COP up to 1.6. Most notable sources of false excess heat signals were changes in electrolyte level and difficulties in accounting for electromigration input power into the thermal system boundary owing to the high currents and small voltages. These small voltages can change drastically in the event of a bad contact.

Due to these shortcomings, we transferred the experiment into a closed-system calorimeter, while maintaining the general design of the electrolytic cell. We saw much fewer false excess heat signals in the closed system, most of them caused by spontaneous bursts in recombination after a buildup of oxyhydrogen, which could be easily diagnosed from pressure changes.

We would like to highlight that Staker's excess heat event reportedly was a one-off, was not published in a peer-reviewed reputable journal and that the report contained many shortcomings, including unintelligible axis labels on the central COP plot. Moreover, the central outcome of the report was later redacted in a corrigendum. In addition to excess heat reports, Staker's papers contain lengthy speculations about the mechanism producing the alleged excess heat. However, no experimental evidence is provided, calling into question his scientific rigor. We conclude that most likely Staker encountered a similar false COP as we did.

## 7.4 Hubler

### 7.4.1 Literature Review

Graham Hubler is a nuclear physicist that worked for the Naval Research Laboratory for 40 years, is a professor at the University of Missouri, and was the leader of the Sydney Kimmel Institute for Nuclear Resonance (SKINR). Over the years he has published multiple works spanning topics of nuclear energy, material science, and even brain related research. Amongst these works, he collaboratively published works focused on investigating and reproducing low-energy nuclear reactions (LENR) [247–249] as well as presented LENR experiments at the International Conference for Cold Fusion (ICCF) [250]. Collaborators include the European Nuclear Energy Agency (ENEA). In the 2015 work entitled 'Progress towards understanding anomalous heat effect in metal deuterides', he reported that an anomalous heat event (AHE) yielding hundreds of kilojoules of energy and an average COP of more than 15 was observed. These experiments were carried out through electrolysis in heavy water ($D_2O$) with either pure palladium (Pd), palladium alloys, or composite Pd cathodes coated in carbon nanotubes as the working electrodes. Pt counter electrodes were used in all experiments. Three of his experiments – experiment #64, Pd under ultrasonic wave and 'SuperWave' stimulation, and Pd coated with single-walled carbon nanotubes (SWCNTs) – which reportedly show excess heat are described in detail.

Experiment #64 was carried out using a pure Pd cathode in 0.1 M $LiOD/D_2O$. The Pd cathode was cold-rolled to a thickness of 50 µm, annealed at 850 °C for an hour, and finally quenched in 50 % aqua regia for 1 minute. The electrochemical stimulation is called 'SuperWaves' which consist of a superposition of time-dependent regulated currents having several different amplitudes and frequencies [251]. They are designed to dynamically modify the interface between the electrodes and electrolyte so as to increase the flux of deuterium

in and out of a Pd cathode [247]. The heat of the cell was measured using an isoperibolic calorimeter which was placed in a temperature controlled water bath with a temperature measurement accuracy of ±0.01 °C. The results of the application of SuperWave stimulation to the Pd sample was reported to be an event exhibiting excess power for a 17 hour period, starting 5 hours into the experiment. A maximum of 34 W and average of 21 W of output power on just 0.81 W of input power was observed. This translated to a COP of 2.5 (21 W out on 0.81 W in). It was also observed that during this event, the cell voltage increased from 3 V to nearly 15 V with about 20 % fluctuation around the newly established average voltage. At the end of the reported event voltage fluctuations ceased and the voltage returned back to 3 V. Post-mortem sample analysis was carried out on the purportedly AHE active Pd samples using scanning electron microscopy (SEM) and energy dispersive X-ray sepctroscopy (EDS). The SEM and EDS showed that the surface of the AHE active cathode was covered in black spots compared to an non-AHE active sample made from the same parent Pd. However, these black spots were mainly comprised of C and O and were the only detectable difference between the electrodes.

A similar experiment was carried out with the pure Pd cathodes being stimulated in LiOD with the SuperWave technique, however, this experiment also exposed samples to ultrasonic (US) waves during the course of electrolysis. This was "...expected to excite cathodes through mechano-chemical cleaning of cathode surfaces and by causing surface pits which are created by shockwave-generated cavitation jets. US-induced pits are expected to be especially significant relative to promoting AHE because they cause dynamic mechanical deformation of the near-surface layer of the cathode resulting in defects (e. g. dislocations and vacancies) that can potentially trap deuterium." [247] This surface pitting was confirmed via SEM. The authors claim that this pitting/ultrasonic excitation led to the observation of D/Pd loadings ~95% using minimal current densities (6-10 mA/cm$^2$) and the long duration of the Pd $\beta$-phase (~100 days). Ultimately, this experiment was reported to have exhibited excess heat over the duration of the experiment with two major 'burst' events releasing 1) 1.32 MJ of excess heat over 18 days with a maximum COP of 5.25 and 2) 185 kJ over the course of 23 days with a maximum COP of 1.40.

The final experiment reported to have exhibited excess heat used a composite cathode made from Pd foils coated with SWCNTs. Samples were created by drop casting a 0.1 mg/cm$^2$ SWCNT dispersion onto pre-treated Pd foils, followed by electrodeposition of 0.1 M $PdCl_2$ at 2.5 mA, and finally constant current application in 0.1 M LiOD. Two occurrences of excess heat were observed during this experiment: 1) a 3 hour period releasing 75 kJ of excess heat with peak and average COPs of 55 and 35 respectively and 2) a 1.5 hour period releasing 13 kJ of excess heat with a peak and average COPs of 27 and 16.6 respectively. Researchers observed that for a constant input power, the voltage increased from the original steady state near 2.5 V to fluctuations between 7 - 10 V during the excess heat event. Resistance also was reportedly 2.1 times the baseline value with no input power during the events. The authors report D/Pd loading of ~75%, though the resistance data in the plots is hard to decipher to corroborate. It is important to note that the data does not show resistance data returning to the original baseline resistance until after the second event.

Most recently, Hubler gave an oral presentation of reportedly excess heat reactions at the ICCF 23 conference in Xiamen, China in 2021 [250]. He presented data describing an anomalous heat event producing ~90 mW of power on 42 mW of input power (authors report COP of ~1.9, though the raw calculation of COP is 2.14) over a 58 day period, yielding an estimated 453 kJ during this time. These results are shown in Figures 7.17a and 7.17b which have been reproduced here for convenience. This experiment had a Pd cathode (100 mm x 8 mm x 0.1 mm) under tension to prevent buckling which purportedly releases deposited nanoparticles. However, we draw attention to the fact that there is no data presented showing that buckling releases nanoparticles nor is there data that shows excess heat without nanoparticles present. These samples were placed in a mixed isotope electrolyte of 0.1 M LiOD in $H_2O$, Pt wire anodes wrapped about the

support pillars, and 4-point resistance measurements (Figure 7.17c). 9 nm Pd nanoparticles were added to the electrolyte which turned the solution black until 2 days after the start of electrolysis where the solution became clear, indicating that all of the nanoparticles had plated out on the cathode. The experimental vessel was an open cell calorimeter and the sample apparatus is pictured in Figure 7.17c. The experiment exhibited excess power within the first 10 hours of the experiments and persisted for nearly 100 hours after input power was terminated. They report that their sample loaded to D/Pd of ~0.7 and was fully loaded after 30 minutes of stimulation current. It is important to highlight some shortcomings of the data presented such as: $R/R_0$ value being higher than expected in the presence of significant amounts of protium, quick loading times of 30 minutes at low currents (1.5 $mA/cm^2$) compared to our sample where we observed loadings taking ~5 hours, lack of temperature stabilization before the test (based on the scale in the red trace 7.17b), and the quite small change of the electrolyte temperature (0.1 °C) upon which the claim of AHE is based. We attempted a replication of this most recent experiment, as it exceeded our replication threshold COP and it was published during our project runtime. The shortcomings of the work were improved upon in our subsequent experiments to provide the highest accuracy possible.

### 7.4.2 Replication Experiments

Our samples were synthesized from Pd foils 25 x 4 x 0.1 mm from Alfa Aesar, and the nanoparticle solution was created according to the same patent referenced by Hubler that he published in 2013 [252]. The nanoparticle deposition was comprised of an 1.6 mM $Na_2PdCl_4$ and 0.8 mM Epigallocatechin gallate (EGCG) mixture in 25 mL of DI water for 3 days. 0.1 M LiOD was added to create the final electrolyte and deposition on the cathode was done at a current density of 1.5 $mA/cm^2$. Nanoparticles were deposited for 30 hours for which Hubler reported the electrolyte to have returned to completely clear from black, indicating the full deposition of the suspended Pd nanoparticles. In Figure 7.18 we show SEM images comparing our in-situ deposited Pd nanoparticle samples on Pd foils in 0.1 M LiOD in $H_2O$ (7.18a) and $D_2O$ (7.18b) to Hubler's in-situ depositions in 0.1 M LiOD in $H_2O$ (7.18c) and in $D_2O$ (7.18d). It is clear that our surface morphologies closely match those of his samples after scaling concentration for our sample size. After ensuring our samples were prepared in the same manner, we replicated (i.e., EC current density (1.5 $mA/cm^2$), duration (30 hours), electrochemical environment (0.1 M LiOD in $H_2O$), etc.) the most recent Hubler work claiming excess power of 90 mW. Figure 7.19 shows representative results of two variations of the Hubler experiment. Figure 7.19a shows a Hubler-like replication with a Pd nanoparticle-deposited Pd cathode in 0.1 M LiOD in $D_2O$ exposed to 20 mW of input current. Figure 7.19b shows a direct replication of Hubler's experiment with the Pd nanoparticle-deposited Pd cathode in 0.1 M LiOD in $H_2O$ with 20 mW of input current. The top plots in both Figures 7.19a and 7.19b show the EC power and current for both the Pd cathode and the Pt control cell. In the last 25 hours of the experiment, input power was changed in an effort to trigger an AHE event. 10 mW negative heat flow at the beginning of the experiment can be ascribed to the difference in the heat of recombination as Pd loads. The baseline data before EC is applied is shown in 7.19b between 0 and 15 hours. A few hours of baseline data are present in 7.19a but appear small due to scaling. As shown in the bottom plots in both figures, no excess heat was observed over the duration of the 200 hour experiment. Considering that Hubler observed an event after the first 10 hours of power application, we would have expected to observe some excess power over a 200 hour window if the event was reproducible.

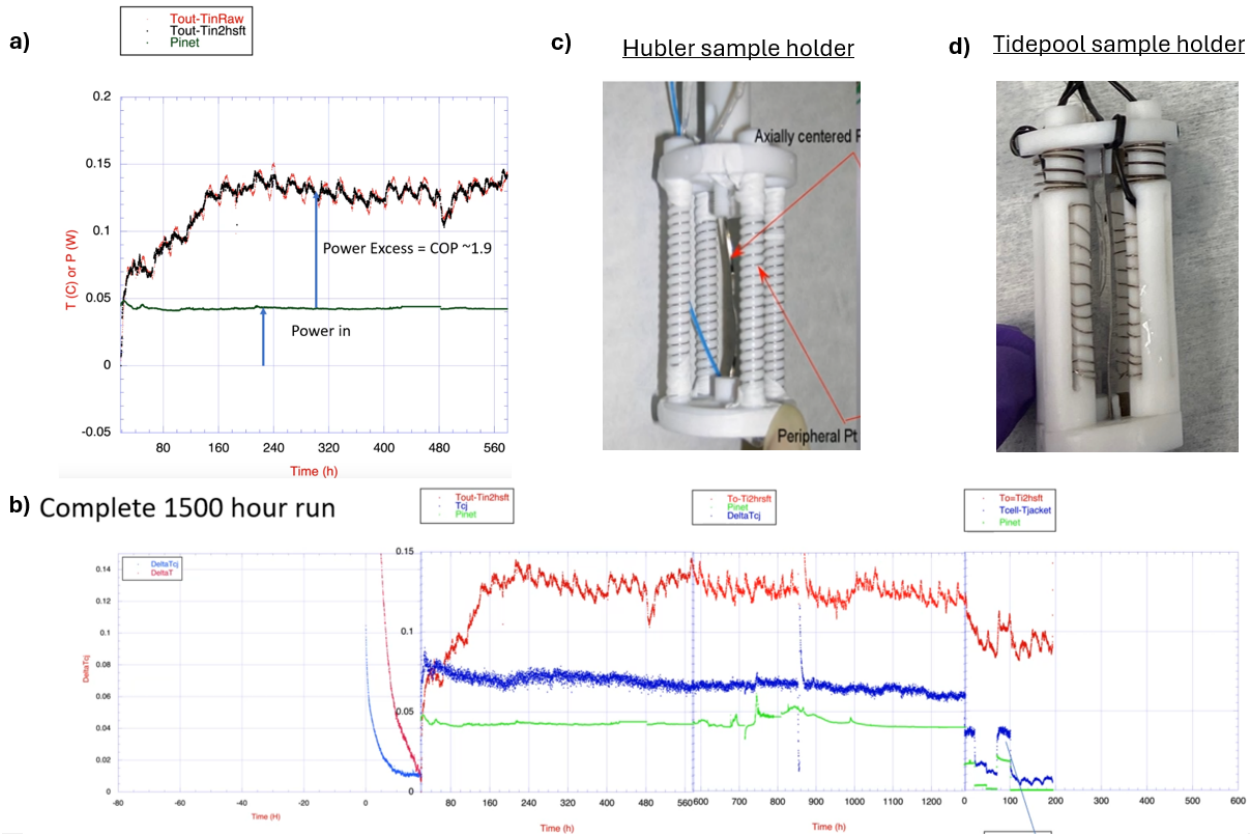



Fig. 7.17: a) to c) Summary of Hubler's major findings (replicated from [250]): a) Excess power of 90 mW (red) on 42 mW of input power (green), yielding a COP of 1.9. b) Full duration of the experiment showing input power (green), output power (red), and the temperature of the outer vessel (blue). Examples of the experimental retention housing the Pd cathode under tension and the wound Pt anodes are shown for both c) Original Hubler sample holder and sample. [250]. d) Callisto sample holder and sample.

### 7.4.3 Conclusions

We could not replicate the excess heat events that Hubler reported. Our replication efforts focused on his most recent report at ICCF23 [250], assuming that his latest work represents the culmination of his research and is thus most worthwhile to replicate. While the exact cause for the discrepancy between the replication and the report remains unclear, we would like to highlight that his work was not published in a peer-reviewed reputable journal and that it contained some inconsistencies. Most notably, in the central heat flow plot illustrating the excess heat event, the outlet temperature of the mass flow calorimeter exceeded the inlet temperature of the mass flow calorimeter (indicating excess heat) even at times when the cell temperature did not significantly exceed the jacket temperature, suggesting that the cell was not the heat source.

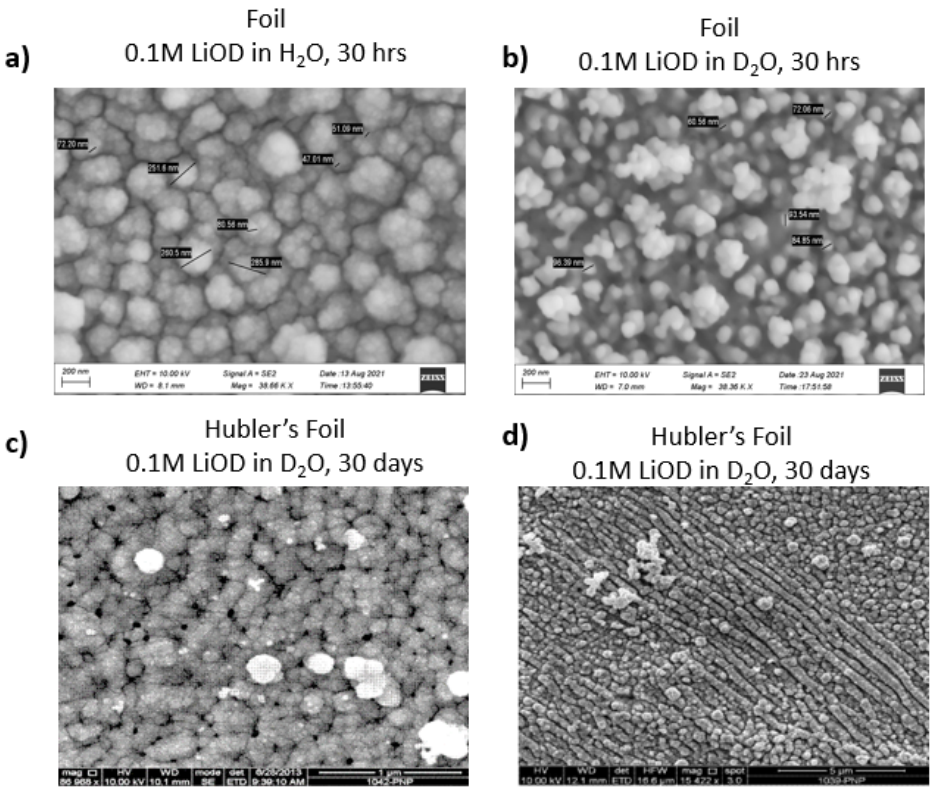



Fig. 7.18: Scanning electron microscopy (SEM) images of in-situ deposited Pd nanoparticles on a Pd cathode. a) Shows the results of our in-situ deposition following Hubler's original electrolyte composition of 0.1 M LiOD in $H_2O$ for 30 hours. b) Shows the result of the same in-situ deposition in a different electrolyte mixture of 0.1 M LiOD in $D_2O$ for 30 hours. These images are compared to Hubler's original 2013 work where this method was developed and patented. c) Shows Hubler's Pd foil after in-situ deposition in 0.1 M LiOD in $H_2O$ and d) 0.1 M LiOD in $D_2O$ for 30 hours. Scale bars for a) and b) are 200 nm and 1 µm and 5 µm for c) and d), respectively [250].

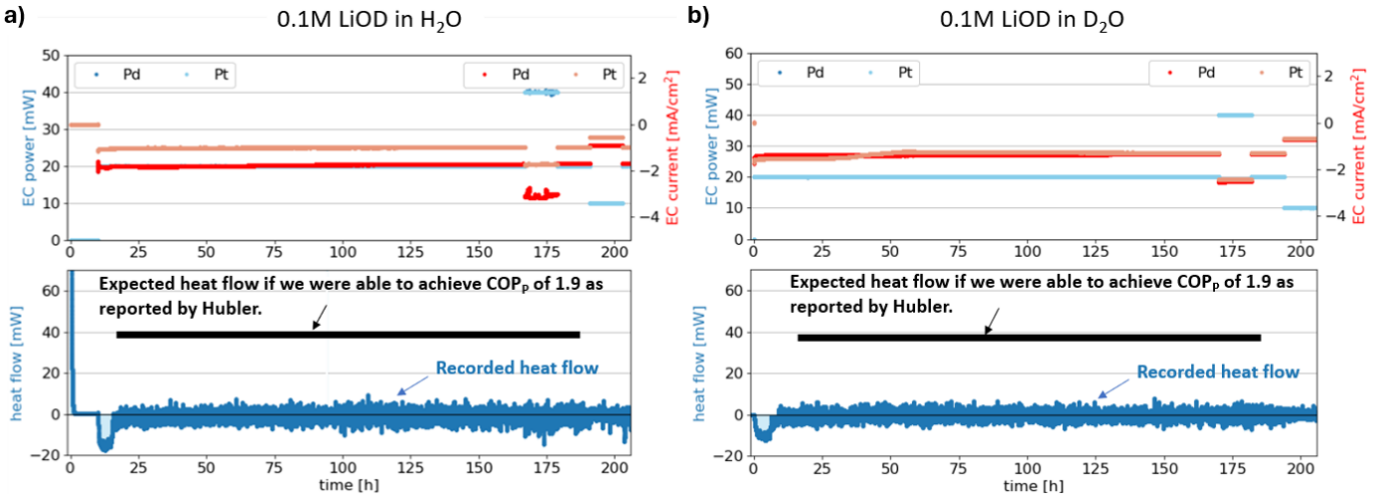



Fig. 7.19: Shows summary data for two variations of the Hubler experiment replicated in the high-precision MS80 calorimeter. a) A direct replication of Hubler's experiment with the Pd nanoparticle-deposited Pd cathode in 0.1 M LiOD in $H_2O$ with 20 mW of input current and b) a Hubler-like replication with a Pd nanoparticle-deposited Pd cathode in 0.1 M LiOD in $D_2O$ exposed to 20 mW of input current. There is a horizontal bar indicating Hubler's reported COP of 1.9. The heat flow is from the probed cell (Pd) to the reference cell (Pt), as the MS80 calorimeter only provides relative heat measurements.

## 7.5 Storms

### 7.5.1 Literature Review

Edmund Storms has been a prominent figure in the LENR community, conducting experiments since the early 1990s. He has been a strong advocate for the use of Seebeck-style calorimeters, arguing that they address the shortcomings of many isoperibolic designs. Storms has disseminated his findings through various channels, including books, scientific articles, and conference proceedings. Despite the breadth of his work, he has not provided incontrovertible evidence of LENR. This review focuses on Callisto's attempt to replicate the experimental conditions described in a series of six reports and conference proceedings from the International Conference for Cold Fusion (ICCF) by Storms, which outline his experimental findings, methodologies, and theoretical insights into reliably replicating and understanding LENR. Storms' research primarily involved palladium (Pd) and palladium-silver (Pd-Ag) alloys loaded with deuterium (D) to explore their potential for producing excess heat.

In his first two progress reports, Storms described the construction of a Seebeck calorimeter designed to measure small amounts of excess heat with high precision [253, 254]. This calorimeter was built to facilitate electrochemical experiments similar to those proposed by Fleischmann and Pons. It was calibrated using various heat sources, including resistors and quartz light bulbs, and had a time constant of approximately 40 minutes to reach equilibrium. This setup allowed for the precise detection of excess power levels as low as ±0.05 W (50 mW). In subsequent reports, he made changes to the hardware that brought the claimed detection limit to ±0.013 W (13 mW).

Progress reports three and four shifted focus to examining the behavior of pure palladium when loaded with deuterium [255, 256]. Storms treated palladium samples with heat to maximize their deuterium loading capacity, reporting high loading ratios, with D/Pd values reaching 0.98. Based on Callisto's replication efforts and extensive experience with electrochemical loadings, such high loading results should be approached with extreme skepticism. It is likely that Storms overestimated his loadings by as much as 10 to 15 %. Storms claimed that the high loading was achieved by treating the Pd with concentrated $HNO_3$, followed by heating at 900 °C and slow cooling, which resulted in a reactive PdO surface. He argued that this surface oxide led to superior deuterium uptake. However, it is possible that the reduction of the oxide affected his ability to accurately calculate loading. If the sample was more heavily oxidized than Storms estimated, this could lead to significant overestimation of the true loading. A simple calculation using his reported palladium masses indicates that for 1 %, 5 %, and 10 % oxidation, the true loading would be approximately 96 %, 88 %, and 78 % D/Pd, respectively.

During these experiments, Storms observed that the samples exhibited expansion behavior inconsistent with changes in lattice parameters alone, suggesting internal stress and crack formation. This excess volume observation has been corroborated by other researchers and appears to be a valid finding. However, Storms hypothesized that these cracks were essential for LENR, proposing that they could create nuclear active environments (NAEs) within the material. It is unclear that his samples are in fact nuclear active, and therefore the cracking may be inconsequential.

In his fifth progress report, Storms focused on the role of temperature in excess heat production [257]. He claimed that once the palladium was loaded with deuterium and activated, increasing the temperature significantly enhanced excess power production. This challenged the previously held belief that high applied current was necessary to initiate LENR, suggesting instead that thermal conditions at the nuclear active sites were more critical. This claim should be scrutinized due to a lack of evidence showing that the calibration coefficients of his Seebeck calorimeter were insensitive to temperature variations.

Storms noted a distinct pattern when varying the temperature of the cathode, claiming that excess power production increased with temperature, reaching between 0.3 and 0.5 W when the cell temperature was raised to around 60 °C. He correlated this increase with a reduction in the open circuit voltage (OCV), which he attributed to changes in surface deuterium activity. However, it is important to note that electrolyte resistance typically decreases as temperature rises, which can lead to a substantial reduction in voltage. In fact, the electrolyte resistance of LiOH solutions at similar concentrations can decrease by up to half an order of magnitude, explaining the observed drop in OCV with temperature. Storms also claimed that his calorimeter detected excess heat production after the applied current was turned off, a phenomenon he termed 'heat-after-death'. When electrochemical biases are removed from palladium deuteride, the sample enters a chemically dynamic state of deloading, and it is unclear that his calorimetric analysis is sophisticated enough to account for this.

In his final report, Storms sought to correlate excess heat production with radiation emission, a common expectation in nuclear reactions [258]. Although initial results suggested a correlation, further analysis showed that this was an experimental artifact. The apparent radiation was actually due to the temperature sensitivity of the Geiger-Müller (GM) detector used in the calorimeter. Storms demonstrated that temperature changes alone, without deuterium loading or nuclear reactions, produced similar apparent radiation signals, highlighting the importance of eliminating artifacts in LENR research.

More recently, Storms presented his work at ICCF 23, where he discussed his latest protocol for fabricating oxidized, nanoporous palladium [259]. Callisto adopted that fabrication protocol, as it represented the most up-to-date conditions provided by Storms. Rather than relying on crack formation to create NAEs, Storms intentionally incorporated nanoporosity into the sample design to eliminate the need for extensive sample conditioning.

Throughout his investigations, Storms claimed to identify key factors influencing LENR in palladium-deuterium systems. He observed that temperature was the primary factor affecting excess heat production, more so than the applied electrolytic current. Storms also noted that the physical state of the palladium, including impurity content and structural characteristics, played a critical role in LENR. He suggested that samples showing minimal excess volume changes and maintaining high deuterium loading ratios were more likely to produce excess heat. These conclusions supported his theory that LENR requires specific conditions of crack formation and deuterium concentration, aligning with his earlier theoretical work on nuclear active environments.

### 7.5.2 Replication Experiments

Callisto chose to replicate what we believed to be the critical aspects of Storms' reported conditions for LENR, primarily the sample fabrication and electrochemical conditions. As is often the case in the LENR literature, incomplete details are provided and therefore some replication details require an educated guess. With that said, we replicated such conditions in our MS80 differential calorimeter due to this system having the lowest detection limits and highest sensitivity of any calorimeter in our arsenal (section 2.8.1). Necessary details are discussed herein.

As with many of our replications, we set out to replicate the alleged nuclear active material first. For our Storms replications, we decided to follow the details outlined in his most recent public communication, i.e., his conference proceedings from ICCF-23. In this conference paper, Storms describes the sample fabrication as follows:

"The samples were prepared by pressing the powders in a steel die to form a disk shape about 12 mm in diameter and about 2 mm thick. This disk was then subjected to various treatments including heating in a

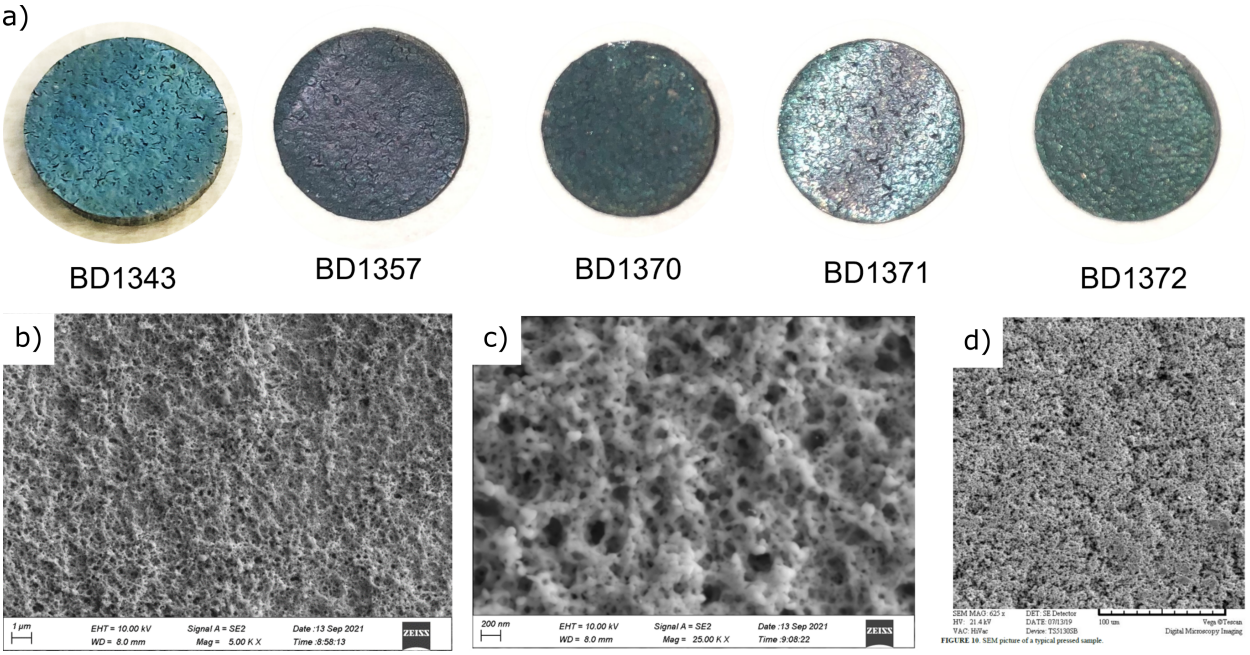



Fig. 7.20: a) Photograph of some replicated Storms samples, with varying degrees of oxidation. b) SEM micrograph of BD1343 (scale bar 1 µm). c) High magnification SEM micrograph of BD1343 (scale bar 200 nm). d) SEM micrograph of Storms sample in ICCF-23 report (scale bar 100 µm).

vacuum at 900 to 1000 °C and/or heating in air at various temperatures and times. The amount of physical pressure used to compact the powder was not explored but is expected to affect the amount of generated power. The formation of an oxide layer and the addition of inert material in the form of a fine powder are also found to affect success. Even though the conditions were not optimized, active samples could be made with reliability. Although many variables and treatments were explored during this study, this paper is focused only on a few behaviors produced by a few samples to show examples of typical behavior."

From the above excerpt, we have very little information to rely on. However, we decided to attempt to make the samples, as Storms states the conditions were not optimized and still yielded results, indicating an insensitivity to processing conditions. In our attempts to replicate the material, we sourced palladium micropowder with a mean diameter of 3 µm from Goodfellow. The samples were pressed at a constant displacement rate to a thickness corresponding to 50 % full density using an Instron-3369 tensile testing machine. During our first attempt at fabrication, an error in the pressing protocol led to the sample being compacted to full density. The sample was removed, placed in a vitreous carbon dish, and sintered in high vacuum and at 1000 °C for 19 hours. However, upon removal from the pressing-die and prior to sintering, the sample fractured into several large pieces. We suspected the 'addition of inert material' in the report was alluding to a powder-lubricant which is common practice in powder metallurgy. In subsequent attempts to replicate the material and after optimization, we included 1.5 wt.% polymeric lubricant N,N'-ethylenebis(stearamide) in the powder mixture. This allowed for removal of the pellet from the pressing-die without catastrophically compromising the form factor. In subsequent fabrications, the pressed pellet was

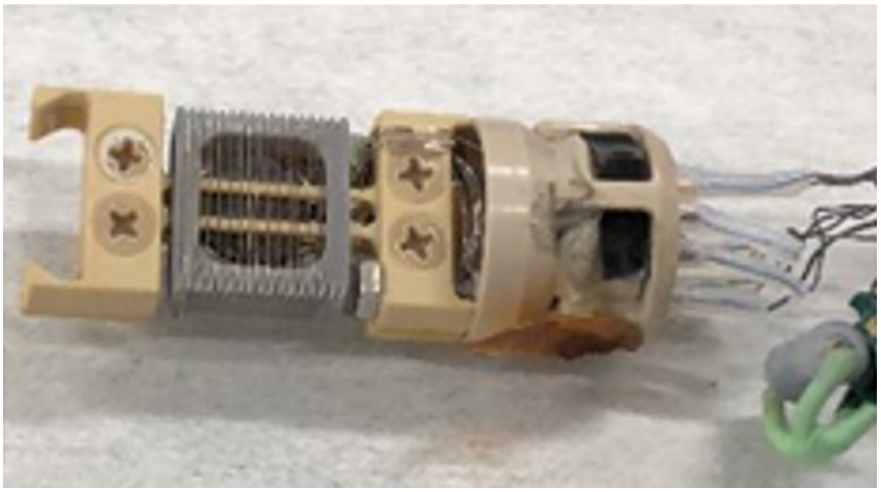


Fig. 7.21: Modified sample retention with 3D printed cage.

then annealed in argon by ramping up to 800 °C in 100 °C increments in order to reduce cracking. We settled on temperatures below the 900 to 1000 °C range due to embrittlement of the samples. Once samples were sintered, they were oxidized by bringing them up to 800 °C, this time in air, and then allowed to cool to room temperature. Mass was measured prior to and following oxidation to approximate the stoichiometry of the samples. In general, we were aiming for approximately 5 $\%_{\text{at}}$ oxygen, or $Pd_{0.95}O_{0.05}$. Additionally, a significant color change from gray to green was noted when the samples were oxidized, indicating the protocol's success. This green color is apparent in Fig. 7.20.

The result of the optimized process is shown in a SEM micrograph in Fig. 7.20b,c) and compared to one provided by Storms in his ICCF-23 report in Fig. 7.20d). As we can see, there is generally good agreement in microstructures, and we felt justified that our fabrication protocol was a reasonable replication of what Storms described. Specifically, we noted the length scales of the roughness of the samples were in good agreement, as well as the size of the pores themselves.

Once we optimized the sample fabrication, we proceeded to perform replication experiments in our MS80 differential calorimeter. The first experiment was documented in BE1025. For these replication experiments, we modified our typical sample retention in order to accommodate the large, pellet form factor. An example of this modification is shown in Fig. 7.21, where we show a 3D printed cage that surrounds the cathode and has channels for the wrap-around platinum anode. This ensured that there was no shorting between the electrodes. The electrolyte used was a 0.5 M LiOD solution, and the test was performed near room-temperature at 30 °C. The sample was loaded at a constant current of -100 mA and held for 90 hours. After 90 hours, we explored other currents in order to determine if there was an effect on our ability to produce excess heat. Recall that in differential calorimetry we are applying a nominally identical input power to a thermally connected control cell so that there is zero heat flow in the bridging thermopile. In circumstances where the test cell produces more heat, a non-zero heat flow will be measured by the thermopile. If for whatever reason the control cell is outputting more heat, a negative heat signal is recorded. The former case will result in a coefficient of performance (COP) greater than one, while the latter will result in a COP less than one. In the case of this experiment and follow-up experiments, a platinum cathode in identical heavy

water electrolyte was used as a control.

We can see an overview of the relevant parameters, telemetry, and calorimetry analysis in Fig. 7.22. Each of these plots contains four subplots, which overview the electrochemical (EC) power and current, the cell pressure and relevant temperatures, the measured, expected, unaccounted for heat flow, and COP, as well as the resistance of the palladium cathode. The resistance of the palladium cathode serves as an indicator that the sample is loaded with deuterium and also allowed us to look for any correlations between palladium deuteride stoichiometry and excess heat production (although none was ever observed). It is important to note that the EC power is the measured power, not the set power, as using the set power could lead to gross miscalculations of the expected heat flow in the calorimeter. Additionally, we found it critical to measure the cell pressure in these thermodynamically closed systems, as we would see spurious recombination of oxyhydrogen gas throughout testing which resulted in apparent heat flows. Accurately accounting for the pressure and other state variables allowed us to rule out any anomalous mechanisms.

For the most part, cell pair 3-4 remained quiescent throughout the 160-hour period with two apparent heat flows, one near 90 hours and one towards the end of the test (Fig. A.3). The second of these two events as we understand it, resulted from this spurious and transient recombination in the head space which released chemical energy abruptly into the thermal environment.

More notably, we observed a very large apparent heat flow in cell pair 1-2 around 89 hours into the test, with a measured and briefly sustained differential heat flow of 500 mW and a calculated coefficient of performance of around 2.67. This heat flow eventually decayed to baseline after one to two hours. A zoom-in of this behavior is shown in Fig. (Fig. A.4). Prior to this major heat event, we observed a peculiar ±100 mW oscillation in differential heat flow that seemed to time correlate with a small change in pressure. However, the delta in pressure did not seem to correspond to what we would expect from recombination of oxyhydrogen gas. Note that the heat flow in the MS80 saturates around 500 mW and so the event likely produced more heat than we measured. While there was an associated 15 psi pressure drop, the calculation we typically use to justify a heat flow as transient recombination returned much less heat than was measured. This was initially a very interesting result, prior to being able to perform postmortem on the samples and the assembly.

It should be noted that postmortem inspections of the test assembly and samples were often critical in understanding test results. Oftentimes our diagnosis of wiring issues, chemical reactions, and component failure was limited while the calorimeter was buttoned up. Following the test, it became very important to carefully inspect various aspects of the assembly and try to rationalize any peculiar behavior that occured during the test. This proved particularly important for BE1025. Upon disassembly, we uncovered an interesting charring of the PEEK sample retention, which is highlighted in Fig. 7.23. Given the order of magnitude higher enthalpy of reaction for hydrocarbon oxidation (PEEK ~8.9E3 kJ/mol) compared to the deuterium oxidation reaction (2.9E2 kJ/mol), and in combination with forensic evidence for charring, we concluded that we observed a classical chemical reaction. While we routinely used PEEK in our experiments, not just this replication, this particularly chemical reaction was quite rare and was not observed during any other of our tests throughout our campaigns. The likely reason behind this lied in the mass of the Pd sample. The Pd samples used in this replication campaign were notably larger than typical wire samples, by approximately 100x. Additionally, they were intentionally oxidized prior to the experiment, and then reduced upon deuterium loading. The result of this is an excessive amount of free oxygen in the head space, which served as a reactant. Beyond this apparent excess heat flow from PEEK oxidation, we did not observe any anomalous results from BE1025.

Storms hypothesized that LENR follows an Arrhenius law, and therefore the amount of excess heat should increase with temperature. In order to test this, we performed 3 more replications at 80 °C. These

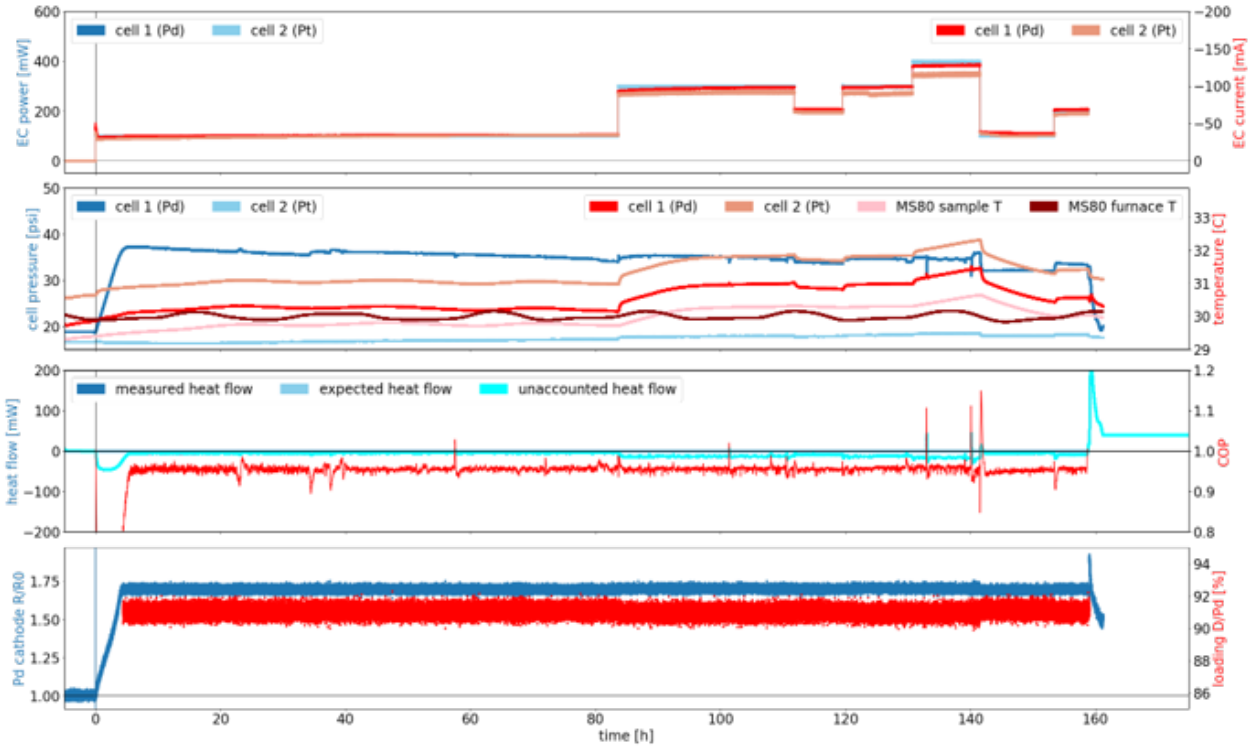



Fig. 7.22: Overview of BE1025 showing experimental parameters, telemetry, and heat flow for cell pair 1,2. Data for a similar experiment is shown in the Appendix (Fig. A.3).

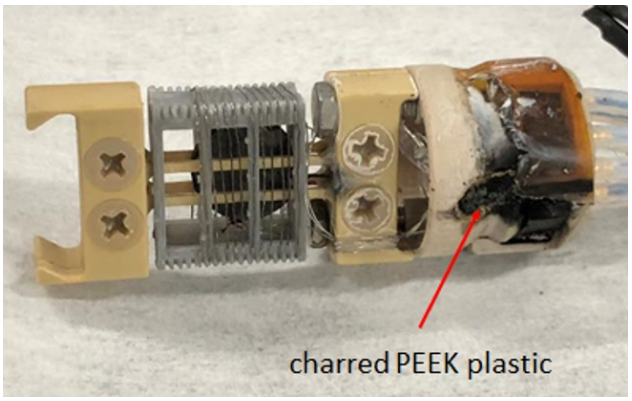



Fig. 7.23: Charred sample assembly from BE1025.

experiments are described in BE1137, BE1199, and BE1226. In all three cases, we did not observe any anomalous heat, although we did observe examples of apparent excess heat caused by classical phenomena. In BE1137 we increased the EC power from 100 mW to 400 mW over 100 hours and then decreased it to 100 mW between 100 and 120 hours (Figs. A.5, A.6). During this period, cell pair 1-2 showed a suppressed heat flow and oscillations that time-correlated with changes in the head space pressure for the Pt control cell. Otherwise, there are no major excursions in heat flow that were observed in cell pair 1-2. Upon disassembly, a leak was noted which would provide a plausible explanation for the suppression in heat flow. When oxyhydrogen gas leaves the system, it can lead to a loss in chemical energy that would normally be present due to deuterium oxidation in the recombiner. The amount of unaccounted heat flow does increase with increasing input power, maximizing at ~35 mW and resulting in a COP of around 0.925. Cell pair 3-4 shows better heat flow accounting than pair 1-2. There were no anomalous excursions in measured heat for this test.

The test was repeated in BE1199 (Figs. A.7, A.8). This test did not result in any anomalous heat, although we observed small oscillations in differential heat flow that time correlated with changes in pressure in the platinum control cell. A zoom in on these oscillations is shown in Fig. A.9. From this data, we observed that approximately 250 mpsi fluctuations in pressure resulted in anywhere from 5 mW to 20 mW in measured heat flows. Over time we learned to engineer better recombiners, and at this time we were beginning to understand that water was condensing on the catalytic surface and then evaporating. Eventually, we encapsulated our recombiners in porous PTFE jackets which prevented the condensation of vapor into macroscopic water droplets, ultimately leading to lower failure rates and better overall recombiner performance. Again, however, these improved recombiners were not being used at the time of this replication campaign.

Our final attempt to replicate Storms was documented in BE1226 (Figs. A.10, A.11). In this final test, we observed a fairly large heat flow of 150 mW. However, again it corresponded to a pressure drop in the head space which not only time correlated well with the heat pulse, but also returned the expected amount of energy for hydrogen oxidation. A zoom-in of this event is shown in Fig. A.12. In this plot, we see the heat flow in cell pair 3,4 plotted against both the head space pressure and temperature. A roughly 12 psi pressure drop occurred over a one-minute time frame. A 150 mW spike in measured heat was observed, as well as an increase in the head space temperature by 200 mK. Using a simple ideal gas model, we can calculate the moles

of oxyhydrogen recombined and convert the pressure drop to total energy released. Comparing this value to the integrated area under the heat flow curve, we get one-to-one correspondence. This formalism allowed us to rule out any anomalous sources of heat and attribute this particularly large spike to the deuterium oxidation reaction.

Two years following this investigation, we received samples from Storms himself. These samples, he claimed, were nuclear active and should give us the result that we were looking for. After analyzing and running these samples extensively in our HTCal calorimeter, we never observed any excess heat. There was no commentary provided by Storms as to why we did not see heat with the samples he claimed would give us the result. At the conclusion of our investigations, we remain unconvinced that his results were robust and repeatable in any capacity.

### 7.5.3 Conclusions

In all our attempts to replicate Storms' samples and apply similar electrochemical conditions, we did not observe any excess heat. We did observe conventional chemical reactions which resulted in major heat flow transients. These, however, were unlike the observations made by Storms using his Seebeck calorimeter. It is unfortunately inconclusive that either Storms made some unwitting mistake in his calorimetry (possible calibration drift or other user errors) or he accidentally stumbled on a working recipe for LENR but could not provide sufficient details for replication.

We would like to note that Storm's report was not published in a reputable peer-reviewed journal. We highlight that he did not provide proper control experiments. To the contrary, he reported that light water experiments also produced excess heat [113]. Furthermore, it is suspicious that he observed excess heat only at elevated temperatures (obtained by heating the calorimeter). While he points to an Arrhenius behavior, we consider it likely that a miscalibration of his calorimeter resulted in apparent excess heat at elevated temperatures and no excess heat at ambient temperature. Finally, he did not use a strictly closed system and the reported excess powers are small compared to the overall input power (including the heater power).

## 7.6 Miles

### 7.6.1 Literature Review

Shortly after the 1989 announcement of cold fusion by Martin Fleischmann and Stanley Pons, Melvin Miles began his experiments at the China Lake Naval Weapons Center. He aimed to replicate their findings of excess heat, focusing on improved material preparation, more precise calorimetry, and nuclear product detection. In his 1994 paper 'Calorimetric Principles and Problems in Measurements of Excess Power during Pd-$D_2O$ Electrolysis' Miles described the shortcomings and challenges associated with isoperibolic calorimeters used in electrochemical experiments [260]. He highlighted issues arising from changes in electrolyte levels and heat transport pathways, arguing that many reported experiments assumed steady-state conditions and failed to account for all terms in the differential equation governing calorimetry, leading to significant errors. According to Miles, accurate measurements required careful control of external conditions and consideration of time-dependent factors. Controversially, he claimed that early detractors of the LENR effect made faulty calorimetry measurements, rather than accepting their null results. He re-analyzed a study by Lewis et al., claiming that interpreting the beginning stages of PdD loading as a calibration would suggest around 75 mW of excess heat from their experiment after reaching steady state [261].

Miles' interpretation is weakly supported due to the questionable use of a PdD sample as a calibration standard. A more robust approach is to use either a platinum cathode in heavy water, a palladium cathode in light water, or preferably both, to characterize the thermal response of the isoperibolic calorimeter. Relying on a PdD sample as a control raises a critical question: how can one ensure there is no excess heat during the initial calibration? While discrepancies between input power and measured heat flow may emerge later in a test – an intriguing result – such findings would still require protium and platinum controls for validation. Callisto addressed this issue by employing isotopic contrast and/or platinum controls in our experiments and apparatus characterizations to enhance confidence in any observed excess heat. While simplifying assumptions are often necessary in scientific analysis, they carry risks.

In the same year, Miles, along with Bush and Lagowski, reported in the paper 'Anomalous Effects Involving Excess Power, Radiation, and Helium Production During $D_2O$ Electrolysis Using Palladium Cathodes' observations of excess power, helium production, and anomalous radiation [262]. They claimed measurable helium was detected in gas samples during excess power production episodes, with control samples showing no helium. They established a minimum helium detection limit of 6E10 atoms/ml and reported helium production rates ranging from 10E11 to 10E12 atoms per second per watt of excess power, consistent with typical fusion reactions. Despite occasionally recording high radiation counts correlating with excess power and helium production, many experiments yielded normal radiation counts with no significant excess power. Measuring helium-4 above background levels in a mixture predominantly containing gaseous deuterium was acknowledged to be challenging. In the 1996 report 'Anomalous Effects in Deuterated Systems' Miles and his co-authors discussed further observations of excess power, helium-4 production, and anomalous radiation during $D_2O$ electrolysis using palladium cathodes [263]. They reported excess power in 28 out of 94 experiments, primarily using palladium-boron cathodes. The rationale for using the alloyed cathodes was that the interstitial boron improved the mechanical properties and removed oxygen impurities from the cathode, mitigating electrode cracking during the charging and discharging of deuterium into and out of the lattice and reducing volumetric expansion. Although there is no known mechanism for LENR, the authors believed these factors were critical for observing the effect. Despite these claims, significant reproducibility issues were encountered, attributed to unknown variables in the palladium metal. They continued to report anomalous helium-4 production rates. However, these findings were met with skepticism due to potential experimental errors, including atmospheric helium contamination and calorimetric inaccuracies. The lack of reproducibility continued to challenge the acceptance of these anomalous effects within the broader scientific community.

In the study 'Calorimetric Studies of $Pd/D_2O$+LiOD Electrolysis Cells' published in 2000, Miles conducted experiments using an improved isoperibolic calorimeter to investigate excess power production during $Pd/D_2O$+LiOD electrolysis [264]. Excess power was reported in one cell, ranging from 50 to 100 mW, despite a gradually decreasing input power, while a second cell exhibited normal behavior. The excess power effect was identified by an anomalous increase in cell temperature, with two thermistors in each cell showing nearly identical temperature changes. Various chemical processes were considered to explain the excess power, but none satisfactorily accounted for the observations (according to the authors), and Faradaic efficiencies were assumed to be near unity to rule out recombination effects of the electrolysis gases, which is a questionable assumption based on Callisto's own measurements. Certainly, at high current densities the Faradaic efficiency is close to one, but this is not necessarily the case at lower currents. Additionally, over time the palladium surface becomes fouled with other elements which can also contribute to a drop in Faradaic efficiency. Despite the claims made in these reports, the gradual onset of excess power and inconsistent reproducibility highlighted ongoing challenges and skepticism of Miles' work. The claims of nuclear reactions required extraordinary evidence, which these studies did not conclusively provide.

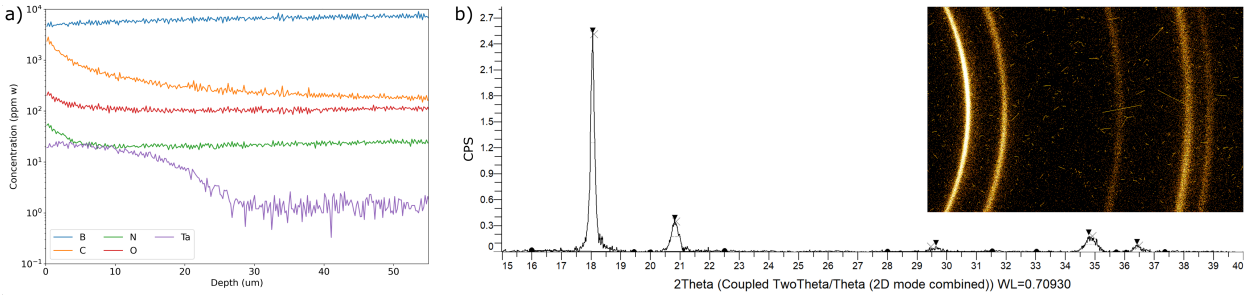



Fig. 7.24: a) Elements with composition gradient by GDMS. b) XRD: Diffraction intensity in CPS (counts per second) vs. diffraction angle 2Θ. The inset shows the 2D diffractogram.

### 7.6.2 Replication Experiments

The first step in our replication was to reproduce the alloyed cathodes as described by Miles and his co-authors. In their investigations, they claimed that boron compositions between 0.50 and 0.75 wt% were required to observe the anomalous heat effect under electrochemical conditions. As such, we worked with ACI Alloys to fabricate PdB cathodes with the relevant compositions. Rods with a length of 30 mm and diameters of 3 and 6 mm were fabricated, however, we found that the 6 mm rods produced too much orphaned oxygen during the loading process. As a result, the 6 mm diameter rods resulted in over-pressurization of our HTCal vessels and only the 3 mm rods realized completed replication tests. Nevertheless, we independently confirmed the composition of the cathodes using depth profiling glow discharge mass spectrometry (GDMS) and x-ray diffraction, shown in figures 7.24. We noted a few other impurities in the alloy, as indicated by the GDMS depth profile, including nitrogen, carbon, oxygen and tantalum. These impurities seemed to be concentrated at the first 20 microns of the surface, but ultimately they were at very low absolute concentrations in the bulk. While GDMS provides a direct composition measurement, x-ray diffraction (XRD) allowed us to look at the lattice expansion caused by interstitial boron. According to the literature, we can calculate the fraction of boron in the lattice as a function of the lattice parameter:

$$x_B = \frac{a - 0.3892}{0.06882} \tag{7.1}$$

where $x_B$ is the fraction of boron and $a$ is the lattice parameter measured by XRD [265]. Both methods give good agreement, with a measured alloy composition of $Pd_{0.9484}B_{0.0516}$ or ~0.55 wt.% B. These results indicated that we satisfactorily replicated the reported cathode composition and structure.

In the initial replication experiment BE2280, we tested three PdB cathodes and one Pt cathode as a control. In all cases, 44 mL of 0.1 M LiOD was used as the electrolyte, and a Pt wire was used as an anode. The construction of a typical sample holder is shown in figure 7.25a). As discussed in earlier chapters, important features of the holder include the mechanical clamping of the sample to achieve reliable electrical contact, a platinized carbon recombiner, a pressure-sensor (not shown), and an RTD. The electrochemical conditions, telemetry, and calorimetric analysis are shown in figure 7.26. Over a 120-hour period, the EC power was increased to a maximum of 1 W and then decreased back to 0 W. During this initial test, we observed a detonation in cell 3, which resulted in the catastrophic failure of the calorimeter channel and adversely affected the integrity of the calorimetry in adjacent channels. This detonation can be seen around 80 hours into the test, where the pressure builds rapidly, and the EC power in cell 3 suddenly drops to

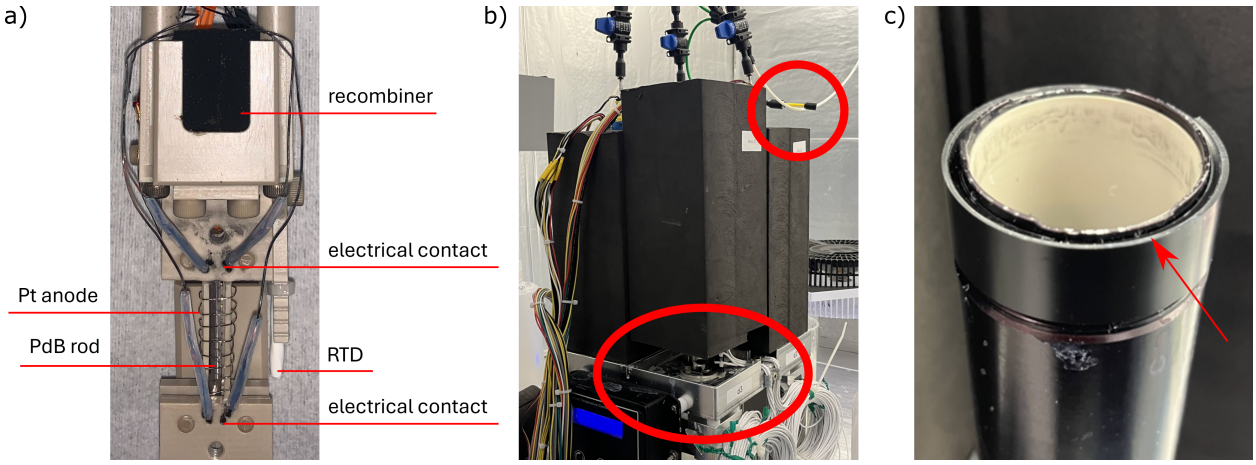



Fig. 7.25: a) HTcal sample holder with typical sample used in Miles replication experiments. b) Four-cell HTcal calorimeter with foam insulation lifted from cap failure (large red marking) and detached backpress line (small red marking). c) Top of the electrolytic vessel with remainder of plastic retaining ring, which used to hold down the top cap, sealing off the vessel. The fracture surface is indicated with a red arrow.

zero, accompanied by an abrupt drop in the electrolyte and thermal enclosure temperatures. A zoom-in on this event is shown in figure 7.27. Upon inspection of the setup following the completion of the test, catastrophic failure of the pressure vessel was observed, as shown in figure 7.25b), d). Here, we see the cap to cell 3 was ripped off and ejected. The back-pressure line supplying gas to the check-valve was dangling inside the enclosure and directing airflow at channel 2 of the HTCal cluster. Additionally, the foam on cell 3 was raised, exposing the baseplate to the thermal environment. With the termination of power in cell 3 and its exposed baseplate, the cross-talk to the adjacent cells is also expected to be impacted. As a result of these combined effects, the heat transfer of the adjacent channel was fundamentally altered, resulting in an apparent suppression of the measured heat flow and calculated coefficient of performance (COP) in that cell. Although this failure mode was not arrived at intentionally, it does provide a strong illustrative example of how a change to the heat transfer environment can result in significant calorimetric errors.

Otherwise, no excess heat was observed in this initial replication experiment. As discussed in the previous chapter on the HTCal, spikes upward and downward in COP are observed whenever the EC power is changed. This mathematical artifact is due to the contrast between the finite thermal time response of the calorimeter vs. the instantaneous change in EC input power. Later in our research program, we implemented a convolution function which uses the calorimeter's instrument response function to better account for these transients. However, this methodology was not implemented at the time of this experiment.

As part of our program's rigor, we consistently inspected the samples with electron microscopy following tests to look for additional information, whether to improve the experimental details, understand a failure mechanism more fully, or to look for any physical manifestations of excess heat production, e.g., sample melting. An example of the SEM and EDS results is shown in figure 7.28. Notably, the samples are all covered by a layer of copper, which is a result of the corrosion of exposed contacts inside the calorimeter. Although contacts were covered with shrink-tubing and Miccrostop lacquer, over long durations they become compromised and leach impurities into solution. Given routine observation of impurities on the cathode

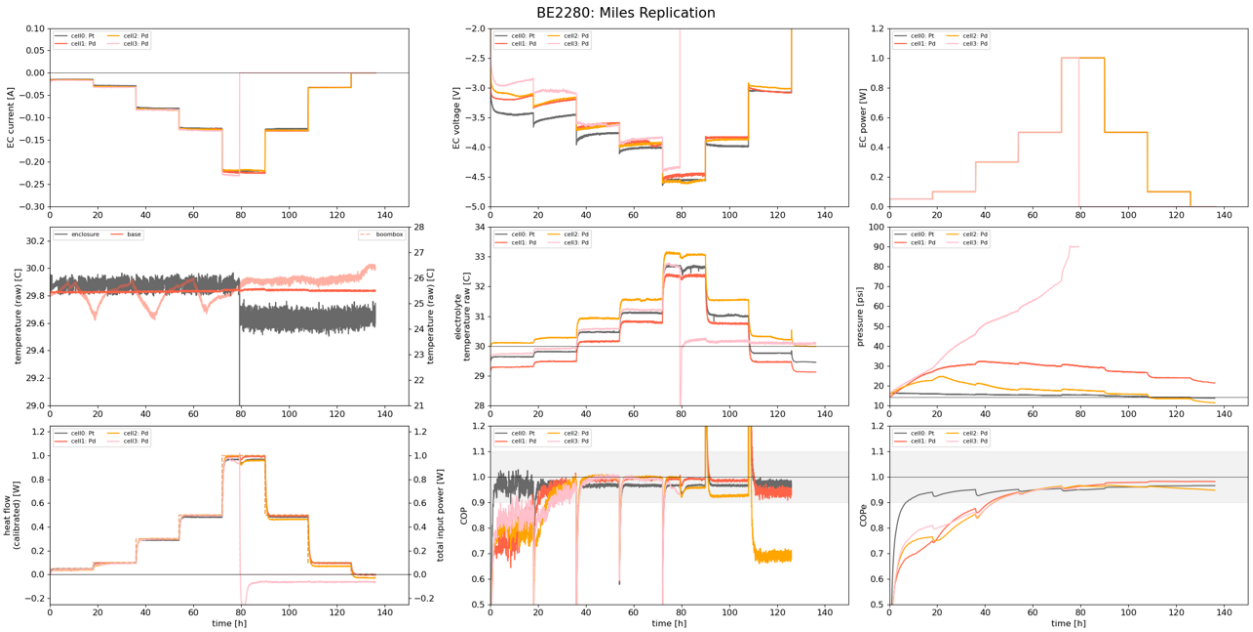



Fig. 7.26: Overview of electrochemical conditions, telemetry, and heat flow analysis for BE2280.

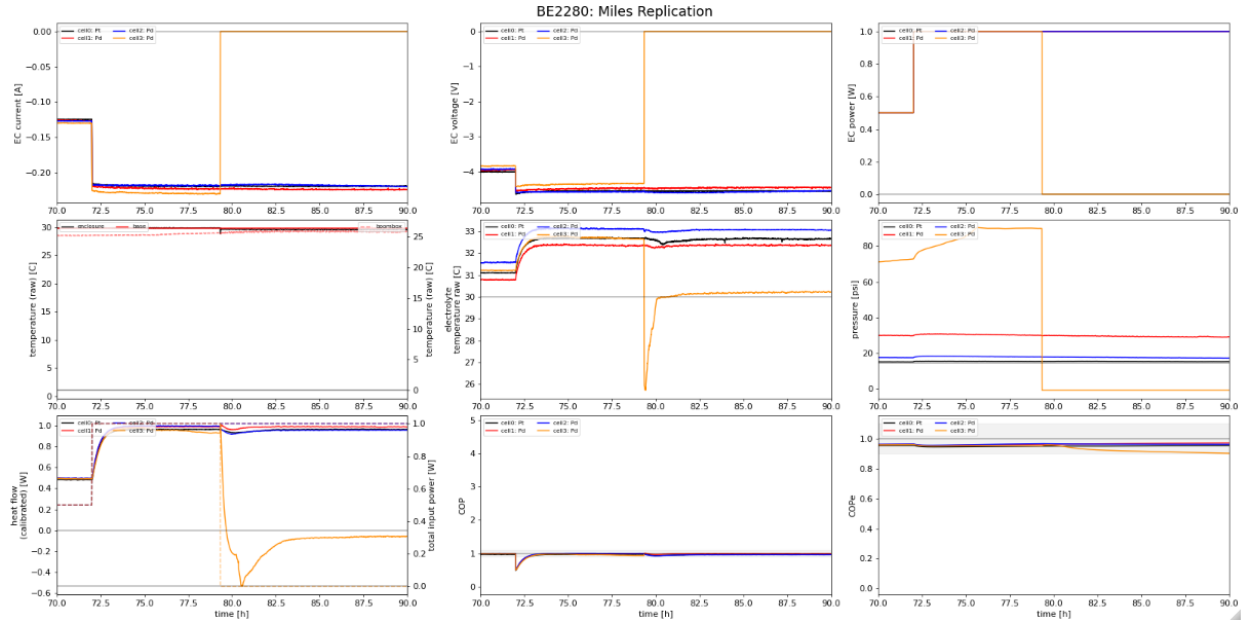



Fig. 7.27: Zoom in on detonation.

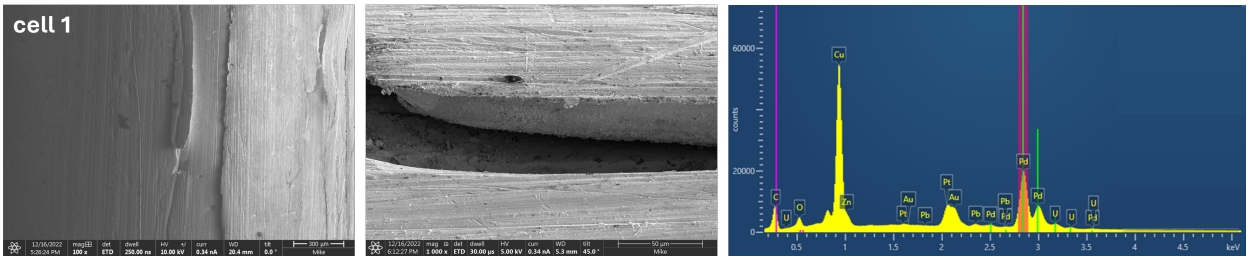



Fig. 7.28: SEM and EDS analysis of post-experiment PdB cathode.

surface after long-duration tests, in this replication campaign and others, we concluded that it is incredibly challenging to maintain a high purity surface for long periods of time. Electrode fouling is a commonly observed phenomena in non-LENR electrolysis experiments and is fairly well documented. Another notable observation was the prevalence of cracking in the cathodes, contradicting Miles' claims about the mechanical integrity of PdB alloys. These cracks were typically longitudinal, extending along the long axis of the rod, and could have an opening width of many microns.

The Miles experiments were replicated several more times in BE2280, BE2469, BE2634, BE2918, BE3067, and BE3152, which are summarized in figure 7.1. In some cases, various failure modes and false positives were observed. In these experiments, failure modes and false positives were primarily associated with inconsistent recombiner performance. Whenever recombiner efficiency degrades and then recovers abruptly, this leads to a sharp decrease in the calorimeter's headspace pressure. This delta in pressure leads to a substantial heat burst, which is registered in the electrolyte temperature and COP analysis. An illustrative example of this failure as it manifested in the Miles experiments is shown in figure 7.29. Here, we see that a sharp drop in pressure correlated in time with a rise in measured heat flow. Assuming an ideal gas, the amount of energy calculated from the pressure drop corresponds very well to the heat measured by the calorimeter.

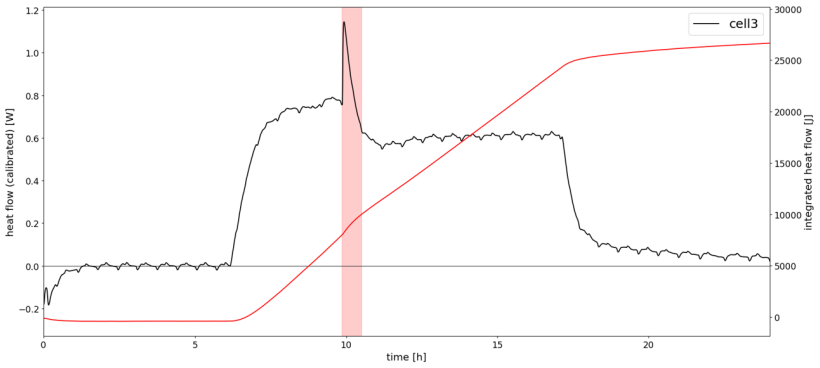



Fig. 7.29: Gaseous oxyhydrogen recombination resulting in a heat burst.

| Experiment ID | PdB samples tested | Test Status | Excess Heat | Reason for Elevated or Suppressed Excess Heat |
|---|---|---|---|---|
| BE2280 | 3 | Completed | Yes | Detonation |
| BE2469 | 3 | Contact failure | N | Not applicable |
| BE2634 | 3 | Completed | Yes | Recombination |
| BE2918 | 3 | Completed | No | Not applicable |
| BE3067 | 3 | Completed | Yes | Recombination |
| BE3152 | 3 | Completed | No | Not Applicable |

Table 7.1: Overview of Miles replication experiments.

### 7.6.3 Conclusions

Although we observed apparent excess heat in our investigations of PdB alloys, we were always able to ascribe these to classical phenomena. Our replication of the experimental details provided by Melvin Miles failed to produce any anomalous heat. We would like to highlight that Miles' report lacks light water control experiments.

## 7.7 Navy Codeposition

### 7.7.1 Literature Review

In response to the excitement generated by Fleischmann and Pons in 1989, a team from the Naval Laboratory in San Diego developed the Pd/D codeposition process to replicate observations of excess heat. Led by Szpak and Mosier-Boss, the Space and Naval Warfare (SPAWAR) team sought to improve Fleischmann and Pons' methods by increasing deuterium loading in the palladium lattice. Their approach used a solution of palladium chloride ($PdCl_2$) and lithium chloride (LiCl) in deuterated water ($D_2O$) to deposit palladium onto a working electrode. They claimed that this process rapidly achieved high deuterium loadings, with simultaneous reduction of palladium salt and hydrogen evolution. Various substrates, including copper (Cu), gold (Au), platinum (Pt), and nickel (Ni), were used to assess the influence of different materials on the co-deposited palladium.

Throughout the 1990s, SPAWAR continued exploring the co-deposition method [266]. Using Dewar-type calorimeters, they reported cases where Pd/D codeposited electrodes appeared to generate more heat than expected from the electrical input. Infrared imaging indicated this excess heat was localized to specific points on the electrode surface. Additionally, they observed phenomena such as positive feedback and "heat-after-death", where heat production persisted after the electrical input ceased. By the late 1990s, research shifted from calorimetry to identifying potential nuclear byproducts [266]. The team employed CR-39 solid-state nuclear track detectors, which reveal tracks from high-energy particles after chemical etching. Based on track morphology, they reported possible signs of alpha particles, protons, and neutrons.

Surface analysis via SEM revealed complex features, such as pseudo-fractal patterns and micro-volcanoes, resulting from Pd/D co-deposition. These formations can be explained by the hydrogen evolution reaction (HER) during electrodeposition, where hydrogen gas bubbles disrupt mass diffusion, causing material buildup around the bubble perimeter. SPAWAR also experimented with external electric and magnetic fields during

co-deposition, which significantly altered the electrode's surface morphology. The authors speculated that these fields might affect the palladium deuteride system.

Szpak's team also collaborated with organizations like Energetics Technologies and researchers such as Dr. Mitchell Swartz to refine the co-deposition process. They focused on optimizing reaction rates and control through methods like Superwave charging (see section 7.8), as well as studying the effects of chemical additives and varied cathode materials. Despite over two decades of experimentation, the Pd/D co-deposition method has not produced irrefutable evidence of LENR, and the results must be interpreted with caution.

There are some weaknesses in the claims of the co-deposition work that we observed. Among these, the micro-volcanoes on the Pd surface observed by SPAWAR due to hydrogen gas bubbles building up and escaping to the surface were also observed in our work. These crater-like structures have been observed in our own control experiments with protium as well as deuterium, suggesting no link to nuclear activity. The simplicity of this explanation seems to have been overlooked by the SPAWAR team. As stated previously, the SPAWAR team speculated that external electric and magnetic fields during co-deposition may have affected the palladium deuteride system. However, classical physics, specifically magnetohydrodynamic (MHD) effects, provides a well-established explanation. Magnetic fields influence ion motion, affecting both heat transfer (via MHD convection) and the electric double layer (EDL) near the electrode surface. These effects alter the structure and dynamics of the EDL, impacting electrochemical reactions (i. e., electro-reduction and HER), but the SPAWAR team did not fully account for these classical phenomena in the interpretation of their results.

Most recently, research by the Naval Surface Warfare Center at Indian Head led by Oliver Barham, built on SPAWAR's work, aimed to resolve lingering questions in LENR. Published in APL-Energy in 2024 [267], Barham's team reported thermal anomalies in some of their 33 experiments, where energy output exceeded input at statistically significant levels (up to 5 W of excess output power). These experiments were carried out with 0.25 mm Pt electrodes (anodes and cathodes) in $D_2O$ with DC current application of up to 900 mA in the presence of chlorine (Cl) based salts of lithium (Li), palladium (Pd), and/or rhodium (Rh) metals. The experimental values were monitored using temperature sensors, solid state nuclear track detectors (CR-39), and radio frequency (RF) sensors. The calorimeter employed Seebeck senors tiled around all sides of the experimental vessel to measure a voltage difference created from a temperature gradient across the sensors, which with proper calibration is ultimately translated into a heat flow. A photograph of our experimental vessel based upon Barham's design can be seen in Figure 7.32a).

The findings of Barham's experiments do not conclusively indicate nuclear reactions, as alternative explanations like measurement errors or chemical effects remain viable. Barham's detection of radio-frequency emissions and particle tracks using CR-39 detectors mirrors earlier reports of nuclear byproducts but does not confirm nuclear reactions. False signals from chemical origins and inadequate background testing often complicate results with these detectors. Despite their low cost, CR-39 detectors are poorly suited to such experiments, though more reliable solid-state detectors have emerged over the past two decades. Critically, CR-39 (composed of polyallyl diglycol carbonate) is known to be unstable in alkaline environments. KOH and NaOH are routinely used to etch it [268]. Likely, similar effects occur when CR-39 is exposed to corrosive electrolyte. In particular, the hydroxide concentration is expected to be elevated near the cathode, which could explain the differences in CR-39 etching between the electrodes observed by Barham. The team also monitored for evidence of tritium production, but found none (such claims have been widely disputed in the past). In our view, he lack of proper protium controls significantly weakens Barham's claims of excess heat production. In fact, he reported excess heat in platinum control cells, but ascribed it to palladium contamination.

Most notably, the reported excess heat strongly correlated with the anode temperature (see [106] Sup-

plemental Information). Repeatedly, elevated anode temperatures occurred during periods of excess heat (runs #19, #21 to #31) and suppressed anode temperatures occurred during periods of suppressed heat (run # 15). If the temperature difference of almost 10 K within the electrolyte is real, it means that the heat source is the anode, not the cathode. Suspiciously, in two other experiments (runs #12, #15), the electrolyte temperature dropped by ~20 K while the input power was constant (or even increasing). This clearly calls into question the reliability of their calorimetry.

In the experiment with the highest excess heat (run #19), the excess heat is fairly constant at 5 W from the beginning of the experiment, as evidenced by the quick rise in temperature at 0 h. This is curious, as palladium is expected to deposit on the cathode over time, forming a coating, which then gets hydrided and potentially serves as the host lattice for the hypothesized nuclear reactions. For that reason, one would not expect constant excess heat from the very beginning.

Although Callisto was skeptical of the co-deposition body of work, the experiments contained enough detail for replication. Callisto has conducted two iterations of replication experiments covering more than 100 individual experiments at the time of this report – one set replicating the experiments of the SPAWAR work led by Mosier-Boss, and another set replicating the recent experiments from Barham. The outcomes of these replication attempts are described below.

### 7.7.2 Boss Replication

Callisto performed 13 experiments to replicate the work of Mosier Boss, based on a patent filed. To briefly summarize experimental conditions: 0.25 mm diameter Pt electrodes were placed in 0.03 - 3 M $PdCl_2$ in $D_2O$ with a magnetic field being applied to the vessel by two magnets fixtured to the external walls. The following current profile was applied for the indicated time: 1 mA for 2 hours, 2 mA for 6 hours, 5 mA for 24 hours, 10 mA for 24 hours, 25 mA for 24 hours, 50 mA for 24 hours, 75 mA for 24 hours, 100 mA for 24 hours. Boss et al. reported a reaction that produced excess heat (enough to form melt spots on the Pd cathode) and nuclear emission of high energy particles, suggesting LENR. Several of our experiments were exact replication attempts based on the Navy patent [269], while others aimed to deepen understanding of the system, including modifications for improved conditions and calorimetry. Notably, we modified our HTCal setup to fixture N55 magnets, resulting in magnetic fields of 100 to 200 mT inside the cell.

#### 7.7.2.1 Experimental Results

We initially tested palladium thin films (100 nm) in 0.5 M LiCl in $D_2O$ and observed corrosion of the palladium. This was concluded to be an issue for thin films but likely not for bulk palladium cathodes. We then tested arsenic enhancement of Pd wire cathodes in 0.5 M LiCl in $D_2O$. However, this chemical enhancement strategy was incompatible with the electrolyte, possibly due to the corrosive properties counteracting the formation of the surface Pd-As layer. The resistance ratio is shown in Figure 7.30a), showing no enhanced loading. Pd loading during and after Pd electrodeposition on a Pt wire was measured using 4-point resistance measurements (Fig. 7.30b). An initial drop in resistance likely corresponded with wire diameter growth from electroplating. Following that, when the EC voltage exceeded water-splitting potentials, resistance began to increase again. Electroreduction and HER did not appear to occur simultaneously, challenging the co-deposition framework. The Pd shell loadings did not exceed 75 to 80 % (based on 4-point resistance measurement of the entire sample, subtracting the contribution of the core), lower than SPAWAR's claimed stoichiometric loadings.

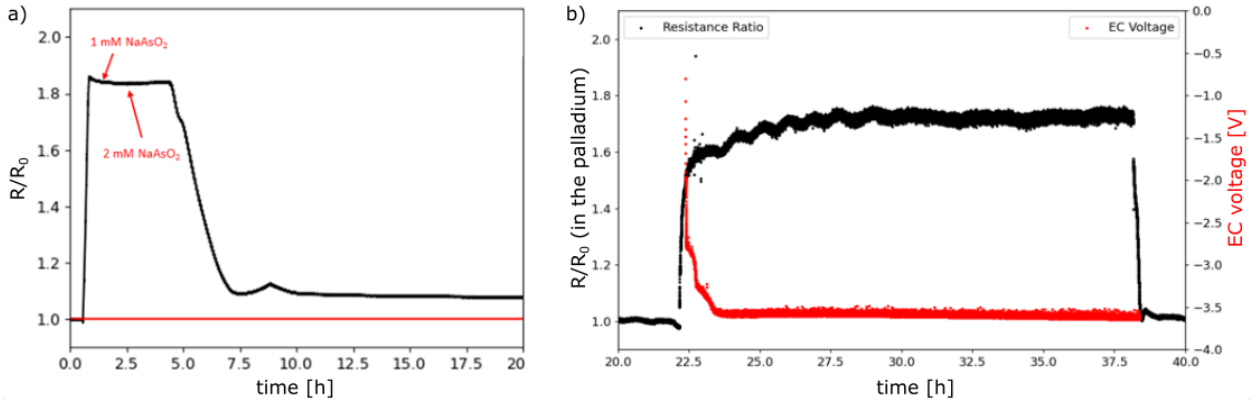



Fig. 7.30: a) Resistance ratio during arsenic-enhanced Pd wire cathode in LiCl electrolyte. Arsenic dosings are indicated by arrows. No loading enhancement is observed. b) Estimated Pd resistance ratio during codeposition of Pt and loading of Pd core.

In the initial closed HTCal experiments (BE2152, BE2368), the generation of chlorine gas during electrolysis compromised our platinized carbon recombiners, leading to vessel pressurization. This prompted us to improve our recombiner design for the rest of the closed-system calorimetry experiments. Using an improved recombiner design, we encapsulated the platinized carbon paper in a PTFE porous membrane to prevent condensation of corrosive fluids. Despite this improvement, over-pressurization occurred at high current densities due to non-recombinable chlorine gas. The heat flow analysis showed suppressed heat flow at high currents, requiring a major correction to the analysis. The heat balance of the system was indeterminate due to the inability to quantify the relative amounts of chlorine and hydrogen evolution.

In the final replication experiments, we modified the electrolyte from 0.3 M LiCl to 0.3 M LiOD. We hypothesized that this would avoid the formation of intermediate salts such as LiOCl and LiOH/D, which may have influenced prior results. Although clean test results were obtained, no excess heat was observed in these experiments. Postmortem SEM inspections of samples from this replication are shown in Figure 7.31. We replicated crater-like formations and nanostructuring of the surface (Figure 7.31), but the lack of isotopic contrast between protonated and deuterated electrolytes suggests these features are non-nuclear in origin. Blister formations with nanoscopic voids were observed (Figure 7.31 d) and e), likely caused by gas bubble nucleation within lattice defects, and again were found present in systems loaded with either hydrogen isotope (H or D).

Given the lack of coherent scientific evidence in the literature and our experimental results, including minimal simultaneous electroreduction and HER, moderate Pd loadings, and the absence of excess heat, we concluded there was little merit in pursuing further replication of the Boss experiments.

### 7.7.3 Barham Replication

Callisto performed well over 50 Barham and Barham-like experiments where we either exactly or closely replicated the experimental conditions that were reported to show excess heat [106]. To achieve results similar to Barham we designed a custom experimental vessel tiled with Seebeck sensors (Fig. 7.32a), closely matching the dimensions of the calorimeter reported by Barham. Our standard experimental setup consisted of two 0.5

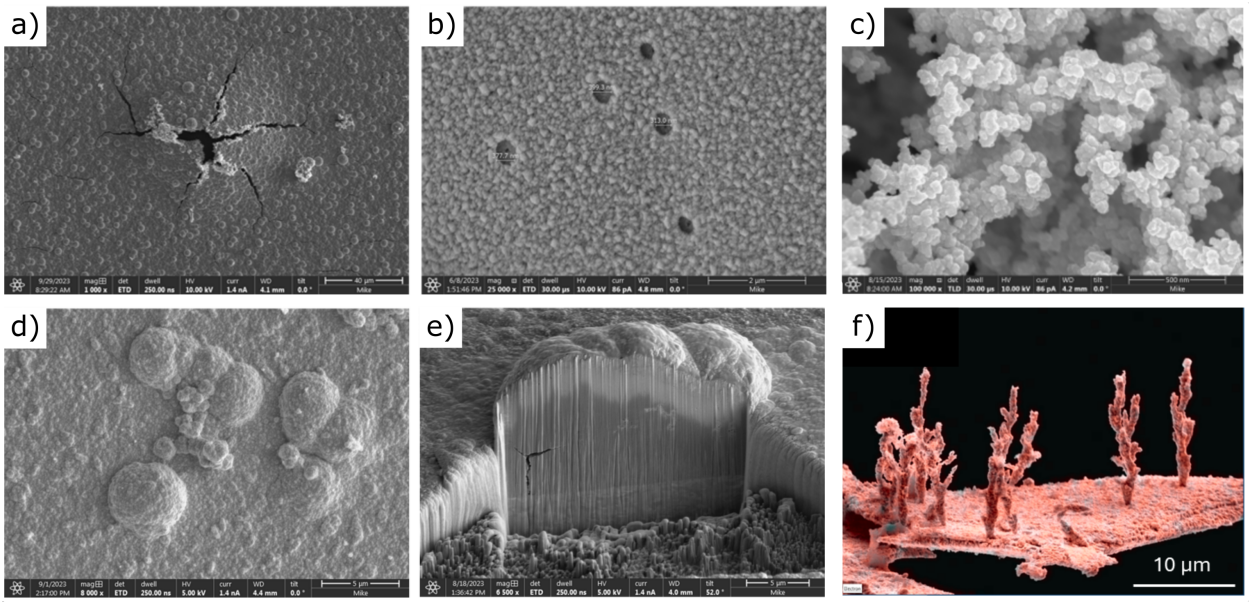



Fig. 7.31: SEM images depicting a) volcano-like (scale bar 40 µm) and b) crater formations (scale bar 2 µm) on palladium cathode surfaces. c) High magnification (scale bar 500 nm). d) Blister formations with subterranean nanoscopic voids (scale bar 5 µm) and e) a representative blister sample which was cut with focused ion beam (FIB) to expose the cross-section (scale bar 5 µm). f) EDS false color map of dendritic growth (red: Pd, blue: Cl).

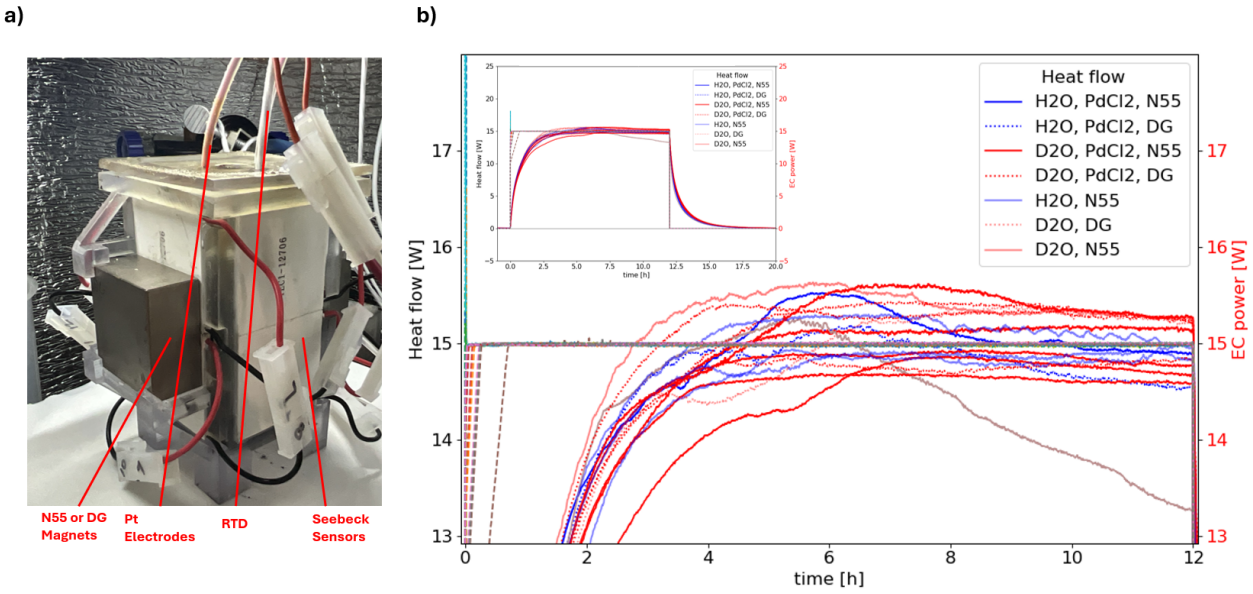



Fig. 7.32: a) Photograph of the experimental vessel used in our Barham replication experiments with Seebeck senors tiled around the vessel and other components labeled. b) Shows a summary figure of the results of the Barham and Barham-like replication experiments (solid red and dotted red traces) as well as various control experiments. Input power of 15 W are shown in the dashed traces. There was one outlier experiment (brown trace) that had excessively suppressed heat flows due to the vessel lid being ajar halfway through the experimental run. The smaller inset shows the full heat flow data showing the heat flow of all experiments returns to baseline.

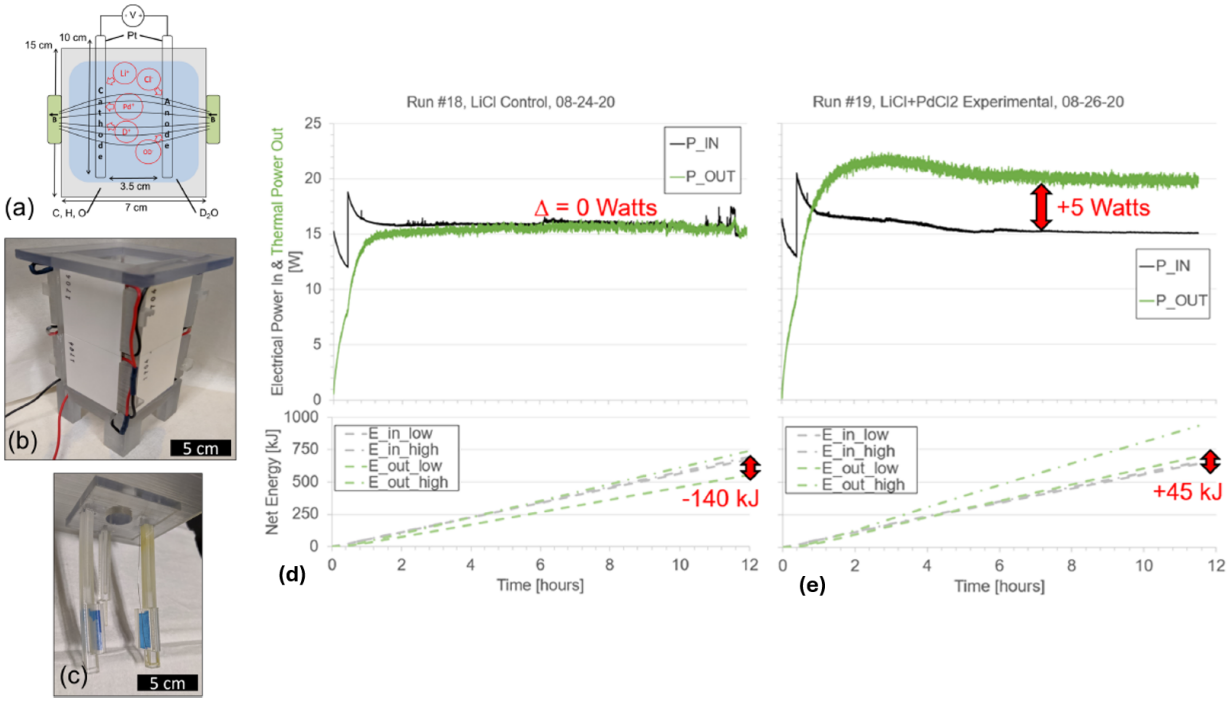



Fig. 7.33: a) Shows a 2D mock up of the Barham vessel with its dimensions and components, b) shows the Barham open-cell calorimeter with Seebeck sensors used in their experiments, and c) shows the lid of the calorimeter with the RTDs placed in sleeves. d) Shows the heat flow and net energy results of the control experiment (#18) run by Barham with Pt electrodes and 150 mM LiCl in $D_2O$. There is no excess heat reported in the control experiment. e) Shows the heat flow and net energy results of the experiment (#19) run under the exact conditions as experiment #18 but with 1.25 mM $PdCl_2$ added. The figure reports a nominal 5 W of excess heat, although after the authors subtracted their estimated "6-sigma" noise margin, they are effectively claiming only about 1 W (45 kJ over 12 hours) of statistically significant excess heat based on their 6-sigma requirement.

mm diameter and 30 mm long Pt electrodes laser welded to copper wire and housed in shrink-tube shielding to protect the connections from corrosion from the electrolyte. The electrolyte was typically 150 mM LiCl in $D_2O$ ($H_2O$ for control experiments) with 1.25 mM $PdCl_2$ and/or 0.68 mM $RhCl_3$ additives. We applied powers of 15 W for 12 hours based on data shown for the main positive result of excess power (experiment 19) reported by Barham (Figure 7.33)e. We specifically focused on experiment 19 which purportedly exhibited 5 W of excess heat compared to the input power [267]. This experiment had Pt electrodes (anode and cathode), an electrolyte containing a LiCl salt in $D_2O$ creating a 150 mM solution, and a $PdCl_2$ additive that ends in 1.25 mM concentration in the solution. Barham also added a $RhCl_3$ additive in addition to the $PdCl_2$ in nearly half of the reported experiments, which we also replicated in our work. In some of the Barham-like experiments we also exchanged the N55 magnets for degaussed (DG) magnets, to probe the effects of magnetic field.

#### 7.7.3.1 Experimental Results

The summary results of the Barham and Barham-like replications are shown in Figure 7.32b. These experiments used a constant 15 W of power applied across the Pt electrodes (anode and cathode) in 150 mL of an 150 mM LiCl electrolyte made with $D_2O$ and 1.25 mM $PdCl_2$ additive. N55 magnets were interchanged for DG magnets in some of the Barham-like experiments. Other control experiments (i. e., $H_2O$, no $PdCl_2$ additive) are also shown in this plot. Overall, no anomalous heat events were observed in any of our direct replications as well as our Barham-like replications. Our control experiments showed a maximum of 15.5 W of output power on 15 W of input power and thus that became our minimum limit to indicate an anomalous event. No experiments showed heat flow beyond ±0.5 W except for an outlier (Fig. 7.32b, brown trace, BE4477) where the vessel lid came ajar during the test and led to a severely suppressed heat flow. One observation that we noticed during this experimental campaign is that electrolyte composition seemed to change between experiments and even when it was refilled with fresh electrolyte, it exhibited suppressed heat flow behavior compared to a completely fresh electrolyte. This is likely due to the depletion of the electrolyte and precipitation of lithium salts during electrolysis.

Furthermore, we monitored the loss of electrolyte by placing the Seebeck calorimeter containing the electrolytic cell onto a scale during experiments. We continuously recorded the mass and typically observed an electrolyte loss of ~30 ml over 12 h at 15 W. It is curious that Barham et al. did not discuss this issue despite their longer durations of typically 40 h. Likely, the calorimeter calibration is sensitive to the electrolyte level. Additionally, any open system calorimeter calibration is not only sensitive to the input power, but also to the electrochemical current, which determines the chemical heat leaving the system in the form of oxyhydrogen gas. This introduces additional error in the heat flow calculation in runs with varying input power despite constant current (runs #5, #15, #17, #28).

### 7.7.4 Conclusions

In almost fifty Barham replication experiments, we have been unable to reproduce the reported excess heat of 5 W at 15 W input power (or any excess heat beyond the error of the control experiments). While Barham's paper [106] is one of the few papers published in a mainstream peer-reviewed journal, we point out various issues. Most importantly, all reports of excess heat show an elevated temperature near the anode, suggesting the anode as the heat source (as opposed to the palladium deuteride on the cathode). In addition, several runs show temperature instabilities of ~20 K at constant input power, calling into question the quality of the calorimetry.

## 7.8 Energetics: *Superwaves* and Other Variable Electrochemical Currents

### 7.8.1 Literature Review

Energetics Technologies was an Israel-based company that claimed spectacular cold fusion results with COPs in excess of 30 [102]. At the 2004 International Conference on Cold Fusion, they claimed 20 W output on less than 1 W input. The secret sauce to these spectacular results was ostensibly the application of a specific current history to the electrodes, for which they coined the term *Superwave*. *Superwaves* are self-similar waves that increase in frequency and amplitude as the amplitude of the kernel increases. In theory, there is no limitation in frequency, but in practice the lower frequency is determined by the length of the loading cycle and the higher frequency is determined by the instrument (typically 100 Hz, Fig. 7.34). The mechanism through which the *Superwaves* affect the sample and the heat production is unknown. Their data suggests that loading is not affected by the shape of the *Superwaves*. Two instances of excess heat include sample 56, which yielded a fairly constant COP of ~2 for 300 h, without spikes or runaways. Sample 64a showed a COP of 25, with 20 W out over 0.74 W in, with many spikes and peaks. They used an isoperibolic calorimeter to measure heat. While the cell did contain a recombiner, it is suspicously placed outside of the calorimeter. It is unclear what the vessel pressure was and if it was monitored. The samples they used were palladium foils prepared by Violante (ENEA [Italian National Agency for New Technologies, Energy and Sustainable Economic Development], Italy), measuring $60 \times 7 \times 0.05\,\mathrm{mm}^3$ (preparation protocol unpublished).

In general the experiments are poorly documented, with many graphs missing labels or units. Output powers appear very noisy, often at frequencies impossibly high when considering the thermal time constant of the system. In several instances (samples 64a and 64b), high COPs coincide with the onset of a faulty resistance measurement, which could hint at a bad contact in the resistance measurement and hence unaccounted electrical power from ohmic heating in the resistance measurement entering the calorimeter.

In 2011, McKubre et al. at SRI reported a replication of the Energetics experiments, using the electrolytic cell and calorimeter provided by Energetics [270]. Another replication took place at ENEA [270]. While this report was published in a Conference Series of the American Chemical Society, it does not seem to have undergone peer review, as many of the plots are missing axis labels or units. It is unclear what led to the design of placing the recombiner outside of the calorimeter, such that most of the heat of recombination is not accounted for in the calorimetry, but some of it does re-enter the calorimeter in the form of warm water droplets. Disappointingly, some of the excess heat plots lack the input power traces ( [102] Fig. 6). For example, a COP of 5 was reported without the application of *Superwaves* (Fig. 7.35) [270]. It is reported that the input power went down at ~ 65 h due to reduced electrolyte resistance as the "Electrolyte Tedmperature" (sic!) went up, even though it is difficult to construct an effect of this magnitude. It is also surprising to see an almost perfect mirror-symmetric effect of input power on output power (apparently convolved with an instrument function). In the absence of a poorly calibrated compensation heater, this relationship suggests that errors in accounting of input power are a likely cause for the elevated COP.

### 7.8.2 Replication Experiments

Despite the shortcomings of the Energetics reports, we implemented *Superwaves* into the electrochemical current applied to the electrodes in the MS80 calorimeter (section 2.8.1). In light of the questionable design of the original Energetics calorimeter, we opted to use our own well-characterized closed system calorimeter. Owing to the undocumented preparation procedure of the palladium samples in the original

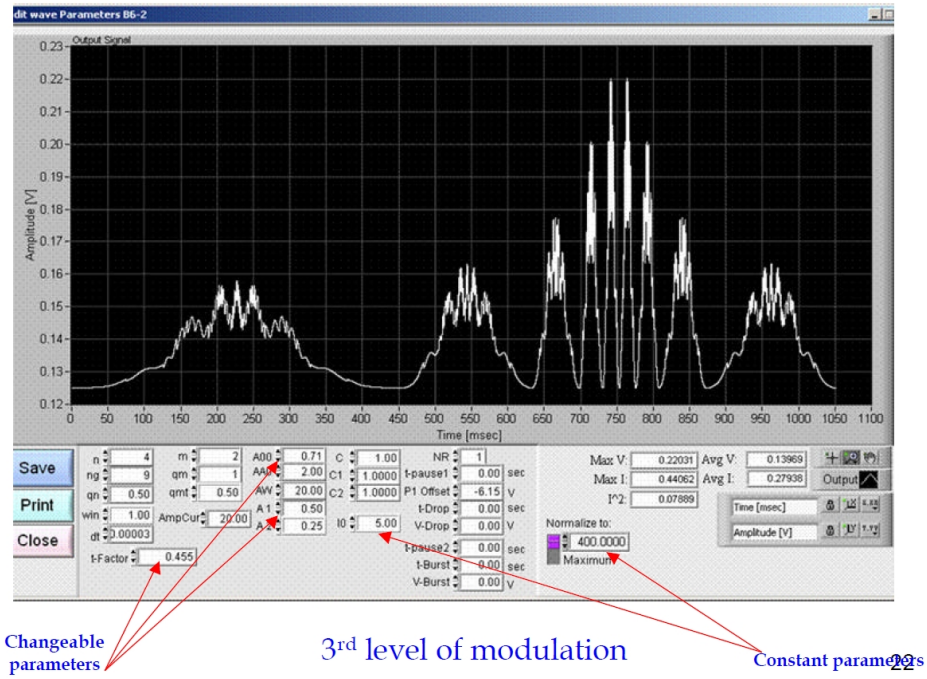



Fig. 7.34: Illustration of a *Superwave* signal applied to the electrodes. Source: [102]

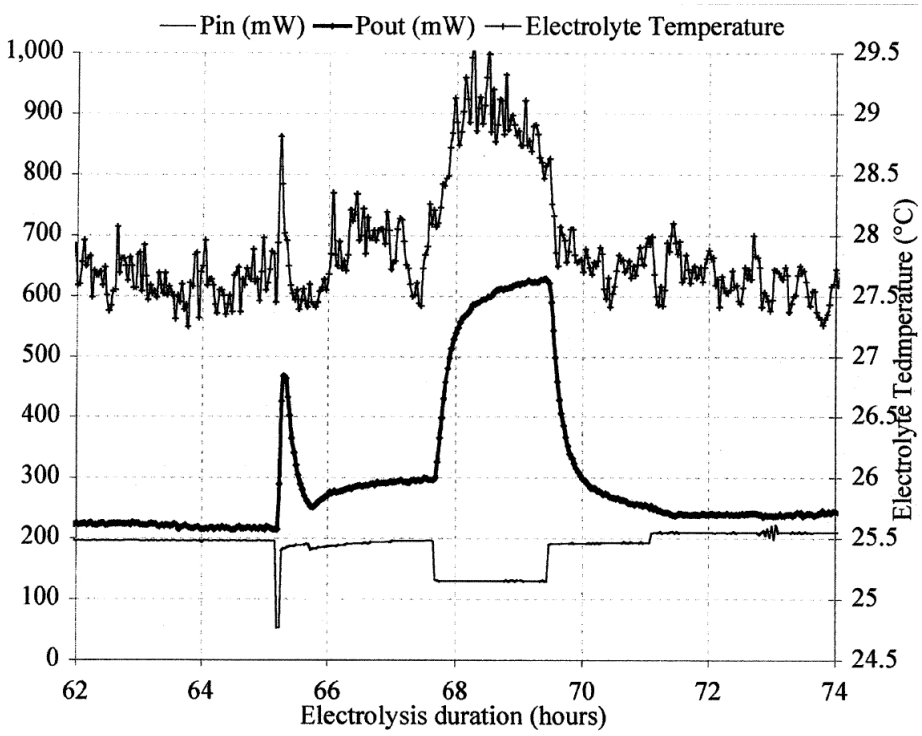



Fig. 7.35: Example of excess heat (COP up to 5) reported by Energetics [270, fig. 13].

experiment, we used as-received palladium wires (Johnson Matthey, 0.5 mm diameter, 28 mm length, in 0.5 M LiOD in $D_2O$). *Superwaves* were implemented using National Instruments source measure units (as standard electrochemistry potentiostats cannot supply these waves). Specifically, we applied a five-fold nested harmonic wave as illustrated in Fig. 7.36a, with the highest frequency being 700 Hz and the lowest frequency 0.1 Hz. The average current density was 8 $mA/cm^2$. The resulting EC voltage, resistance ratio and heat flow are shown in Fig. 7.36 b. No excess heat was detected. We repeated the experiment and we also performed modified replications with increased current density to achieve higher loading and with simple harmonic waves at various frequencies (frequency sweeps). No excess heat was detected.

### 7.8.3 Conclusions

Neither the Energetics replication experiments (employing *Superwaves*), nor derived experiments with alternating electrochemical currents, showed excess heat. We would like to iterate that the original reports were not published in reputable peer-reviewed journals and are of exceedingly poor quality (omission of critical details, missing units, missing labels, erratic heat flows). In several instances, high reported COPs coincided with the onset of faulty resistance measurements, pointing to hardware malfunction as potential source of apparent excess heat.

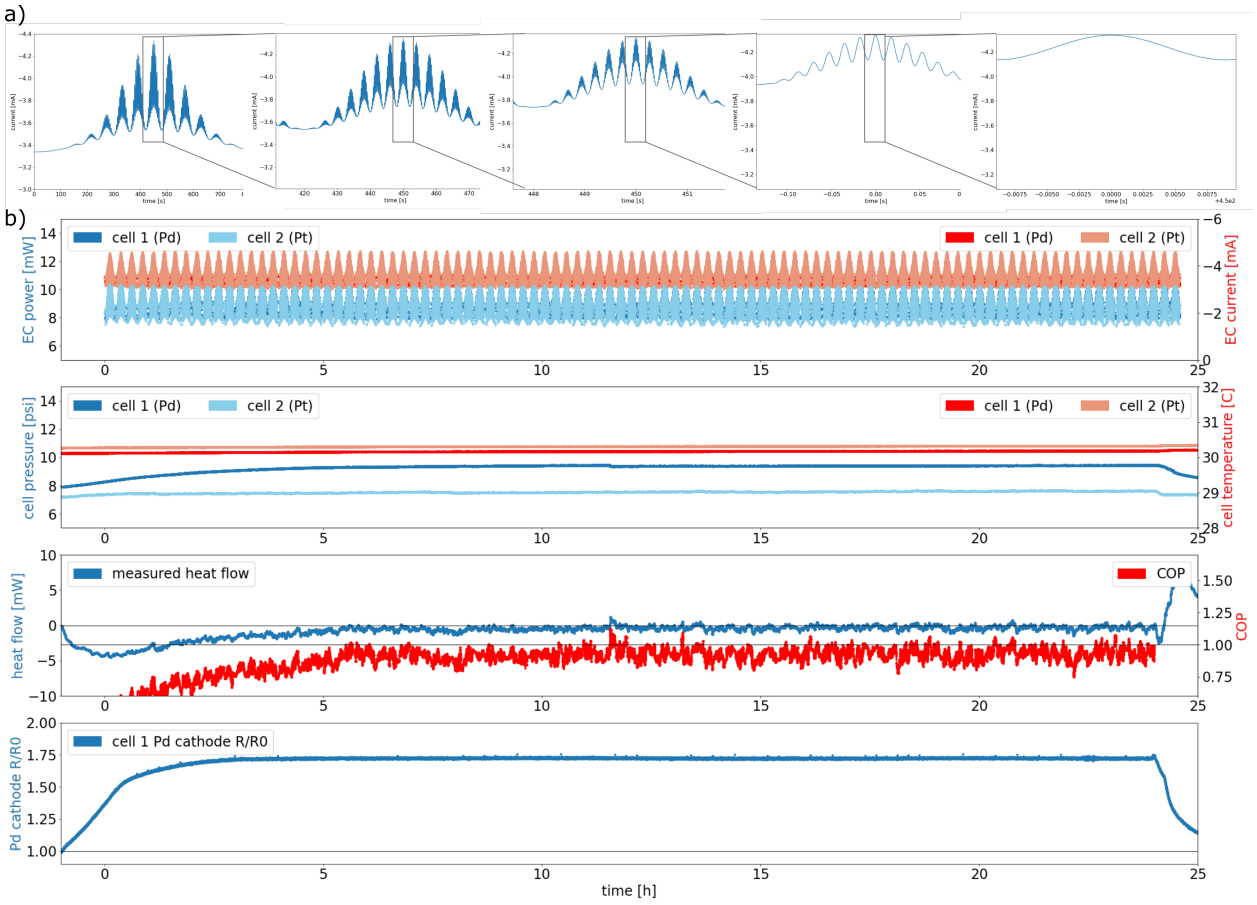



Fig. 7.36: Replication of Energetics *Superwave* experiments in Setaram MS80 calorimeter. a) Applied electrochemical current in the form of a five-fold nested wave (highest frequency 700 Hz, lowest frequencye 0.1 Hz); b) In-situ calorimetry data showing EC power and current (top row), cell pressure and cell temperature (second row), heat flow and COP (third row) and cathode resistance ratio, $R/R_0$ (bottom row). Note the suppressed heat flow during the initial loading as it causes a non-stochiometric head space gas composition and a reduction in recombination. Upon cessation of EC current, the reverse can be observed.

## 7.9 Letts: Laser stimulation

### 7.9.1 Literature Review

In 2003, Letts and Cravens reported excess heat when exposing a palladium deuteride sample located in a magnetic field to laser light [271]. The sample was prepared following a recipe involving repeated polishing, annealing, etching and cold rolling. After electrolytic loading at a moderate current for several days, the current was increased to 1 A and after another day, a layer of gold was electrochemically deposited onto the sample and the laser was turned on. The frequency of the laser light was reported to be relevant, but only a limited number of frequencies was investigated. Among the suitable frequencies was red laser light (682 nm and 662 nm). A crude model was suggested to determine suitable frequencies, however Letts noted "there is no physical reason why they should work, other than luck" [271]. The reported excess heat was typically a few hundred mW up to 1 W for several hours, with a laser power of 30 mW. The electrochemical input power is not specified, but given the current of 1 A, it is likely a few watts. The calorimeter was isoperibolic with two temperature sensors inside the electrolyte. The glass beaker was closed with a lid containing a recombiner and a seal, but it is not clear if the cell was actually gas tight. Performing electrolysis inside a gas tight glass vessel would present a substantial hazard.

The data Letts presented lacks scientific rigor and quality. Figures are missing axis labels, units, and scale bars. In some cases, incorrect units are listed. No baseline heat flow is provided prior to the laser exposure, and in some cases the heat flow does not return to baseline after the laser is turned off.

A few years later, Letts collaborated with Hagelstein, using an additional laser with a slightly offset frequency [104]. The lasers interfere at the sample surface, creating a beat wave in the THz regime, overlapping with optical phonon frequencies in palladium hydride at 8 THz and at 15 THz [189]. Hagelstein's theory proposed that phonon resonances are involved in low energy nuclear reactions. The sample preparation, loading protocol and calorimetry were very similar to the previous work [271]. The authors reported excess heat when the beat frequency coincides with the phonon resonance (Fig. 7.37a). In addition to the compiled figure, they also provided the excess heat measurements in tabular form and figures of individual experiments at a certain frequency range. Our analysis of these datasets is shown in Fig. 7.37b). Interestingly, no trend of excess heat *vs.* frequency is apparent from our analysis.

Suspiciously, there are numerous inconsistencies in the data provided in the paper [104]:

- Figure 9, at a beat frequency of 15.4 THz, shows a huge variation in excess heat from +180 mW to -50 mW. This is confirmed in the text, but not reflected in the table on p. 8.
- In figure 10, the scan rate of excitation frequencies is much too fast for the calorimeter to respond. The calorimeter takes about three hours to equilibrate after turning on power input (p. 5).
- Figure 11 shows excess heat of 200 mW for several hours after the laser is turned off.
- They claim very good reproducibility, but figure 13 shows a repeat experiment and does not support the claim.

In 2015, Letts published a similar paper based on the same dataset [272].

Guffey et al. from ReResearch LLC reported an attempted, but failed replication of the Letts experiments [273]. They directly corresponded with Letts and also tested some of his samples. Because the gold deposition duration was not specified in the original papers, they attempted 10 min to 14 h gold plating durations. As opposed to the original experiment, they used lasers with a lower power of 10 mW instead of

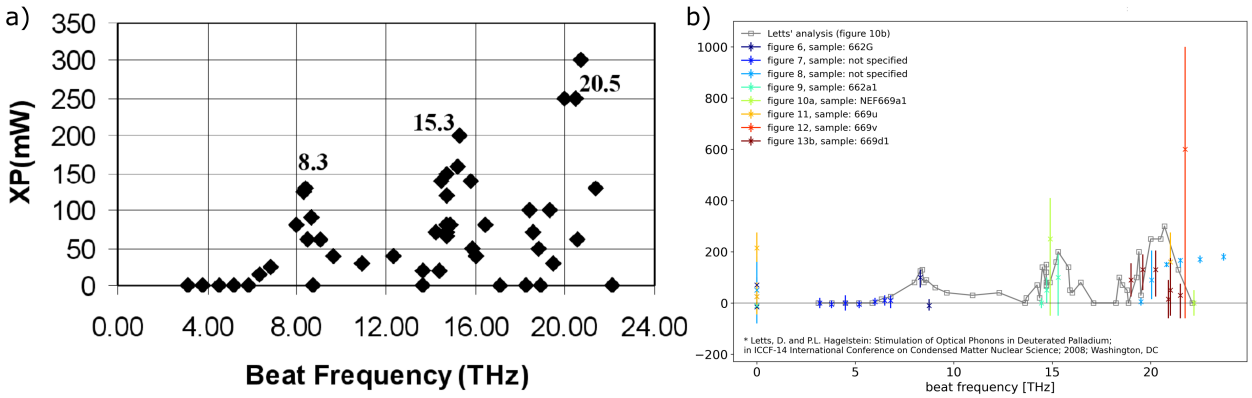



Fig. 7.37: Excess heat *vs.* beat frequency plots of Letts' experiment [104]. a) Plot reported by Letts. Excess heat maxima coincide with the edges of the optical phonon band at 8 THz and at 15 THz Source: [104]. b) Our analysis of the data provided by Letts [104]. No systematic dependence of excess heat on beat frequency is visible. Large variations in excess heat were observed with the laser off (shown at a beat frequency of 0 THz).

30 mW. Ultimately, they provide a histogram of 231 replication experiments, showing an average excess heat of 6 mW (compared to a few W input), concluding that there is no significant excess power. They provide a list of improvement suggestions:

- The heat of recombination has to be included in the heat balance. Apparently, according to their communications, this was not the case in the original papers.
- Variations in the recombiner efficiency can cause heat spikes, which are difficult to diagnose if the pressure is not measured.
- They found >2 K temperature non-uniformity in the electrolyte, which can lead to huge calorimetry errors, especially if the sensor placement if not carefully controlled.
- They encountered several temperature sensor failures, which leads to calorimetry errors.

### 7.9.2 Replication Experiments

Notwithstanding the severe lack of scientific quality of the original Letts papers and the unsuccessful replication attempts by ReResearch, we performed our own replication attempts, attracted by Hagelstein's phonon resonance model, which provided a more physically sound explanation of excess heat than most other stimulations (e. g., *superwaves* or electromigration). Though fundamentally, the concept of lattice assisted fusion is still at odds with known nuclear physics.

Due to the shortcomings of Letts' calorimeter (semi-open, isoperibolic), we designed a device based on the thermal bar heat flow measurement principle of the HTcal. Our system is thermodynamically closed. A quartz window provides optical access for the two laser beams (Fig. 7.38 a). We followed Letts' sample

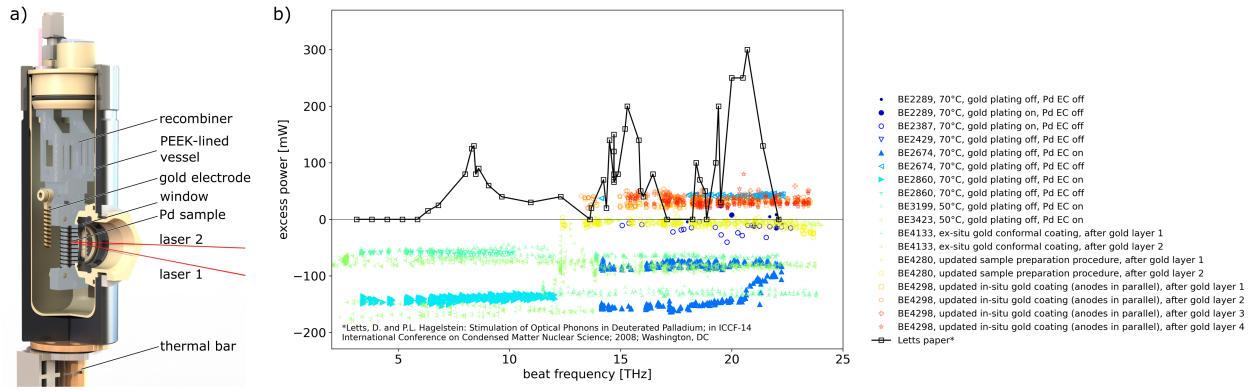



Fig. 7.38: In-house replication of Letts' experiments. a) Schematic of experimental setup showing the HTcal style vessel with a quartz window for optical access. Not shown are the magnets, foam insulation and laser optics including laser sources, optical power meters, spectrometer, polarizers and focusing mirrors. b) Compilation plot of excess heat *vs.* beat frequency of replication experiments.

preparation protocol [104, 271] as closely as possible, and were aided by direct communications with Letts. After loading the sample at 0.1 A for 120 h, the EC current was increased to 0.6 A, resulting in an EC power of ~3 W. 24 h after that, gold was deposited incrementally. To this end, either the bias was applied between the gold and palladium electrodes (with the platinum counterelectrode disconnected) or the gold electrode was connected in parallel with the platinum counterelectrode. The gold plating duration per deposition increment was varied between 10 s and 1 min with typically five to ten depositions. After each deposition, the laser frequencies were scanned such that the beat frequency was scanned up and down across one of the phonon resonance peaks (2 to 14 Thz or 12 to 24 THz). The range of the laser frequencies was not sufficient to cover both phonon resonances; instead one of the lasers had to be swapped to cover the second phonon resonance peak. The duration of each beat frequency scan was typically 50 h. An example dataset of one of the replication experiments is shown in Fig. 7.39. None of the replication experiments showed a clear dependency of excess heat on beat frequency (Fig. 7.38 b). In the initial replication experiments, the excess heat was suppressed by ~100 mW, which is ~3 % of the input power. We ascribe this reduced accuracy to effects of the window on heat transfer, which were exacerbated by the elevated enclosure temperature of 50°C. While the accuracy was initially suppressed, the precision of the calorimeter is <<1 %.

### 7.9.3 Conclusions

The excess heat reported by Letts [104] as a function of laser-stimulated phonon resonances is not supported by the data he provides in the same paper (see Fig. 7.37b), and is therefore an unsubstantiated claim lacking scientific evidence. Previous replication attempts failed as well [273].

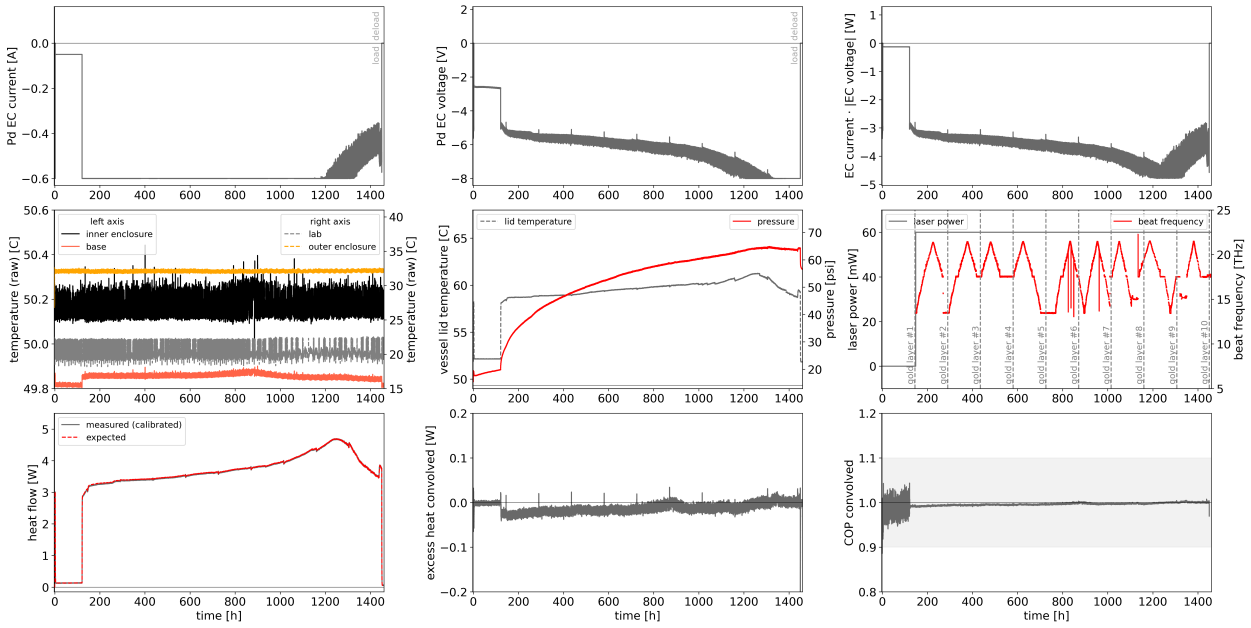



Fig. 7.39: Example dataset of in-house replication of the Letts experiment. Ten layers of gold were deposited. No anomalous heat was detected.

## 7.10 Conclusions

Callisto performed several hundred replication experiments. Some of them were replicated exactly, down to sourcing vintage components based on correspondence with the original scientists. In other cases, critical elements were replicated, but existing infrastructure (e. g. sample holders, calorimeters) was utilized. We found no signs of excess heat. To summarize:

- Fleischmann [26]: The paper is lacking electrochemical or calorimetry data to support their claims. Insufficient details for an accurate replication were provided.
- McKubre [101, 110]: After reporting excess heat in his 1994 paper, in his 1998 paper he admits that the calorimetry was "seriously inaccurate" under the given electromigration conditions and concludes "that the presumption of repeatable excess heat production was premature".
- Staker [105]: Staker reported a one-off excess heat event with a COP of 2.0 using open-system calorimetry. In a corrigendum, he retracted the claim and reported a COP of 1.67 [241]. Retracting the central outcome of a paper sheds a bad light onto his scientific rigor. We observed false COPs of similar magnitude using exact replications of his setup.
- Hubler [250]: Hubler's paper was not published in a peer-reviewed reputable journal and contained inconsistencies in the data, in particular a low cell temperature during periods of reported excess heat, pointing to alternative heat sources.

- Storms [113]: Storms reported relatively small amounts of excess heat using an open-system calorimeter. He also reported excess heat in light water experiments, pointing at a miscalibrated calorimeter or mechanisms other than D-D fusion.
- Barham [106]: Barham reported large amounts of excess heat (5 W at 15 W input) when in-situ depositing palladium onto the cathode in an open-system calorimeter. Curiously, the excess heat is constant and starts before substantial deposition of palladium. Localized temperature measurements indicate that the heat source is the anode, not the cathode.
- Energetics [102]: Energetics' reports were not published in reputable peer-reviewed journals and were of exceedingly poor quality (omission of critical details, missing units, missing labels, erratic heat flows). In several instances, high reported COPs coincided with the onset of hardware malfunctions.
- Letts [104]: The excess heat as a function of laser-stimulated phonon resonances is not supported by the data provided and is therefore an unsubstantiated claim. Previous replication attempts failed as well [273].

# Chapter 8

# Novel Experiments

## 8.1 Mechanical Stimulation

### 8.1.1 Motivation

Numerous reports suggest that the morphology of palladium (or its hydride) is critical to AHE. Mechanically working a metal sample can change its morphology. For instance, Violante used cold rolling to achieve the desired morphology [274]. He also supplied samples to Energetics [102]. Storms and Letts used a similar sample preparation involving cold rolling [104, 113]. Staker preconditioned samples by cyclic loading and deloading to obtain a fine-grained morphology [105]. Fundamentally, the morphology (strain fields, defect densities etc.) determines the energy landscape around hydrogen in interstitial octahedral sites as well as the hydrogen diffusion rates, which in turn could affect AHE.

In-situ mechanical deformation could drastically increase the number of states that are amenable to AHE present within a sample under investigation by continuously changing the energy landscape, creating defects and slipping atoms along each other. It would also create transient states that present potentially favorable configurations to AHE, that will otherwise have relaxed in the time period between ex-situ mechanical deformation and the experiment. To our knowledge, no in-situ mechanical stimulation experiments of palladium hydride during calorimetry have been reported in the literature.

In principle, all kinds of stress fields are possible: uniaxial tension, uniaxial compression, torsion, hydrostatic tension, hydrostatic compression. Hydrostatic compression is common during gas loading, which is outside of the scope of this study. Hydrostatic tension likely has the largest effect on the behavior of hydrogen in palladium hydride, but it is hard to achieve experimentally. Thus, uniaxial tension and torsion are of most interest and are easy to implement in practice. Specifically, in a wire under torsion, the highest strains are located near the sample surface, which is hypothesized to be the location of AHE. For this reason, torsion is the most attractive deformation mode.

### 8.1.2 Background

In unstrained palladium hydride, the hydrogen almost exlusively occupies the octahedral interstitial sites [189]. Tetrahedral sites are used only transitorily as hydrogen moves from one octahedral site to an adjacent octahedral site. Kimizuka and Akiba reported that in strained palladium hydride, the tetrahedral interstitial

sites become more favorable [275, 276]. This can increase the hydrogen diffusion rate by 20 times at room temperature [275]. Valiev reported that severe plastic deformation (SPD) can lead to non-equilibrium grain boundaries, deformation twins, dislocation substructures, vacancy agglomerates, and solute segregation and clustering. SPD-induced lattice defects can act as nucleation sites for hydrogenation [277]. Their stability is critical for the overall reproducibility of the absorption/desorption kinetics. Thus, hydrogen loading and deloading is much faster (or just as fast at a lower temperature) in SPD treated materials than in pristine materials. Hongo applied high-pressure torsion (HPT) to form an ultrafine-grained (UFG) structure with an average grain size of ~ 220 nm, resulting in increased hardness and tensile strength as well as increased plasticity [278]. This is in contrast to pristine palladium (with a grain size of tens of $\mu$m), which embrittles when loaded with hydrogen. The hydrogen-enhanced localized plasticity (HELP) is ascribed to hydrogen serving as solute atoms, increasing the dislocation mobility [279]. Dislocations which are generated during hydrogenation and dehydrogenation remain in the microstructure and enhance the hardness even after deloading [280, 281]. At an atomic level, the strain field around a dislocation effects an increase in hydrogen concentration within a radius of five to ten unit cells around the dislocation [279]. Increased diffusion rates and increased residence times of hydrogen ions in tetrahedral interstitial sites could present favorable conditions for AHE reactions.

### 8.1.3 Implementation

The mechanical properties of palladium hydride are shown in Fig. 8.1. For reasons listed above, we settled on a torsion geometry. The expected torsion angle at yield for a 0.5 mm diameter palladium wire is 14°, the torsion angle at break is 48°, and the torque at break is on the order of a few mNm. With increasing wire diameters, more torque is needed and the torsion angle at break will be reduced.

We defined the requirements for an in-situ mechanical deformation device during calorimetry as follows:

- The power transfer across the thermal boundary must be measured accurately. It might be easiest to measure electrical power and convert it to mechanical motion inside the boundary (as opposed to having a shaft crossing the thermal boundary).
- Torque or force must be enough to achieve yield on typical sample dimensions, ideally going beyond yield towards fracture.
- The strain rates must be high enough to perform cyclic experiments.
- Hydrogen loading must be measured at least prior to deformation, ideally also during deformation, using resistance measurements.
- Motor and gearing must be protected from corrosive electrolyte.
- The setup should fit into an HTcal vessel (section 2.7).

Our first design centered around a geared stepper motor (GM15BY-VSM1527-100-10D). However, with no eyes on the sample and long cyclic deformations applied to the sample, even occasional missed steps resulted in an indeterminate sample state. For that reason, an angle encoder (US Digital E4T-360-250-S-H-D-B, connected to a NI PXI-6608) was added and the stepper motor was replaced with a DC motor (Pololu Micro Metal Gear motor with 1000:1 gear ratio, #2373, run by a NI PXI-4141). The design of the mechanical stimulation cell that fits into an HTcal vessel is shown in Fig. 8.2.

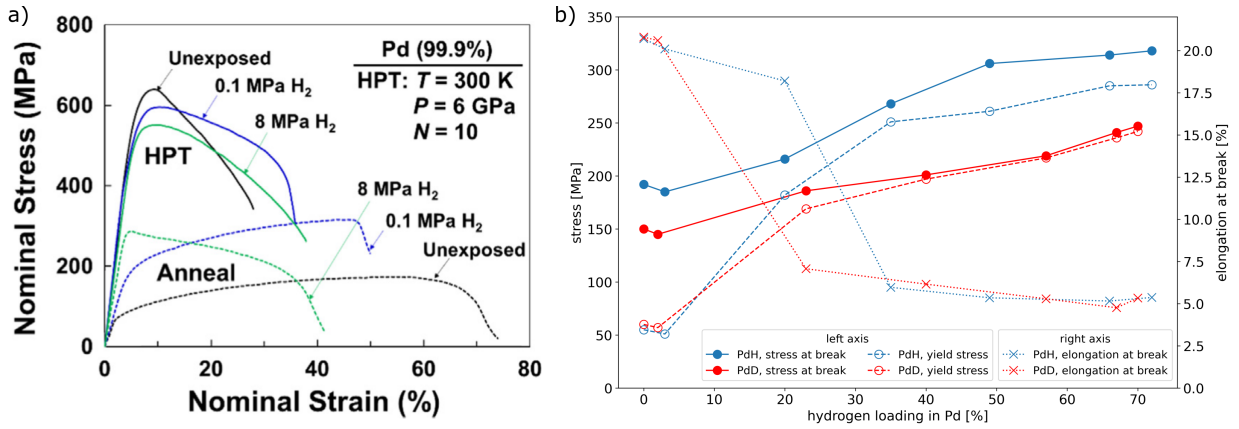



Fig. 8.1: Mechanical properties of palladium and palladium hydride. a) Stress-strain curves of palladium ("unexposed") and palladium hydride (with gas loading pressures as indicated). Source: [278]. b) Yield stress, stress at break and elongation at break as function of hydrogen loading. Composed with data from [282].

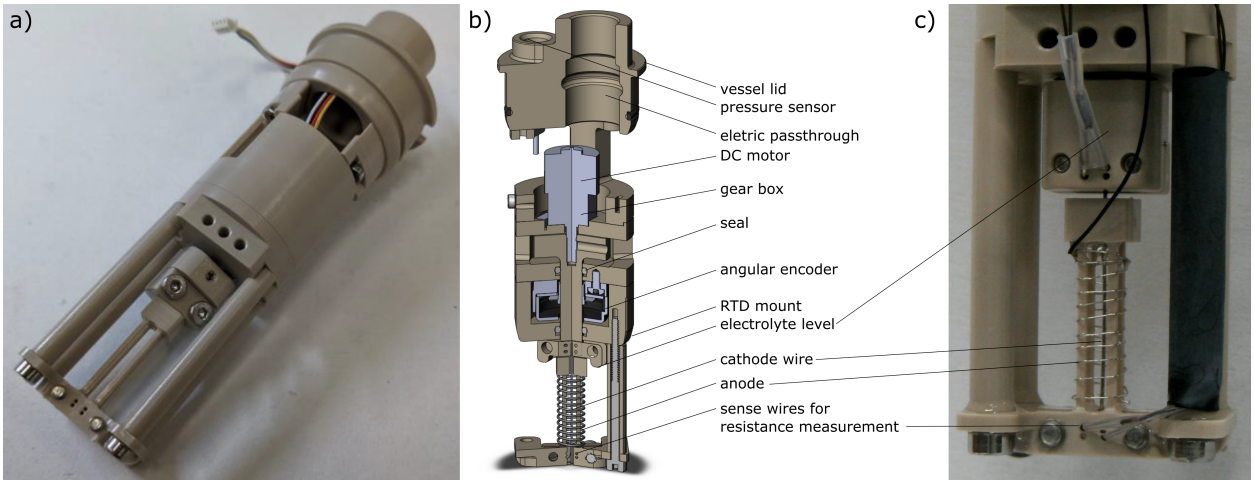



Fig. 8.2: Design of mechanical stimulation cell for in-situ deformation during calorimetry in HTcal. a) Photograph of mechanical stimulation cell during assembly. b) CAD rendering of mechanical stimulation cell with labeled components. c) Photograph of sample assembly with electrodes and four-wire resistance measurement.

### 8.1.4 Experiments and Results

Various mechanical deformation histories were applied to palladium and palladium hydride samples – before, during and after hydrogen loading. An example is illustrated in Fig. 8.3. Here, a 0.5 mm diameter palladium wire (99.9 %, Sigma Aldrich, surface treated with centerless grinding) is electrochemically loaded with deuterium in 0.5 M LiOD in $D_2O$ at -55 mA for 9 h. During the 9 h electrochemical loading period, a combination of cyclic deformation and hold periods is applied (8.3 a). Every 95 cycles, a hold period of 5 minutes is applied and the torsional amplitude is increased. An overview of all calorimetry data channels is provided in Fig. 8.3 b. The magnitude of the excess heat is small compared to the input power, resulting in a COP close to unity. Similar results with no significant excess heat were obtained in all mechanical stimulation experiments.

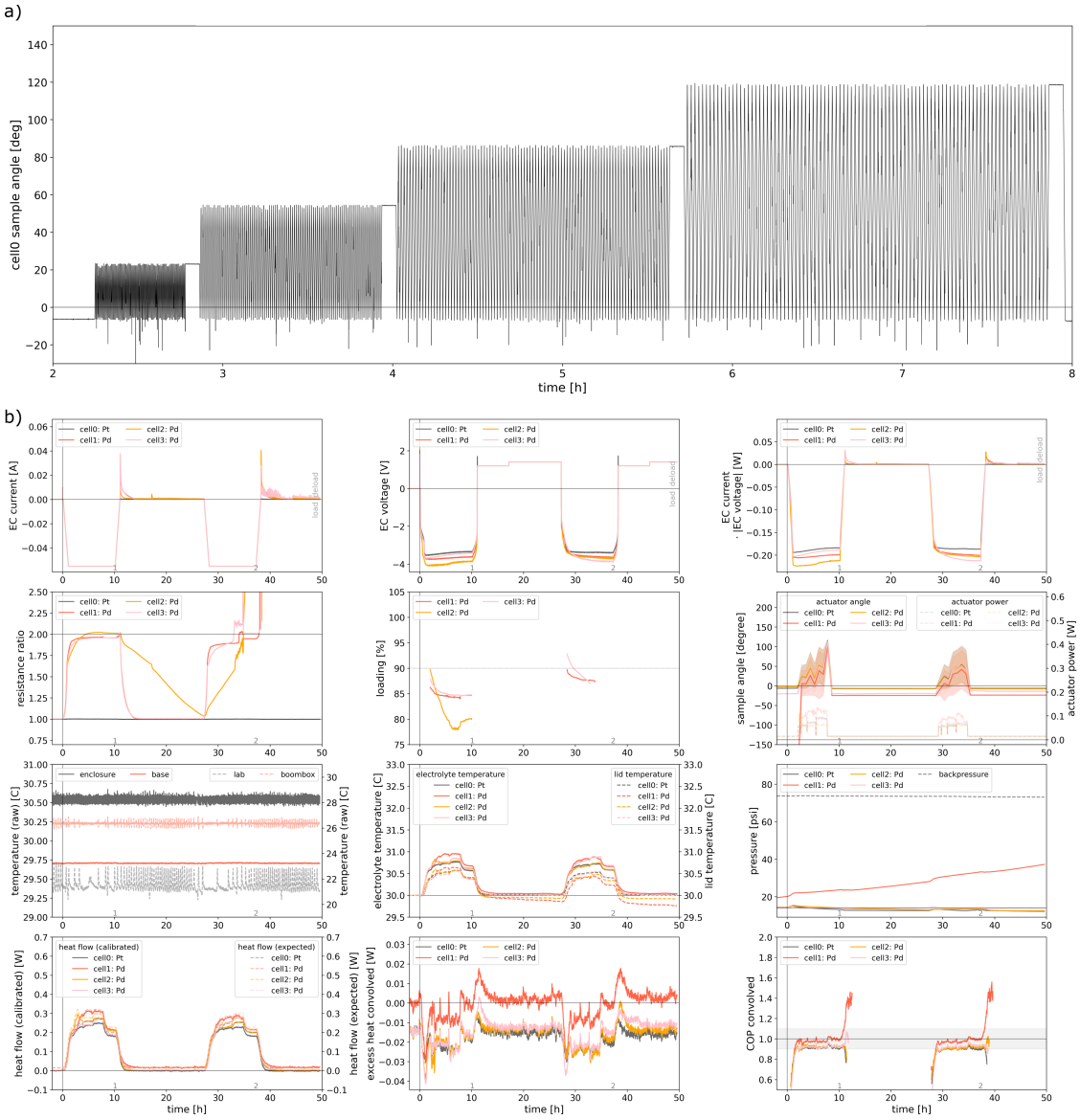



Fig. 8.3: Example of a mechanical stimulation calorimetry experiment in the HTcal with several hundred mechanical load cycles, mechanical load holds and two electrochemical load-deload cycles. a) Torsional deformation history applied to the sample during the nine-hour hydrogen loading period. b) Data channels of calorimetry experiments. The sample angle is resampled for better illustration. The actual sample deformation is indicated in a). The measured heat flow and the expected heat flow (from the total input power and the instrument response function) generally agree closely, resulting in a COP of unity. Cell 1 exhibits an elevated COP while the input power is being stepped down, indicating that the instrument response is not well modeled.

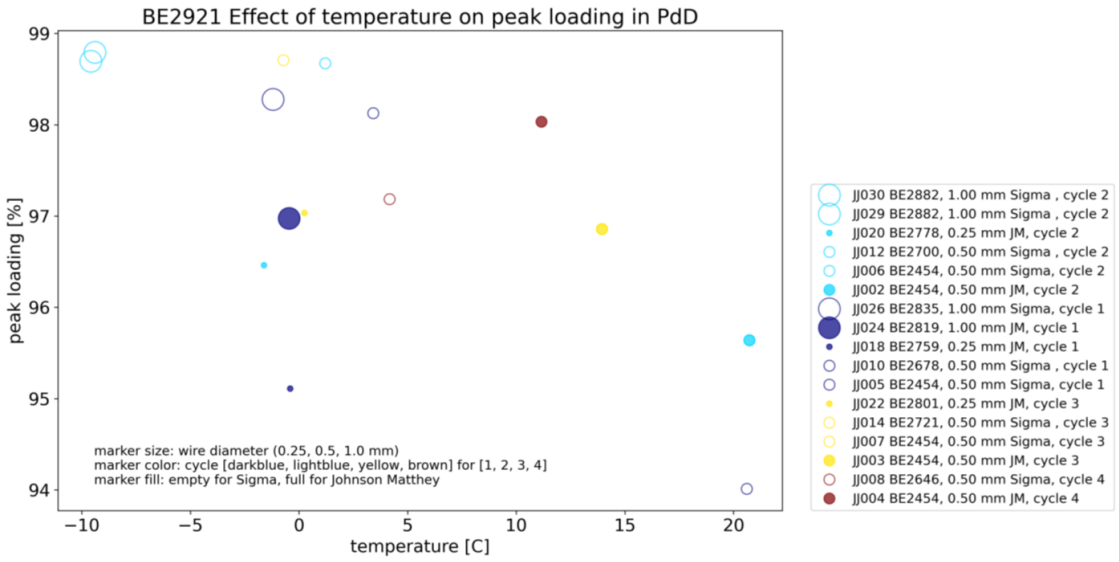



Fig. 8.4: Summary plot showing results of open cell loadings as a function of temperatures ranging from 20 to -10 °C.

## 8.2 Loading Enhancers

### 8.2.1 Loading Enhancers: Arsenic at Low Temperatures

From the results shown in Figure 6.2, it was clear that arsenic was the loading enhancer of choice. However, the loading enhancement achieved from the introduction of As was short lived and thus we began working on extending the longevity of the enhancement. We initially started with optimizing 'Coating X' further as we observed excess Pt content in the overlayer correlating with decreased peak loadings. This led us to studying As dosant in the previously mentioned membrane separator compartment. We then began to study the effect of lower temperatures on peak loading, as lower temperatures should slow the kinetics of HER during loading and 'Coating X' formation. Figure 8.4 shows the peak D loading values for loading experiments dosed with 25 mM $NaAsO_2$ dosant and carried out at temperatures between 20 and -10 °C. We observe a clear increase in loading enhancement as temperatures decrease though the mechanism of this enhancement is not clear. We believe it is related to a slowing of HER kinetics, specifically V-T, in conjunction with V-T pathway inhibition from 'Coating X' formation as stated earlier.

We needed to find an antifreeze additive to continue to explore this loading enhancement effect as a function of temperature below 0 °C. We screened ethylene glycol ($(CH_2OH)_2$), methanol ($CH_3OH$), and ammonia ($NH_3$) as additives to allow electrolysis at and below 0 °C without electrolyte freezing or ionic conductivity falling too low. Our studies showed excellent performance for loadings carried out below 0 °C in electrolytes containing ~20 % methanol, with multiple experiments showing above 98 % D loading for 15 hours. These studies clearly display the benefits of loading Pd at low temperatures in conjunction with As enhancement. Unfortunately, during electrolysis methanol generates $CO_2$ which accumulates in the headspace and leads to pressure build up. This was not a problem in open cell testing but would cause issues

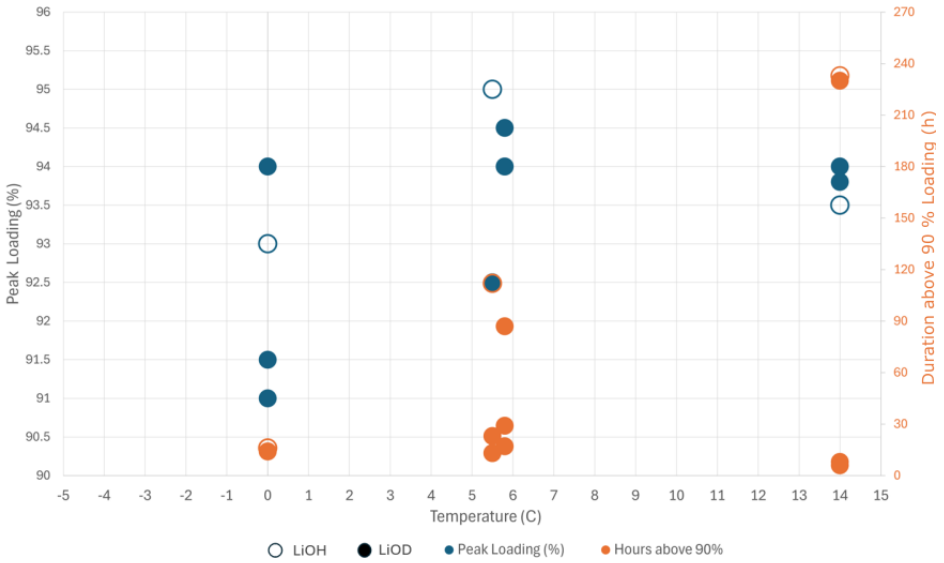



Fig. 8.5: Summary of the closed-cell, below room temperature loading studies with arsenic enhancement. Shown are the correlations between low temperatures (15 - 0 °C) and peak loadings (blue) and between low temperatures and loading longevity in this case, hours above 90% D/Pd (orange). Open circles indicate control cells in LiOH and closed cells represent LiOD.

in closed calorimetry testing.

As we investigated new additives, we found $NH_3$ to be a viable alternative to methanol as, while it could still produce unwanted gases in the headspace (i. e., $N_{2(g)}$, $H_{2(g)}$, and $NH_{3(g)}$), it could be used in much lower weight percentages in the electrolyte. In our control experiments using $NH_3$, we observed loading enhancement (~94 %) at room temperature without adding As enhancer and before lowering the temperature below 25 °C. This led us to the investigation of $NH_3$ as both a standalone loading enhancer and an additive to the electrolyte in conjunction with the As enhancer.

Continuing our investigation of loading enhancement with As below 25 °C, we moved our experiments to closed cell calorimeters as we've observed increased longevities (likely due to stabilization of electrolyte) in closed cells vs. open cells. In the open cell tests shown in Figure 8.4, an average time of loading enhancement was around 15 hours once the temperature set point was reached, with one outlier experiment being held for multiple days at D loadings ≥90 %. We developed an in-situ dosing strategy using syringe pumps and flexible polyethylene tubing lined with an inert fluoride coating tubing that allowed us to remotely introduce As enhancer into the system without opening the cells.

Figure 8.5 shows a summary of all of the closed-cell calorimetry experiments with peak loadings achieved and longevity of loadings ≥90 % as a function of average temperature. In these experiments we had not fully optimized anti-freeze additives to the electrolyte and subsequently avoided lowering temperature below 0 °C to avoid electrolyte freezing. Our open-cell results showed that the majority of our highest loadings occurred below 5 °C. As observed in the figure, we were able to achieve peak longevities for D loadings of ≥ 90 % for more than 230 h. We also achieved peak loadings of 95 % but did not see near 100 % loadings as

observed in open cell testing at -10 °C. We did observe some higher peak loadings as temperatures decreased, however freezing near 0 °C introduced major obstacles to closed cell As dosing and prevented long duration experiments.

### 8.2.2 Loading Enhancers: Ammonia Additives

Considering our previously observed loading enhancement at room temperature using $NH_3$ as an additive, we wanted to answer two major questions: 1) what is the mechanism by which $NH_3$ was enhancing loading and 2) what are the optimal conditions to achieve maximum loading enhancement using $NH_3$. We first tried to understand the loading enhancement and considered what was occurring in our system as we electrolyzed $NH_3$ containing electrolyte. A major question was if the electrolysis of $NH_3$ yielded a compound that acted as an additive to 'Coating X' or whether there was a surface effect that ultimately acted as a Tafel poison. The electrolysis reactions of $NH_3$ in alkaline media are:

$$\text{anode}: \quad NH_3 \rightarrow \frac{1}{2}N_2 + 3H^+ + 3e^- \tag{8.1}$$

$$\text{cathode}: \quad 3H^+ = 3e^- \rightarrow \frac{3}{2}H_2 \tag{8.2}$$

$$\text{overall}: \quad NH_3 \rightarrow \frac{1}{2}N_2 + \frac{3}{2}H_2 \tag{8.3}$$

In aqueous media, $NH_3$ partially dissociates into $NH_4^+$ and $OH^-$. The ratio of $NH_3$ to $NH_4^+$ depends on the pH. In alkaline media, most of the species are present in the form of $NH_3$, about 10,000 times more abundant than $NH_4^+$ at pH = 13.5 (0.5 M LiOH) [283, 284]. $NH_3$ can form complexes with $Pd^{2+}$ and $Pt^{2+}$ at positive bias [285]. It is possible that $Pt^{2+}$ ions going into solution are complexed and no longer poison the working electrode surface, leading to higher loading [285]. Another plausible mechanism is through tetraamine palladium complexes ($Pd(NH3)_4X$) which are known to form strong bonds with $OH^-$ [286]. This strong bonding can extract $OH^-$ from the surface, pushing the Volmer reaction equilibrium to the right, increasing the amount of adsorbed H on the Pd surface. We also observe a deviation from a trend observed with As enhancement where loading enhancements increased with cycling. Deviation in $NH_3$ containing electrolyte is possibly because during the deload, some of the Pd (now positively biased) gets complexed with $NH_3$ [285]. Another possibility is during deload, oxidation of $NH_3$ on the Pd surface forms $N_2$. $N_2$ is known to form strong bonds with Pd [285], which could deactivate some of the active surface similar to $H_2$ bubbles adhering to the surface.

We then investigated various concentrations of $NH_3$ to find the optimum amount of additive possible to achieve loading enhancement while simultaneously preventing excessive pressure build up from $NH_3$ electrolysis. These experiments are shown in Figure 8.6 where loadings are shown for multiple concentrations ranging from 5 to 28 % $NH_3$ in 0.5 M LiOH. From the plot it is clear that there was a negligible difference in peak loadings achieved between the lowest concentration (5 % $NH_3$) and the highest (28 % $NH_3$). Subsequently we carried out all of our resulting experiments out at this lower concentration to keep gases produced from electrolysis to a minimum.

### 8.2.3 Loading Enhancers: Arsenic with Single Crystal Palladium

One parameter that we adjusted in our experiments was the form factor of our Pd cathodes. We know that changing the form factor can impact loading and deloading as there is more (or less) Pd that can be loaded

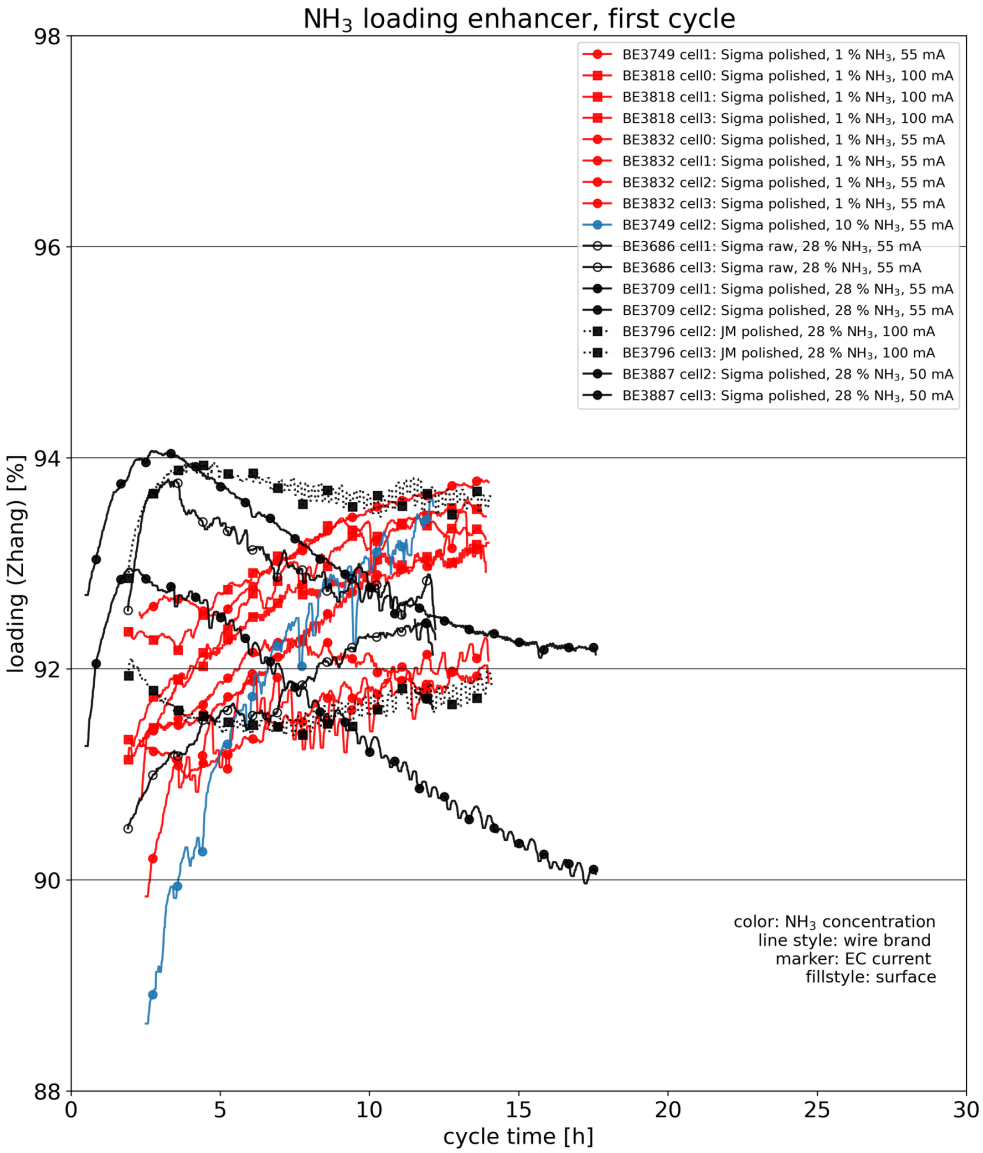
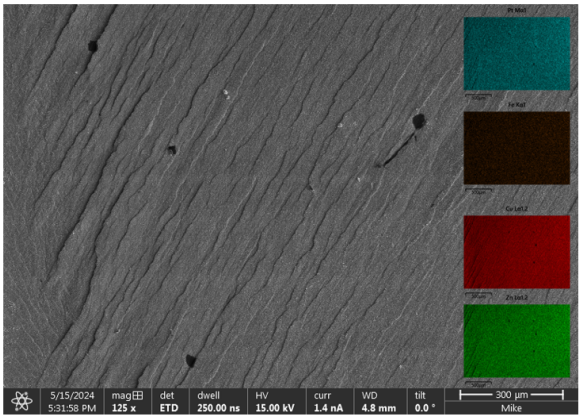
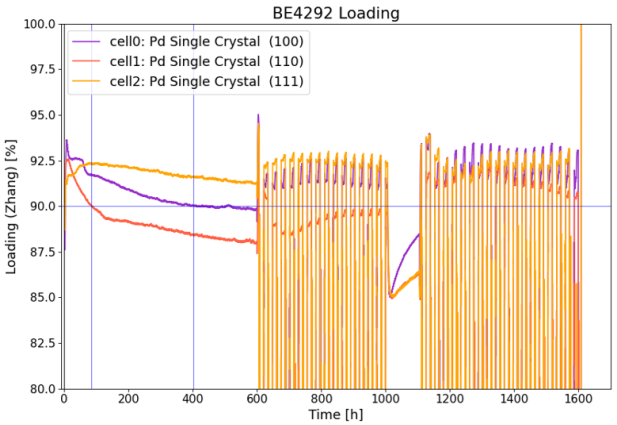



Fig. 8.6: Effect of $NH_3$ concentrations in 0.5 M LiOH electrolyte, EC current and wire preparation on hydrogen loading in palladium. The 0.5 mm diameter and 30 mm long Pd samples also had varying wire manufacturers (Johnson-Matthey, Goodfellow, and Sigma-Aldrich) with different processing (as-received or polished).

a)




b)




c)

| Sample (in LiOD) | Cycle 1 (h) (BE4261) | Cycle 2 (h) (BE4261) | | Cycle 3 (h) (BE4292) | | Cumulative Time (h) >90% D/Pd |
|---|---|---|---|---|---|---|
| | Dose 1 | Dose 1 | Dose 2 | Dose 1 | Dose 2 | |
| **Cell 0 (100)** | 0 | 370 | 189 | 401 | 900 | 1860 |
| **Cell 1 (110)** | 10 | 144 | 59 | 83 | 494 | 780 |
| **Cell 2 (111)** | 0 | 0 | 237 | 600 | 870 | 1707 |

Fig. 8.7: a) Representative SEM with EDS false color map of sample surface post mortem. (No As represented on surface, though it was present in various areas on the samples.) b) Results from a long duration single crystal experiment with both DC and AC stimulation applied to all three (100), (110), and (111) orientations. The system was dosed with 25 mM $NaAsO_2$ three times, once at the start of long duration constant current application (~1 hour), followed by a dose at the start of each AC stimulation application (~600 and ~1100 hours). The horizontal line depicts the 90 % D/Pd loading threshold. c) Table summarizing the cumulative time above the 90 % D/Pd loading threshold for the total experimental time for the samples, spanning two experimental campaigns (BE4261 and BE4292).

and currents have to be adjusted to accommodate that change. Additionally, it has been established that differences in the crystal orientation of exposed facets in Pd cathodes exhibit different hydrogen absorption and desorption mechanisms, and by extension have a direct impact on loading [287]. Johnson et al. monitored the $\alpha$- to $\beta$-phase transition in Pd (100), (111), and mixed (100) and (111) nanocrystals using in-situ X-ray diffraction (XRD) to indicate rate of H adsorption and desorption. This $\alpha$- to $\beta$-phase transition in the Pd crystal structure is indicated by a shift in $2\theta$ peak position in the XRD diffractogram. The rate of this transition can directly correlate the amount of H entering and exiting the Pd lattice. They discovered that the initial H uptake and release was much quicker for the mixed Pd and Pd (100) nanocrystals, with the transition from $\beta$- to $\alpha$-phase (deloading) being an order of magnitude slower for the Pd (111) nanocrystal compared to other samples. Of course, this sluggish $\beta$- to $\alpha$-phase transition observed in the Pd (111) orientation translates to a slower deloading process once loaded and ultimately highlights a difference in crystal orientation regarding H loading that could be leveraged for AHE.

To investigate further, we set up a series of experiments observing the effect of different Pd single crystal

orientations ((100), (110), (111)) on loading with As loading enhancement. The results of these studies are shown in Figure 8.7. The figure shows post-mortem SEM/EDS sample analysis showing the presence of Coating X elements on the surface (As is absent from the coating despite dosing, likely due to the long duration of the experiment), loading analysis for the final 1600 h of the experiment for each (100), (110), and (111) Pd orientation, and a summary plot of time of D loading ≥90 % for each orientation resulting from As enhancement doses. While the representative data shows our champion results from long-duration AC stimulation current on Pd single crystal samples (well over two months above ≥90 % loading), multiple DC stimulation studies were also carried out. Our studies aligned with the hypothesis we formed from Johnson et al. where we expected Pd (111) to stay loaded longer than the (110) and (100) orientations due to slower deloading kinetics. Interestingly, we found that the Pd (110) orientation tended to load lower and fall below 90 % D loading quicker than the Pd (100) and (111) upon the first cycle. As stated earlier, we have observed a positive correlation between peak loadings, loading longevities, and cycling (with diminishing returns after the fourth cycle on average). Studies show that with cycling, Pd (111) begins to outperform the Pd (110) and (100) orientations regarding peak loadings and longevities. This behavior could not be explained by postmortem SEM/EDS analysis, as all the Coating X constituents and coating characteristics were similar between orientations. Our hypothesis is that the orientation is initially less favorable to Coating X formation but as cycling progresses the coating is allowed to build up and inhibit D loss. It would appear an opposite effect would be at play for the Pd (110) orientation which exhibited lessened peak loadings and longevities as a function of loading. This change in loading longevity and by extension, lessened V-T inhibition is still being investigated. It is also likely that these differences between orientations could be sample dependent as we carried out multiple single crystal studies, but this was our flagship long-duration test lasting >400 hours.

## 8.3 Single Crystals

### 8.3.1 Introduction

The vast majority of studies in the LENR literature focus on a host palladium (Pd) lattice, which is an exemplary metal for its ability to intake large amounts of hydrogen isotopes with relatively little driving force. The original Fleischmann and Pons studies focused on using polycrystalline Pd [240, 288, 289]. These early studies looked at relatively large samples, with the rods ranging in diameter 1 mm to 20 mm, or in terms of mass between 100 mg and 60 g. The samples were typically sourced from Johnson Matthey and were claimed to be of very high purity (>99.9%$_{at}$). Subsequent work by the community in the 1990s and 2000s continued to focus on polycrystalline palladium, with minimal exploration of other alloys and formfactors. Notably, some people including Edmund Storms looked at Pd-Ag alloys [290]. Groups like SPAWAR explored nanostructured palladium [266]. More recently, the LENR community has explored metals beyond Pd, with one of the major motivations being the prohibitive cost of palladium. Researchers have looked at nickel (Ni) as a possible nuclear active material [291, 292]. One of the critical questions that has plagued researchers throughout the LENR field has been, "Why palladium?" What is special about this material that allows for the production of excess heat? There are certainly characteristics that make it stand out among metal hydrides. These include a relatively low temperature for absorption and desorption of hydrogen isotopes, a relatively high volumetric storage density, and its exceptional hydrogen solubility. Palladium can absorb hydrogen at concentrations approaching a hydrogen-to-palladium ratio of 1:1 (if sufficient gas pressure or electrochemical driving force is applied), much higher than most other metals at standard pressure and near room temperature. Of course, there is no fundamental mapping of these characteristics to the generation

of excess heat, but they are certainly interesting to note. In our own effort, we aimed to test out different purities, form factors, and compositions in order to try and deterministically understand how the material characteristics of a metal hydride influence the ability to generate excess heat. Admittedly, after exploring many different alloy compositions, form factors, sample masses, crystallinities, etc., we never arrived at excess heat. Despite this, the next section will highlight some of the major experimental efforts that we pursued, notably our efforts with single crystals and various alloy compositions.

Solid metals are inherently crystalline, meaning they have a well-defined, periodic atomic structure. However, over extended length scales, defects can occur, disrupting this symmetry. These include point defects, dislocations, and grain boundaries. Interestingly, these defects can be kinetically favorable, so most metals exist in a polycrystalline form. The material's morphology includes characteristics such as grain size (small or large), grain shape (elongated or equiaxed), grain boundary angles (high or low), and surface roughness (which can be influenced by dislocations). Due to variations in sourcing, manufacturing, and post-treatment processes, the morphology of palladium can vary significantly. Palladium from the same vendor and with the same form factor and composition may exhibit similar morphologies, while material from a different vendor, despite having the same nominal composition and form, may have nuanced morphological differences. Changes in the ore source over time can also affect impurity concentrations. For example, in the 1980s the primary source of palladium ore was the Norilsk-Talnakh mining complex in Russia, with modest contributions from South Africa's Bushveld Igneous Complex [293]. Today, although Russia and South African deposits remain significant portions of the market, the Sudbury Basin in Canada and Zimplats mine in Zimbabwe are becoming prominent suppliers. As a result of the change in ore supply and nuanced differences in purification and manufacturing, one of the major challenges facing the LENR community has been understanding why certain palladium samples allegedly exhibited nuclear activity while others did not.

### 8.3.2 Experiments

Figure 8.8a shows an x-ray diffraction pattern of nominally similar palladium from four different manufacturers. The differences in diffraction patterns reveal that there are different grain sizes for each of these manufacturers. These grain sizes are correlated with loading performance which is shown in Figure 8.8b. We found that smaller grains gave higher deuterium electrochemical loadings, when all other parameters were controlled. Assuming the observed instances of excess heat are not simply false positives (which is plausible and currently the conclusion of our team's work), we must ask how we can map these material characteristics to any observed excess heat deterministically. We decided that using single crystal palladium samples would provide the best chance for this determinism. Unlike polycrystalline palladium, single crystal palladium maintains pristine lattice symmetry across its entire macroscopic dimension, with few to no point defects, dislocations, or grain boundaries. This not only provided a blank canvas for monitoring changes to the morphology directly resulting from our experiments, but also allowed us to know with high confidence, the exact nature of our material. However, growing single crystal materials is challenging. When we decided to pursue single crystal palladium, there were no commercial suppliers available. We commissioned Princeton Scientific, experts in single crystal materials, to begin growing single crystal palladium for us. Initially, we obtained small ingots approximately 8 mm in diameter and 25 mm in length. We specified three surface terminations corresponding to the primary crystallographic planes in face-centered cubic materials: (100), (110), and (111), as shown in Figure 8.9. As Princeton Scientific improved their growth techniques, we were able to source larger samples.

The ultimate goal was to machine single crystal bars with a high aspect ratio for electrical resistance studies. The high aspect ratio would allow us to make accurate resistance measurements and better under-

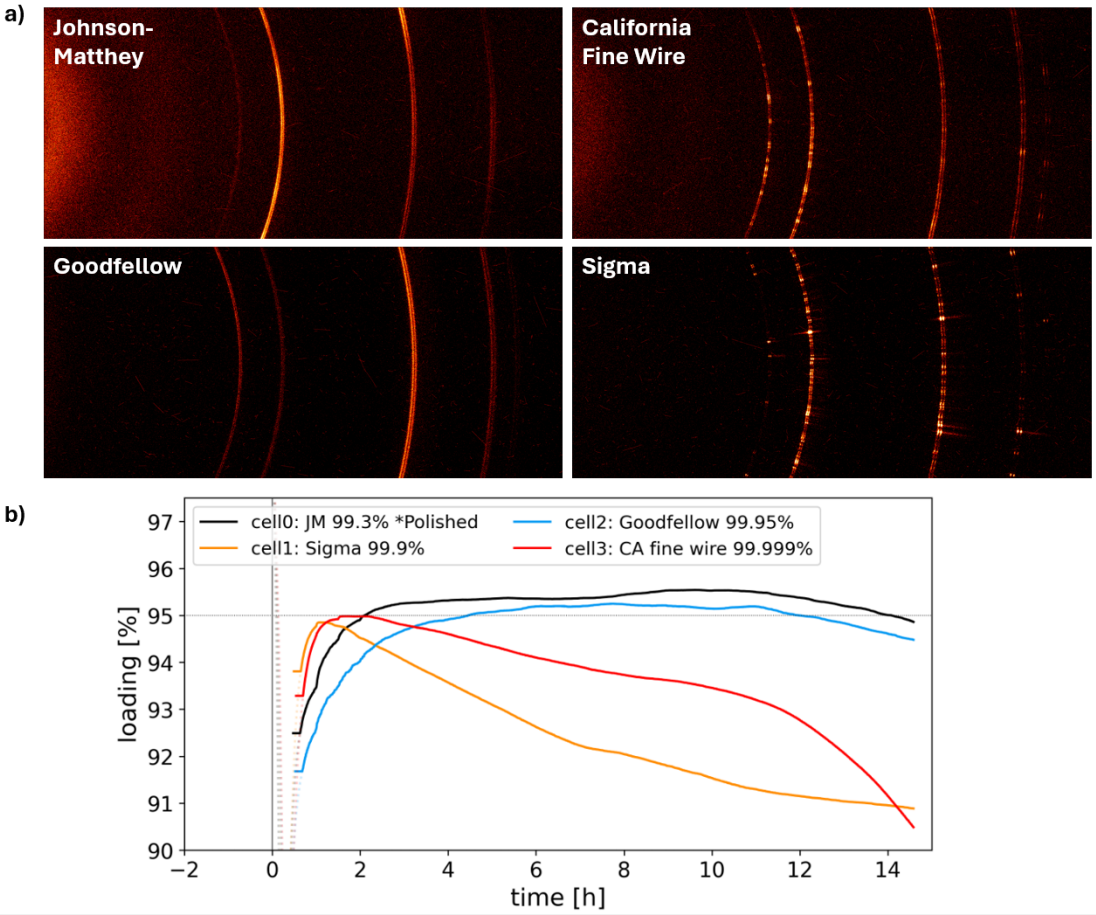



Fig. 8.8: a) X-ray diffraction (XRD) pattern of as-received Pd samples from four different manufacturers (Johnson-Matthey (polished), California Fine Wire, Goodfellow, and Sigma-Aldrich). The peaks in the XRDs are (from left to right) 111, 002, 022, and 222. b) Is a comparison of deuterium loading performance of each wire manufacturer as a function of time when exposed to similar loading conditions (i.e., 0.5 M LiOH, -50 mA of current, and 2 mL of 25 mM $NaAsO_2$).

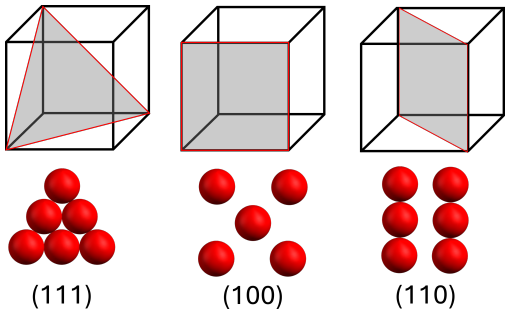



Fig. 8.9: 3D representation made in house of surface terminations corresponding to the primary crystallographic planes in face-centered cubic materials: (111), (100), and (110).

stand the effect of crystal orientation on loading capacity and kinetics. Ultimately, we went through four generations of sample sizes. The first generation consisted of 10 mm diameter disks with a thickness of around 500 $\mu$m. The second generation featured small bars, 4 mm x 8 mm x 500 $\mu$m, cut from the center of the ingots. The third generation involved medium-sized bars, 3 mm wide and 12-15 mm long, requiring more advanced machining techniques. For these, we cut ingots with different orientations, such as a (111) ingot, at off angles to expose the (100) surface. X-ray diffraction was used to orient the samples before machining to ensure accuracy. In the final generation, we achieved high aspect ratio single crystal bars with dimensions of 3 mm x 30 mm x 500 $\mu$m by contracting Princeton Scientific to grow 50 mm diameter single crystal wafers, from which the bars were cut using electrical discharge machining. All generations were polished to <5 nm roughness through a combination of mechanical polishing and ion milling. The final generation of samples was likely the largest diameter single crystal palladium ever produced –a notable achievement for our materials research efforts, even if not broadly significant. Due to the precious nature of these single crystal samples, we were more selective in deploying them for calorimetry studies. In total, we performed 35 studies, which are briefly described below. It is important to note that although the use of these samples would have allowed for deterministic understanding, the lack of excess heat precluded this type of understanding.

### 8.3.3 Overview of Experimental Results

We characterized the crystal structure of the prepared samples using x-ray diffraction (XRD). The diffraction patterns revealed excellent monocrystallinity, particularly in contrast to polycrystalline samples, which showed distinct patterns. This quality check was especially important for the medium-sized samples, which were obtained through off-angle cuts. Miscalculations or poor cutting could have compromised monocrystallinity, but we consistently produced high-quality monocrystalline surfaces across all sample generations. Nearly a dozen experiments comprised the initial calorimetry tests on single crystal samples, conducted using the MS80 differential calorimeter (section 2.8.1), which offered excellent sensitivity. However, as the number of tests increased, the calorimeter became difficult to operate, and we eventually replaced it with the HTCal model. These experiments explored high-frequency electrochemical stimulation and the use of arsenic salts to enhance deuterium loading. No definitive excess heat was detected, with false signals attributed to transient recombination events and electrical interference due to corroded contacts, which were easily explained. It

should be noted that there was a COP ~1.05 in one experiment (BE1320) that was never explained, however the test conditions were repeated, and the result was never reproduced. There was not sufficient confidence in this one-time result to attribute it to a nuclear origin. Several experiments (BE1724, BE1785, BE1779, and BE2071) mirrored the previous set but were conducted using the HTCal system. Although HTCal had a higher detection threshold than the MS80, its increased throughput allowed us to test twice as many single crystals at one time. High-frequency electrochemical currents were again applied to perturb the electric field at the surface, but no excess heat was observed. The most prominent false signals were due to transient recombination. With the development of large aspect ratio single crystal bars, we expanded our testing conditions using the HTCal calorimeter. These experiments applied high DC current densities to optimize deuterium loading without the need for arsenic enhancement. No excess heat was observed, and again the primary false signals came from transient recombination events. Additional large aspect ratio experiments aimed to induce excess heat by applying high-frequency perturbations to the electric field at the surface of palladium deuteride single crystals were carried out. We focused on frequencies between 10 mHz and 10 Hz, where we expected the greatest impact on the structure of the electric double layer. This is due to both experimental availability and because of the inverse relationship between frequency and measured capacitance of the the electronic double layer. The ability of the double layer interface to store charge at high frequencies is reduced because only ions near the electrode surface have enough time to respond to the rapidly changing potential [294]. No excess heat was observed during these tests.

### 8.3.4 Overview of Single Crystal Morphology Changes from Electrochemical Loading and Stimulation

Electrochemical testing led to significant changes in sample structure and surface composition of palladium single crystals. Deuterium cycling resulted in a loss of monocrystallinity, increased surface roughness, and substantial distortion of the form factor. Figure 8.10a illustrates the transition from point-diffraction to ring-diffraction patterns, as well as the broadening of peaks, indicating the introduction of grain boundaries, point defects, and line defects. Cycled foil samples often became twisted and crumpled, with large volumetric changes due to the stresses developed during deuterium charging and discharging. This is shown in Figure 8.10b. These changes, more significant than those typically reported in the literature, are likely due to the starting single crystal state, where the introduction of defects caused more pronounced macroscopic distortions. Additionally, Coating X (see section 6.3) was observed on most samples, regardless of whether DC or AC conditions were applied. The composition of Coating X varied depending on the reaction vessel used, with Pt, Cu, Fe, Sn, and Pb often present. These morphological changes were noted in both hydrogen and deuterium isotopes.

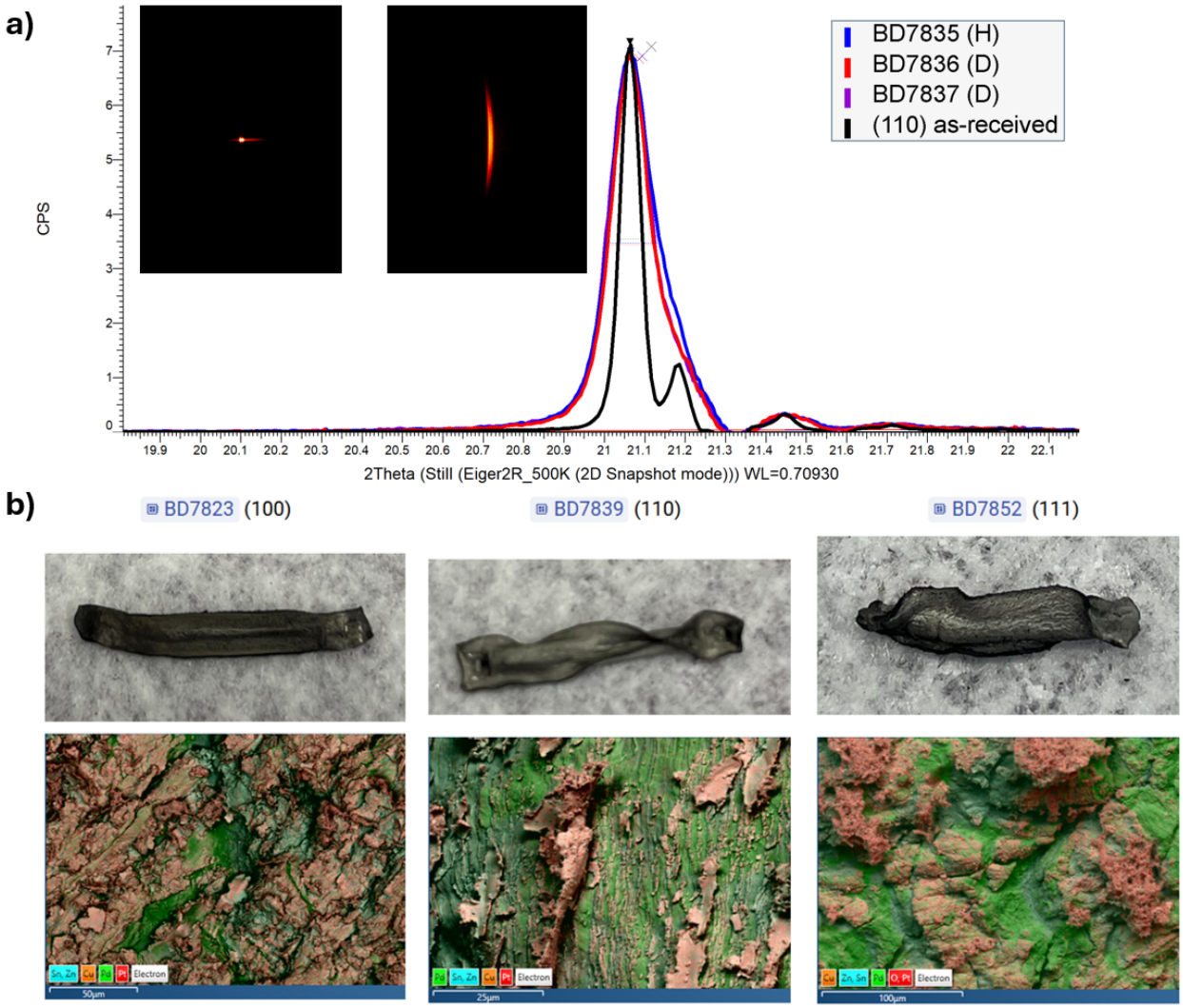



Fig. 8.10: a) Pre (left) and post (right) experimental XRD of the Pd (110) single crystal (BE3883). The diffractogram shows the peak broadening of the Pd single crystal after electrochemical loading (blue, red, and purple) compared to its original state (black). b) Shows the sample deformation that occurs after AC cycling (BE4182) for each crystal orientation (100), (110), and (111) respectively. Samples are 3 mm x 29 mm. Below each image is an EDS false color map scan showing the presence of coating-x and its typical elements (i.e., Zn, Cu, and Pt).

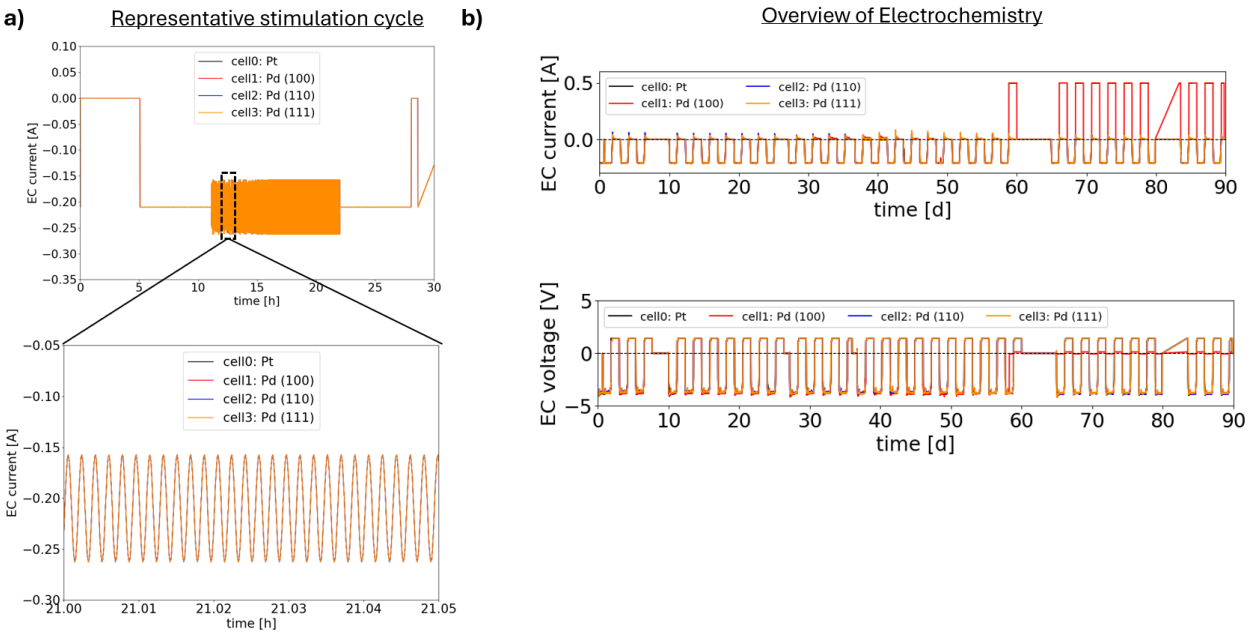



Fig. 8.11: a) Representative example of the AC EC stimulation applied to the Pd single crystal samples where current was alternated between -0.25 A to -0.15 A with an average current of -0.20 A. b) Overview of the current and voltage application (36 cycles) for the Pd single crystal samples (BE4182).

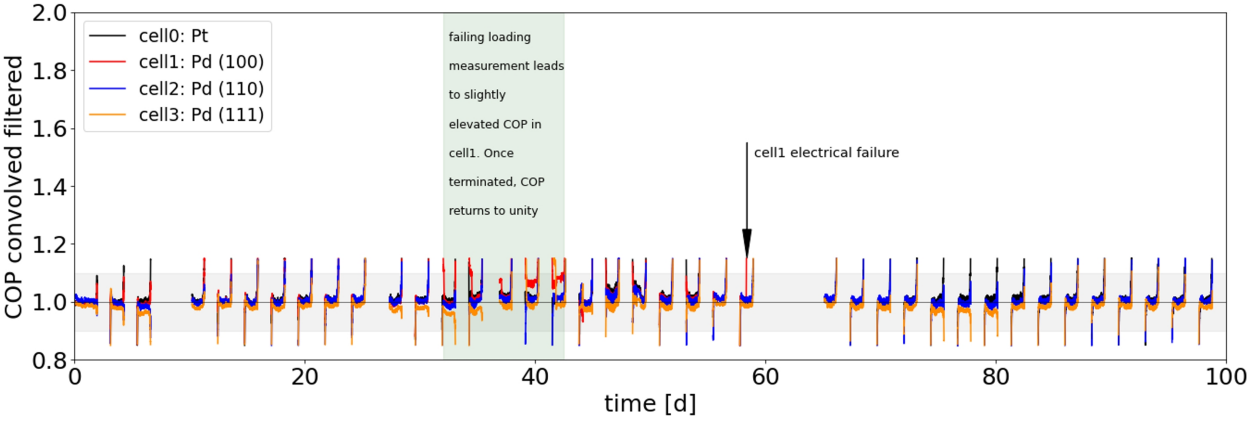



Fig. 8.12: Overview of the Pd (100), (110), and (111) single crystals AC EC stimulation (BE4182). Transients in signal are due changes in input power. The region highlighted in green is where a failed loading measurement led to a slightly elevated COP in cell 1.

## 8.4 Alloys

When palladium alloys with other metals, its material characteristics can change significantly. These changes can affect mechanical, electronic, and optical properties – often a combination of these. Fundamentally, these alterations arise from the way different alloying elements modify bonding within the crystal lattice. One key aspect is atomic size effects: elements with atomic radii different from palladium can introduce atomic strain into the alloy. This strain can impact both the mechanical strength and the electronic structure of the material, influencing properties such as ductility and hardness. For instance, alloying palladium with larger atoms may induce lattice distortions, increasing stress and possibly affecting hydrogen diffusion and absorption [295, 296]. In addition to size effects, the electronic structure of the alloying element plays a crucial role. When elements with different electron configurations are introduced into the palladium lattice, they can alter the electronic density and band structure. This can shift palladium's catalytic properties and hydrogen solubility, affecting how hydrogen isotopes enter and interact with the lattice [295, 296].

These electronic and structural changes can also impact the electrocatalytic properties of the alloy, especially in reactions like water splitting. The kinetics of the Volmer, Tafel, and Heyrovsky steps in hydrogen evolution reactions (HER) can differ between pure palladium and its alloys. For example, larger alloying elements could reduce the energy barrier for hydrogen recombination, leading to slower Tafel kinetics, while simultaneously allowing for higher hydrogen loadings. Conversely, other alloys may reduce deuterium loading. Ultimately, our interest in alloys was pragmatic. It wasn't that we were attached to palladium per se, but any material that could produce excess heat was of value. Given the materials explored in the literature and the reports of excess heat in palladium systems, we reasoned that alloying palladium could minimize the risks in our experimental exploration, especially considering the resources, instrumentation, and time constraints. With this in mind, we explored several alloy systems, including PdAg (palladium-silver), PdRh (palladium-rhodium), PdNi (palladium-nickel), and what we termed complex palladium alloys. The PdAg system, for example, is well known for its improved hydrogen absorption kinetics and mechanical properties compared to pure palladium. PdRh alloys, on the other hand, are valued for their enhanced stability and resistance to hydrogen embrittlement, which makes them suitable for long-term hydrogen cycling.

Our most ambitious effort was in the category of complex palladium alloys, where we synthesized two distinct alloys containing palladium and 12 different elements, each at around 1% by weight. These elements were chosen based on their natural occurrence in palladium ores, representing the most common impurities introduced from the mining-to-manufacturing process. This approach aligns with recent interest in high-entropy alloys (HEAs) - materials composed of multiple principal elements that potentially exhibit novel and often superior properties, such as improved mechanical strength, corrosion resistance, and enhanced hydrogen storage [297]. Although we cannot conclusively verify the uniqueness of our complex palladium alloys, based on a thorough review of the literature, they appear to be relatively unexplored. We subjected these alloys to different types of electrochemical stimulation (typically -50 mA of DC current with alternating loading/deloading cycles), but ultimately did not observe any excess heat. Here is an overview of the experiments: PdRh (Figure 8.13), PdAg (Figure 8.14), and PdNi (Figure 8.15) wires were all subjected to electrochemical conditions described previously in the HTCal system. No excess heat was observed in any of these sample compositons. Ni cathodes were also subjected to typical electrochemical conditions in the HTCal system. Additionally, we explored depositing thin films of palladium onto Ni cathodes in order to try and increase deuterium loading into the nickel lattice. We did not observe any resistance changes other than what was expected from temperature changes. This contradicts claims in the literature that pure nickel cathodes uptake hydrogen isotopes under ambient electrochemical conditions [298]. In these tests, no excess heat was observed. An example of overview data is shown in Figure 8.16.

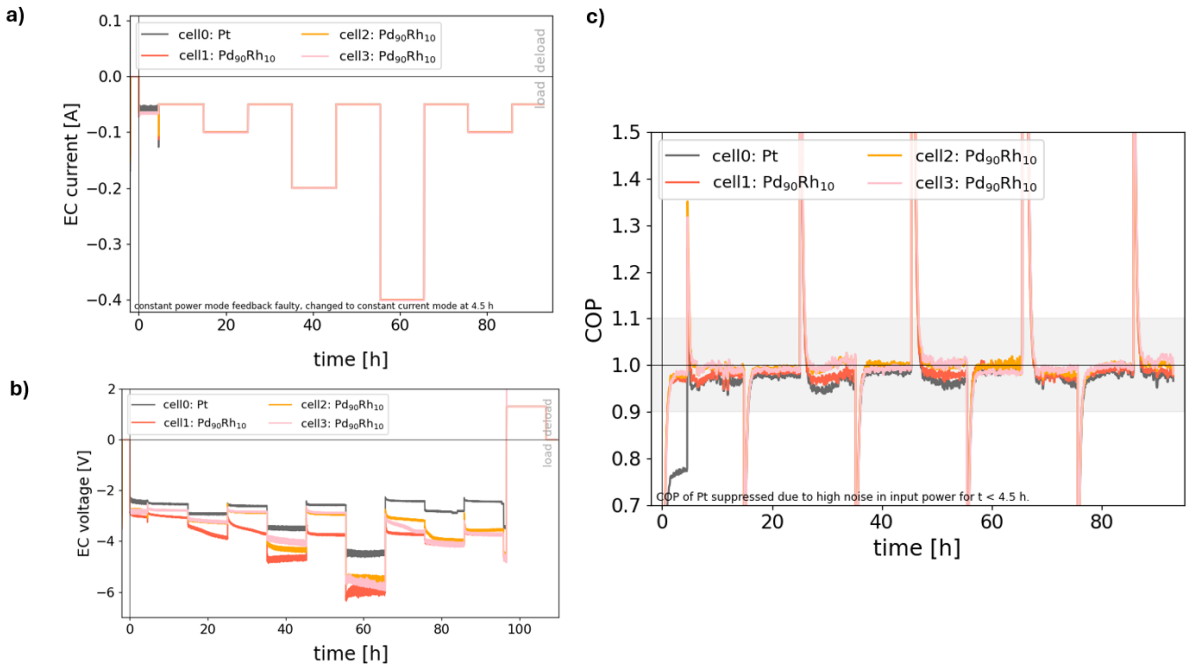



Fig. 8.13: Summary figure of the $Pd_{90}Rh_{10}$ alloy sample with a) current, b) voltage, and c) COP data. Transients are due to changes in input power.

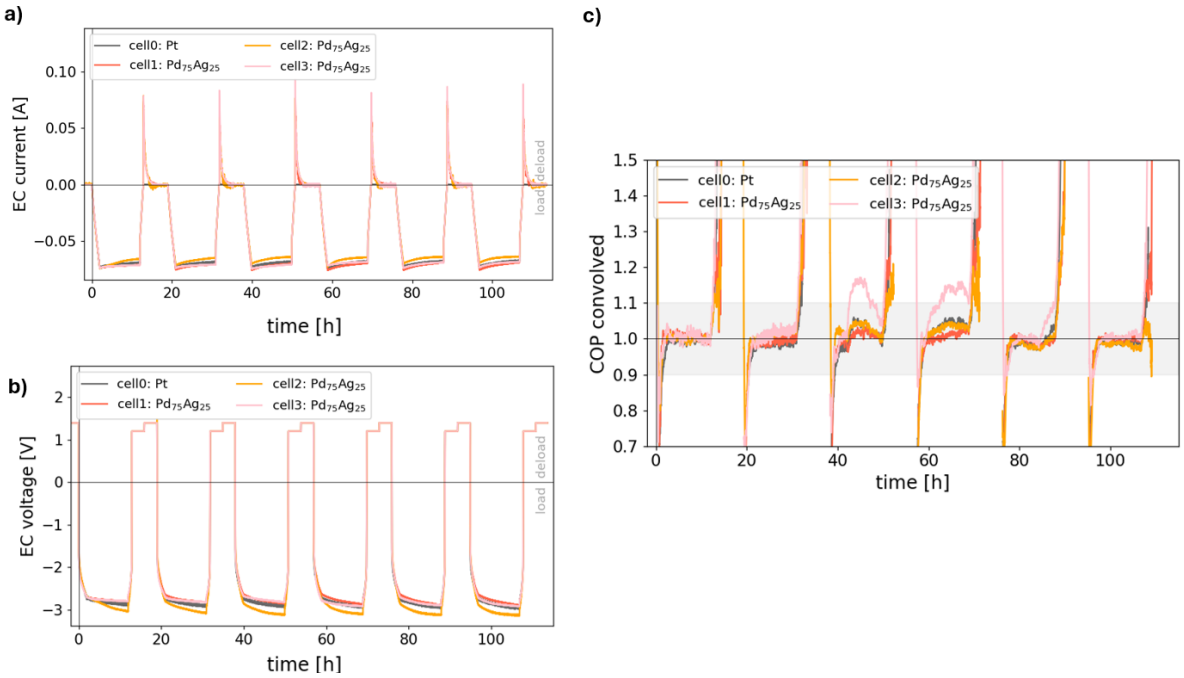



Fig. 8.14: Summary of the $Pd_{75}Ag_{25}$ alloy sample with a) current, b) voltage, and c) COP data. Transients are due to changes in input power.

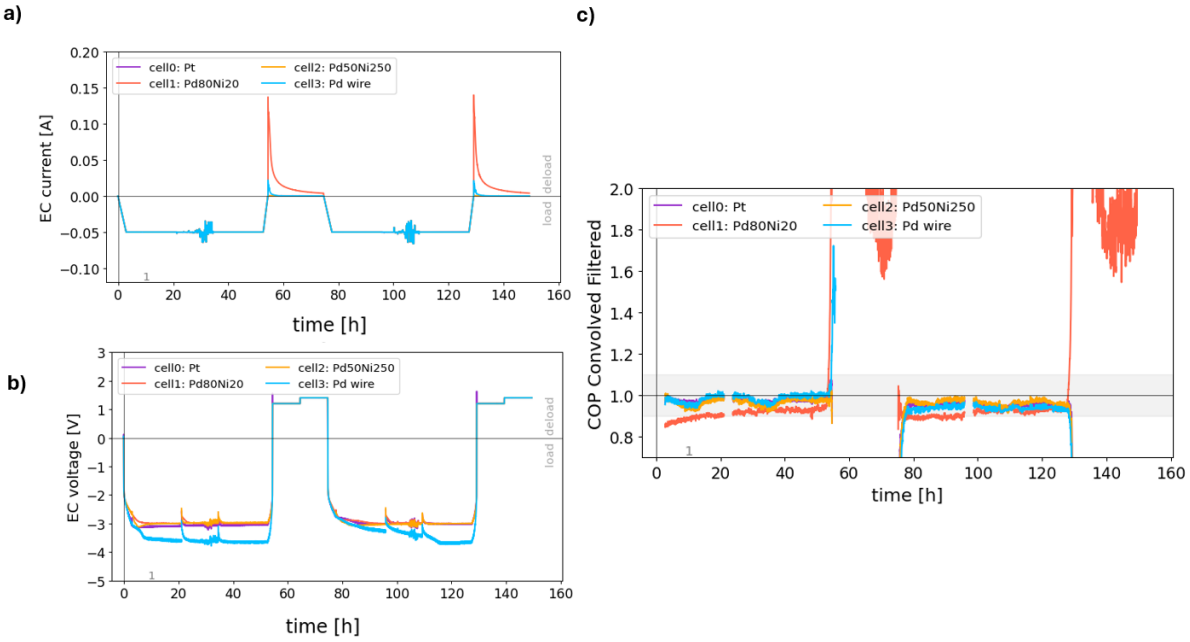



Fig. 8.15: Summary of the $Pd_{80}Ni_{20}$ alloy sample with a) current, b) voltage, and c) COP data. Transients are due to changes in input power, and noise in the COP of $Pd_{80}Ni_{20}$ (red) sample during deload is an artificial reading due to recombination during deloading.

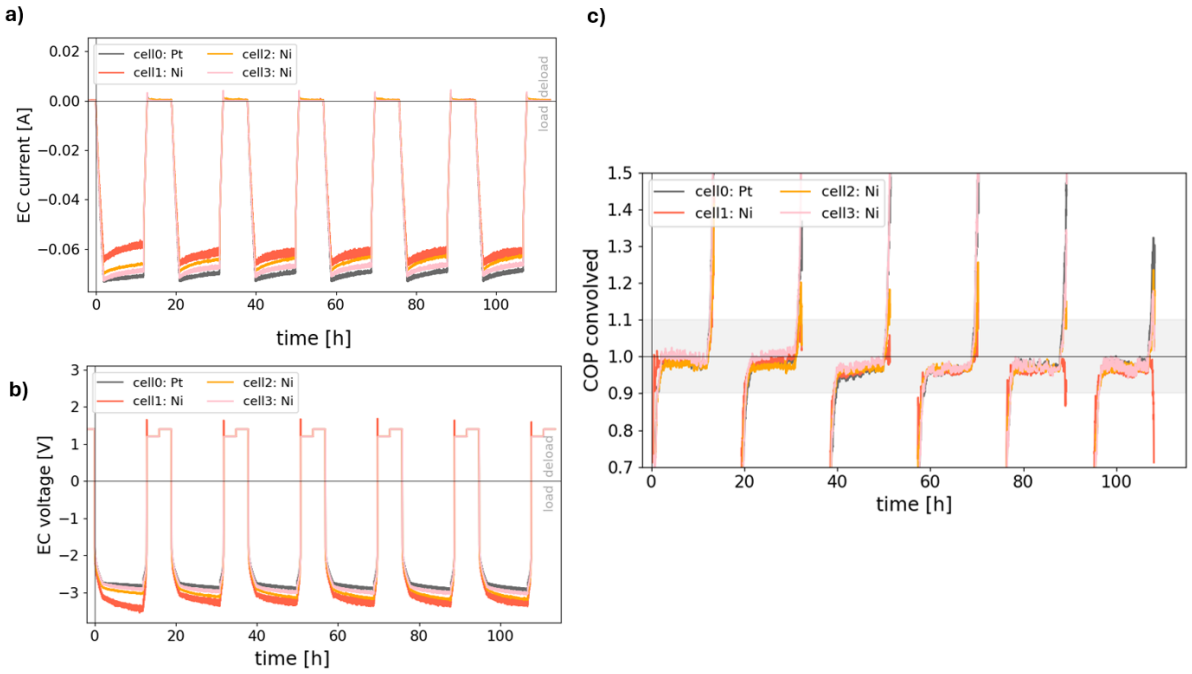



Fig. 8.16: Summary of the Ni cathode sample with a) current, b) voltage, and c) COP data. Transients are due to changes in input power.

We wanted to explore a wider range of impurities found in Pd alloys in an efficient amount of time. In order to address this, we worked with Goodfellow to manufacture custom, complex Pd alloys with 12 different alloyed elements, as previously described. Complex 1's composition is (Pd (88%), Si (1%), S (1%), Fe (1%), Zn (1%), Ge (1%), Se (1%), Ag (1%), In (1%), Sb (1%), Te (1%), Pb (1%), Bi (1%)) and Complex 2's composition is (Pd (88%), Fe (1%), Ni (1%), Cu (1%), Zn (1%), Ge (1%), Se (1%), In (1%), Sn (1%), Sb (1%), Te (1%), Pb (1%), Bi (1%)). Upon receiving the complex alloys, we performed x-ray diffraction to ensure that the cathode was still a single-phase material. Despite the incredible compositional complexity of these materials, at 1 wt% of each element present, we were able to confirm them as single phase materials – to the detection limits of our x-ray diffraction technique, which is around 0.1 % by volume. We subjected these materials to long duration electrochemical stimulation (>65 days of DC current held at 200 mA after three pre-cycles), however, we only observed false heat signals. These false signals arose from transient recombination, failed electrical contacts, and network errors that resulted in the loss of data for brief periods of time. Given the several month long duration of these tests which pushed the limit of the HTCal without any servicing or repair, these failure modes were not entirely unexpected. Examples of the data from these tests are shown in Figure 8.17.

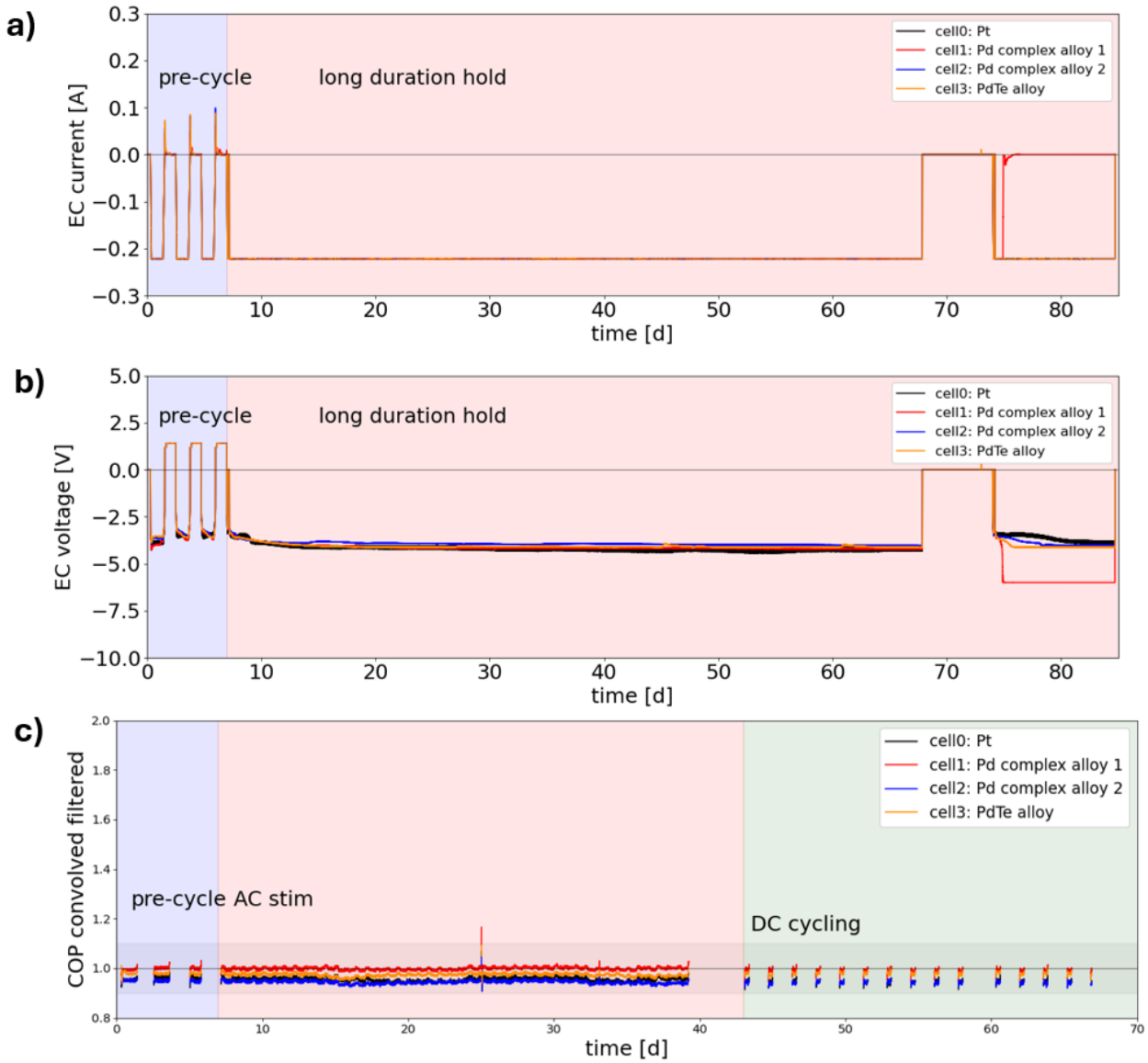



Fig. 8.17: Summary of the two experiments carried out with complex alloy samples a) current and b) voltage for the long duration EC hold (BE4309), and c) COP data of the AC stimulation and DC cycling experiment (BE4308). Pre-cycle highlighted in blue, AC stim cycle is in red, and the DC cycle is in green. Transients are due to changes in input power.

# Chapter 9

# Conclusions

## 9.1 Our Test Campaigns in Numbers

As laid out in chapter 2, we attempted to follow any seemingly credible report that could lead us to AHE. We replicated all major published electrochemical LENR experiments, even those with weak evidence of AHE. On top of that, we designed our own experiments in order to create conditions that had been reported to be conducive to AHE. When performing replications, we either re-created the original experiments as close as possible, including the calorimeter, or we abstracted it and performed the experiment in our own, well characterized calorimeters. After all, a scientific phenomenon should be agnostic to the diagnostic tools used to observe it.

Exact replications include those of Staker [105] and Barham [106]. Replications with the sample geometry, composition and stimulation closely resembling the original paper, but placed in our closed-system calorimeters (as opposed to lower performing open system calorimeters) include Letts [104, 271, 272], Staker [105], Storms [113, 299, 300], Energetics [102, 270], McKubre [101, 110], Miles [301], Hubler [302], Boss [32, 72, 106]. Additional experiments were more loosely based on literature reports (e. g., Fleischmann and Pons [26]) or were novel experiments motivated by our quest to find the right conditions for AHE (e. g., by enhanced loading or minimizing or maximizing lattice defects). Overall, we investigated over 500 samples and performed a total of over 200,000 h (23 sample years) of calorimetry. Almost 90 % of the samples and over 95 % of the calorimeter hours were accumulated in closed system calorimeters, which are significantly more precise and less error prone than the open system calorimeters widely used in the LENR literature. Fig. 9.1 shows an overview of the number of samples and the accumulated duration of AHE tests (calorimetry on potentially AHE-active samples, not including calibrations and reference experiments, nor the numerous samples and time spent optimizing hydrogen loading outside of calorimeters).

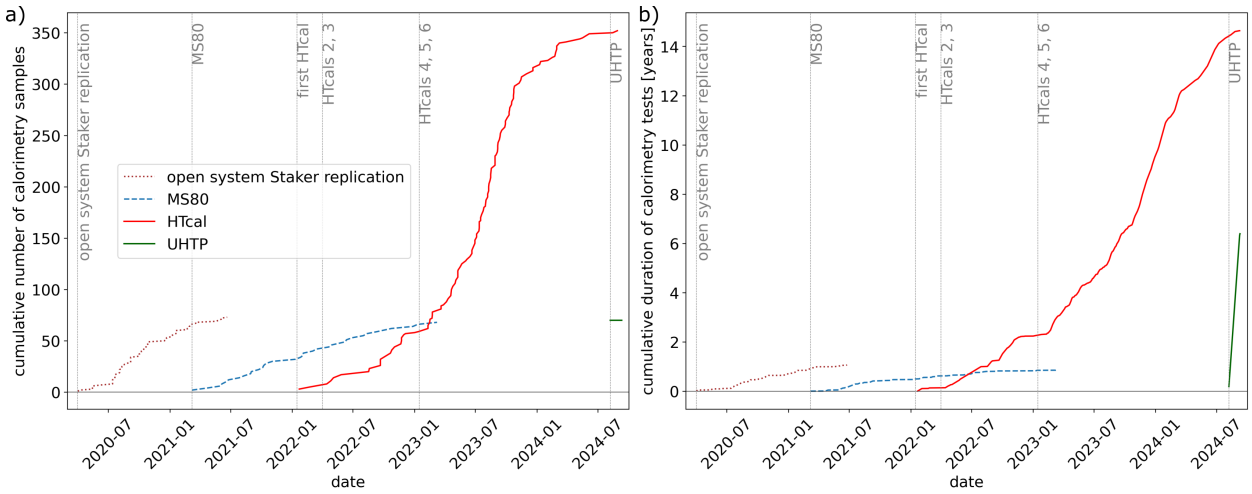



Fig. 9.1: History of calorimetry experiments in search for AHE within the Callisto project, grouped by calorimeter type. a) Accumulated number of samples; b) Accumulated number of calorimeter years.

## 9.2 List of False COPs

Unsurprisingly, while performing these several hundred experiments, we have observed numerous incidents in which the apparent COP deviated from unity to various degrees. However, we have been able to track down each and every single case so far to a classical explanation, i. e., an explanation not requiring the presence of LENR. The most frequent elevated COP we have observed in closed system calorimetry was due to recombiner malfunction, resulting in a temporary accumulation of oxyhydrogen in the headspace, which then would recombine spontaneously after a certain pressure buildup, resulting in a prolonged small heat suppression followed by a short and comparatively larger heat release. This error is easy to identify using the pressure data. In open system calorimetry, the most common error was a change in thermal properties due to changes in electrolyte level, rendering the calibration invalid. This error could be diagnosed using continuous video surveillance of the cells. Across all calorimeters, we have seen frequent hardware failures, especially temperature sensors (RTDs), owing to the corrosive electrolyte. In most cases, the failure is obvious, but in some cases, the sensor would continue to produce data that was deceptively close to the real data, or it would even recover. We mostly overcame this problem by potting sensors in epoxy resin and introducing redundant sensors.

A complete list of all observed false COPs is provided below:

1. Incorrect accounting in COP calculation due to input power measurement error: Assembly errors (e. g., incorrectly wired pins in the electrical passthrough); corrosion of wire insulation in long duration tests; incorrectly specified power from source measure units or input power devices can lead to accounting errors in the COP calculations. High-frequency inputs (AC or pulsed) are particularly error-prone. Another source of error is the measurement of input voltage not at the thermal system boundary. This is especially a concern for wires carrying large currents (e. g., electromigration). This category can cause any level of COP error, in both thermodynamically open and closed calorimeters.

2. Changes to the thermal transfer coefficient of the calorimeter (output heat measurement error):
    - Changes to liquid level and electrolyte foaming: In certain thermodynamically open calorimeters, liquid level variations and electrolyte foaming both cause changes to the thermal transport properties of the calorimeter. We have observed consequent false COPs as high as 1.6 in our Staker replication experiments.
    - Environmental temperature instability: Good calorimetry requires temperature stability of the surrounding enclosure(s) on the order 100 mK for valid, high-precision measurements. When the surrounding environment temperature changes, the heat transfer of the calorimeter will be impacted.
    - Calibration drift: Heat flow measurements often rely on accurately and precisely measuring temperature, or some other proxy for heat flow. Whether using thermocouples, RTDs, or Seebeck sensors, all are susceptible to component failure, placement errors, and offsets which can drift over time.
    - Insufficient understanding of reactor design: We characterized temperature heterogeneity in some replicated isoperibolic calorimeters. Certain designs can lead to false COPs on the order of 1.3.
3. Unlocking stored energy via chemical reactions: We have observed at least two types of chemical reactions in the headspace to date: Oxyhydrogen recombination and hydrocarbon combustion. These reactions produce large near-instantaneous heat releases, which can present as a temporarily elevated COP. There is the possibility that slower timescale corrosion reactions are releasing heat in certain experiments.
4. One-off experimental errors: Equipment malfunctions, calculation errors, incorrect analysis code, etc. can lead to false COPs. This is especially true if sensors are non-redundant and experiments involve manual steps (such as manually changing EC current or manually reading voltmeters).

## 9.3 Call for Quality Research

Since its inception in 1989, the field of LENR research has been on the fringes of science, often mocked as pseudo science. Several DOE reviews have concluded that there is no evidence of LENR that withstands the rigor of scientific standards, though the most recent DOE review has resulted in a modest funding of 10 M$ for LENR research through ARPA-E [303]. Many times, researchers have complained about their field being stigmatized, e. g., as "voodoo science" or "pathological science".

The truth is that the quality of almost all papers in the field is very low compared to most other fields of science. Even if the LENR effect is accepted to be erratic, rendering replications almost impossible, the vast majority of papers does not fulfill the standards of publication in the common scientific journals. Let alone high impact journals – which would be justified given the consequences if a positive LENR result held to common scientific standards was reported. Hence, almost all LENR papers are found in dedicated marginalized journals and conferences, e. g., *Journal of Condensed Matter Nuclear Science*, *Current Science*, *New Energy Times*, or *International Conference on Cold Fusion*, all of which have minimal requirements for publication.

After carefully studying the LENR literature, we found that the most common shortcomings are (with examples):

- No rigorous peer review and no team work. There is a large body of work published in papers with a single author. However, most modern science, in particular experimental work, is done in teams. Close collaboration between researchers could make sure that fewer mistakes are overlooked and that data is being treated without preconceived notions. Rigorous review processes could ensure minimum scientific standards for published papers.
- Most papers lack control experiments or a thorough characterization of their calorimeters. Even when accepting that the effect is spurious and hard to replicate, control experiments (with light water or a platinum cathode that does not form a hydride) could illuminate the accuracy of the calorimeter and expose potential sources of error.
  - McKubre claims that the calorimeter had an accuracy of 0.4 %. Yet, the noise alone is on that level, let alone systematic offsets [110].
- Often, calorimetry is performed in a poor manner.
  - The heat flow is not stable before starting the experiment or the baseline is not shown [271, 302].
  - Conditions are changed rapidly, much faster than the thermal time constant of the calorimeter [104].
- Many researchers claim that certain additives, stimulations or other experimental features are critical to the production of AHE. However, no control experiments with the feature absent are shown.
  - The SRI replication of the Energetics *superwave* experiments found that even with constant EC current (no *superwaves*), the COP was 5 [270].
  - Letts' early paper was using a single laser, reporting that visible light can trigger AHE [271]. His later papers use two lasers, reporting that beat waves in the THz regime can trigger AHE [104,272].
  - Oftentimes, sample preparation procedures are rather intricate, with up to 17 steps. No data is presented showing that this sample preparation is critical to generating excess heat [104].
  - Hagelstein stated that "it was important to not see an exothermic response when the beat frequency was below 8 THz" [104], based on his hypothesis of optical phonon resonances triggering AHE. However, Fleischmann and Pons reported AHE without stimulation by optical phonons.
- Many times, data is presented in a poor format. Plots are missing axis labels or units, or are not intelligible [93, 102, 270, 271, 304].
- Most studies use their own home-built calorimeters. While this might be due to budget restrictions and is not necessarily a problem, it requires careful characterization of the instrument and published documentation thereof to provide a confidence interval for the excess heat. As shown in chapter 2, it is possible to build a simple, yet reliable and accurate calorimeter in-house. However, many designs reported in the literature have shortcomings (e. g., single sensor potentially exposed to corrosive electrolyte, open system calorimeter, recombiner placed outside of the calorimeter [270], disagreement between calorimeters [103]).
- Conclusions are highly speculative or not supported by data. In some cases, they are in conflict with the data presented.

  - An independent analysis of the excess heat data tabulated in Letts' report [104] shows no systematic relationship between excess heat and beat frequency (Fig. 7.37), contrary to the paper's conclucions.
  - In Hubler's recent ICCF contribution [302], inconsistent data was reported, where in a flow calorimeter, the output temperature was reported to be larger than the input temperature, even though the cell temperature did not exceed the jacket temperature, suggesting the heat source was not the cell.
  - In Staker's report of COP = 2 [93], the temperatures vary greatly and inconsistently when the EC currents are adjusted slightly (e. g. from 444 mA to 435 mA).

- Researchers report replicability of the effect, but fail to back this up with data [304].
- Experiments are insufficiently described to allow to be replicated. Essential details are left out, structures of papers are chaotic [106], important details are made available only in personal communication [113].
- Independent replications have typically failed at replicating excess heat [273]. However, this might also be caused by the inability to perfectly replicate experiments if they are insufficiently documented. Replications with the original party involved have been reported to be successful though [270].

If the field of LENR research aims to be taken seriously by other disciplines, it needs to play along and fulfill the criteria set up by the mainstream scientific community.

## 9.4 Outlook

The field of LENR has been guided by experimental findings, with no commonly accepted theoretical foundation predicting the effect. Given the lack of guidance by theory, our focus has been on replicating experiments with reported excess heat. We have observed apparent excess heat many times, with similar magnitudes as reported by others. However, every single time we have been able to trace it back to a classical explanation. Over the course of performing hundreds of experiments, we have unearthed a plethora of artifacts that can cause false excess heat signals. With significantly more sophisticated hardware and data processing than in most historic excess heat reports, we have been able to greatly reduce the frequency of the occurrence of false signals in our calorimetry campaigns, but we were not able to completely eliminate these false signals (section 9.2). We deduce that previous researchers, often equipped with fewer diagnostics and less redundancy, must have encountered similar false signals. Combining this with the lack of scientific rigor in the field (section 9.3), we conclude that there is no unambiguous observation of excess heat caused by LENR that holds up to common scientific standards. We therefore recommend terminating LENR research.

# Glossary

| | |
|---|---|
| COP | coefficient of performance, ratio of *power out* to *power in* in a calorimetry experiment (eq. 2.8) |
| $COP_e$ | COP energy, integral of *power out* to *power in* in a calorimetry experiment, i.e., *energy out* over *energy in*, see eq. 2.9 |
| D | deuterium |
| EC | electrochemistry, electrochemical |
| EDS | **E**nergy-**D**ispersive X-ray **S**pectroscopy |
| EM | electromigration, also called referred to as *axial current* |
| FIB | focused ion beam |
| H | *H* generally refers to both isotopes, protium and deuterium. However, in some cases, depending on the context, it can refer to protium only (as opposed to deuterium). |
| HTcal | high-throughput calorimeter (section 2.9.1) |
| hydrogen | *Hydrogen* is used to encompass both isotopes, protium and deuterium. |
| PCB | **P**rinted **C**ircuit **B**oard |
| QCM | **Q**uartz **C**rystal **M**icrobalance |
| $R/R_0$ | resistance ratio, i. e. resistance of a sample normalized with its initial (deloaded) resistance |
| RTD | **R**esistance **T**emperature **D**etector, a resistance-based temperature sensor |
| UHTP | ultra-high throughput calorimeter (section 2.10) |
| UPD | **U**nder**p**otential **D**eposition |
| XRD | X-ray diffraction (section 3.12) |

# Bibliography


[1] NOAA News, "Carbon dioxide now more than 50 % higher than pre-industrial levels." https://www.noaa.gov/news-release/carbon-dioxide-now-more-than-50-higher-than-pre-industrial-levels, 2023. Accessed: 2024-10-02.

[2] NOAA News, "Trends in Atmospheric Carbon Dioxide." https://www.esrl.noaa.gov/gmd/ccgg/trends/, 2023. Accessed: 2024-10-02.

[3] NOAA News, "Overview of Greenhouse Gases: Methane Emissions." https://www.epa.gov/ghgemissions/overview-greenhouse-gases, 2023. Accessed: 2024-10-02.

[4] NOAA News, "Overview of Greenhouse Gases: Nitrous Oxide Emissions." https://www.epa.gov/ghgemissions/overview-greenhouse-gases, 2023. Accessed: 2024-10-02.

[5] NOAA News, "Overview of Greenhouse Gases: Fluorinated Gases." https://www.epa.gov/ghgemissions/overview-greenhouse-gases, 2023. Accessed: 2024-10-02.

[6] World Economic Forum, "Climate change is costing the world $16 million per hour." https://www.weforum.org/agenda/2023/01/climate-change-costing-world-16-million-per-hour/, 2023. Accessed: 2024-10-02.

[7] UN News, "Human, economic, environmental toll of climate change on the rise." https://news.un.org/en/story/2023/01/1132432, 2023. Accessed: 2024-10-02.

[8] World Economic Forum, "This is what climate change costs economies around the world." https://www.weforum.org/agenda/2023/01/what-climate-change-costs-economies/, 2023. Accessed: 2024-10-02.

[9] UN News, "Extreme weather caused two million deaths, cost $4 trillion over last 50 years." https://news.un.org/en/story/2023/01/1132412, 2023. Accessed: 2024-10-02.

[10] P. Friedlingstein, M. O'sullivan, M. W. Jones, R. M. Andrew, D. C. Bakker, J. Hauck, P. Landschützer, C. Le Quéré, I. T. Luijkx, G. P. Peters, *et al.*, "Global carbon budget 2023," *Earth System Science Data*, vol. 15, no. 12, pp. 5301–5369, 2023.

[11] S. Arrhenius, "On the influence of carbonic acid in the air upon the temperature of the ground," *Philosophical Magazine and Journal of Science*, vol. 41, no. 251, pp. 237–276, 1896.

[12] IPCC, "The Intergovernmental Panel on Climate Change: History." https://www.ipcc.ch/about/history/, 2021. Accessed: 2024-10-02.

[13] UNFCCC, "United Nations Framework Convention on Climate Change." https://unfccc.int/resource/docs/convkp/conveng.pdf, 1992. Accessed: 2024-10-02.

[14] UNFCCC, "Kyoto Protocol." https://unfccc.int/resource/docs/convkp/kpeng.pdf, 1997. Accessed: 2024-10-02.

[15] UNFCCC, "The Paris Agreement." https://unfccc.int/process-and-meetings/the-paris-agreement/the-paris-agreement, 2015. Accessed: 2024-10-02.

[16] UNFCCC, "Conference of the Parties (COP)." https://unfccc.int/process/bodies/supreme-bodies/conference-of-the-parties-cop, 2022. Accessed: 2024-10-02.

[17] "Green Climate Fund." https://www.greenclimate.fund, 2023. Accessed: 2024-10-02.

[18] "Renewable Capacity Statistics 2023 (IRENA)." https://www.irena.org/Publications/2023/Mar/Renewable-Capacity-Statistics-2023, 2023. Accessed: 2024-10-02.

[19] "REDD+ Programme (UN-REDD)." https://www.un-redd.org, 2023. Accessed: 2024-10-02.

[20] "Global Energy Review: CO2 Emissions in 2023 (IEA)." https://www.iea.org/reports/co2-emissions-in-2023, 2023. Accessed: 2024-10-02.

[21] "International Energy Outlook 2023 (U.S. Energy Information Administration)." https://www.eia.gov/outlooks/ieo/pdf/IEO2023_Narrative.pdf, 2023. Accessed: 2024-10-02.

[22] "Steel's Contribution to a Low Carbon Future (World Steel Association)." https://worldsteel.org/wp-content/uploads/2023/Steel-Climate-Change.pdf, 2023. Accessed: 2024-10-02.

[23] "Greenhouse Gas Emissions from Agriculture. Food and Agriculture Organization of the United Nations (FAO)." https://www.fao.org/3/cb9757en/cb9757en.pdf, 2023. Accessed: 2024-10-02.

[24] "Special Report on Climate Change and Land. Intergovernmental Panel on Climate Change (IPCC)." https://www.ipcc.ch/srccl/, 2019. Accessed: 2024-10-02.

[25] "Inventory of U.S. Greenhouse Gas Emissions and Sinks. U.S. Environmental Protection Agency (EPA)." https://www.epa.gov/ghgemissions/inventory-us-greenhouse-gas-emissions-and-sinks, 2023. Accessed: 2024-10-02.

[26] M. Fleischmann, S. Pons, and M. Hawkins, "Electrochemically induced nuclear fusion of deuterium," *J. Electroanal. Chem.*, vol. 261, p. 301, 1989.

[27] J. Huizenga and N. Ramsey, "Cold fusion research: A report of the energy research advisory board to the united states department of energy; nov, 1989," tech. rep., DOE/S-0073.

[28] D. Morrison, "Review of cold fusion," *Soviet Physics Uspekhi*, vol. 34, no. 12, p. 1055, 1991.

[29] C. G. Beaudette, *Excess heat: Why cold fusion research prevailed*. Oak Grove Press, 2002.

[30] T. Mizuno *et al.*, *Nuclear transmutation: the reality of cold fusion*. Infinite Energy Press Concord, 1998.

[31] I. Dardik, T. Zilov, H. Branover, A. El-Boher, E. Greenspan, B. Khachaturov, V. Krakov, S. Lesin, and M. Tsirlin, "Excess heat in electrolysis experiments at energetics technologies," in *Condensed Matter Nuclear Science*, pp. 84–101, World Scientific, 2006.

[32] P. A. Mosier-Boss, S. Szpak, F. E. Gordon, and L. P. Forsley, "Triple tracks in cr-39 as the result of pd–d co-deposition: evidence of energetic neutrons," *Naturwissenschaften*, vol. 96, pp. 135–142, 2009.

[33] F. Celani, E. Marano, A. Spallone, A. Nuvoli, B. Ortenzi, S. Pella, E. Righi, G. Trenta, F. Micciulla, S. Bellucci, *et al.*, "Experimental results on sub-micro structured cu–ni alloys under high temperatures hydrogen/deuterium interactions," in *X International Workshop on Anomalies in Hydrogen-Metal Systems*, pp. 2225–0956, 2013.

[34] P. L. Hagelstein, "Recent progress on phonon-nuclear theoretical models," *Journal of Condensed Matter Nuclear Science*, vol. 36, no. 1, pp. 210–246, 2022.

[35] "Industrial Heat Acquires E-Cat Technology, Opening Commercial LENR Frontier." https://www.OilPrice.com, 2014. Accessed: 2024-10-02.

[36] U.S. Department of Energy, "Report of the review of low energy nuclear reactions," tech. rep., 2004.

[37] C. P. Berlinguette, Y.-M. Chiang, J. N. Munday, T. Schenkel, D. K. Fork, R. Koningstein, and M. D. Trevithick, "Revisiting the cold case of cold fusion," *Nature*, vol. 570, no. 7759, pp. 45–51, 2019.

[38] R. S. Sherbo, M. Moreno-Gonzalez, N. J. Johnson, D. J. Dvorak, D. K. Fork, and C. P. Berlinguette, "Accurate coulometric quantification of hydrogen absorption in palladium nanoparticles and thin films," *Chemistry of Materials*, vol. 30, no. 12, pp. 3963–3970, 2018.

[39] B. MacLeod, P. Schauer, K. Hu, B. Lam, D. Fork, and C. Berlinguette, "High-temperature high-pressure calorimeter for studying gram-scale heterogeneous chemical reactions," *Review of Scientific Instruments*, vol. 88, no. 8, 2017.

[40] N. J. Johnson, B. Lam, B. P. MacLeod, R. S. Sherbo, M. Moreno-Gonzalez, D. K. Fork, and C. P. Berlinguette, "Facets and vertices regulate hydrogen uptake and release in palladium nanocrystals," *Nature materials*, vol. 18, no. 5, pp. 454–458, 2019.

[41] M. Moreno-Gonzalez, A. Huang, P. A. Schauer, K. Hu, B. Lam, J. W. Grayson, A. Bottomley, D. J. Dvorak, D. K. Fork, and C. P. Berlinguette, "Sulfuric acid electrolyte impacts palladium chemistry at reductive potentials," *Chemistry of Materials*, vol. 32, no. 21, pp. 9098–9106, 2020.

[42] R. Weed, D. Sblendorio, J. Machacek, B. Ramamurthy, and G. Laguisma, "Positron-electron annihilation momentum transfer to trapped deuterons," *AIP Advances*, vol. 9, no. 11, 2019.

[43] J. D. Benck, D. Rettenwander, A. Jackson, D. Young, and Y.-M. Chiang, "Apparatus for operando x-ray diffraction of fuel electrodes in high temperature solid oxide electrochemical cells," *Review of Scientific Instruments*, vol. 90, no. 2, 2019.

[44] K. J. Palm, J. B. Murray, T. C. Narayan, and J. N. Munday, "Dynamic optical properties of metal hydrides," *Acs Photonics*, vol. 5, no. 11, pp. 4677–4686, 2018.

[45] J. B. Murray, K. J. Palm, T. C. Narayan, D. K. Fork, S. Sadat, and J. N. Munday, "Apparatus for combined nanoscale gravimetric, stress, and thermal measurements," *Review of Scientific Instruments*, vol. 89, no. 8, 2018.

[46] J. D. Benck, A. Jackson, D. Young, D. Rettenwander, and Y.-M. Chiang, "Producing high concentrations of hydrogen in palladium via electrochemical insertion from aqueous and solid electrolytes," *Chemistry of Materials*, vol. 31, no. 11, pp. 4234–4245, 2019.

[47] P.-W. Guan, R. J. Hemley, and V. Viswanathan, "Combining pressure and electrochemistry to synthesize superhydrides," *Proceedings of the National Academy of Sciences*, vol. 118, no. 46, p. e2110470118, 2021.

[48] B. MacLeod, D. Fork, B. Lam, and C. Berlinguette, "System identification calorimetry," *arXiv preprint arXiv:1808.04518*, 2018.

[49] Defense Intelligence Agency, "Technological forecast: Worldwide research on low-energy nuclear reactions increasing and gaining acceptance," tech. rep., 2016.

[50] , "National defense authorization act (ndaa) for fiscal year 2020," tech. rep., 2019.

[51] Zawodny, J. M., "Low energy nuclear reaction (lenr) power for manned deep space missions. nasa technical reports server.," tech. rep., 2012.

[52] European Commission, "Horizon 2020 CEHMS Project."

[53] ARPA-E, "U.S. Department of Energy Announces $10 Million in Funding to Projects Studying Low-Energy Nuclear Reactions," 2023.

[54] H. A. Bethe, "Energy production in stars," *Physical Review*, vol. 55, no. 5, p. 434, 1939.

[55] J. P. Freidberg, *Plasma physics and fusion energy*. Cambridge university press, 2008.

[56] J. Wesson and D. J. Campbell, *Tokamaks*, vol. 149. Oxford university press, 2011.

[57] M. McKubre, S. Crouch-Baker, A. Riley, S. Smedley, and F. Tanzella, "Excess power observations in electrochemical studies of the d/pd system; the influence of loading," in *Third International Conference on Cold Fusion," Frontiers of Cold Fusion*, p. 5, 1992.

[58] E. Storms, *Science of Low Energy Nuclear Reaction, the: A Comprehensive Compilation of Evidence and Explanations about Cold Fusion*. World Scientific, 2007.

[59] T. Mizuno *et al.*, *Nuclear transmutation: the reality of cold fusion*, vol. 2. Infinite Energy Press Concord, 1998.

[60] Y. Arata and Y.-C. Zhang, "Anomalous difference between reaction energies generated within d2o-cell and h2o-cell," *Japanese journal of applied physics*, vol. 37, no. 11A, p. L1274, 1998.

[61] P. Mosier-Boss, S. Szpak, F. Gordon, and L. Forsley, "Use of cr-39 in pd/d co-deposition experiments," *The European Physical Journal-Applied Physics*, vol. 40, no. 3, pp. 293–303, 2007.

[62] S. Szpak, P. A. Mosier-Boss, and F. E. Gordon, "Further evidence of nuclear reactions in the pd/d lattice: emission of charged particles," *Naturwissenschaften*, vol. 94, pp. 511–514, 2007.

[63] H. P. S. M. Godes, R., "LENR Theory and Experiment: Status and Patents," *Journal of Condensed Matter Nuclear Science*, vol. 11, pp. 1–16, 2013.

[64] C. Gotzmer, L. F. DeChiaro, K. Conley, M. Litz, M. Millett, J. Ewing, L. P. Forsley, K. J. Long, W. A. Wichart, P. A. Mosier-Boss, *et al.*, "Li–pd–rh-d2o electrochemistry experiments at elevated voltage," *APL Energy*, vol. 1, no. 3, 2023.

[65] D. Letts and D. Cravens, "Laser stimulation of deuterated palladium: past and present," *Condensed Matter Nuclear Science*, pp. 159–170, 2006.

[66] P. L. Hagelstein, D. Letts, and D. Cravens, "Terahertz difference frequency response of pdd in two-laser experiments," *Condensed Matter Nuclear Science*, vol. 3, pp. 59–76, 2010.

[67] M. Miles and B. Bush, "Heat and helium measurements in deuterated palladium," *Journal of Condensed Matter Nuclear Science*, vol. 19, pp. 195–204, 1994.

[68] M. Fleischmann, S. Pons, and M. Hawkins, "Electrochemically induced nuclear fusion of deuterium," 1989.

[69] M. Fleischmann, S. Pons, M. W. Anderson, L. J. Li, and M. Hawkins, "Calorimetry of the palladium-deuterium-heavy water system," *Journal of Electroanalytical Chemistry and Interfacial Electrochemistry*, vol. 287, no. 2, pp. 293–348, 1990.

[70] M. Fleischmann and S. Pons, "Calorimetry of the pd-d2o system: from simplicity via complications to simplicity," *Physics Letters A*, vol. 176, no. 1-2, pp. 118–129, 1993.

[71] M. McKubre, S. Crouch-Baker, A. Riley, S. Smedley, and F. Tanzella, "Excess power observations in electrochemical studies of the d/pd system; the influence of loading," in *Third International Conference on Cold Fusion," Frontiers of Cold Fusion*, p. 5, 1992.

[72] P. Mosier-Boss, L. Forsley, F. Gordon, D. Letts, D. Cravens, M. Miles, M. Swartz, J. Dash, F. Tanzella, P. Hagelstein, *et al.*, "Condensed matter nuclear reaction products observed in pd/d co-deposition experiments," *Current Science*, pp. 656–659, 2015.

[73] M. McKubre, S. Crouch-Baker, F. Tanzella, S. Smedley, M. Williams, S. Wing, M. Maly-Schreiber, R. Rocha-Filho, P. Searson, J. Pronko, *et al.*, "Development of advanced concepts for nuclear processes in deuterated metals," *Electric Power Res. Institute Report TR-104195*, 1994.

[74] S. Weinberger, "Warming Up to Cold Fusion (Washington Post; November 21, 2004; Page W22)." https://www.washingtonpost.com/wp-dyn/articles/A54964-2004Nov16.html, 2004. Accessed: 2024-10-02.

[75] Storms, E., "Study of pdd as a host for lenr. progress report #1," tech. rep., Kiva Labs, 2015.

[76] Storms, E., "Insights obtained during the initial study. progress report #3," tech. rep., Kiva Labs, 2015.

[77] Storms, E., "Initial studies showing the effect of important variables. progress report #4," tech. rep., Kiva Labs, 2015.

[78] Storms, E., "Behavior of pure pdd. progress report #5," tech. rep., Kiva Labs, 2015.

[79] P. Mosier-Boss, L. Forsley, F. Gordon, D. Letts, D. Cravens, M. Miles, M. Swartz, J. Dash, F. Tanzella, P. Hagelstein, *et al.*, "Condensed matter nuclear reaction products observed in pd/d co-deposition experiments," *Current Science*, pp. 656–659, 2015.

[80] S. M. S. MR, "Coupled calorimetry and resistivity measurements, in conjunction with an emended and more complete phase diagram of the palladium–isotopic hydrogen system," *Journal of Condensed Matter Nuclear Science*, vol. 29, no. 1, pp. 129–168, 2019.

[81] Y. Fukai, *The metal-hydrogen system: basic bulk properties*, vol. 21. Springer Science & Business Media, 2006.

[82] S. Harada, D. Ono, H. Sugimoto, and Y. Fukai, "The defect structure with superabundant vacancies to be formed from fcc binary metal hydrides: Experiments and simulations," *Journal of Alloys and Compounds*, vol. 446, pp. 474–478, 2007.

[83] Y. Fukai and N. Ōkuma, "Formation of superabundant vacancies in pd hydride under high hydrogen pressures," *Physical Review Letters*, vol. 73, no. 12, p. 1640, 1994.

[84] Y. Fukai, Y. Ishii, Y. Goto, and K. Watanabe, "Formation of superabundant vacancies in pd–h alloys," *Journal of alloys and compounds*, vol. 313, no. 1-2, pp. 121–132, 2000.

[85] D. Letts, "Highly reproducible lenr experiments using dual laser stimulation," *Current Science*, vol. 108, no. 4, p. 559, 2015.

[86] D. Letts and D. Cravens, "Laser stimulation of deuterated palladium: Past and present," in *Condensed Matter Nuclear Science*, pp. 159–170, World Scientific, 2006.

[87] D. Letts and P. Hagelstein, "Stimulation of optical phonons in deuterated palladium," in *Proceedings of the 14th International Conference on Condensed Matter Nuclear Science*, 2008.

[88] P. Mosier-Boss, S. Szpak, F. Gordon, and L. Forsley, "Use of cr-39 in pd/d co-deposition experiments," *The European Physical Journal - Applied Physics*, vol. 40, no. 3, pp. 293–303, 2007.

[89] S. Szpak, P. A. Mosier-Boss, and F. E. Gordon, "Further evidence of nuclear reactions in the pd/d lattice: emission of charged particles," *Naturwissenschaften*, vol. 94, pp. 511–514, 2007.

[90] C. Gotzmer, L. F. DeChiaro, K. Conley, M. Litz, M. Millett, J. Ewing, L. P. Forsley, K. J. Long, W. A. Wichart, P. A. Mosier-Boss, *et al.*, "Li-pd-rh-d2o electrochemistry experiments at elevated voltage," *APL Energy*, vol. 1, no. 3, 2023.

[91] M. H. Miles, B. F. Bush, and D. E. Stilwell, "Calorimetric principles and problems in measurements of excess power during pd-d2o electrolysis," *The Journal of Physical Chemistry*, vol. 98, no. 7, pp. 1948–1952, 1994.

[92] M. H. Miles, B. F. Bush, and J. J. Lagowski, "Anomalous effects involving excess power, radiation, and helium production during d2o electrolysis using palladium cathodes," *Fusion Technology*, vol. 25, no. 4, pp. 478–486, 1994.

[93] C. P. Berlinguette, Y.-M. Chiang, J. N. Munday, T. Schenkel, D. K. Fork, R. Koningstein, and M. D. Trevithick, "Revisiting the cold case of cold fusion," *Nature*, vol. 570, no. 7759, pp. 45–51, 2019.

[94] B. MacLeod, P. Schauer, K. Hu, B. Lam, D. Fork, and C. Berlinguette, "High-temperature high-pressure calorimeter for studying gram-scale heterogeneous chemical reactions," *Review of Scientific Instruments*, vol. 88, no. 8, 2017.

[95] D. Young, A. Jackson, D. Fork, S. Sadat, D. Rettenwander, J. D. Benck, and Y.-M. Chiang, "An operando calorimeter for high temperature electrochemical cells," *Journal of Physics: Energy*, vol. 3, no. 3, p. 034007, 2021.

[96] R. S. Sherbo, M. Moreno-Gonzalez, N. J. Johnson, D. J. Dvorak, D. K. Fork, and C. P. Berlinguette, "Accurate coulometric quantification of hydrogen absorption in palladium nanoparticles and thin films," *Chemistry of Materials*, vol. 30, no. 12, pp. 3963–3970, 2018.

[97] J. D. Benck, D. Rettenwander, A. Jackson, D. Young, and Y.-M. Chiang, "Apparatus for operando x-ray diffraction of fuel electrodes in high temperature solid oxide electrochemical cells," *Review of Scientific Instruments*, vol. 90, no. 2, 2019.

[98] S. Mishra, S. Verma, G. Dwivedi, and S. Upadhyay, "In-depth analysis of various aspects of charging station infrastructure for electric vehicle," *Renewable Energy Systems: Modeling, Optimization and Applications*, pp. 265–293, 2022.

[99] W. Hug, J. Divisek, J. Mergel, W. Seeger, and H. Steeb, "Highly efficient advanced alkaline electrolyzer for solar operation," *International journal of hydrogen energy*, vol. 17, no. 9, pp. 699–705, 1992.

[100] C. Scott, J. Mrochek, E. Newman, T. Scott, G. Michaels, and M. Petek, "A preliminary investigation of cold fusion by electrolysis of heavy water," tech. rep., Oak Ridge National Lab.(ORNL), Oak Ridge, TN (United States), 1989.

[101] M. McKubre, S. Crouch-Baker, A. Hauser, N. Jevtic, S. Smedley, F. Tanzella, M. Williams, S. Wing, B. Bush, F. McMahon, *et al.*, "Energy production processes in deuterated metals," tech. rep., Electric Power Research Institute Report, 1998.

[102] I. Dardik, T. Zilov, H. Branover, A. El-Boher, E. Greenspan, B. Khachaturov, V. Krakov, S. Lesin, and M. Tsirlin, "Excess heat in electrolysis experiments at energetics technologies," in *Condensed Matter Nuclear Science*, pp. 84–101, World Scientific, 2006.

[103] G. Preparata, "Everything you always wanted to know about cold fusion calorimetry," in *The Sixth International Conference on Cold Fusion rogress in New Hydrogen Energy: Proceedings*, pp. 136–143, 1996.

[104] D. Letts and P. Hagelstein, "Stimulation of optical phonons in deuterated palladium," in *Proceedings of the 14th International conference on Condensed Matter Nuclear Science*, 2008.

[105] S. M. S. MR, "Coupled calorimetry and resistivity measurements, in conjunction with an emended and more complete phase diagram of the palladium–isotopic hydrogen system," *Journal of Condensed Matter Nuclear Science*, vol. 29, no. 1, pp. 129–168, 2019.

[106] C. Gotzmer, L. F. DeChiaro, K. Conley, M. Litz, M. Millett, J. Ewing, L. P. Forsley, K. J. Long, W. A. Wichart, P. A. Mosier-Boss, *et al.*, "Li–pd–rh-d2o electrochemistry experiments at elevated voltage," *APL Energy*, vol. 1, no. 3, 2023.

[107] T. Fahidy, "Magnetoelectrolysis," *Journal of Applied Electrochemistry*, vol. 13, pp. 553–563, 1983.

[108] L. Holysz, A. Szczes, and E. Chibowski, "Effects of a static magnetic field on water and electrolyte solutions," *Journal of Colloid and Interface Science*, vol. 316, pp. 996–1002, 2007.

[109] Y.-H. Li and Y.-J. Chen, "The effect of magnetic field on the dynamics of gas bubbles in water electrolysis," *Scientific Reports*, vol. 11, 2021.

[110] M. McKubre, S. Crouch-Baker, F. Tanzella, S. Smedley, M. Williams, S. Wing, M. Maly-Schreiber, R. Rocha-Filho, P. Searson, J. Pronko, *et al.*, "Development of advanced concepts for nuclear processes in deuterated metals," tech. rep., Electric Power Research Institute Report, 1994.

[111] B. MacLeod, P. Schauer, K. Hu, B. Lam, D. Fork, and C. Berlinguette, "High-temperature high-pressure calorimeter for studying gram-scale heterogeneous chemical reactions," *Review of Scientific Instruments*, vol. 88, no. 8, 2017.

[112] D. Young, A. Jackson, D. Fork, S. Sadat, D. Rettenwander, J. D. Benck, and Y.-M. Chiang, "An operando calorimeter for high temperature electrochemical cells," *Journal of Physics: Energy*, vol. 3, no. 3, p. 034007, 2021.

[113] E. Storms, "The nature of D+D fusion reaction in palladium and nickel," *ICCF23 (23. International Conference on Cold Fusion)*, 2022.

[114] F. Schubert, M. Gollner, J. Kita, F. Linseis, and R. Moos, "First steps to develop a sensor for a tian–calvet calorimeter with increased sensitivity," *Journal of Sensors and Sensor Systems*, vol. 5, no. 1, pp. 205–212, 2016.

[115] N. Klopčič, I. Grimmer, F. Winkler, M. Sartory, and A. Trattner, "A review on metal hydride materials for hydrogen storage," *Journal of Energy Storage*, vol. 72, p. 108456, 2023.

[116] R. D. Gardner, W. H. Ashley, and P. Bergstresser, "The gravimetric determination of hydrogen in molybdenum metal," tech. rep., Los Alamos National Lab.(LANL), Los Alamos, NM (United States), 1965.

[117] R. D. Gardner and W. H. Ashley, *The Gravimetric Determination of Trace Amounts of Hydrogen in Sodium Metal*, vol. 3049. Los Alamos Scientific Laboratory of the University of California, 1964.

[118] C. I. Contescu, C. M. Brown, Y. Liu, V. V. Bhat, and N. C. Gallego, "Detection of hydrogen spillover in palladium-modified activated carbon fibers during hydrogen adsorption," *The Journal of Physical Chemistry C*, vol. 113, no. 14, pp. 5886–5890, 2009.

[119] T. Green and T. Quickenden, "Electrolytic preparation of highly loaded deuterides of palladium," *Journal of Electroanalytical Chemistry*, vol. 368, no. 1-2, pp. 121–131, 1994.

[120] W. Oates and T. B. Flanagan, "The reaction of hydrogen atoms with palladium and its alloys," *Canadian Journal of Chemistry*, vol. 53, no. 5, pp. 694–701, 1975.

[121] W. Auer and H. Grabke, "The kinetics of hydrogen absorption in palladium ($\alpha$-and $\beta$-phase) and palladium-silver-alloys," *Berichte der Bunsengesellschaft für physikalische Chemie*, vol. 78, no. 1, pp. 58–67, 1974.

[122] A. Alraeesi and T. Gardner, "Assessment of sieverts law assumptions and n values in palladium membranes: experimental and theoretical analyses," *Membranes*, vol. 11, no. 10, p. 778, 2021.

[123] V. Vons, H. Leegwater, W. Legerstee, S. Eijt, and A. Schmidt-Ott, "Hydrogen storage properties of spark generated palladium nanoparticles," *International Journal of Hydrogen Energy*, vol. 35, no. 11, pp. 5479–5489, 2010.

[124] A. Viola, F. Maillard, and G. Tsirlina, "Voltammetric quantification of h: Pd ratio complicated by $\alpha$ $\beta$ phase transition in pdhx: Electrodes with low pd loadings," *Electrochimica Acta*, vol. 485, p. 144085, 2024.

[125] M. Miles, K. B. Johnson, and M. Imam, "Electrochemical loading of hydrogen and deuterium into palladium and palladium-boron alloys," in *Sixth International Conference on Cold Fusion, Progress in New Hydrogen Energy*, p. 208, Tokyo Institute of Technology Lake Toya, Japan, 1996.

[126] R. S. Sherbo, M. Moreno-Gonzalez, N. J. Johnson, D. J. Dvorak, D. K. Fork, and C. P. Berlinguette, "Accurate coulometric quantification of hydrogen absorption in palladium nanoparticles and thin films," *Chemistry of Materials*, vol. 30, no. 12, pp. 3963–3970, 2018.

[127] A. T. Landers, H. Peng, D. M. Koshy, S. H. Lee, J. T. Feaster, J. C. Lin, J. W. Beeman, D. Higgins, J. Yano, W. S. Drisdell, *et al.*, "Dynamics and hysteresis of hydrogen intercalation and deintercalation in palladium electrodes: a multimodal in situ x-ray diffraction, coulometry, and computational study," *Chemistry of Materials*, vol. 33, no. 15, pp. 5872–5884, 2021.

[128] D. R. Lawson, M. J. Tierney, I. Cheng, L. S. Van Dyke, M. Espenscheid, and C. R. Martin, "Use of a coulometric assay technique to study the variables affecting deuterium loading levels within palladium electrodes," *Electrochimica Acta*, vol. 36, no. 9, pp. 1515–1522, 1991.

[129] G. T. Cheek and W. E. O'Grady, "Measurement of hydrogen uptake by palladium using a quartz crystal microbalance," *Journal of Electroanalytical Chemistry and Interfacial Electrochemistry*, vol. 277, no. 1-2, pp. 341–346, 1990.

[130] G. T. Cheek and W. E. O'Grady, "Measurement of h/d uptake characteristics at palladium using a quartz crystal microbalance," *Journal of Electroanalytical Chemistry*, vol. 368, no. 1-2, pp. 133–138, 1994.

[131] P. Ferrari, D. Diaz-Droguett, S. Rojas, and A. Cabrera, "Inhibition of hydrogen absorption in bulk pd by the formation of ru–pd surface alloy," *Thin solid films*, vol. 550, pp. 732–737, 2014.

[132] M. Grdeń, K. Kuśmierczyk, and A. Czerwiński, "Study of hydrogen electrosorption in pd-ni alloys by the quartz crystal microbalance," *Journal of Solid State Electrochemistry*, vol. 7, pp. 43–48, 2002.

[133] N. Yamamoto, T. Ohsaka, T. Terashima, and N. Oyama, "In situ electrochemical quartz crystal microbalance studies of water electrolysis at a palladium cathode in acidic aqueous media," *Journal of Electroanalytical Chemistry and Interfacial Electrochemistry*, vol. 296, no. 2, pp. 463–471, 1990.

[134] C. Kuhrt and R. Anton, "On the origin of a lattice expansion in palladium and pd au vapour deposits on various substrates," *Thin Solid Films*, vol. 198, no. 1-2, pp. 301–315, 1991.

[135] W. Lindsay, "Measurement of the partial molar volume and solubility of hydrogen in its dilute solutions in palladium-silver alloys," *International Journal of Thermophysics*, vol. 18, pp. 1051–1061, 1997.

[136] M. Slaman, R. Westerwaal, H. Schreuders, and B. Dam, "Optical hydrogen sensors based on metal-hydrides," in *Photonic Applications for Aerospace, Transportation, and Harsh Environment III*, vol. 8368, pp. 41–48, SPIE, 2012.

[137] R. R. Maier, B. J. Jones, J. S. Barton, S. McCulloch, T. Allsop, J. D. Jones, and I. Bennion, "Fibre optics in palladium-based hydrogen sensing," *Journal of Optics A: Pure and Applied Optics*, vol. 9, no. 6, p. S45, 2007.

[138] T. L. Pedersen, C. Liesch, C. Salinga, T. Eleftheriadis, H. Weis, and M. Wuttig, "Hydrogen-induced changes of mechanical stress and optical transmission in thin pd films," *Thin Solid Films*, vol. 458, no. 1-2, pp. 299–303, 2004.

[139] K. J. Palm, J. B. Murray, T. C. Narayan, and J. N. Munday, "Dynamic optical properties of metal hydrides," *Acs Photonics*, vol. 5, no. 11, pp. 4677–4686, 2018.

[140] R. Matelon, J. Avila, U. Volkmann, A. L. Cabrera, E. H. Morales, and D. Lederman, "Substrate effect on the optical response of thin palladium films exposed to hydrogen gas," *Thin Solid Films*, vol. 516, no. 21, pp. 7797–7801, 2008.

[141] H. Conrad, G. Ertl, and E. Latta, "Adsorption of hydrogen on palladium single crystal surfaces," *Surface Science*, vol. 41, no. 2, pp. 435–446, 1974.

[142] M. Johansson, E. Skulason, G. Nielsen, S. Murphy, R. M. Nielsen, and I. Chorkendorff, "Hydrogen adsorption on palladium and palladium hydride at 1 bar," *Surface science*, vol. 604, no. 7-8, pp. 718–729, 2010.

[143] R. Silverstein, D. Eliezer, and E. Tal-Gutelmacher, "Hydrogen trapping in alloys studied by thermal desorption spectrometry," *Journal of Alloys and Compounds*, vol. 747, pp. 511–522, 2018.

[144] C. Tapia-Bastidas, A. Atrens, and E. M. Gray, "Thermal desorption spectrometer for measuring ppm concentrations of trapped hydrogen," *International Journal of Hydrogen Energy*, vol. 43, no. 15, pp. 7600–7617, 2018.

[145] F. Leardini, J. Fernández, J. Bodega, and C. Sanchez, "Isotope effects in the kinetics of simultaneous h and d thermal desorption from pd," *Journal of Physics and Chemistry of Solids*, vol. 69, no. 1, pp. 116–127, 2008.

[146] H.-W. Suh, T. J. Schmeier, N. Hazari, R. A. Kemp, and M. K. Takase, "Experimental and computational studies of the reaction of carbon dioxide with pincer-supported nickel and palladium hydrides," *Organometallics*, vol. 31, no. 23, pp. 8225–8236, 2012.

[147] N. K. Nag, "A study on the formation of palladium hydride in a carbon-supported palladium catalyst," *The Journal of Physical Chemistry B*, vol. 105, no. 25, pp. 5945–5949, 2001.

[148] J. López-Serrano, S. B. Duckett, and A. Lledós, "Palladium-catalyzed hydrogenation: Detection of palladium hydrides. a joint study using para-hydrogen-enhanced nmr spectroscopy and density functional theory," *Journal of the American Chemical Society*, vol. 128, no. 30, pp. 9596–9597, 2006.

[149] H. Kobayashi, M. Yamauchi, H. Kitagawa, Y. Kubota, K. Kato, and M. Takata, "On the nature of strong hydrogen atom trapping inside pd nanoparticles," *Journal of the American Chemical Society*, vol. 130, no. 6, pp. 1828–1829, 2008.

[150] K. Kusada, M. Yamauchi, H. Kobayashi, H. Kitagawa, and Y. Kubota, "Hydrogen-storage properties of solid-solution alloys of immiscible neighboring elements with pd," *Journal of the American Chemical Society*, vol. 132, no. 45, pp. 15896–15898, 2010.

[151] L. H. Rayhel, R. L. Corey, D. T. Shane, D. F. Cowgill, and M. S. Conradi, "Hydrogen nmr of palladium hydride: Measuring the hydride- gas exchange rate," *The Journal of Physical Chemistry C*, vol. 115, no. 11, pp. 4966–4970, 2011.

[152] J. Worsham Jr, M. Wilkinson, and C. Shull, "Neutron-diffraction observations on the palladium-hydrogen and palladium-deuterium systems," *Journal of Physics and Chemistry of Solids*, vol. 3, no. 3-4, pp. 303–310, 1957.

[153] J. Bergsma and J. Goedkoop, "Thermal motion in palladium hydride studied by means of elastic and inelastic scattering of neutrons," *Physica*, vol. 26, no. 9, pp. 744–750, 1960.

[154] S. Setayandeh, C. Webb, and E. M. Gray, "Electron and phonon band structures of palladium and palladium hydride: a review," *Progress in Solid State Chemistry*, vol. 60, p. 100285, 2020.

[155] R. Schwarz, H. Bach, U. Harms, and D. Tuggle, "Elastic properties of pd–hydrogen, pd–deuterium, and pd–tritium single crystals," *Acta materialia*, vol. 53, no. 3, pp. 569–580, 2005.

[156] A. Switendick, "The change in electronic properties on hydrogen alloying and hydride formation," *Hydrogen in Metals I: Basic Properties*, pp. 101–129, 2005.

[157] J. Gao, W.-S. Zhang, and J.-J. Zhang, "An explanation of hysteresis of electrical resistance–composition relationship in the pd–h (d) and pd alloy–h (d) systems measured by a gas phase method," *International journal of hydrogen energy*, vol. 39, no. 36, pp. 21328–21334, 2014.

[158] H. Bakker, M. van Sprang, and R. Griessen, "Isotope effect in electron scattering by h or d in palladium," *Journal of Physics F: Metal Physics*, vol. 15, no. 1, p. 63, 1985.

[159] S. Wagner and A. Pundt, "Electrical resistivity and hydrogen solubility of pdhc thin films," *Acta materialia*, vol. 58, no. 4, pp. 1387–1394, 2010.

[160] H. Akaki, Y. Sakamaki, S. Harada, and M. Kubota, "Phase boundary study of pd–h (d) systems by means of electrical resistivity measurements," *Journal of alloys and compounds*, vol. 446, pp. 436–438, 2007.

[161] S. Wagner and A. Pundt, "Combined impact of microstructure and mechanical stress on the electrical resistivity of pdhc thin films," *Acta Materialia*, vol. 59, no. 5, pp. 1862–1870, 2011.

[162] A. Pozio and S. Tosti, "Pd-ag electrical resistivity in hydrogen and deuterium: temperature effect," *Materials*, vol. 12, no. 21, p. 3551, 2019.

[163] J. D. Benck, A. Jackson, D. Young, D. Rettenwander, and Y.-M. Chiang, "Producing high concentrations of hydrogen in palladium via electrochemical insertion from aqueous and solid electrolytes," *Chemistry of Materials*, vol. 31, no. 11, pp. 4234–4245, 2019.

[164] F. Yang, S.-C. Kung, M. Cheng, J. C. Hemminger, and R. M. Penner, "Smaller is faster and more sensitive: the effect of wire size on the detection of hydrogen by single palladium nanowires," *ACS nano*, vol. 4, no. 9, pp. 5233–5244, 2010.

[165] W.-S. Zhang, Z.-F. Zhang, and Z.-L. Zhang, "Some problems on the resistance method in the in situ measurement of hydrogen content in palladium electrode," *Journal of Electroanalytical Chemistry*, vol. 528, no. 1-2, pp. 1–17, 2002.

[166] F. A. A. Nugroho, I. Darmadi, V. P. Zhdanov, and C. Langhammer, "Universal scaling and design rules of hydrogen-induced optical properties in pd and pd-alloy nanoparticles," *ACS nano*, vol. 12, no. 10, pp. 9903–9912, 2018.

[167] W.-S. Zhang, Z.-F. Zhang, and Z.-L. Zhang, "Some problems on the resistance method in the in situ measurement of hydrogen content in palladium electrode," *Journal of Electroanalytical Chemistry*, vol. 528, no. 1-2, pp. 1–17, 2002.

[168] B. Guigue, G. Geneste, B. Leridon, and P. Loubeyre, "An x-ray study of palladium hydrides up to 100 gpa: Synthesis and isotopic effects," *Journal of Applied Physics*, vol. 127, no. 7, 2020.

[169] N. Verma, R. Delhez, N. M. van der Pers, R. Hendrikx, R. Huizenga, and A. J. Böttger, "Dislocations, texture and stress development in hydrogen-cycled pd thin films: An in-situ x-ray diffraction study," *international Journal of Hydrogen Energy*, vol. 47, no. 24, pp. 12119–12134, 2022.

[170] R. Gremaud, M. Gonzalez-Silveira, Y. Pivak, S. De Man, M. Slaman, H. Schreuders, B. Dam, and R. Griessen, "Hydrogenography of pdhx thin films: Influence of h-induced stress relaxation processes," *Acta Materialia*, vol. 57, no. 4, pp. 1209–1219, 2009.

[171] A. Yau, R. J. Harder, M. W. Kanan, and A. Ulvestad, "Imaging the hydrogen absorption dynamics of individual grains in polycrystalline palladium thin films in 3d," *ACS Nano*, vol. 11, no. 11, pp. 10945–10954, 2017.

[172] T. Harumoto, Y. Suzuki, J. Shi, and Y. Nakamura, "X-ray diffraction study on a (111)-textured palladium thin film under hydrogen loading and unloading: film structure evolution and its mechanism," *Journal of Applied Crystallography*, vol. 50, no. 5, pp. 1478–1489, 2017.

[173] H. Peisl, "Lattice strains due to hydrogen in metals," *Hydrogen in metals I: Basic properties*, pp. 53–74, 2005.

[174] M. Yamada, "Science repts. tóhoku imp. univ., 11, 451-453 (1922)," *Phil. Mag*, vol. 45, pp. 241–243, 1923.

[175] T. Harumoto, Y. Ohnishi, K. Nishio, T. Ishiguro, J. Shi, and Y. Nakamura, "In-situ x-ray diffraction study of hydrogen absorption and desorption processes in pd thin films: Hydrogen composition dependent anisotropic expansion and its quantitative description," *AIP Advances*, vol. 7, no. 6, 2017.

[176] T. Harumoto, Y. Suzuki, J. Shi, and Y. Nakamura, "X-ray diffraction study on a (111)-textured palladium thin film under hydrogen loading and unloading: film structure evolution and its mechanism," *Journal of Applied Crystallography*, vol. 50, no. 5, pp. 1478–1489, 2017.

[177] J. Hanawalt, "X-ray study of the system palladium-hydrogen," *Physical Review*, vol. 33, no. 3, p. 444, 1929.

[178] F. Krüger and G. Gehm, "Lattice constants and electrical conductivity of electrolytically loaded palladium-silver alloys as a function of hydrogen loading," *Ann Phys*, vol. 16, pp. 174–189, 1933.

[179] J. D. Benck, A. Jackson, D. Young, D. Rettenwander, and Y.-M. Chiang, "Producing high concentrations of hydrogen in palladium via electrochemical insertion from aqueous and solid electrolytes," *Chemistry of Materials*, vol. 31, no. 11, pp. 4234–4245, 2019.

[180] J. Schirber and B. Morosin, "Lattice constants of $\beta$- p d h x and $\beta$- p d d x with x near 1.0," *Physical Review B*, vol. 12, no. 1, p. 117, 1975.

[181] I. Balbaa, P. Hardy, A. San-Martin, P. Coulter, and F. Machester, "The effect of lattice distortions on the x-ray measurement of lattice parameters for pdhx. i. empirical relationships," *Journal of Physics F: Metal Physics*, vol. 17, no. 10, p. 2041, 1987.

[182] J. Gauthier, K. Bruening, K. Ritter, D. Tuckerman, and M. Hovish, "Dynamic changes in hydrogen evolution catalysis impose an upper bound on electrochemical hydrogen storage in pd," *under review*, 2025.

[183] G. O. Larrazábal, P. Strøm-Hansen, J. P. Heli, K. Zeiter, K. T. Therkildsen, I. Chorkendorff, and B. Seger, "Analysis of Mass Flows and Membrane Cross-over in CO2 Reduction at High Current Densities in an MEA-Type Electrolyzer," *ACS Applied Materials & Interfaces*, vol. 11, no. 44, pp. 41281–41288, 2019.

[184] M. Jarrell, *Chapter 11: Dielectric Properties of Materials*. LSU, 2017.

[185] "Coolescence LLC, retrieved from archive.org." https://web.archive.org/web/20170707125504/http://www.coolescence.com/. Accessed: 2024-11-01.

[186] S. C. Hamm, O. Dmitriyeva, D. L. Knies, R. Cantwell, and M. McConnell, "Engineering palladium surfaces to enhance the electrochemical storage of hydrogen," *Journal of The Electrochemical Society*, vol. 164, no. 14, p. A3462, 2017.

[187] F. Westheimer, "The magnitude of the primary kinetic isotope effect for compounds of hydrogen and deuterium," *Chemical Reviews*, vol. 61, no. 3, pp. 265–273, 1961.

[188] P.-W. Guan, R. J. Hemley, and V. Viswanathan, "Combining pressure and electrochemistry to synthesize superhydrides," *Proceedings of the National Academy of Sciences*, vol. 118, no. 46, p. e2110470118, 2021.

[189] S. Setayandeh, C. Webb, and E. M. Gray, "Electron and phonon band structures of palladium and palladium hydride: a review," *Progress in Solid State Chemistry*, vol. 60, p. 100285, 2020.

[190] B. Hammer, L. B. Hansen, and J. K. Nørskov, "Improved adsorption energetics within density-functional theory using revised perdew-burke-ernzerhof functionals," *Physical Review B*, vol. 59, no. 11, p. 7413, 1999.

[191] J. P. Perdew, A. Ruzsinszky, G. I. Csonka, O. A. Vydrov, G. E. Scuseria, L. A. Constantin, X. Zhou, and K. Burke, "Restoring the density-gradient expansion for exchange in solids and surfaces," *Physical review letters*, vol. 100, no. 13, p. 136406, 2008.

[192] J. Schmidt, H.-C. Wang, T. F. Cerqueira, S. Botti, and M. A. Marques, "A dataset of 175k stable and metastable materials calculated with the pbesol and scan functionals," *Scientific Data*, vol. 9, no. 1, p. 64, 2022.

[193] G. Kresse and J. Hafner, "Ab initio molecular dynamics for liquid metals," *Physical Review B*, vol. 47, no. 1, p. 558, 1993.

[194] G. Kresse and J. Furthmüller, "Efficiency of ab-initio total energy calculations for metals and semiconductors using a plane-wave basis set," *Computational materials science*, vol. 6, no. 1, pp. 15–50, 1996.

[195] G. Kresse and J. Furthmüller, "Efficient iterative schemes for ab initio total-energy calculations using a plane-wave basis set," *Physical review B*, vol. 54, no. 16, p. 11169, 1996.

[196] A. H. Larsen, J. J. Mortensen, J. Blomqvist, I. E. Castelli, R. Christensen, M. Dułak, J. Friis, M. N. Groves, B. Hammer, C. Hargus, *et al.*, "The atomic simulation environment – a python library for working with atoms," *Journal of Physics: Condensed Matter*, vol. 29, no. 27, p. 273002, 2017.

[197] G. Kresse and D. Joubert, "From ultrasoft pseudopotentials to the projector augmented-wave method," *Physical review b*, vol. 59, no. 3, p. 1758, 1999.

[198] H. J. Monkhorst and J. D. Pack, "Special points for brillouin-zone integrations," *Physical Review B*, vol. 13, no. 12, p. 5188, 1976.

[199] A. Bajpai, P. Mehta, K. Frey, A. M. Lehmer, and W. F. Schneider, "Benchmark first-principles calculations of adsorbate free energies," *Acs Catalysis*, vol. 8, no. 3, pp. 1945–1954, 2018.

[200] E. Schneider, L. Dai, R. Q. Topper, C. Drechsel-Grau, and M. E. Tuckerman, "Stochastic neural network approach for learning high-dimensional free energy surfaces," *Physical Review Letters*, vol. 119, no. 15, p. 150601, 2017.

[201] E. M. Lee, T. Ludwig, B. Yu, A. R. Singh, F. Gygi, J. K. Nørskov, and J. J. de Pablo, "Neural network sampling of the free energy landscape for nitrogen dissociation on ruthenium," *The Journal of Physical Chemistry Letters*, vol. 12, no. 11, pp. 2954–2962, 2021.

[202] J. A. Gauthier, Z. Lin, M. Head-Gordon, and A. T. Bell, "Pathways for the formation of c2+ products under alkaline conditions during the electrochemical reduction of co2," *ACS Energy Letters*, vol. 7, no. 5, pp. 1679–1686, 2022.

[203] J. A. Gauthier, C. F. Dickens, H. H. Heenen, V. Sudarshan, S. Ringe, and K. Chan, "Unified approach to implicit and explicit solvent simulations of electrochemical reaction energetics," *Journal of chemical theory and computation*, 2019.

[204] J. A. Gauthier, C. F. Dickens, S. Ringe, and K. Chan, "Practical considerations for continuum models applied to surface electrochemistry," *ChemPhysChem*, vol. 20, no. 22, pp. 3074–3080, 2019.

[205] M. Askari, R. C. Huckabee, and J. A. Gauthier, "A simple evaluation of adiabatic proton tunneling across the electrified double layer," *The Journal of Physical Chemistry C*, vol. 128, no. 30, pp. 12386–12398, 2024.

[206] K. Mathew, R. Sundararaman, K. Letchworth-Weaver, T. Arias, and R. G. Hennig, "Implicit solvation model for density-functional study of nanocrystal surfaces and reaction pathways," *The Journal of Chemical Physics*, vol. 140, no. 8, p. 084106, 2014.

[207] K. Mathew, V. C. Kolluru, S. Mula, S. N. Steinmann, and R. G. Hennig, "Implicit self-consistent electrolyte model in plane-wave density-functional theory," *The Journal of Chemical Physics*, vol. 151, no. 23, p. 234101, 2019.

[208] S. Sakong, M. Naderian, K. Mathew, R. G. Hennig, and A. Groß, "Density functional theory study of the electrochemical interface between a pt electrode and an aqueous electrolyte using an implicit solvent method," *The Journal of Chemical Physics*, vol. 142, no. 23, p. 234107, 2015.

[209] J. K. Nørskov, J. Rossmeisl, A. Logadottir, L. Lindqvist, J. R. Kitchin, T. Bligaard, and H. Jonsson, "Origin of the overpotential for oxygen reduction at a fuel-cell cathode," *The Journal of Physical Chemistry B*, vol. 108, no. 46, pp. 17886–17892, 2004.

[210] N. Lalith, A. Singh, and J. Gauthier, "The importance of reaction energy in predicting chemical reaction barriers with machine learning models," 2023.

[211] J. A. Gauthier, L. D. Chen, M. Bajdich, and K. Chan, "Implications of the fractional charge of hydroxide at the electrochemical interface," *Physical Chemistry Chemical Physics*, vol. 22, no. 13, pp. 6964–6969, 2020.

[212] J. A. Garrido Torres, P. C. Jennings, M. H. Hansen, J. R. Boes, and T. Bligaard, "Low-scaling algorithm for nudged elastic band calculations using a surrogate machine learning model," *Physical review letters*, vol. 122, no. 15, p. 156001, 2019.

[213] J. P. Perdew, "Density functional theory and the band gap problem," *International Journal of Quantum Chemistry*, vol. 28, no. S19, pp. 497–523, 1985.

[214] P. Virtanen, R. Gommers, T. E. Oliphant, M. Haberland, T. Reddy, D. Cournapeau, E. Burovski, P. Peterson, W. Weckesser, J. Bright, *et al.*, "Scipy 1.0: fundamental algorithms for scientific computing in python," *Nature methods*, vol. 17, no. 3, pp. 261–272, 2020.

[215] G. I. Csonka, J. P. Perdew, A. Ruzsinszky, P. H. Philipsen, S. Lebègue, J. Paier, O. A. Vydrov, and J. G. Ángyán, "Assessing the performance of recent density functionals for bulk solids," *Physical Review B Condensed Matter and Materials Physics*, vol. 79, no. 15, p. 155107, 2009.

[216] C. N. Lininger, J. A. Gauthier, W.-L. Li, E. Rossomme, V. V. Welborn, Z. Lin, T. Head-Gordon, M. Head-Gordon, and A. T. Bell, "Challenges for density functional theory: calculation of co adsorption on electrocatalytically relevant metals," *Physical Chemistry Chemical Physics*, vol. 23, no. 15, pp. 9394–9406, 2021.

[217] J. Worsham Jr, M. Wilkinson, and C. Shull, "Neutron-diffraction observations on the palladium-hydrogen and palladium-deuterium systems," *Journal of Physics and Chemistry of Solids*, vol. 3, no. 3-4, pp. 303–310, 1957.

[218] H. Frieske and E. Wicke, "Magnetic susceptibility and equilibrium diagram of pdhn," *Berichte der Bunsengesellschaft für physikalische Chemie*, vol. 77, no. 1, pp. 48–52, 1973.

[219] Y. Fukai, *The metal-hydrogen system: basic bulk properties*, vol. 21. Springer Science & Business Media, 2006.

[220] V. Vons, H. Leegwater, W. Legerstee, S. Eijt, and A. Schmidt-Ott, "Hydrogen storage properties of spark generated palladium nanoparticles," *International journal of hydrogen energy*, vol. 35, no. 11, pp. 5479–5489, 2010.

[221] C. Langhammer, E. M. Larsson, V. P. Zhdanov, and I. Zoric, "Asymmetric hysteresis in nanoscopic single-metal hydrides: palladium nanorings," *The Journal of Physical Chemistry C*, vol. 116, no. 40, pp. 21201–21207, 2012.

[222] P.-W. Guan, R. J. Hemley, and V. Viswanathan, "Combining pressure and electrochemistry to synthesize superhydrides," *Proceedings of the National Academy of Sciences*, vol. 118, no. 46, p. e2110470118, 2021.

[223] T. Green and D. Britz, "Kinetics of the deuterium and hydrogen evolution reactions at palladium in alkaline solution," *Journal of Electroanalytical Chemistry*, vol. 412, no. 1-2, pp. 59–66, 1996.

[224] P.-W. Guan, Y. Sun, R. J. Hemley, H. Liu, Y. Ma, and V. Viswanathan, "Low-pressure electrochemical synthesis of complex high-pressure superconducting superhydrides," *Physical Review Letters*, vol. 128, no. 18, p. 186001, 2022.

[225] A. G. Oshchepkov, A. Bonnefont, V. N. Parmon, and E. R. Savinova, "On the effect of temperature and surface oxidation on the kinetics of hydrogen electrode reactions on nickel in alkaline media," *Electrochimica Acta*, vol. 269, pp. 111–118, 2018.

[226] D. Letts and P. L. Hagelstein, "Stimulation of Optical Phonons in Deuterated Palladium," tech. rep., 2008.

[227] G. Wang, J. Liu, Y. Sui, M. Wang, L. Qiao, F. Du, and B. Zou, "Palladium structure engineering induced by electrochemical H intercalation boosts hydrogen evolution catalysis," *J. Mater. Chem. A*, vol. 7, no. 24, pp. 14876–14881, 2019.

[228] T. Green and D. Britz, "Kinetics of the deuterium and hydrogen evolution reactions at palladium in alkaline solution," tech. rep., 1996.

[229] S. Shibuya, H. Matsushima, and M. Ueda, "Study of Deuterium Isotope Separation by PEFC," *Journal of The Electrochemical Society*, vol. 163, p. F704, 5 2016.

[230] M. Staker, "The role of superabundant vacancy delta to delta prime transformation in stopping fleischmann-pons heat effect in palladium-deuterium," *International Journal of Hydrogen Energy*, vol. 48, no. 40, pp. 15195–15202, 2023.

[231] H. Wipf, "Electro-and thermotransport of hydrogen in metals," *Hydrogen in metals II: application-oriented properties*, pp. 273–304, 2005.

[232] M. Fleischmann and S. Pons, "Electrochemically induced nuclear fusion of deuterium," *Journal of Electroanalytical Chemistry*, vol. 261, pp. 301–308, 1989.

[233] D. Morrison, "Review of cold fusion," *Soviet Physics Uspekhi*, vol. 34, no. 12, p. 1055, 1991.

[234] M. Fleischmann, S. Pons, M. W. Anderson, L. Jun Li, and M. Hawkins, "Calorimetry of the palladium–deuterium–heavy water system," *Journal of Electroanalytical Chemistry*, vol. 287, pp. 293–348, 1990.

[235] M. Fleischmann and S. Pons, "Calorimetry of the Pd–D2O system: from simplicity via complications to simplicity," *Physics Letters A*, vol. 176, pp. 118–129, 1993.

[236] G. Zhuang, Y. Chen, and P. N. Ross, "The reaction of lithium with carbon dioxide studied by photo-electron spectroscopy," *Surface Science*, vol. 418, pp. 139–149, 11 1998.

[237] M. R. Staker, "Coupled Calorimetry and Resistivity Measurements, in Conjunction with an Emended and More Complete Phase Diagram of the Palladium-Isotopic Hydrogen System," *M.R. Staker / Journal of Condensed Matter Nuclear Science*, vol. 29, pp. 129–168, 2019.

[238] M. R. Staker, "The role of superabundant vacancy delta to delta prime transformation in stopping Fleischmann Pons heat effect in palladium deuterium," *International Journal of Hydrogen Energy*, vol. 48, pp. 15195–15202, 5 2023.

[239] M. R. Staker, "How to achieve the Fleischmann Pons heat effect," *International Journal of Hydrogen Energy*, vol. 48, pp. 1988–2000, 1 2023.

[240] M. Fleischmann and S. Pons, "Calorimetry of the Pd-D2O system: from simplicity via complications to simplicity," *Physics Letters A*, vol. 176, no. 1, pp. 118–129, 1993.

[241] M. R. Staker, "Corrigendum to The role of superabundant vacancy delta to delta prime transformation in stopping Fleischmann Pons heat effect in palladium deuterium," 1 2024.

[242] Y. Fukai, "Superabundant Vacancies Formed in Metal-Hydrogen Alloys," tech. rep., 2003.

[243] Y. Fukai, "The structure and phase diagram of M-H systems at high chemical potentials - High pressure and electrochemical synthesis," *Journal of Alloys and Compounds*, vol. 404-406, pp. 7–15, 12 2005.

[244] S. Harada, D. Ono, H. Sugimoto, and Y. Fukai, "The defect structure with superabundant vacancies to be formed from fcc binary metal hydrides: Experiments and simulations," *Journal of Alloys and Compounds*, vol. 446-447, pp. 474–478, 10 2007.

[245] Y. Dong, Y. Zhou, H. Huang, B. Zhang, X. Li, K. Chen, L. Sun, and G. Dou, "Etching of quartz crystals in liquid phase environment: A review," 6 2024.

[246] O. CAMBON, M. DELEUZE, J. P. MICHEL, J. P. AUBRY, A. GOIFFON, and E. PHILIPPOT, "Controlled dissolution of quartz material.Part II. Quartz chemical etching applied to blanks industrial manufacturing," *Le Journal de Physique IV*, vol. 04, pp. 2–85, 2 1994.

[247] A. El-Boher, G. K. Hubler, D. Pease, O. Azizi, H. J. He, W. Issacson, V. Violante, and S. Gangopadhyay, "Progress towards understanding anomalous heat effect in metal deuterides," tech. rep., 2015.

[248] G. K. Hubler, "Anomalous effects in hydrogen-charged palladium - A review," 8 2007.

[249] S. E. Jones, F. W. Keeney, A. C. Johnson, D. B. Buehler, F. E. Cecil, G. Hubler, P. L. Hagelstein, J. E. Ellsworth, and M. R. Scott, "Charged-particle Emissions from Metal Deuterides," tech. rep., 10th International Conference on Cold Fusion, 2003.

[250] G. Hubler, D. Pease, A. E. Boher, O. Azzizi, J. He, K. Katti, and K. Katti, "Long Term Anomalous Heat from 9 nm Pd Nanoparticles in an Electrochemical Cell," (Xiamen,China), InternationalConferenceonColdFusion, 6 2021.

[251] I. I. Dardik, "Pulsed Electrolytic Cell," US 2003/0213696A1, 2003.

[252] Kattesh V. Katti, Kavita K. Katti, Raghuraman Kannan, and Satish Kumar Nune, "Egcg stabilized pd nanoparticles, method for making, and electrochemical cell," Tech. Rep. 6, 9 2007.

[253] E. Storms, "Study of pdd as a host for lenr," 2015.

[254] E. Storms, "Calibration of the seebeck calorimeter," 2015.

[255] E. Storms, "Insights obtained during the intial study," 2015.

[256] E. Storms, "Effect of important variables," 2015.

[257] E. Storms, "Behavior of pure pdd," 2015.

[258] E. Storms, "Additional behavior of pure pdd," 2015.

[259] E. Storms, "The nature of the d+d fusion reaction in palladium and nickel," *ICCF-23*, 2021.

[260] M. H. Miles, B. F. Bush, and D. E. Stilwell, "Calorimetric principles and problems in measurements of excess power during pd-d2o electrolysis," *Journal of Electroanalytical Chemistry*, vol. 482, no. 1, pp. 56–65, 1994.

[261] N. Lewis, C. Barnes, M. Heben, A. Kumar, S. Lunt, G. McManis, G. Miskelly, R. Penner, M. Sailor, P. Santangelo, G. Shreve, B. Tufts, M. Youngquist, R. Kavanagh, S. Kellog, R. Vogelaar, T. Wang, R. Kondrat, and R. New, "Searches for low-temperature nuclear fusion of deuterium in palladium," *Nature*, vol. 340, pp. 525–530, 1989.

[262] M. H. Miles, B. F. Bush, and J. J. Lagowski, "Anomalous effects involving excess power, radiation, and helium production during d2o electrolysis using palladium cathodes," *Fusion Technology*, vol. 25, no. 4, pp. 478–486, 1994.

[263] M. H. Miles, B. F. Bush, and K. B. Johnson, "Anomalous effects in deuterated systems," tech. rep., NAWCWPNS TP 8302, 1996.

[264] M. H. Miles, "Calorimetric studies of pd/d2o+liod electrolysis cells," *Journal of Electroanalytical Chemistry*, vol. 482, no. 1, pp. 56–65, 2000.

[265] M. Beck, *Boron in palladium: Interaction, phase formation and phase transformation.* PhD thesis, University of Stuttgart, 2001.

[266] S. Szpak, P. A. Mosier-Boss, F. Gordon, J. Dea, M. Miles, J. Khim, and L. Forsley, "LENR Research Using Co-Deposition," tech. rep., 2008.

[267] C. Gotzmer, L. F. DeChiaro, K. Conley, M. Litz, M. Millett, J. Ewing, L. P. Forsley, K. J. Long, W. A. Wichart, P. A. Mosier-Boss, J. Sullivan, E. Perry, and O. M. Barham, "Li-Pd-Rh-D2O electrochemistry experiments at elevated voltage," *APL Energy*, vol. 1, 12 2023.

[268] B. Jaleh, A. Nasri, N. Shahbazi, and H. Nikfarjad, "Surface properties of uv irradiated cr-39 polymer before and after chemical etching and registration of fingerprints on cr-39," *Radiation Measurements*, vol. 101, pp. 22–28, 2017.

[269] P. A. Boss, F. E. Gordon, S. Szpak, and L. P. G. Forsley, "System and Method for Generating Particles," tech. rep., US Patent, 4 2013.

[270] M. McKubre, F. Tanzella, I. Dardik, A. El Boher, T. Zilov, E. Greenspan, C. Sibilia, and V. Violante, "Replication of condensed matter heat production," ACS Publications, 2008.

[271] D. Letts and D. Cravens, "Laser stimulation of deuterated palladium: past and present," in *Condensed Matter Nuclear Science*, pp. 159–170, World Scientific, 2006.

[272] D. Letts, "Highly reproducible lenr experiments using dual laser stimulation," *Current Science*, vol. 108, no. 4, p. 559, 2015.

[273] M. J. Guffey, Y. Tang, and P. King, "Attempted replication of excess heat in the letts dual-laser experiment," *Journal of Condensed Matter Nuclear Science*, vol. 20, no. 1, pp. 1–28, 2016.

[274] V. Violante, P. Tripodi, D. Di Gioacchino, R. Borelli, A. Pizzuto, M. McKubre, F. Tanzella, A. Adrover, M. Giona, and L. Capobianco, "Metallurgical effects on the dynamic of hydrogen loading in pd," in *The 9th International Conference on Cold Fusion, Condensed Matter Nuclear Science*, p. 383, 2002.

[275] H. Kimizuka, S. Ogata, and M. Shiga, "Mechanism of fast lattice diffusion of hydrogen in palladium: Interplay of quantum fluctuations and lattice strain," *Physical Review B*, vol. 97, no. 1, p. 014102, 2018.

[276] H. Akiba, M. Kofu, H. Kobayashi, H. Kitagawa, K. Ikeda, T. Otomo, and O. Yamamuro, "Nanometer-size effect on hydrogen sites in palladium lattice," *Journal of the American Chemical Society*, vol. 138, no. 32, pp. 10238–10243, 2016.

[277] R. Z. Valiev, Y. Estrin, Z. Horita, T. G. Langdon, M. J. Zehetbauer, and Y. Zhu, "Producing bulk ultrafine-grained materials by severe plastic deformation: ten years later," *Jom*, vol. 68, pp. 1216–1226, 2016.

[278] T. Hongo, K. Edalati, H. Iwaoka, M. Arita, J. Matsuda, E. Akiba, and Z. Horita, "High-pressure torsion of palladium: Hydrogen-induced softening and plasticity in ultrafine grains and hydrogen-induced hardening and embrittlement in coarse grains," *Materials Science and Engineering: A*, vol. 618, pp. 1–8, 2014.

[279] H. K. Birnbaum and P. Sofronis, "Hydrogen-enhanced localized plasticity: a mechanism for hydrogen-related fracture," *Materials Science and Engineering: A*, vol. 176, no. 1-2, pp. 191–202, 1994.

[280] H. Jamieson, G. Weatherly, and F. Manchester, "The $\beta$ $\alpha$ phase transformation in palladium-hydrogen alloys," *Journal of the Less Common Metals*, vol. 50, no. 1, pp. 85–102, 1976.

[281] S. Goods and S. Guthrie, "Mechanical properties of palladium and palladium hydride," *Scripta Metallurgica;(United States)*, vol. 26, no. 4, 1992.

[282] G. Jimenez, E. Dillon, J. Dahlmeyer, T. Garrison, T. Garrison, S. Darkey, K. Wald, J. Kubik, D. Paciulli, M. Talukder, *et al.*, "A comparative assessment of hydrogen embrittlement: palladium and palladium-silver (25 weight% silver) subjected to hydrogen absorption/desorption cycling," *Advances in Chemical Engineering and Science*, vol. 6, no. 03, p. 246, 2016.

[283] G. P. Chambers, G. K. Hubler, and K. S. Grabowski, "Search for energetic charged particle reaction products during deuterium charging of metal lattices," pp. 383–396, AIP Publishing, 6 2008.

[284] M. Maeda and T. Iwata, "Dissociation Constants of Ammonium Ion and Activity Coefficients of Ammonia in Aqueous Ammonium Sulfate Solutions," tech. rep., 1997.

[285] R. Dawson and G. Kelsall, "Recovery of platinum group metals from secondary materials. I. Palladium dissolution in iodide solutions," *Journal of Applied Electrochemistry*, vol. 37, pp. 3–14, 12 2006.

[286] A. Muiioz-Phezt and D. C. Koningsberger, "Decomposition of the Precursor [Pt(NH&](OH)z, Genesis and Structure of the Metal-Support Interface of Alumina Supported Platinum Particles: A Structural Study Using TPR, MS, and XAFS Spectroscopy," tech. rep., 1995.

[287] N. J. Johnson, B. Lam, B. P. MacLeod, R. S. Sherbo, M. Moreno-Gonzalez, D. K. Fork, and C. P. Berlinguette, "Facets and vertices regulate hydrogen uptake and release in palladium nanocrystals," 5 2019.

[288] M. Fleischmann and S. Pons, "Electrochemically induced nuclear fusion of deuterium," *Journal of Electroanalytical Chemistry and Interfacial Electrochemistry*, vol. 261, pp. 301–308, 4 1989.

[289] M. Fleischmann, S. Pons, M. W. Anderson, L. J. Li, and M. Hawkins, "Calorimetry of the palladium-deuterium-heavy water system," *Journal of Electroanalytical Chemistry and Interfacial Electrochemistry*, vol. 287, pp. 293–348, 7 1990.

[290] E. Storms, "PROGRESS REPORT #4," tech. rep., 9 2015.

[291] E. Storms, "Ways to Initiate a Nuclear Reaction in Solid Environments," tech. rep.

[292] M. Swartz, ""Optimal Operating Point Characteristics of Nickel Light Water Experiments"," in *Proceedings of The Seventh International Conference on Cold Fusion*, (SaltLakeCity), ICCF, 1998.

[293] L. J. Cabri, T. Oberthür, and R. R. Keays, "Origin and depositional history of platinum-group minerals in placers - A critical review of facts and fiction," *Ore Geology Reviews*, vol. 144, p. 104733, 5 2022.

[294] K. J. Aoki, "Frequency dependence of electric double layer capacitance without Faradaic reactions," *Journal of Electroanalytical Chemistry*, vol. 779, pp. 117–125, 10 2016.

[295] F. A. A. Nugroho, I. Darmadi, V. P. Zhdanov, and C. Langhammer, "Universal scaling and design rules of hydrogen-induced optical properties in Pd and Pd-alloy nanoparticles," *ACS Nano*, vol. 12, no. 10, pp. 9903–9912, 2018.

[296] Z. Li and X. Meng, "Recent development on palladium enhanced photocatalytic activity: A review," *Journal of Alloys and Compounds*, vol. 830, p. 154669, 7 2020.

[297] F. Marques, M. Balcerzak, F. Winkelmann, G. Zepon, and M. Felderhoff, "Review and outlook on high-entropy alloys for hydrogen storage," 10 2021.

[298] L. Jiang and M. J. Demkowicz, "Surface coverage-limited hydrogen uptake into nickel under cathodic charging," *Corrosion Science*, vol. 202, p. 110280, 7 2022.

[299] E. Storms, "How the explanation of lenr can be made consistent with observed behaviour and natural laws," *Current Science*, pp. 531–534, 2015.

[300] E. Storms, "Introduction to the main experimental findings of the lenr field," *Current Science*, pp. 535–539, 2015.

[301] M. H. Miles, B. F. Bush, and K. B. Johnson, *Anomalous effects in deuterated systems*. Citeseer, 2019.

[302] G. K. Hubler, K. K. Katti, D. Pease, A. El Boher, O. Azzizi, J. He, and K. V. Katti, "Long term anomalous heat from 9 nm pd nanoparticles in an electrochemical cell," *Journal of Condensed Matter Nuclear Science*, vol. 36, no. 1, pp. 38–47, 2022.

[303] "Press Release: U.S. Department of Energy Announces $10 Million in Funding to Projects Studying Low-Energy Nuclear Reactions." https://arpa-e.energy.gov/news-and-media/press-releases/us-department-energy-announces-10-million-funding-projects-studying. Accessed: 2024-09-16.

[304] D. Alexandrov, "Low-energy nuclear fusion reactions in solids: Experiments," *International Journal of Energy Research*, vol. 45, no. 8, pp. 12234–12246, 2021.

# Appendix A

# Appendix

## A.1 Staker-like replication with ultra-long duration

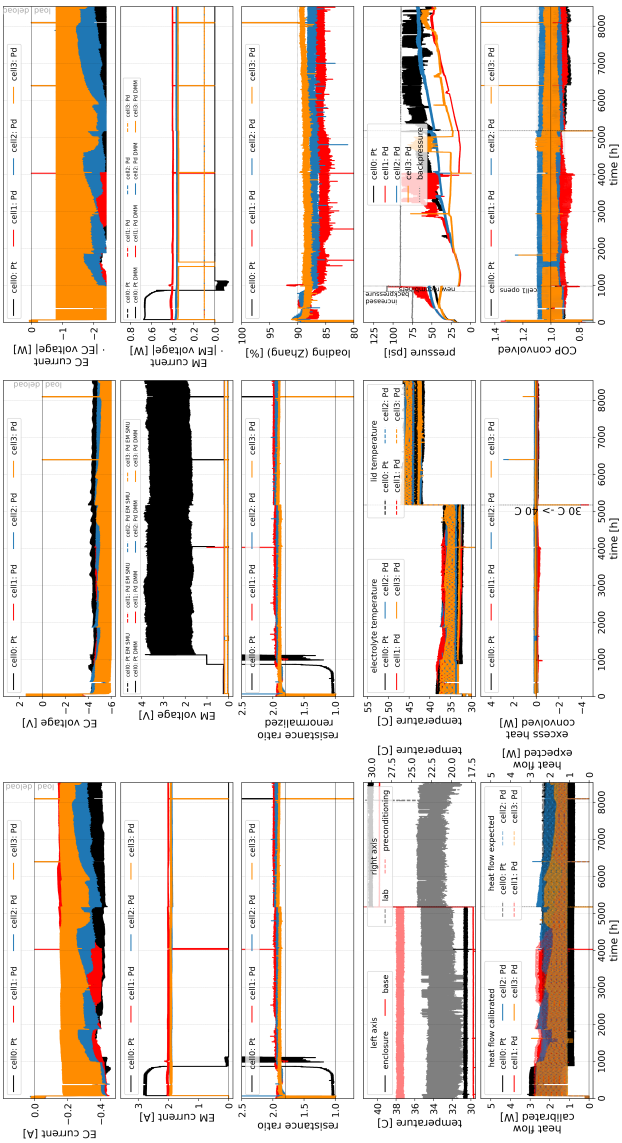


Fig. A.1: Full dataset for Staker-like ultra-long duration experiment.

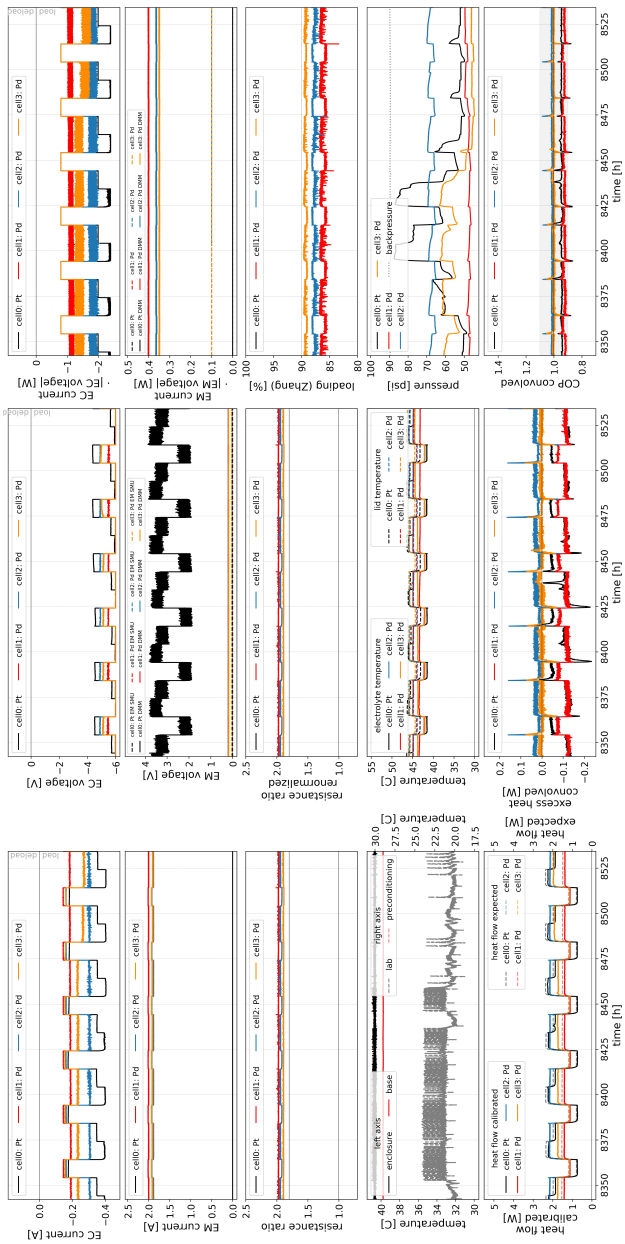


Fig. A.2: Zoom into an arbitrary week towards the end of the experiment shown in fig. A.1.

## A.2 Storms Replication

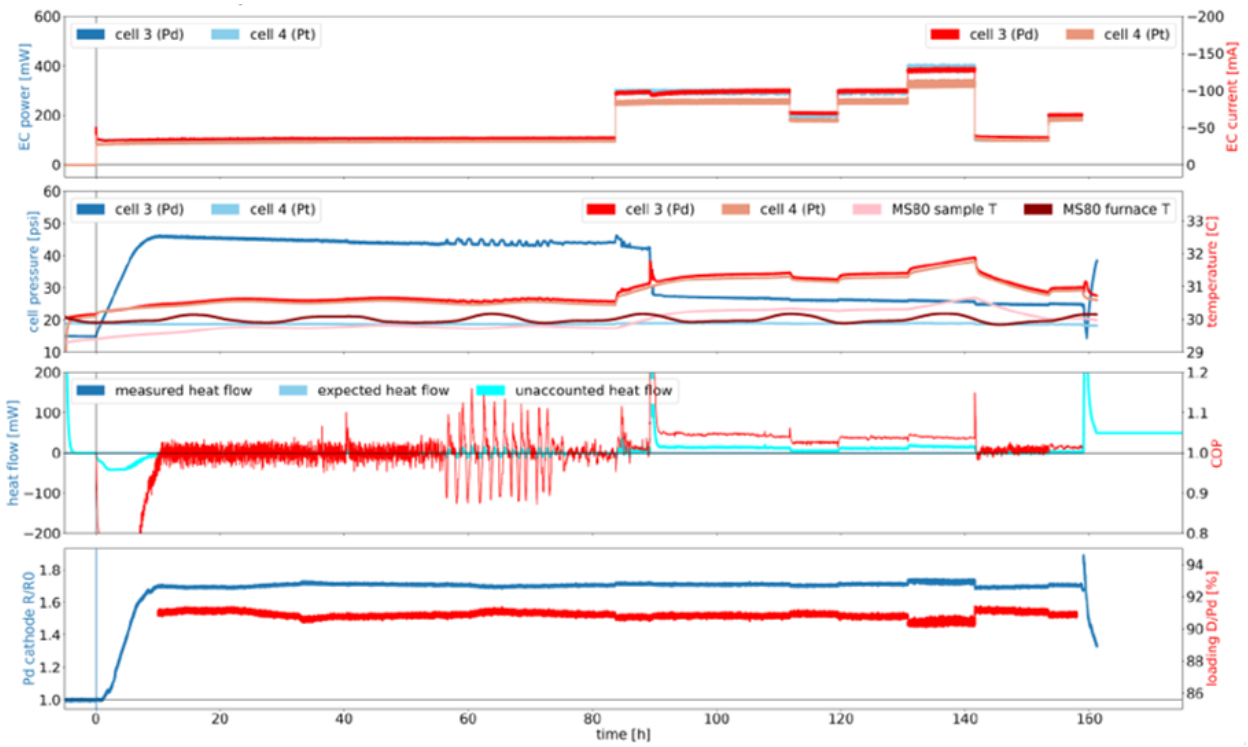



Fig. A.3: Overview of BE1137 showing experimental parameters, telemetry, and heat flow for cell pair 3,4.

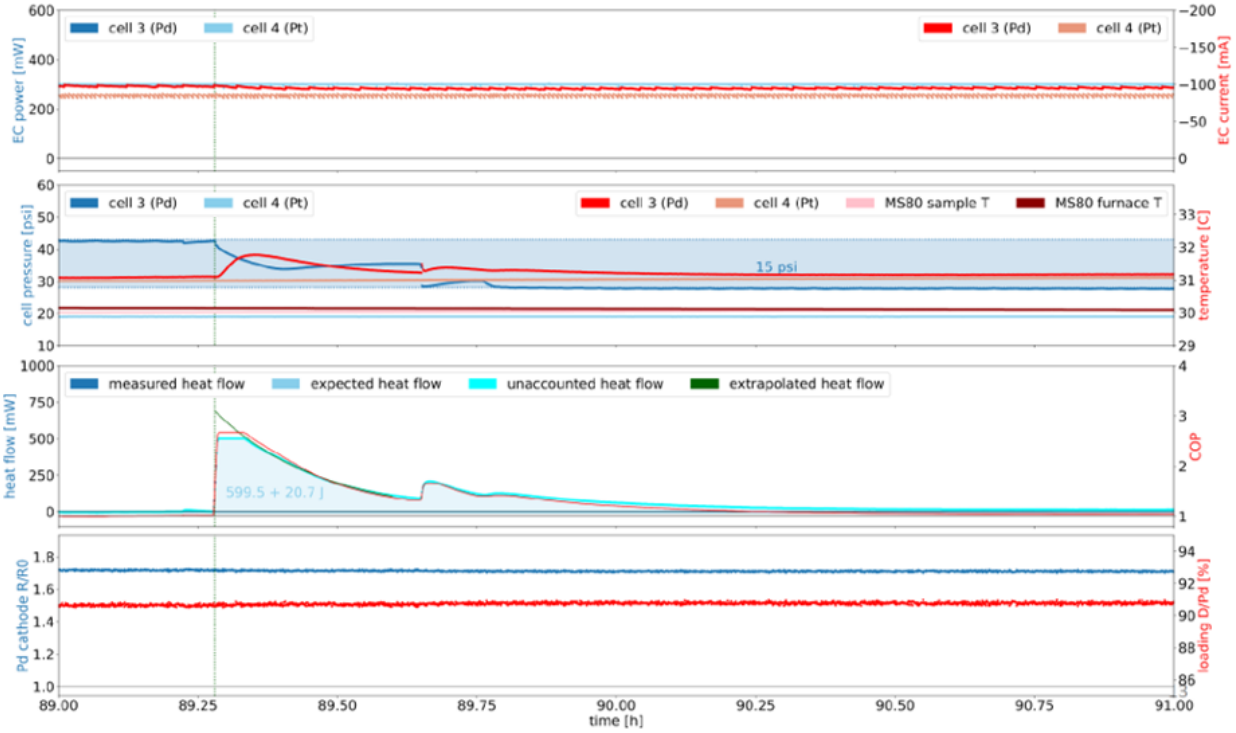



Fig. A.4: Overview of BE1137 showing experimental parameters, telemetry, and heat flow for cell pair 3,4.

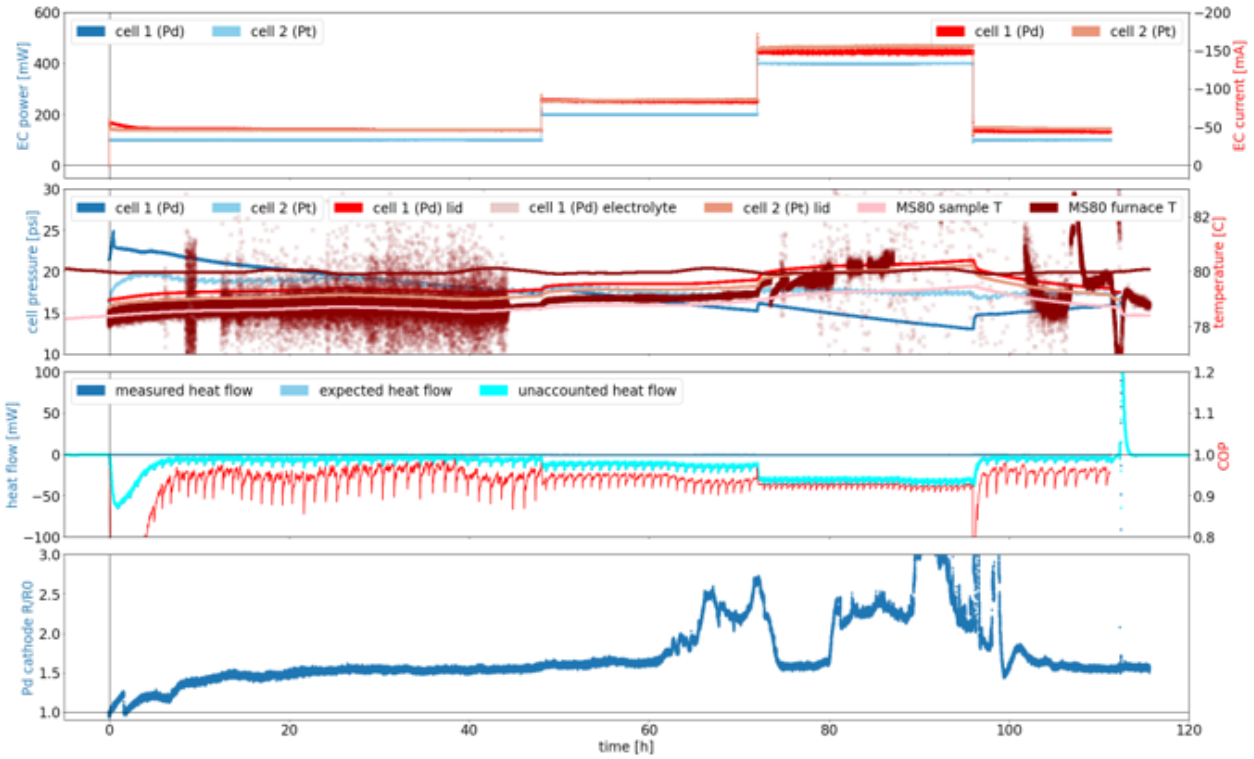



Fig. A.5: Overview of BE1137 showing experimental parameters, telemetry, and heat flow for cell pair 1,2.

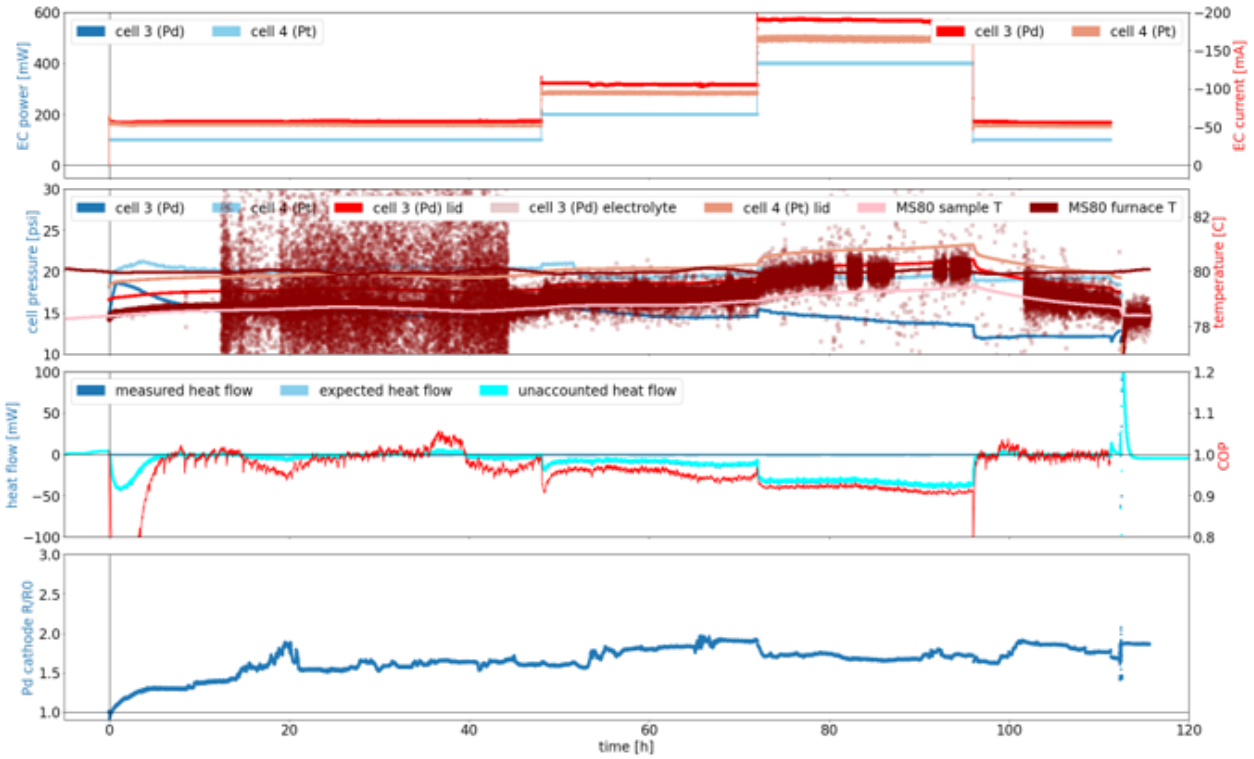



Fig. A.6: Overview of BE1137 showing experimental parameters, telemetry, and heat flow for cell pair 3,4.

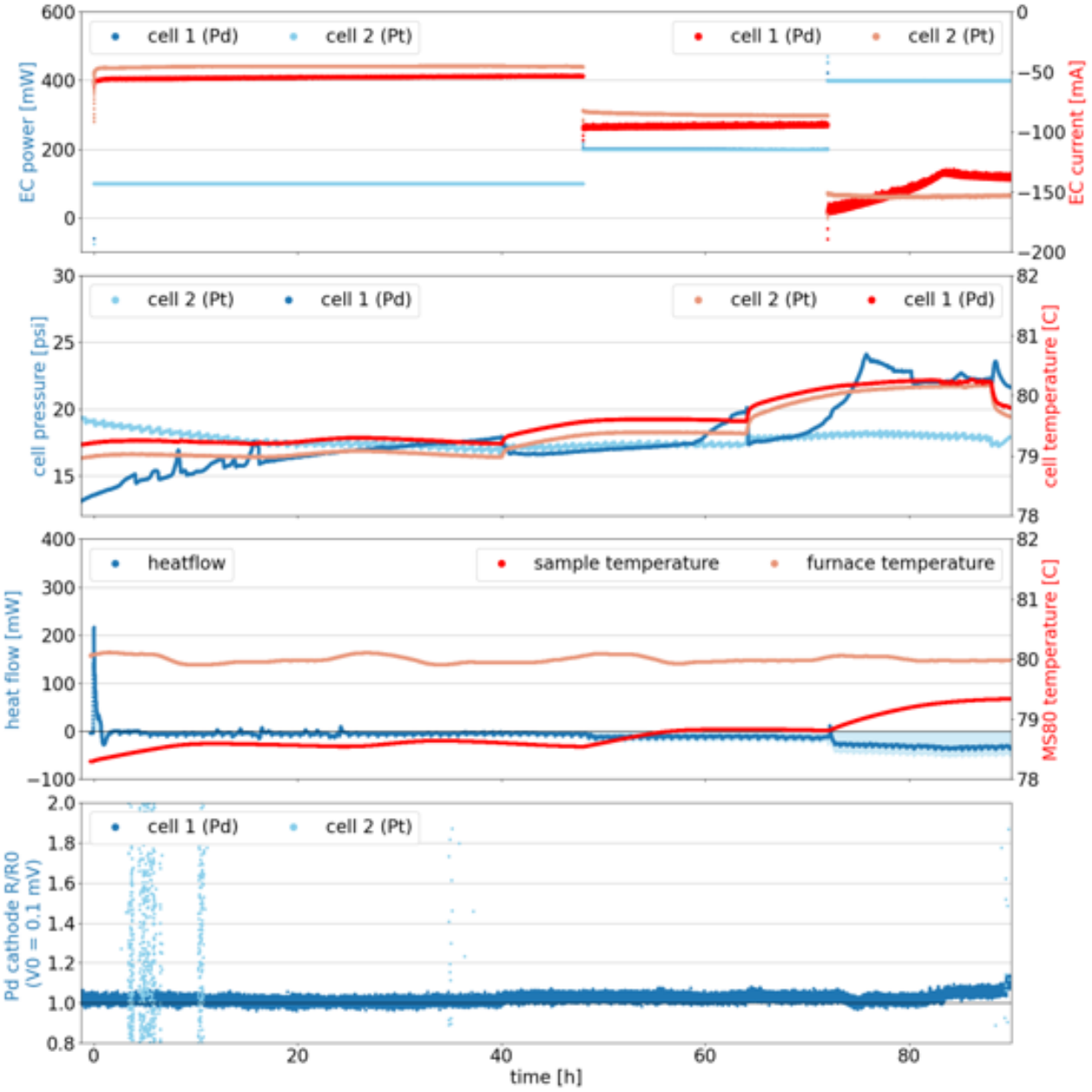



Fig. A.7: Overview of BE1199 showing experimental parameters, telemetry, and heat flow for cell pair 1,2.

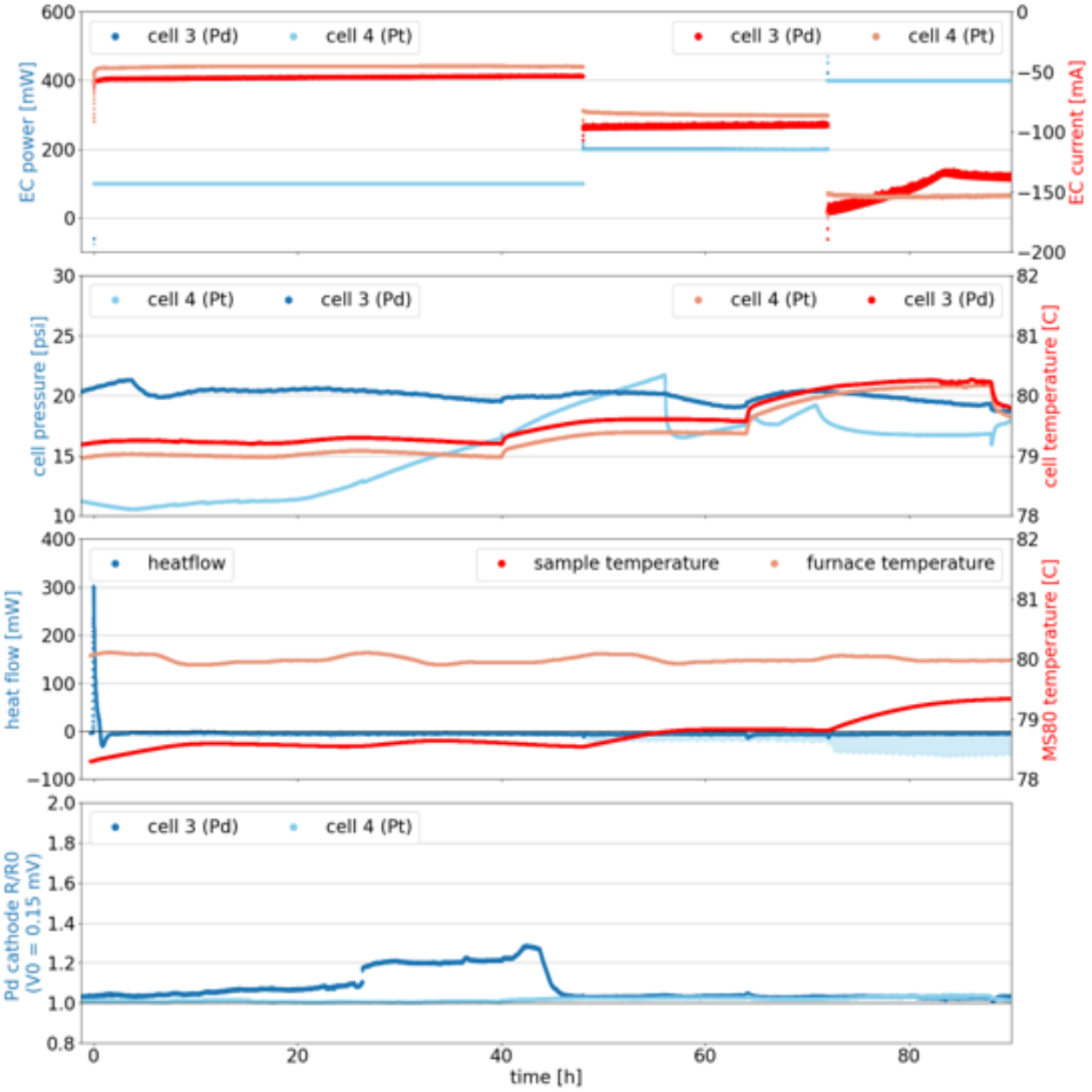



Fig. A.8: Overview of BE1199 showing experimental parameters, telemetry, and heat flow for cell pair 3,4.

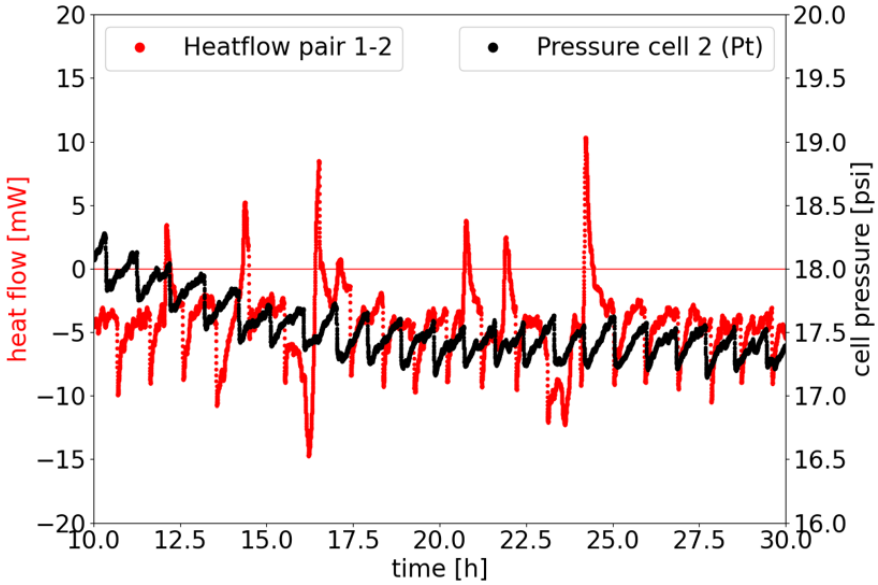



Fig. A.9: Zoom-in of oscillations observed in test BE1199.

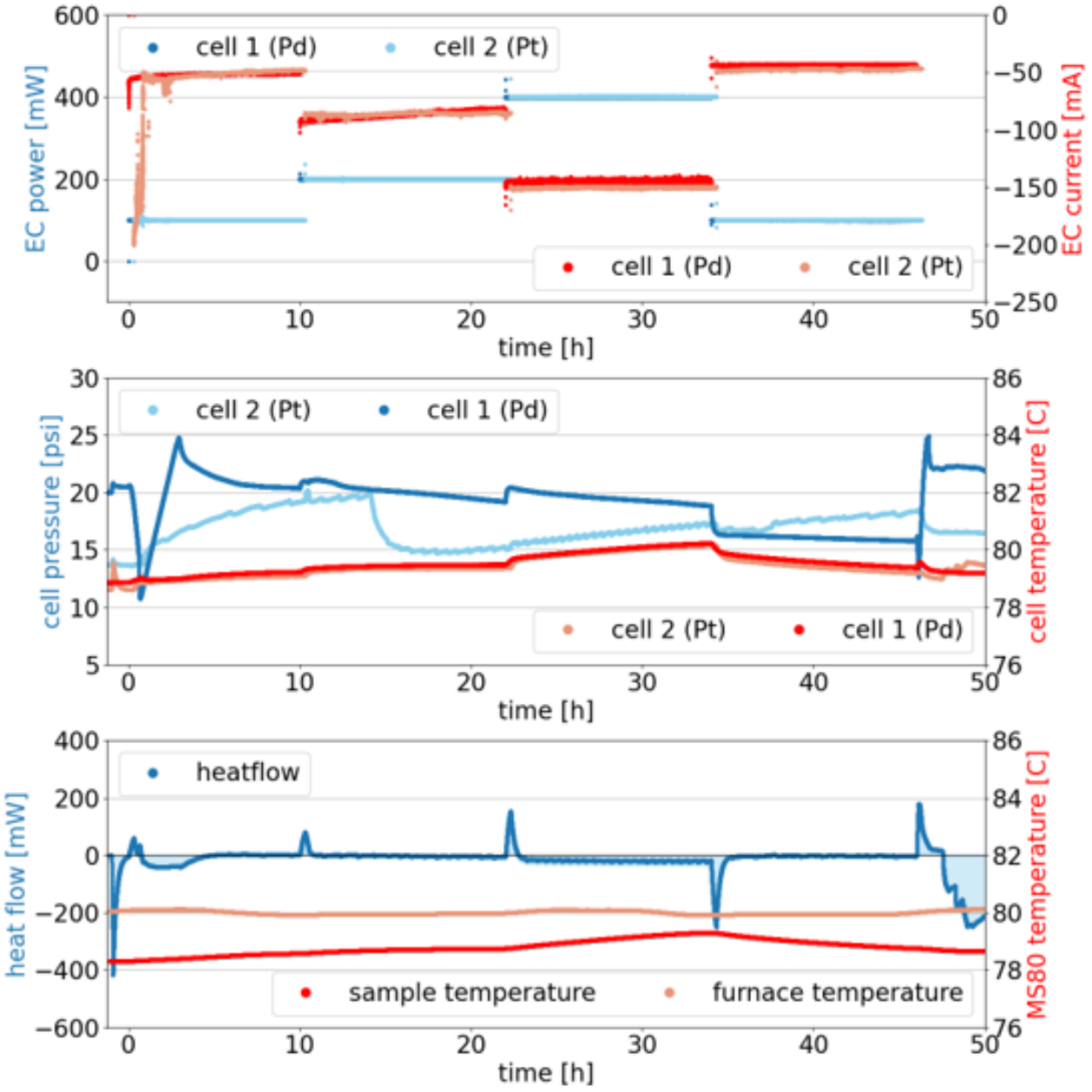



Fig. A.10: Overview of BE1226 showing experimental parameters, telemetry, and heat flow for cell pair 1,2.

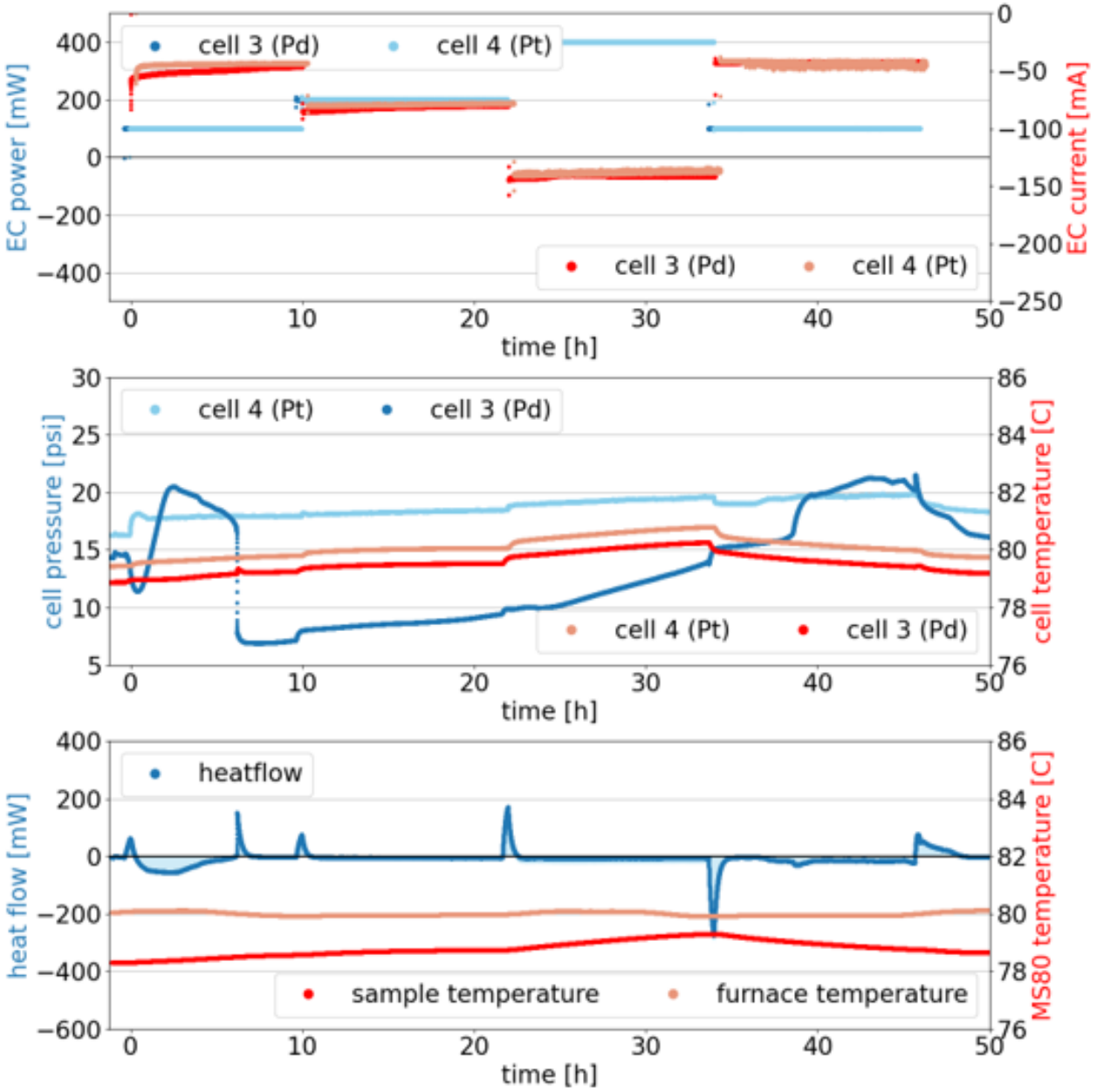



Fig. A.11: Overview of BE1226 showing experimental parameters, telemetry, and heat flow for cell pair 3,4.

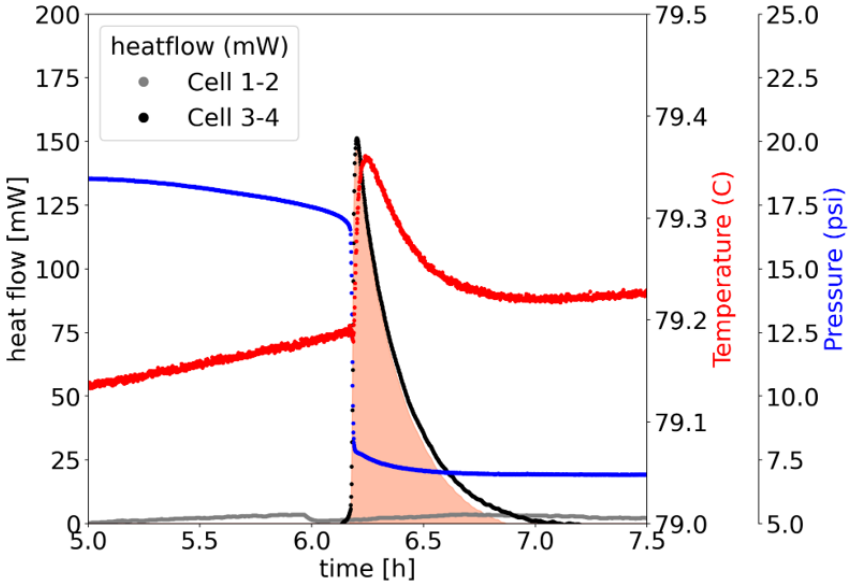



Fig. A.12: BE1226: Transient recombination leads to measured heat flow.

## A.3 Acknowledgments

The Callisto Electrochemical Research Team would like to acknowledge the following individuals for their invaluable contributions throughout the duration of this project. Their talent, dedication, and hard work were instrumental in making this endeavor possible:

[Redacted. Names may be added in a later revision of this document.]